National Library of Canada
Acquisitions and Bibliographic Services Branch
395 Wellington Street
Ottawa, Ontario
K1A 0N4

Bibliothèque nationale du Canada
Direction des acquisitions et des services bibliographiques
395, rue Wellington
Ottawa (Ontario)
K1A 0N4

Your file Votre référence

Our file Notre référence

NOTICE

The quality of this microform is heavily dependent upon the quality of the original thesis submitted for microfilming. Every effort has been made to ensure the highest quality of reproduction possible.

If pages are missing, contact the university which granted the degree.

Some pages may have indistinct print especially if the original pages were typed with a poor typewriter ribbon or if the university sent us an inferior photocopy.

Reproduction in full or in part of this microform is governed by the Canadian Copyright Act, R.S.C. 1970, c. C-30, and subsequent amendments.

AVIS

La qualité de cette microforme dépend grandement de la qualité de la thèse soumise au microfilmage. Nous avons tout fait pour assurer une qualité supérieure de reproduction.

S'il manque des pages, veuillez communiquer avec l'université qui a conféré le grade.

La qualité d'impression de certaines pages peut laisser à désirer, surtout si les pages originales ont été dactylographiées à l'aide d'un ruban usé ou si l'université nous a fait parvenir une photocopie de qualité inférieure.

La reproduction, même partielle, de cette microforme est soumise à la Loi canadienne sur le droit d'auteur, SRC 1970, c. C-30, et ses amendements subséquents.

Canada

NONLINEAR FINITE ELEMENT ANALYSIS OF NORMAL AND HIGH STRENGTH CONCRETE STRUCTURES

by

Mohsen Ali Shayanfar

August 1995

Department of Civil Engineering and Applied Mechanics
McGill University
Montreal, Canada

A thesis submitted to
the Faculty of Graduate Studies and Research
in partial fulfilment of the requirements for the degree of
Doctor of Philosophy

National Library
of Canada

Acquisitions and
Bibliographic Services Branch

395 Wellington Street
Ottawa, Ontario
K1A 0N4

Bibliothèque nationale
du Canada

Direction des acquisitions et
des services bibliographiques

395, rue Wellington
Ottawa (Ontario)
K1A 0N4

Your file Votre référence

Our file Notre référence

ISBN 0-612-12482-7

Canada

In the name of God

To:

My Parents, My Wife: Futemeh

and

My Daughters: Elham and Azadeh

ABSTRACT

This thesis presents a new hypoelasticity model which was implemented in nonlinear finite formulation to analyze normal and high strength reinforced concrete structures under both monotonically increasing and reversed cyclic loadings. The model includes a new hypoelasticity constitutive relationship utilizing the rotation of material axis through subsequent iterations, employment of both fixed and rotating crack models, compressive strength degradation in post-cracking regime, new uniaxial stress-strain relationships for concrete under monotonically increasing and reversed cyclic loadings, accounting for mesh sensitivity, and utilizing the tensile strength degradation due to extensive internal microcracking of the concrete. The model can account for high nonlinearity of the stress-strain behaviour of concrete in the pre-peak regime, the softening behaviour of concrete in the post-peak regime, the stiffness degradation caused by the extension of microcracks during subsequent unloadings and reloadings and the irrecoverable volume dilatation at high levels of compressive load.

The effect of element size on different behaviourial aspects of reinforced concrete elements including the load-displacement and load-strain characteristics, crack pattern and ultimate load are discussed along with a comparison with the experimental data where available. Various analyses indicated that the length of the descending branch of the tensile stress-strain curve of concrete defined by the value of the ultimate tensile strain, ε_{tu}, has a significant effect on the computed results. If the value of ε_{tu} is adjusted appropriately according to the element size, it can help eliminate the mesh sensitivity drawback. To adjust an appropriate value for ε_{tu}, two models have been used: a) crack band model, as a function of the fracture energy, mesh size and tensile strength of concrete, and b) a new proposed model as a function of only the element size. The analytical results obtained using the different models are compared with the experimental results; the proposed model gives good agreement. The proposed formula is very simple and can be used for both square and non-square elements.

The effect of steel reinforcement details on the general behaviour of the structure and its mode of failure, the criterion for using the rotating crack model versus the fixed crack model, and the importance of compressive strength degradation in the post-crack regime are established using

detailed analysis of five shear panels tested by Vecchio and Collins (1982). The effect of a sudden drop of the stress after the tensile strength of concrete has been exceeded on the load-deflection response, the ductility ratio and the crack pattern for two high strength concrete beams are also examined. Further analyses of a squat shear wall and a shear panel are carried out to examine the reliability of the computer program HODA developed in this study for analysis of concrete structures under both monotonic and reversed cyclic loads.

Complete response of three structural walls in a low-rise building is studied under monotonically increasing loads until failure using the nonlinear finite element program HODA. The influence of the tension-stiffening, steel strain-hardening on the load-deflection response and the ultimate load are studied for the case of the rectangular wall. The influence of smeared steel idealization and bar element idealization on the wall response are also investigated. The ultimate loads of walls are compared with the values calculated using the current CSA Standard CAN3-A23.3-M84.

This research program demonstrates the feasibility of nonlinear finite element analysis as an alternative to costly experimental work in the future, however, the reliability of using nonlinear finite element analysis for a given structural system under a given loading system could be established in each case by comparing the computed results with the experimental data, where available.

SOMMAIRE

Cette thèse propose un nouveau modèle hypoélastique, incorporé dans une formulation d'éléments finis non-linéaires, pour l'analyse des structures en béton (normal ou haute performance) sous un chargement monotonique ou cyclique. La formulation fait appel à la rotation des axes des éléments à chaque itération, à l'utilisation de modèles de fissures fixes et de révolution, tient compte de la perte de résistance en compression dans le régime fracturé, incorpore une nouvelle relation contraintes-déformations pour le béton sous chargement monotonique et cyclique, et finalement tient compte de l'influence de la discrétisation, et de la dégradation de la résistance en tension associée à la micro-fissuration interne du béton. Le modèle peut représenter le caractère non-linéaire de la relation contraintes-déformations du béton dans la régime post-fissuration, la perte de rigidité associée au développement de micro-fissures lors du déchargement et de chargements subséquents de l'élément, et les changements de volumes irréversibles (expansion) associés avec des forces de compressions élevées.

L'effet du degré de discrétisation de l'élément par rapport à différents aspects du comportement sont étudiées, entre autres, l'estimation de la courbe contraintes-déformations ou forces-déplacements, le patron de fissuration, et la charge ultime. Les résultats sont comparés à des observations expérimentales lorsque disponibles. Les analyses indiquent que la déformation ultime en tension (e_u), contrôlant la partie descendante de la courbe contraintes-déformations en tension, a un effet majeur sur les résultats. Un ajustement approprié de ce paramètre en fonction de la dimension des éléments minimise l'influence de la discrétisation sur les résultats. Deux méthodes sont utilisées pour sélectionner e_u : (1) un modèle de fissuration continu en fonction de l'énergie de fissuration, le niveau de discrétisation et la résistance en tension du béton, et (2) un nouveau modèle qui n'est fonction que du niveau de discrétisation. Les résultats analytiques pour les deux modèles sont comparés à des résultats expérimentaux et démontrent que le modèle proposé reproduit les résultats expérimentaux. La formule proposée est simple et applicable à des éléments de toute forme.

Une analyse détaillée des résultats expérimentaux de Vecchio et Collins (1982) sur cinq panneaux de cisaillement permet d'établir l'influence des détails d'armature d'acier sur le comportement général de la structure ainsi que sur le mode de rupture. Ceux-ci sont aussi utilisés pour analyser l'influence du modèle de fissuration de révolution par rapport au modèle de fissuration fixe, ainsi que l'influence de la dégradation de la résistance en compression sur le comportement post-fissuration. L'effet d'une baisse soudaine des contraintes suite à un chargement jusqu' à la résistance en tension, le rapport de ductilité, et le patron de fissuration sont également analysés pour deux poutres en béton à haute résistance. Des analyses supplémentaires sont faites sur un mûr et un panneau de cisaillement afin d'établir la fiabilité du logiciel d'analyse HODA développé dans le cadre de ce projet pour les structures de béton sous chargement monotonique et cyclique.

Le comportement complet de trois mûrs porteurs pour un édifice à faible hauteur sont étudiés sous un chargement monotonique avec le logiciel HODA jusqu''à la rupture. L'influence du raidissement sous tension, et de l'accroissement de la résistance de l'acier avec les déformations sur la courbe forces-déplacements ainsi que sur la charge ultime sont analysés pour le cas du mûr rectangulaire. L'influence de l'idéalisation de l'acier par une zone homogénéisée et des barres d'armature sur la réponse sont aussi examinés. Les charges ultimes sont comparées avec les valeurs calculées selon le code CSA CAN3-A23.3-M84.

Ce programme de recherche démontre que les analyses numériques non-linéaires peuvent être substituées à des programmes expérimentaux dispendieux. Par contre, la fiabilité des analyses numériques devrait être établie pour chaque type de structure et de chargement à l'aide de résultats expérimentaux.

ACKNOWLEDGEMENTS

The author would like to take this opportunity to express his deepest gratitude to his thesis supervisor, Professor M.S. Mirza, for his valuable suggestions, constant encouragement and support throughout the course of this research program. The author will never forget what he learned, all with great pleasure, and wishes to follow Professor Mirza's path both in teaching and research in the future. I must express my appreciation for dozens of long consultation meetings to discuss complex technical problems; his emphasis on fundamentals always provided a clear picture of the problem. His promptness in returning the draft of the various chapters and the final thesis draft was amazing, with not more than one or two working days, and with detailed constructive and critical comments. I am deeply grateful to him for all his assistance.

The authors would like to thank Dr. A. G. Razaqpur of the Department of Civil Engineering, Carleton University, Ottawa, for making available the NONLACS computer program for ongoing research activity at McGill University.

Special thanks are also due to the consultants and operations staff of the McGill University Computer Center, specially Dr. H. Young, Mr. H. Heitner and Mr. G. L. Lebovics for their advice and generous allocation of the required computer funds.

The excellent French translation of the abstract by Prof. L. Chouinard is very much acknowledged.

The assistance and guidance provided by Mr. C. Manatakos at the early stage of this work, the collaboration of Mr. A. Kheyroddin in investigating the mesh size effect phenomenon, and the assistance of Mr. S.A. Lim in the analysis of structural walls are gratefully acknowledged.

The financial assistance provided by the Ministry of Culture and Higher Education of the Islamic Republic of Iran is highly appreciated. The support of the Natural Science and Engineering Research Council to the ongoing research program at McGill University are also gratefully acknowledged.

Most of all, the author is grateful to his parents, wife and his two daughters: Elham and Azadeh, because without their patience, encouragement, and understanding, this undertaking could never have been achieved .

TABLE OF CONTENTS

CHAPTER 3

CHAPTER 4

CHAPTER 5

CHAPTER 6

LIST OF FIGURES

LIST OF TABLES

LIST OF SYMBOLS

$\{\Delta\varepsilon\}$ = incremental strain vector in local coordinate system

$\{\Delta\varepsilon_{iu}\}$ = incremental equivalent uniaxial strain vector

$\{\Delta\varepsilon'_i\}$ = incremental principal strain vector in new principal coordinate system

$\{\varepsilon\}$ = vector of initial strains

$\{\varepsilon\}$ = strain vector at any point within the finite element

$\{\varepsilon_{i\,new}\}$ = current principal strain vector

$\{\varepsilon_{i\,old}\}$ = previous principal strain vector

$\{\varepsilon_{iu\,old}\}$ = previous equivalent uniaxial strain vector

$\{\varepsilon_{new}\}$ = current strain vector in local coordinate system

$\{\varepsilon_{old}\}$ = previous strain vector in local coordinate system

$\{\varepsilon'_{i\,old}\}$ = previous principal strain vector transformed to the new principal coordinate system

$\{\varepsilon'_{iu\,old}\}$= previous equivalent uniaxial strain vector transformed to the new principal coordinate

$\{\sigma\}$ = stress vector at any point within the finite element

$\{\sigma\}$ = vector of initial stresses

$\{\chi\}$ = vector of curvature

$\{D\}$ = nodal displacement of the structure in global coordinate system

$\{D\}_n$ = vector of element nodal displacements in global coordinate system

$\{D_i\}$ = nodal displacement vector of the structure in global coordinate system in i^{th} iteration

$\{F\}$ = vector of equivalent nodal forces of the structure

$\{F\}_n$ = vector of element nodal forces in global coordinate system

$\{F_0\}^1$ = Norm vector

$\{P\}$ = vector of body forces

$\{R\}$ = vector of applied external loads

$\{S\}_n$ = vector of element nodal forces in local coordinate system

$\{T\}$ = vector of surface traction

$\{U\}$ = displacement vector at any point of the structure

$\{U\}_n$ = element nodal displacement vector in local coordinate system

$\{U_b\}$ = element nodal bending displacement vector

$\{U_p\}$	=	element nodal inplane displacement vector
β	=	shear retention factor
γ	=	engineering-shear strain; softening parameter
δ_{ij}	=	Kronecker delta
ε	=	strain
ε_{cr}	=	cracking strain of concrete
ε_{cu}	=	concrete strain at peak stress
ε_{en}	=	Strain corresponding to unloading point on envelope curve
ε_i	=	strain corresponding to σ_i
ε_{ic}	=	Equivalent uniaxial strain corresponding to σ_{ic}
ε_{ij}	=	strain tensor
ε_{it}	=	Equivalent uniaxial tensile strain of concrete corresponding to σ_{it}
ε_{itu}	=	Ultimate equivalent uniaxial tensile strain of concrete in ith direction; i=1, 2
ε_{iu}	=	Equivalent uniaxial strain in ith direction; i=1, 2
ε_p	=	Plastic strain
ε_{pp}	=	Plastic strain corresponding to peak stress
ε_s	=	strain in steel
ε_{su}	=	ultimate strain at rupture for reinforcing steel
ε_{sy}	=	steel strain at yield
ε_t	=	Strain corresponding to the uniaxial tensile strength
ε_{tu}	=	Ultimate uniaxial tensile strain of concrete
ε_{tu}	=	ulimate concrete strain in uniaxial tension
ε_u	=	ultimate compressive strain of concrete
θ_{new}	=	angle between new principal axis 1 with respect to the local coordinate axis X
θ_{old}	=	angle between previous principal axis 1 with respect to the local coordinate axis
θ_x	=	plate normal rotation about X-axis
θ_y	=	plate normal rotation about Y-axis
λ, μ	=	material constants (Lamé's constants)
ν	=	equivalent Poisson's ratio
ν_i	=	Initial Poisson's ratio
ν_{ij}	=	Poisson's ratio in ith direction due to uniaxial loading in jth direction; i, j=1, 2
σ	=	Stress

$\sigma_1(\sigma_2)$	=	major (minor) principal stress
σ_{en}	=	Stress corresponding to unloading point on envelope curve
σ_{ic}	=	compressive strength of biaxially loaded concrete in direction i, i=1, 2
σ_{ij}	=	stress tensor
σ_{it}	=	tensile strength of concrete in ith direction; i=1, 2
σ_m	=	hydrostatic or mean stress
τ_{xy}	=	shear stress
ϕ	=	fracturing surface
$\Phi(\varepsilon_{ij})$	=	strain energy function
ω	=	drilling degree of freedom in membrane element
$\Omega(\sigma_{ij})$	=	complementary energy-density function
A	=	element area in mm^2, or in^2
A_s	=	area of steel reinforcement
C_{ijkl}	=	material constant (component of the costitutive matrix)
$d\varepsilon^p_{ij}$	=	plastic strain increment
$d\varepsilon^e_{ij}$	=	elastic strain increment
$d\varepsilon_{kl}$	=	incremental strain
$d\sigma_{ij}$	=	incremental stress
D^p_{ijkl}	=	plastic tangential stiffnesse
D^e_{ijkl},	=	elastic tangential stiffnesse
D^t_{ijkl}	=	total tangential stiffnesse
D^{ep}_{ijkl}	=	elasto-plastic tangential stiffnesse
D^{fr}_{ijkl}	=	fracturing tangential stiffnesse
E_B	=	the tangent modulus of the bar element
E_i	=	tagent moduli in principal direction i;i=1,2
E_{ij}	=	the weighted Young's modulus of elasticity corresponding to the plane i-j
E_o	=	initial modulus of elasticity of concrete
E_s	=	initial tangent modulus for reinforcing steel
E_s^*	=	tangent modulus for reinforcing steel in the strain hardening region (bi-modulus)
E_{sc}	=	Secant modulus at peak stress
E_t	=	modulus of elasticity of concrete in tension
f	=	loading surface

f_{eq}	=	equivalent tensile strength
f_{max}	=	maximum value of the loading function
FPZ	=	fracture process zone
f_r	=	modulus of rupture of concrete
f_y	=	yield strength of reinforcing steel
f'_c	=	concrete uniaxial compressive strength
f'_t	=	concrete uniaxial tensile strength
g	=	plastic potential function
G	=	shear modulus
G_I	=	fracture energy
G_{ij}	=	the shear modulus of elasticity in plane i-j
h	=	element size
h_0	=	element size corresponding to the vertical drop on concrete tensile stress-strain
H_k, H'_k	=	hardening parameters
J_2	=	second invariant of the deviatoric stress tensor
K	=	the bulk modulus
K_{IC}	=	critical stress intensity factor
LEFM	=	linear elastic fracture mechanics
MDEP	=	mesh dependency option
n_c	=	number of concrete layers in a shell element
n_{ij}	=	direction cosine of axis i with respect to axis j
NLFM	=	nonlinear fracture mechanics
n_{sp}	=	number of steel plate layers in a shell element
n_s	=	number of smeared steel layers in a shell element
P	=	nominal capactiy calculated using CSA Standard CAN3-A23.3-M84
P_{Exp}	=	experimental ultimate load
P_{HODA}	=	analytical ultimate load
P_r	=	design capacity calculated using CSA Standard CAN3-A23.3-M84
P_u	=	ultimate load
P_u	=	failure load from HODA program
S_{ij}	=	deviatoric stress tensor
S_{klmn}	=	material constant (component of the compliance matrix)

SOM	=	strength of material
t_{si}	=	thickness of smeared steel layer i
t_x, t_y	=	thickness of smeared steel layer in x and y direction
u,v,w	=	displacements in x,y, and z directions
V	=	total lateral shear
w	=	unit weight of the concrete
W_c	=	crack band width
$x^*y^*z^*$	=	local coordinate system
x,y,z	=	cartesian axes
XYZ	=	global coordinate system
$x'y'z'$	=	principal coordinate system
$[B_b]$	=	strain-bending displacement matrix
$[B_P]$	=	strain-inplane displacement matrix
[B]	=	matrix relating strains and element nodal displacements
$[C_C]_i$	=	constitutive matrix for concrete layer i
$[C_{i-1}]$	=	tangent constitutive matrix at the beginning of the iteration i
$[C_{sp}]_i$	=	constitutive matrix for steel plate layer i
$[C_S]_i$	=	constitutive matrix for smeared steel layer i
[C]	=	constitutive matrix
$[K_{BP}]$	=	inplane stiffness matrix resulted from the bar elements
$[K_i]$	=	stiffness matrix of the structure in iteration i
$[K_m]_n$	=	element stiffness matrix in local coordinate system
[K]	=	structure stiffness matrix in global coordinate system
$[k]_{bb}$	=	bending element stiffness matrix
$[K]_n$	=	element stiffness matrix in global coordinate system
$[k]_{pb}$	=	coupling element stiffness matrix
$[k]_{pp}$	=	in-plane element stiffness matrix
[N]	=	shape functions matrix
[t]	=	strain transformation matrix of bar element
$\Delta\varepsilon$	=	incremental strain
$\Delta\sigma$	=	incremental stress

CHAPTER 1

INTRODUCTION

1.1 GENERAL

Reinforced concrete is one of the most commonly used materials in civil engineering with application in all kinds of structures, such as high rise buildings, cooling towers and offshore platforms. The design of these structures is usually based on linear elastic analysis to calculate the internal forces in the structure which are then used to design and detail the section and reinforcement for the structure using appropriate Code provisions. These Codes are usually based on empirical approaches developed using experimental data, and provide design rules to satisfy safety and serviceability requirements. Although the design of reinforced concrete structures is based normally on a linear, elastic stress analysis is adequate and reliable in most cases, for complex structures under complex loading conditions, nonlinear finite element analyses are often required for design of these systems at the ultimate limit state. Reliable information on strength, failure mode, ductility and energy absorption capacity is required for the design of important reinforced concrete structures such as nuclear containments, and for the development of new types of the building systems such as coupled frame-structural wall systems, especially for the seismic loading conditions.

Prior to the development of powerful numerical methods and computers, investigation of the behaviour of concrete structures required extensive experimental work, followed by development of behavioural or empirical models for examination of responses at the serviceability and the ultimate limit states. These experiments are usually expensive, time-consuming and

required considerable human and physical resources.

The use of the finite element method as a supplement to the experiments, and in situations where experiments are difficult to perform and cumbersome, such as the determination of complete response of a 20-storey, multiple core subjected to monotonically increasing loads, has been increasing ever since the pioneering work of Ngo and Scordelis (1967) on finite element analysis of reinforced concrete beams. Extensive research has resulted in significant advances in the area of concrete constitutive relationships which have led to the development of a substantial number of finite element programs with nonlinear analysis capabilities. A partial listing of such programs is available in the reports of the ASCE Committee on Finite Element Analysis of Reinforced Concrete Structures (1982 and 1991). It is pertinent to mention that most of these nonlinear programs are within the academic environment and only a few commercial programs are available for nonlinear analysis of concrete structures.

The versatility of the finite element method as a tool for analysis of concrete structures is enhanced significantly by the incorporation of nonlinear material models. Consequently, the method is able to predict the response of a structure at all stages of its loading history, accounting for the various forms of material non-linearities and time-dependent effects.

The complexities involved in predicting the behaviour of a reinforced concrete (R C) structure up to the ultimate load, involving highly nonlinear nature of the response of the constituent composite materials- concrete and steel. This highly nonlinear behaviour is caused by many contributing factors such as nonlinear stress-strain relationships, tensile cracking, microcracking resulting from compression in concrete, crushing of the concrete, aggregate interlock, bond slip, dowel action, tension-stiffening phenomenon, shrinkage, creep, and yielding of the steel reinforcement. The incorporation of all of these nonlinear phenomena in the analysis of R C structures is a difficult task. However, the computer-based finite element method using very powerful computers now offers a strong computational tool through which the effect and interaction of the different nonlinear characteristics of R C can be studied, and thus a better understanding of the internal stress distribution can be obtained. To ascertain the reliability of the results of these nonlinear analysis, it is essential that the composite behaviour of the concrete and the steel reinforcement is modelled accurately, besides verifying the accuracy of the results of analysis of some selected structures for which detailed experimental data is available.

As pointed out earlier, one of the earliest finite element (FE) models for the analysis of R C beams was presented by Ngo and Scordelis (1967). This was followed by considerable works

in the area of the FE analysis of R C structures under monotonically increasing load such as the works by Nilson (1968), Rashid (1968), Cervenka (1970), Mufti, et al. (1971), Scanlon (1971), Hand et al. (1973), Argyris et al. (1973), Mikkola and Schnobrich (1970), Lin (1973), Kabir (1976), Gilbert and Warner (1978), Cope et al. (1980), Peterson (1981), ASCE Task Committee (1982), and Meyer and Okamura (1985), Barzegar Barzegar and Schnobrich (1986). Good reviews of these works could be found in ASCE Task Committee (1982), Bahlis (1986), Nagaraja (1987) and ASCE/ ACI Committee 447 (1991).

The FE analysis of R C members subjected to cyclic loading dates to the early 1970's. Thereafter, significant contributions in this area have been made by Muto and Masuda (1972), Imoto and Takeda (1973), Cervenka and Gerstle (1971, 1972), Darwin and Pecknold (1974), Agrawal, et al. (1976), Shipman and Gerstle (1979), Nomura, et al. (1978), Sorensen (1979), Mochizuki and Kawabe (1980), Aktan and Hanson (1980), Noguchi (1985), Stevens, et al. (1991), Rule and Rowlands (1992). An extensive overview of some of these research programs can be found in ASCE Task Committee (1982), and Meyer and Okamura (1985).

Realization of the full potential of the finite element method will require an extensive verification to determine the accuracy of the deformational response of different classes of structural elements when compared with the available experimental results. There is also a need to determine the simplest material model that best represents the behaviour of the various classes of structures.

In this research program, firstly it is attempted to find appropriate analytical models to represent the material characteristics of both concrete and steel accurately depending on the loading conditions. Secondly, all of these models are incorporated in a nonlinear finite element formulation in order to model the majority of the aforementioned material nonlinearities and their interactions. Thirdly, to evaluate the reliability of the analytical results, some well documented experimental works on normal and high strength reinforced concrete members are modeled and analyzed, and the analysis results are compared with the experimental findings. At the end, some parametric studies on three structural walls constituting the lateral load resisting system of a 4-storey building are undertaken to develop the basic data to understand the behaviour of such complex structures.

1.2 OBJECTIVES OF THE THESIS

The objectives of this thesis can be summarized as follows

1) To present a general state-of-the-art report of the constitutive relationships for concrete.

2) To introduce the hypoelasticity models as suitable models for stress-strain relationships of concrete, under both monotonically increasing and reversed cyclic loadings.

3) To introduce new constitutive relationships and new analytical stress-strain curves for normal and high strength concretes under both monotonic and reversed cyclic loads accounting for rotation of material axis, rotation of crack direction after cracking and volume dilatancy of concrete at high compressive stresses.

4) To verify the effect of finite element mesh size on the computed behaviour of selected concrete structural elements subjected to monotonically increasing loads.

5) To derive formulations to eliminate the mesh dependency phenomenon permitting analysis of structural elements using relatively large size elements with an adequate level of confidence and savings in the required computational time.

6) To incorporate the above model into a nonlinear finite element formulation to carry out nonlinear analysis.

7) To examine the reliability of the proposed material models and the finite element formulation by analyzing some specimens for which experimental results are available.

8) To investigate the influence of the various tension-stiffening models on the overall behaviour of reinforced concrete structural elements.

9) To undertake some parametric studies on relatively complex structures to generate the basic data which can be used for development of appropriate practice-oriented design procedures for structural wall systems.

1.3 THESIS ORGANIZATION

The thesis is presented in eight chapters and one appendix as follows

Chapter 1, "Introduction" explains the importance of nonlinear finite element analysis to design complex structures such as nuclear power plants, offshore structures and others to ensure all safety and serviceability requirements. It also deals with the objectives of the thesis and its organization.

Chapter 2, "Review of Constitutive Models for Concrete", presents a general state-of-the-art report of the constitutive relationships for concrete. It starts with a review of the behaviour of concrete under uniaxial, biaxial and triaxial loadings at both micro- and macro-levels. Then a brief description of five common types of constitutive relations is presented along with their advantages and disadvantages. This includes elasticity-based models, plasticity-based models, plastic-fracturing models, elastic-plastic-damage models, and endochronic models.

Chapter 3, "The Proposed Material Model", presents the proposed constitutive model for concrete and the required material properties including, the stress-strain curve, the instantaneous modulus of elasticity, the Poisson's ratio, etc. The crack modelling techniques (discrete and smeared crack models) and a brief description of the different smeared crack models (fixed, rotating and multiple crack models) in connection with the proposed hypoelasticity model are also presented. The compressive strength-degradation of the concrete in the compression-tension state after cracking is also included. The monotonic and cyclic stress-strain curves which can be used effectively for both normal and high-strength concretes, the Poisson's ratio, the failure criteria for the concrete and the constitutive model for the steel reinforcement are presented in the last part of this chapter.

Chapter 4, "Nonlinear Finite Element Formulation", describes the key features of the nonlinear finite element program, HODA, developed during the course of this study. The various program capabilities and limitations are outlined, followed by the finite element displacement formulation based on energy considerations. The element library of the program, the layered discretization technique, the transformation of strain, stress, constitutive matrix and coordinates, the assembly process, and the numerical algorithms in nonlinear analysis including the solution process, the unbalanced forces, the convergence criteria and the divergence criteria are also outlined in this chapter.

Chapter 5, "Element Size Effect Phenomenon", presents the results of an investigation into the effect of finite element size in nonlinear finite element analysis of concrete structures. To eliminate the dependence of the computed results on the finite element size, two models have been used: a) crack band model and b) a new proposed model. These models have been implemented into the nonlinear finite element analysis program HODA. The analytical results obtained using the different models are compared with the experimental results.

Chapter 6, "Analysis of Experimental Specimens", compares the computed and the experimental responses of several specimens using the HODA program. These are composed of a total of five panels tested at the University of Toronto under monotonically increasing in-plane loadings (Vecchio, 1981; Vecchio and Collins, 1982), a squat shear wall tested by Cardenas et al. (1980) under monotonically increasing load up to the ultimate load carrying capacity of the structure, two high strength concrete beams, LS1 and HUCB, tested by Leslie et al. (1976) and Abrishami et al. (1995), respectively, and a shear panel (W-4) tested by Cervenka (1970) under reversed cyclic loading. Along with the analysis of each specimen, the effect of different nonlinear characteristics of reinforced concrete (tension-stiffening, failure criteria, cracking model, ...) are also examined.

Chapter 7, "Analytical Study of Structural Walls", presents the computed responses of three structural walls subjected to distributed lateral loads using the HODA program. These include a rectangular wall, an L-shaped wall and a C-shaped wall constituting the lateral load resisting system of a 4-storey building (Manatakos, 1989). Some parametric studies are also carried out on the three walls to show the effect of tension-stiffening of the concrete and strain-

hardening of the steel reinforcement along with the type of steel idealization on the analytical response of these walls. In each case, the computed results are compared with the wall strength calculated using the CSA standard A23.3-M84.

Chapter 8, "Conclusions", summarizes the results of the thesis, highlights the key results, and makes recommendations for future work.

Appendix A presents a list of the input data file required for the HODA program.

CHAPTER 2

REVIEW OF CONSTITUTIVE MODELS FOR CONCRETE

This chapter presents a general state-of-the-art report of the constitutive relationships for concrete. It starts with a review of the behaviour of concrete under uniaxial, biaxial and triaxial loadings at both micro- and macro-levels. Then a brief description of five common types of constitutive relations is presented along with their advantages and disadvantages. This includes elasticity-based models, plasticity-based models, plastic-fracturing models, elastic-plastic-damage models, and endochronic models.

2.1 CONCRETE BEHAVIOUR

The response of concrete to uniaxial (compressive or tensile) and combined stresses is nonlinear due to the progressive microcracking at the transition zone between the aggregates and the bulk cement paste. According to the experimental observations at the micro-level, concrete can be treated to be composed of three basic phases: (1) mortar, (2) coarse aggregate, and (3) mortar-coarse aggregate interface or transition zone (see Fig. 2.1). Mortar is defined as cement paste plus sand or fine aggregate particles as illustrated in Fig. 2.1(b) and (c). In general, microcracks are initiated at the aggregate-mortar interfaces due to external loading and shrinkage of the concrete, because they represent the weakest links or flaws in the concrete.

2.1.1 Uniaxial Behaviour

The response of plain concrete in uniaxial compression is governed by the microcracks in the transition zone between the hydrated cement paste and the aggregate (Vonk, 1990). These microcracks are relatively stable and do not propagate until an applied load equal to about 30% of the concrete strength, $0.30f'_c$; within this range, the response of concrete is basically linear-elastic. With further loading up to the maximum load, these microcracks grow and propagate resulting in a decrease in the material stiffness (nonlinear response). This crack propagation does not lead to the immediate loss of load-carrying capacity, because concrete at this stage behaves as a highly redundant structure. In the pre-peak region (ascending branch of the stress-strain curve), most of the microcracks are within the so called transition zone but beyond that, in the post-peak region or the descending branch of the stress-strain curve, the extensive development of mortar cracks (cracks through mortar) is observed. The onset of mortar cracking results in increasing the Poisson's ratio of concrete (Kupfer et al., 1969) leading to the volume expansion of concrete which is termed as dilatancy (refer to Fig. 2.2). Beyond the maximum load, macrocracks localize in narrow bands and lead to a decrease in the applied load; This constitutes the strain-softening response in uniaxial compression. Finally at failure (rupture), the interface cracks and the mortar cracks interconnect leading to a discontinuous fracture surface.

The response of a concrete specimen loaded in uniaxial tension is normally linear up to the maximum load, when the microcracks due to shrinkage and external load localize in a narrow band to form macrocracks leading to a reduction in the load carrying capacity (Feenstra and de Borst, 1993). It must be noted that a significant energy input is required for formation and extension of cracks under compressive loads, while by contrast, much less energy is required for propagation of cracks under tensile loads. This is why tensile strength of concrete is a fraction of its compressive strength and it behaves linearly under tensile loads up to the maximum load (ascending branch).

In repeated loading tests under compression (refer to Fig. 2.3), the envelope curve, the line on which lie both the starting points of the unloading and the end points of the reloading cycles, has been found to be coincide with the compression stress-strain curve under monotonically increasing loads (Sinha, Gerstle and Tulin, 1964). The unloading curve is concave from the unloading point and it is characterized by the high stiffness when the unloading starts. The slope of the unloading curve decreases gradually when unloading is continued and becomes very flat

at a low stress level. The residual plastic strain has been found to be smaller for stronger concrete (Aoyama and Noguchi, 1979). Karsan and Jirsa (1969) considered the plastic strain as a principal parameter to determine the unloading curve equation. The reloading curve from zero stress changes curvature, becomes rather flat, and it can be represented by a straight line (Sinha, et al., 1964), or a second order parabola (Karsan and Jirsa, 1969). Unloading and reloading curves intersect each other at a locus called "common point limit" (see Fig. 2.3). Cycling within a certain common point until the first unloading curve is reached results in a lowered intersection point with the unloading curve. With an increasing number of cycles, the location of this intersection point converges to a certain point defined as "stability limit" (Karsan and Jirsa, 1969).

In reinforced concrete, the response of concrete in compression and tension is basically similar to that of plain concrete, except that because of bond between the reinforcing steel and the concrete, several cracks form instead of a single crack as is the case for the plain concrete. This leads to a redistribution of stresses from the steel reinforcement to the concrete between the cracks, resulting in the tension stiffening phenomenon. The nonlinear concrete response along with the elastic-plastic-strain hardening behaviour of the slender steel reinforcing bars and the complex behaviour at the steel-concrete interface (pull-out and dowel action) and at the cracks (aggregate interlock) causes the response of any structural reinforced concrete element or structure to any applied loads to be nonlinear, with a decrease in the stiffness immediately after cracking, followed by a considerable stiffness reduction at higher load levels.

2.1.2 Biaxial Behaviour

Based on the experimental observation under biaxial compression, the compressive strength of the concrete increases because of the internal friction and aggregate interlock. The observed strains in both principal stress directions plotted versus σ_2/f'_c are shown in Fig. 2.4. the Stress-strain curve for the same case illustrated in Fig. 2.5. At fairly high stresses, it is evident that the effective stiffnesses are quite different in the two directions. The difference is much greater than can be explained by Poisson effect. This evidence points to "stress-induced orthotropic" behaviour under biaxial stress conditions. The experimental investigation conducted by Liu, Nilson and Slate (1972) indicates that the effect of microcracking confinement is the main cause for the observed increased stiffness under biaxial compression.

Conversely, a lateral compressive stress decreases the tensile strength of concrete because the compressive stress introduces tensile stresses at the micro-level due to the heterogeneity of the material which increases the process of internal damage as reported by Vonk (1990). A lateral tensile stress has no major influence on the tensile strength of concrete. To account for these phenomena, a failure envelope curve should be employed to obtain the compressive and tensile strength of concrete under the biaxial stress state. The lateral tensile stress beyond cracking can also decrease the compressive strength of concrete, as noted by Vecchio and Collins (1986), and Feenstra and de Borst (1993).

2.1.3 Triaxial Behaviour

If concrete is subjected to triaxial compression, both its strength and its ductility increase significantly as the lateral stresses increase. In fact, concrete may sustain a considerably high hydrostatic pressure before fracture. This is because, under high confinement, bond cracking is unlikely to occur and the damage is uniformly distributed throughout the entire specimen. In this case, the concrete behaves like a ductile material without collapse. However, if tensile stress is applied, cracks develop fast in a direction perpendicular to this tensile stress, causing a remarkable reduction in the compressive strength and failure of concrete. Another significant triaxial nonlinear behaviour is the large volume expansion near fracture.

Compared to the uniaxial behaviour, the crack propagation process in the concrete under multi-axial stress conditions has not been well investigated, and not much systematic data is available on this subject. Qualitatively the major difference arises in the post-peak behaviour, where macroscopic observations show that two types of failure modes exist. One is the tensile splitting failure mode and the other is the shear failure mode produced under low to normal confinement, by stepwise joining at the existing microcracks. Both failure modes exhibit strain localization in the post-peak region.

2.2 CONCRETE CONSTITUTIVE RELATIONSHIPS

Extensive research over the past two decades has led to a few constitutive models for concrete which are based on the principles of continuum mechanics and neglect the microstructure of the concrete. These include elasticity-based models, plasticity-based models, plastic-fracturing

models, elastic-plastic-damage models, and the endochronic model. A review of these models is presented in the following sections; more information can be found in two reports published by the ASCE (1982 and 1991).

A more basic approach for describing the general mechanical behaviour of concrete is through the study of its microstructure, but this approach is presently limited to qualitative predictions. Micro-plane model developed by Bazant and Ozbolt (1990) can be introduced as one of these models. The micro-plane model considers the structure at the microstructural level and determines the material stiffness matrix by integrating the elemental behaviour of the micro-planes with various orientations. The micro-planes characterize the deformation of weak planes within the microstructure using the normal deviatoric and volumetric strains, and the shear strain. The model can account for cracking, softening and dilatancy. A drawback for this model is the considerable computational efforts which is required. The relationship between the macroscopic features and the microscopic events for the simple cases of uniaxial tension and uniaxial compression have been recently studied using the finite element method by Yamaguchi and Chen (1991). More information is available in the paper by Chen and Cohen (1992).

2.2.1 ELASTICITY-BASED MODELS

Elasticity-based models are among the most popular constitutive relationships used in conjunction with the finite element analysis of concrete structures. These models are simple and can be easily formulated and implemented. Several elasticity-based constitutive models can be found in the literature, but in general they can be grouped under the following approaches:

1) Linear elastic model; and

2) Non-linear elastic models

A brief review of each approach is outlined in the following sections. First, the generalized Hooke's law for a solid material is introduced and the symmetric properties of elasticity constants are presented irrespective of the type of material (isotropic, orthotropic, etc.). Then two common special cases of generalized Hooke's law for the materials whose elastic properties exhibit symmetry with respect to two orthogonal planes (orthotropic material) or two orthogonal axes (isotropic material) are discussed. If the orthotropic models are expressed in terms of increments of stress and strain, they are called hypoelastic models, and these are presented later in this section. This includes the models proposed by Liu et al. (1972), Darwin and Pecknold (1977),

Elwi and Murray (1979) and Bathe et al. (1989). The description of the hypoelastic model developed in this study is presented in Chapter 3.

2.2.1.1 THE GENERALIZED HOOKE'S LAW

For a large number of solids, the measured strain is proportional to the applied stress over a wide range of loads. This means that as the stress increases, the measured strain increases in the same ratio. Also, when the stress is reduced to zero, the strain disappears. These experimental results lead by inductive reasoning to the generalized Hooke's law of the proportionality of the stress and strain. The general form of the law is expressed by the statement: "Each of the components of the state of stress at a point is a linear function of the components of the state of strain at that point". Mathematically, this is expressed as

$$\sigma_{kl} = C_{klmn}\epsilon_{mn} \tag{2.1}$$

where, C_{klmn} are elasticity constants; there are 81 such constants. The indices k and l are identifying indices and m and n are summation indices, which can take values equal to 1, 2 and 3. For example, for k=1 and l=2 the Eq. 2.1 can be expanded as

$$\begin{aligned}\sigma_{12} = {} & c_{1211}\epsilon_{11} + c_{1222}\epsilon_{22} + c_{1233}\epsilon_{33} + c_{1212}\epsilon_{12} + c_{1221}\epsilon_{21} + \\ & c_{1213}\epsilon_{13} + c_{1231}\epsilon_{31} + c_{1223}\epsilon_{23} + c_{1232}\epsilon_{32}\end{aligned} \tag{2.2}$$

Since the stress and strain tensors are symmetric, it can be shown that the constants C_{klmn} are symmetric with respect to the first and second pairs of indices, i. e.,

$$C_{klmn} = C_{lkmn} \qquad \textit{and} \qquad C_{klmn} = C_{klnm} \tag{2.3}$$

Based on energy considerations, it can also be shown that the first and second pairs of indices can be freely interchanged, namely,

$$C_{klmn} = C_{mnlk} \tag{2.4}$$

Accordingly, the number of independent elastic coefficients for the general anisotropic elastic material is reduced to 21. For example, Eq. 2.2 takes the following form

$$\sigma_{12} = c_{1211}\epsilon_{11} + c_{1222}\epsilon_{22} + c_{1233}\epsilon_{33} + 2(c_{1212}\epsilon_{12} + c_{1213}\epsilon_{13} + c_{1223}\epsilon_{23}) \tag{2.5}$$

In addition, if certain symmetries exist in the material (as will be discussed in the next section), the number of material coefficients, C_{klmn}, will be reduced further. The generalized Hooke's law can now be written in a matrix notation as follows:

$$\begin{Bmatrix} \sigma_{11} \\ \sigma_{22} \\ \sigma_{33} \\ \sigma_{12} \\ \sigma_{13} \\ \sigma_{23} \end{Bmatrix} = \begin{bmatrix} c_{1111} & c_{1122} & c_{1133} & 2c_{1112} & 2c_{1113} & 2c_{1123} \\ c_{2211} & c_{2222} & c_{2233} & 2c_{2212} & 2c_{2213} & 2c_{2223} \\ c_{3311} & c_{3322} & c_{3333} & 2c_{3312} & 2c_{3313} & 2c_{3323} \\ c_{1211} & c_{1222} & c_{1233} & 2c_{1212} & 2c_{1213} & 2c_{1223} \\ c_{1311} & c_{1322} & c_{1333} & 2c_{1312} & 2c_{1313} & 2c_{1323} \\ c_{2311} & c_{2322} & c_{2333} & 2c_{2312} & 2c_{2313} & 2c_{2323} \end{bmatrix} \begin{Bmatrix} \epsilon_{11} \\ \epsilon_{22} \\ \epsilon_{33} \\ \epsilon_{12} \\ \epsilon_{13} \\ \epsilon_{23} \end{Bmatrix} \tag{2.6}$$

The coefficient matrix is symmetric and is called the "stiffness" or the "constitutive" matrix (or the stiffness tensor).

Since the components of stress and strain tensors are functions of the orientation of the system of reference axes, the elastic coefficients in Eq. 2.1 are also functions of this orientation. In a new system of coordinates OX'_1, OX'_2, and OX'_3 (see Fig. 2.6), the new stiffness tensor component is evaluated by

$$C_{prst} = n_{pk} n_{rl} n_{sm} n_{tn} C_{klmn} \tag{2.7}$$

where n_{ij} is the direction cosine of new axis i with respect to initial axis j (i, j= p, r, s, t, k, l, m, and n). The summation on the repeated indices should be carried out in the above equation.

The stress -strain relations given by Eq. 2.1 can be expressed in the inverted form as,

$$\epsilon_{kl} = S_{klmn} \sigma_{mn} \tag{2.8}$$

where S_{klmn} are constants. It is evident that S_{klmn} has the same symmetry properties as C_{klmn} and is called a component of the compliance matrix, [S], (or the compliance tensor).

2.2.1.1.1 ORTHOTROPIC MATERIAL

A material which exhibits symmetry of its elastic properties with respect to two orthogonal planes is called an orthotropic material. Let the two planes be the OX_1, OX_2 plane and the OX_1, OX_3 plane (see Fig. 2.7). The direction cosines of the new axes with respect to initial ones are (1, 0, 0), (0, -1, 0) and (0, 0, -1). The Equation 2.7 gives:

$$C'_{1111} = n_{1k}n_{1l}n_{1m}n_{1n}C_{klmn} = C_{1111}$$

which is correct. The expansion in Eq. 2.7 is simplified, since there are only three non-zero direction cosines, namely:

$$n_{11} = 1, \quad n_{22} = -1, \quad n_{33} = -1$$

Similarly, this type of symmetry requires:

$$C'_{1123} = n_{1k}n_{1l}n_{2m}n_{3n}C_{klmn} = C_{1123}$$

which is impossible since

$$n_{1k}n_{1l}n_{2m}n_{3n}C_{klmn} = -C_{1123}$$

Therefore, C_{1123} must be equal to zero. A similar reasoning will show that the number of elements of the constitutive matrix gets reduced to nine and it is written as follows:

$$[C] = \begin{bmatrix} c_{1111} & c_{1122} & c_{1133} & 0 & 0 & 0 \\ c_{2211} & c_{2222} & c_{2233} & 0 & 0 & 0 \\ c_{3311} & c_{3322} & c_{3333} & 0 & 0 & 0 \\ 0 & 0 & 0 & 2c_{1212} & 0 & 0 \\ 0 & 0 & 0 & 0 & 2c_{1313} & 0 \\ 0 & 0 & 0 & 0 & 0 & 2c_{2323} \end{bmatrix} \tag{2.9}$$

The above stiffness matrix shows that for orthotropic materials, the application of normal stresses results in normal strains alone, and the application of shearing stresses results in shearing strains alone. This is only true, however, in the system of axes with respect to which the

symmetries are defined.

By following the same procedure, as outlined above, the same pattern can be obtained for the compliance tensor, [S], in Eq. 2.8. The stress-strain relationship in multi-axial stress state for an orthotropically anisotropic material (or for brevity, orthotropic) can be written as

$$\begin{Bmatrix} \epsilon_{11} \\ \epsilon_{22} \\ \epsilon_{33} \\ \gamma_{12} \\ \gamma_{13} \\ \gamma_{23} \end{Bmatrix} = \begin{bmatrix} E_1^{-1} & -\nu_{12}E_2^{-1} & -\nu_{13}E_3^{-1} & 0 & 0 & 0 \\ -\nu_{21}E_1^{-1} & E_2^{-1} & -\nu_{23}E_3^{-1} & 0 & 0 & 0 \\ -\nu_{31}E_1^{-1} & -\nu_{32}E_2^{-1} & E_3^{-1} & 0 & 0 & 0 \\ 0 & 0 & 0 & G_{12}^{-1} & 0 & 0 \\ 0 & 0 & 0 & 0 & G_{13}^{-1} & 0 \\ 0 & 0 & 0 & 0 & 0 & G_{23}^{-1} \end{bmatrix} \begin{Bmatrix} \sigma_{11} \\ \sigma_{22} \\ \sigma_{33} \\ \tau_{12} \\ \tau_{13} \\ \tau_{23} \end{Bmatrix} \qquad (2.10)$$

in which the subscripts 1, 2, and 3 stands for the axes of orthotropy; ϵ and γ are normal and engineering-shear strains, respectively; E_i is the modulus of elasticity with respect to the orthotropic direction i (i=1, 2, 3); ν_{ij} is the Poisson's ratio in direction i due to uniaxial stress in direction j (i, j=1, 2, 3); and G_{ij} is the shear modulus of elasticity in plane i-j. A schematic representations of positive directions for stress/strain components, the Poisson's ratio, ν_{ij}, and the shear modulus of elasticity, G_{ij}, are shown in Fig. 2.8.

If equation 2.10 is modified for an orthotropic material under biaxial stresses in the plane consisting of coordinates 1 and 2 (i. e. $\sigma_{33}=\tau_{13}=\tau_{23}=0$), the following equation results:

$$\begin{Bmatrix} \epsilon_{11} \\ \epsilon_{22} \\ \gamma_{12} \end{Bmatrix} = \begin{bmatrix} E_1^{-1} & -\nu_{12}E_2^{-1} & 0 \\ -\nu_{21}E_1^{-1} & E_2^{-1} & 0 \\ 0 & 0 & G^{-1} \end{bmatrix} \begin{Bmatrix} \sigma_{11} \\ \sigma_{22} \\ \tau_{12} \end{Bmatrix} \qquad (2.11)$$

in which, $G=G_{12}$ is the shear modulus of elasticity in the orthotropic plane. By inverting the above equation, the stress-strain relationship for an orthotropic material in a biaxial stress condition can be expressed as,

$$\begin{Bmatrix} \sigma_{11} \\ \sigma_{22} \\ \tau_{12} \end{Bmatrix} = \frac{1}{1-\nu_{12}\nu_{21}} \begin{bmatrix} E_1 & \nu_{21}E_1 & 0 \\ \nu_{12}E_2 & E_2 & 0 \\ 0 & 0 & (1-\nu_{12}\nu_{21})G \end{bmatrix} \begin{Bmatrix} \epsilon_{11} \\ \epsilon_{22} \\ \gamma_{12} \end{Bmatrix} \tag{2.12}$$

2.2.1.1.2 ISOTROPIC MATERIAL

An isotropic material possesses elastic properties which are independent of the orientation of the axes. In other words, these materials have no preferred directions with respect to their elastic properties. In this case, for rotated axes (see Fig. 2.6) the stress-strain relationship can be written as

$$\sigma_{k'l'} = C_{k'l'm'n'}\epsilon_{m'n'} \tag{2.13}$$

where k', l', m' and n' are axes corresponding to the axes k, l, m and n after transformation, respectively; $C_{k'l'm'n'}$ is the elastic coefficient in the transformed coordinate system; $\sigma_{k'l'}$ and $\varepsilon_{k'l'}$ represent stress and strain components in the transformed coordinate system, respectively. For an isotropic material the following equation must hold:

$$C_{k'l'm'n'} = C_{klmn} \tag{2.14}$$

in which C_{klmn} is the elastic coefficient in the reference coordinate system. $C_{k'l'm'n'}$ can be expressed in terms of the reference elastic coefficients, C_{klmn}, using Eq. 2.7. By following the same procedure as outlined in the previous section, it can be shown that the 21 elastic constants in Eq. 2.6 reduce to two independent elastic constants for an isotropic solid (Saada, 1993). Finally, the resulting stiffness matrix for an isotropic material takes the following form:

$$[C] = \begin{bmatrix} c_{1111} & c_{1122} & c_{1122} & 0 & 0 & 0 \\ c_{1122} & c_{1111} & c_{1122} & 0 & 0 & 0 \\ c_{1122} & c_{1122} & c_{1111} & 0 & 0 & 0 \\ 0 & 0 & 0 & \frac{1}{2}(C_{1111} - C_{1122}) & 0 & 0 \\ 0 & 0 & 0 & 0 & \frac{1}{2}(C_{1111} - C_{1122}) & 0 \\ 0 & 0 & 0 & 0 & 0 & \frac{1}{2}(C_{1111} - C_{1122}) \end{bmatrix} \tag{2.15}$$

The elastic constants in Eq. 2.15 are usually written in the following notations:

$$C_{1122} = \lambda \quad , \quad C_{1212} = \frac{1}{2}(C_{1111} - C_{1122}) \quad , \quad C_{1111} = \lambda + 2\mu \qquad (2.16)$$

in which λ and μ are material constants which referred to as Lamé's constants. The stress-strain relationship for an isotropic material using Lamé's constants and index notation can be expressed as:

$$\sigma_{ij} = 2\mu\ \epsilon_{ij} + \lambda\, \epsilon_{kk}\delta_{ij} \qquad (2.17)$$

where σ_{ij} and ϵ_{ij} are current components of stress and strain tensors, respectively; δ_{ij} is Kronecker delta and ϵ_{kk} represents the summation on the repeated indices (i.e. $\epsilon_{kk} = \epsilon_{xx}+\epsilon_{yy}+\epsilon_{zz}$).

2.2.1.2 Linear Elastic Models

In this model, the current state of stress depends on the current state of strain, and it is independent of the strain history (path independent). This model can be characterized (as explained in the previous section) with only two material properties which are either Lamé's constants (λ and μ) or the Young's modulus of elasticity (E) and the Poisson's ratio (ν) or the bulk modulus (K) and the shear modulus (G). The stress-strain relationship in terms of Lamé's constants has been given in Eq. 2.17 and it can be described as a function of the Young's modulus of elasticity (E) and the Poisson's ratio (ν) as

$$\sigma_{ij} = \frac{E}{1+\nu}\ \epsilon_{ij} + \frac{\nu E}{(1+\nu)(1-2\nu)}\epsilon_{kk}\delta_{ij} \qquad (2.18)$$

and in terms of G and K as

$$\sigma_{ij} = 2G\epsilon_{ij} + (K - \frac{2}{3}G)\epsilon_{kk}\delta_{ij} \qquad (2.19)$$

The following empirical formula proposed by the ACI (1989) can be used to evaluate the modulus of elasticity of concrete, E:

$$E = 0.043 w^{1.5} \sqrt{f'_c} \tag{2.20}$$

in which w is the unit weight of concrete in kilograms per cubic meter and f'_c is the uniaxial compressive cylinder strength of concrete in kilograms per square millimetre. The Poisson's ratio ν has been identified to be around 0.2 for plain concrete.

The linear elastic model was adopted initially for the concrete in relation with the finite element analysis of reinforced concrete by Ngo and Scordelis (1967). This model results in satisfactory response under a loading which causes tensile stresses and relatively small compressive stresses (ASCE, 1991); however, it can not identify the nonlinear response and path dependent behaviour of concrete at higher levels of compressive loading.

2.2.1.3 Non-linear Elastic Models

2.2.1.3.1 Cauchy Elastic Model

The performance of linear elastic model can be improved significantly by assuming a nonlinear elastic behaviour in the concrete stress-strain relationships. The simplest way to introduce the nonlinearity between the current state of stress and that of strain is the stress-strain relationships for concrete subjected to a uniaxial compressive load. In this regard many models have been proposed (for example, Smith and Young, 1955; Saenz, 1964; Popovics, 1973; Carreina and Chu, 1985 and Tsai, 1988) in the form of

$$\sigma = f(\epsilon) \tag{2.21}$$

This class of constitutive model is called a Cauchy elastic model. They can be used for uniaxial state of stress and can not be applied directly for the multi-axial state of stress. This Cauchy type of model can be extended to multi-axial stress state (for example, Ahmad and Shah, 1982) as

$$\sigma_{ij} = D^{S}_{ijkl} \epsilon_{kl} \tag{2.22}$$

where D^{s}_{ijkl} represents the secant stiffness, which is a function of the stress state. This is also path-independent, and the reversibility and path-independency of the strain energy function, $\Phi(\varepsilon_{ij})$, and

complementary energy-density function, $\Omega(\sigma_{ij})$ are not generally guaranteed (Chen, 1982).

2.2.1.3.2 Hyper-Elastic (Green Elastic) Model

The current state of stress depends on the current state of strain and mathematically, the constitutive equation for hyper-elastic models takes a form similar to Eq. 2.1. To ensure the path-independency of the strain energy and the complementary energy density functions, the following equation must be satisfied (Chen, 1982)

$$\sigma_{ij} = \frac{\partial \Phi}{\partial \epsilon_{ij}} \tag{2.23}$$

or,

$$\epsilon_{ij} = \frac{\partial \Omega}{\partial \sigma_{ij}} \tag{2.24}$$

where Φ and Ω are the strain energy and complementary energy density functions, respectively.

In general, most of the hyper-elastic models for concrete have been formulated basically as a simple extension of the linear elastic model, by simply replacing two of the elastic moduli (the Young's modulus of elasticity, E, and the Poisson's ratio, ν, or the bulk modulus, K, and the shear modulus, G) with secant moduli (E_s and ν_s or K_s and G_s) which are assumed to be a function of stress and/or strain invariants.

Palaniswamy and Shah (1974) expressed the bulk modulus of elasticity as a function of the first stress invariant and made the Poisson's ratio a function of the first two stress invariants. Both relationships have been developed to fit the experimental data. Cedolin et al. (1977) represented the bulk modulus as a function of the first strain invariant and the shear modulus as a function of the second deviatoric strain invariant. Both models were able to provide a realistic simulation of the response up to about seventy percent of the ultimate strength.

Kotsovos and Newman (1978) also developed a nonlinear elastic isotropic model for concrete based on the bulk and the shear moduli. The volumetric strain that takes place even under deviatoric stress was also included. Simulation of the test results showed that the entire stress-strain curve could be modelled satisfactorily. Ottoson (1979) changed the modulus of elasticity, E, and the Poisson's ratio, ν, according to the prevailing stress and strain conditions. A parabolic

stress-strain relationship was modified to account for multi-axial stress conditions through the use of a nonlinearity index, which relates the current stress state to the stress condition at failure.

The preceding discussion belongs to the general elastic bodies where anisotropy is the result of the internal structure of the material. It also provides a one-to-one relationship between the current state of the total stress and that of the total strain. Thus, by definition this type of formulation is independent of the deformation path in the sense that stresses are uniquely determined from the current state of strain, or vice versa. Therefore, it has an inherent limitation in application with respect to concrete, since the loading-path dependence of the deformation state of concrete has been well recognized (Chen, 1982; ASCE, 1991).

2.2.1.3.3 Hypoelastic Models

An alternative approach to overcome the above deficiency is to describe the material behaviour in terms of increments of stress and strain. The stress-strain relationships are then expressed using the tangent stiffness which varies with the current stress state. Thus, this class of model is generally dependent on the deformation history. The behaviour of this class of model is infinitesimally (or incrementally) reversible (elastic behaviour). Literally, "hypo" means "in a lower sense" or "to a lower degree". Hence, hypoelastic can imply a material that is elastic to a lower or incremental sense. A hypoelastic material can be interpreted to be capable of allowing for inelastic or plastic behaviour. The incremental stress-strain relationship for an orthotropic material takes the form:

$$\begin{Bmatrix} d\sigma_{11} \\ d\sigma_{22} \\ d\tau_{12} \end{Bmatrix} = \frac{1}{1-\nu_{12}\nu_{21}} \begin{bmatrix} E_1 & \nu_{21}E_1 & 0 \\ \nu_{12}E_2 & E_2 & 0 \\ 0 & 0 & (1-\nu_{12}\nu_{21})G \end{bmatrix} \begin{Bmatrix} d\epsilon_{11} \\ d\epsilon_{22} \\ d\gamma_{12} \end{Bmatrix} \qquad (2.25)$$

where E_1 and E_2 are the instantaneous tangent stiffness moduli with respect to directions 1 and 2, respectively; G is the instantaneous shear modulus of elasticity on that plane; and ν_{ij} is the instantaneous Poisson's ratio in direction i due to uniaxial stress in direction j (i, j= 1, 2).

2.2.1.3.3.1 Liu, Nilson, and Slate Model

The first use of the incrementally orthotropic constitutive matrix, Eq. 2.25, in conjunction with the finite element analysis of reinforced concrete structures was reported by Liu, Nilson, and Slate (1972). They introduced the stiffness matrix in Eq. 2.25, in an explicitly symmetric form as:

$$[C] = \frac{E_1}{E_1 - \nu^2 E_2} \begin{bmatrix} E_1 & \nu E_2 & 0 \\ \nu E_2 & E_2 & 0 \\ 0 & 0 & \dfrac{E_2(E_1 - \nu^2 E_2)}{E_1 + E_2 + 2E_2\nu} \end{bmatrix} \tag{2.26}$$

In the above equation, direction 1 coincides with the direction of the major principal stress axis. The tangent moduli E_1 and E_2 are obtained from the uniaxial stress-strain curve of concrete. The Poisson's ratio is assumed to be constant and the same in both principal directions, 1 and 2. The uniaxial stress-strain curve is modified to account for the biaxial action of stresses as follows:

$$\sigma(\epsilon, \alpha) = \frac{1}{1 - \nu\alpha}\sigma(\epsilon) \tag{2.27}$$

where $\sigma(\varepsilon, \alpha)$ and $\sigma(\varepsilon)$ are the stress-strain curves under biaxial and uniaxial loadings, respectively. α is the ratio of the minor principal stress to the major principal stress, and ν is the Poisson's ratio in uniaxial loading. Using this formulation, the biaxial stress-strain relationship is replaced by a uniaxial stress state which is quite simple to be handled. E_1 and E_2 are the tangent moduli defined by Eq. 2.27 corresponding to the strains in directions 1 and 2, respectively.

2.2.1.3.3.2 Darwin and Pecknold Model

Another common application of the orthotropic stress-strain relation was developed by Darwin and Pecknold (1974). Two modifications of Eq. 2.25 were carried out by Darwin and Pecknold. First, they introduced an "equivalent Poisson's ratio", ν, which is defined as

$$\nu^2 = \nu_{12}\nu_{21} \tag{2.28}$$

Secondly, since no information was available on the shear modulus G, they assumed that it is

independent of the axis orientation. This leads to the following relationship:

$$(1-\nu^2)G = \frac{1}{4}(E_1 + E_2 - 2\nu\sqrt{(E_1E_2)}) \tag{2.29}$$

Then, Eq. 2.25 takes the form:

$$\begin{Bmatrix} d\sigma_1 \\ d\sigma_2 \\ d\tau_{12} \end{Bmatrix} = \frac{1}{(1-\nu^2)} \begin{bmatrix} E_1 & \nu\sqrt{E_1E_2} & 0 \\ \nu\sqrt{E_1E_2} & E_2 & 0 \\ 0 & 0 & \frac{1}{4}(E_1+E_2-2\nu\sqrt{E_1E_2}) \end{bmatrix} \begin{Bmatrix} d\epsilon_1 \\ d\epsilon_2 \\ d\gamma_{12} \end{Bmatrix} \tag{2.30}$$

If the incremental equivalent uniaxial strains, $d\varepsilon_{1u}$ and $d\varepsilon_{2u}$, are defined as:

$$d\epsilon_{1u} = \frac{1}{1-\nu^2}\left[d\epsilon_1 + \nu\sqrt{(\frac{E_2}{E_1})}d\epsilon_2\right] \tag{2.31}$$

$$d\epsilon_{2u} = \frac{1}{1-\nu^2}\left[\nu\sqrt{(\frac{E_1}{E_2})}d\epsilon_1 + d\epsilon_2\right]$$

then Eq. 2.30 becomes:

$$\begin{aligned} d\sigma_1 &= E_1 d\epsilon_{1u} \\ d\sigma_2 &= E_2 d\epsilon_{2u} \\ d\tau_{12} &= G d\gamma_{12} \end{aligned} \tag{2.32}$$

These equations have the same form as for the uniaxial stress conditions, which led to the nomenclature "equivalent uniaxial strain" for $d\varepsilon_{1u}$ and $d\varepsilon_{2u}$. The definition of the equivalent uniaxial strain can be restated, using Eq. 2.32 as:

$$\epsilon_{iu} = \int \frac{d\sigma_i}{E_i} \qquad i=1,2 \tag{2.33}$$

or its discrete equivalent:

$$\epsilon_{iu} = \sum_{\substack{Load \\ increments}} \frac{\Delta\sigma_i}{E_i} \tag{2.34}$$

where $\Delta\sigma_i$ is the incremental change in the principal stress σ_i.

This suggests that once the stress-strain relationship has been formulated in a form similar to the uniaxial stress case, similar stress-strain relationships can be used for biaxial action in each principal direction.

The values of E_1 and E_2 for a given principal stress ratio, α, are found as the slopes of the σ_1 versus ε_{1u} and σ_2 versus ε_{2u} curves. The assumed stress-strain curve for the concrete in each principal direction is shown Fig. 2.9. The ascending branch of the envelope curve under compressive load is governed by the Saenz equation (Saenz 1964) as:

$$\sigma_i = \frac{\epsilon_{iu} E_0}{1 + \left(\frac{E_0}{E_s} - 2\right)\frac{\epsilon_{iu}}{\epsilon_{ic}} + \left(\frac{\epsilon_{iu}}{\epsilon_{ic}}\right)^2} \qquad (2.35)$$

where E_0 is the tangent modulus of elasticity at zero stress, $E_s=\sigma_{ic}/\varepsilon_{ic}$ is the secant modulus at the point of maximum compressive stress, and ε_{ic} is the equivalent uniaxial strain at the maximum compressive stress. The descending branch is linear starting at the peak point $(\varepsilon_{ic},\sigma_{ic})$ and ending at point $(4\varepsilon_{cu}, 0.2f'_c)$, where ε_{cu} is the strain corresponding to maximum uniaxial compressive stress. This simple branch has been adopted for simplicity and it represents a reasonable approximation of the experimental results. Concrete under uniaxial tensile load was treated as a perfect brittle material so that it behaves linearly up to its maximum tensile stress, f'_t, and in the post-peak region, it has no load carrying capacity (tension-cut off behaviour).

To account for behaviour of concrete under cyclic loading, at low values of equivalent uniaxial strain unloading and reloading take place on a single line with slope E_0. At higher values of equivalent uniaxial strain, the unloading curve consists approximately three lines: the first with slope E_0; the second parallel to the reloading line; and the third with zero slope, as shown in Fig. 2.9.

The value of equivalent Poisson's ratio, ν, is taken to be 0.2, both in biaxial tension and biaxial compression. A stress dependent value is used in uniaxial compression and tension-compression cases as:

$$\nu = 0.2 + 0.6\left(\frac{\sigma_2}{f'_c}\right)^4 + 0.4\left(\frac{\sigma_1}{\sigma_{1c}}\right)^4 \qquad (2.36)$$

where, σ_1 and σ_2 are the current principal stresses in directions 1 and 2, respectively; f'_c is the uniaxial compressive strength of the concrete; and σ_{1c} is the tensile strength of concrete in major direction 1. More detailed information for this model is presented in a report by Shayanfar and Mirza (1994).

2.2.1.3.3.3 Elwi and Murray Model

Elwi and Murray (1979) developed a three-dimensional stress-strain relationship for concrete under axisymmetric stress conditions (i. e., $\tau_{13} = \tau_{23}$), which incorporates the equivalent uniaxial strain concept of Darwin and Pecknold (1977), the nonlinear uniaxial stress-strain relationship by Saenz (1964), and the Argyris failure surface (Willam and Warnke 1975). The three-dimensional orthotropic constitutive matrix for axisymmetric condition can be obtained from Eq. 2.10 by deleting the fifth and sixth columns and rows of its coefficient matrix. The resulting coefficient matrix, [S], for axisymmetric condition is a 4×4 matrix and the incremental stress-strain relationship takes the form:

$$\{d\epsilon\} = [S]\{d\sigma\} \qquad (2.37)$$

where [S] is the compliance tensor and {dε} and {dσ} are the vector of strain and stress increments, respectively. The following constraints must be fulfilled to ensure the symmetry of the compliance tensor:

$$\nu_{12}E_1 = \nu_{21}E_2$$
$$\nu_{13}E_1 = \nu_{31}E_3$$
$$\nu_{23}E_2 = \nu_{32}E_3$$

By inverting Eq. 2.37 and incorporating the above conditions, the following stress-strain relationship is obtained:

$$\{d\sigma\} = [C]\{d\epsilon\} \qquad (2.38)$$

in which [C] is the constitutive matrix and can be expressed as,

$$[C] = \frac{1}{\phi}\begin{bmatrix} E_1(1-\mu_{32}^2) & \sqrt{E_1E_2}(\mu_{13}\mu_{32}+\mu_{12}) & \sqrt{E_1E_3}(\mu_{12}\mu_{32}+\mu_{13}) & 0 \\ \sqrt{E_1E_2}(\mu_{13}\mu_{32}+\mu_{12}) & E_2(1-\mu_{13}^2) & \sqrt{E_2E_3}(\mu_{12}\mu_{13}+\mu_{32}) & 0 \\ \sqrt{E_1E_3}(\mu_{12}\mu_{32}+\mu_{13}) & \sqrt{E_2E_3}(\mu_{12}\mu_{13}+\mu_{32}) & E_3(1-\mu_{12}^2) & 0 \\ 0 & 0 & 0 & G_{12}\phi \end{bmatrix} \quad (2.39)$$

in which $\mu_{ij}^2 = \nu_{ij}\,\nu_{ji}$ and $\phi = 1 - \mu_{12}^2 - \mu_{23}^2 - \mu_{13}^2 - 2\,\mu_{12}\,\mu_{23}\,\mu_{13}$. The shear modulus of elasticity (G_{12}) is assumed to be invariant with respect to transformation to any non-orthotropic set of axes which results in:

$$G_{12} = \frac{1}{4\phi}\left[E_1 + E_2 - 2\mu_{12}\sqrt{E_1E_2} - \left(\sqrt{E_1}\mu_{23} + \sqrt{E_2}\mu_{31}\right)^2\right] \quad (2.40)$$

The uniaxial compressive stress-equivalent strain relationship, σ_i-ε_{iu}, due to Saenz (1964) is generalized to three dimensions in terms of the equivalent uniaxial strain, ε_{iu}, strength of the concrete under biaxial stress condition, σ_{ic}, and the strain corresponding to this strength, ε_{ic} (Bashur and Darwin 1978). The modulus of elasticity in orthotropic direction "i" is evaluated as the slope of the σ_i-ε_{iu} curve. The Poisson's ratio is assumed to be unique in each orthotropic direction (i. e., $\nu_{i1} = \nu_{i2} = \nu_{i3} = \nu_i$), which is defined as

$$\nu_i = \nu_0\left[1.0 + 1.3763\left(\frac{\epsilon_{iu}}{\epsilon_{ic}}\right) - 5.3600\left(\frac{\epsilon_{iu}}{\epsilon_{ic}}\right)^2 - 8.5860\left(\frac{\epsilon_{iu}}{\epsilon_{ic}}\right)^3\right] \quad (2.41)$$

in which ν_o is the initial Poisson's ratio, ε_{iu} is the current equivalent uniaxial strain in direction "i" and ε_{ic} is the strain corresponding to peak point at failure. The Argyris failure criterion (Willam and Warnke 1975) is used to evaluate σ_{ic} and ε_{ic}.

2.2.1.3.3.4 Bathe et al. Model

Bathe and Ramaswamy (1979) implemented a three-dimensional hypoelastic model for concrete into the commercial finite element program ADINA. This model was later refined by Bathe et al. (1989). In this later version, stresses and strains in the principal directions are related by means of uniaxial stress-strain relationships based on the equation proposed by Kupfer et al.

(1969). This uniaxial stress-strain relation was generalized to take biaxial and triaxial stress conditions into account. Concrete was considered as an orthotropic material with the directions of orthotropy defined as the principal stress directions. The constitutive matrix, [C], corresponding to these directions in the three-dimensional stress state is presented as,

$$[C] = \frac{1}{(1+\nu)(1-2\nu)} \begin{bmatrix} (1-\nu)E_1 & \nu E_{12} & \nu E_{13} & 0 & 0 & 0 \\ \nu E_{21} & (1-\nu)E_2 & \nu E_{23} & 0 & 0 & 0 \\ \nu E_{31} & \nu E_{32} & (1-\nu)E_3 & 0 & 0 & 0 \\ 0 & 0 & 0 & \frac{1}{2}(1-2\nu)E_{12} & 0 & 0 \\ 0 & 0 & 0 & 0 & \frac{1}{2}(1-2\nu)E_{13} & 0 \\ 0 & 0 & 0 & 0 & 0 & \frac{1}{2}(1-2\nu)E_{23} \end{bmatrix} \quad (2.42)$$

in which ν is the Poisson's ratio, E_i is the current tangent modulus of elasticity in the principal direction i which is equal to the slope of the generalized uniaxial stress-strain curve at the current strain, and E_{ij} is the weighted Young's modulus of elasticity corresponding to the plane i-j which is defined as:

$$E_{ij} = \frac{|\sigma_i|E_i + |\sigma_j|E_j}{|\sigma_i| + |\sigma_j|} \quad (2.43)$$

where, σ_i and σ_j are the current principal stresses in directions i and j, respectively. According to this weighted Young's modulus, the shear modulus of elasticity in the plane i-j is calculated as:

$$G_{ij} = \frac{E_{ij}}{2(1+\nu)} \quad (2.44)$$

This hypoelastic model uses a non-constant Poisson's ratio to account for dilation under compressive loading. To characterize loading and unloading conditions, they defined a loading function f:

$$f = \left(\frac{1}{2} S_{ij} S_{ij}\right)^2 = J_2^{\frac{1}{2}} \tag{2.45}$$

where J_2 is the second invariant of the deviatoric stress tensor, ($S_{ij} = \sigma_{ij} - \sigma_m \delta_{ij}$) is the deviatoric stress tensor, ($\sigma_m = 1/3\ \sigma_{ii}$) is the hydrostatic or mean stress, and δ_{ij} is the Kronecker delta. The material is being loaded except the following condition is met:

$$f < f_{max} \tag{2.46}$$

in which f_{max} is the maximum value of the loading function that has been reached during the complete solution. During unloading, only the initial Young's modulus, E_0, is used to form the incremental constitutive matrix, Eq. 2.42, both for stiffness and stress calculations. Tensile cracking and compression crushing conditions are identified using failure surfaces. The strain softening responses are included in the compression and the tensile regions. For more information, refer to Bathe et al. (1989).

2.2.2 PLASTICITY-BASED MODELS

The theory of plasticity was initially developed and successfully used in the representation of metal behaviour. In recent years, plasticity-based models have been used extensively to describe the behaviour of concrete materials, and capture its essential characteristics such as nonlinearity, irreversibility, path-dependency, dilatancy, etc. (Suidan and Schnobrich, 1973; Chen and Chen, 1975; Buyukozturk, 1977; Chen, 1982; Chen and Han, 1988). However, the application of the plasticity-based models has been criticized because of their inability to describe the degradation of the elastic moduli (decrease of the unloading stiffness resulting from extension of microcracks; refer to Figure 2.10) and of strength (decrease of stress because of micro-fracturing leading to the strain-softening branch) in the post-peak regime. In the pre-peak regime, the plasticity-based models do not also idealize the degradation of the elastic moduli, but it is not crucial. Thus, the modelling based on the theory of plasticity can be successfully used in the pre-peak region.

The following three basic assumptions are used in the development of the classical theory of plasticity:

1) An initial yield surface,

2) A hardening rule, and

3) A flow rule

The first assumption states that a stress function, f, exists defining the limit of elasticity of the material. It is called the initial-yield function before plastic deformations occur, and loading function, beyond initial yielding. In fact, this function in stress space can define the stress states at which plastic deformation does not exist ($f<0$), plastic deformation begins ($f=0$) and plastic flow occurs ($f>0$). Before yielding ($f<0$), the elasticity-based constitutive laws, discussed in Section 2.2.1.2, are used to characterize the concrete response. A hardening rule regulates the evolution of the subsequent loading surfaces during the course of plastic flow. A flow rule defines an incremental plastic stress-strain relationship using a plastic potential function, g.

The models based on the theory of plasticity can be classified into two groups: (1) the elastic-strain hardening models; and (2) the elastic-perfectly plastic models. If an elasto-plastic model admits changes of permanent strain under constant stress, it is called an elastic-perfectly plastic model, otherwise it is considered to be an elastic-strain hardening model. A brief description of these models is presented in the following sections.

2.2.2.1 Elastic-Strain Hardening Model

When the state of stress reaches the yield surface, $f=0$, concrete undergoes plastic deformation. At this stage, the total strain increment, $d\varepsilon_{ij}$, is assumed to be composed of elastic and plastic strain increments:

$$d\epsilon_{ij} = d\epsilon^{e}_{ij} + d\epsilon^{p}_{ij} \qquad (2.47)$$

where $d\varepsilon^{e}_{ij}$ and $d\varepsilon^{p}_{ij}$ are elastic and plastic strain increments, respectively. In the theory of plasticity, the direction of the plastic strain vector is defined through a flow rule by assuming the existence of a plastic potential function, g, to which the plastic strain vectors are orthogonal Mathematically, this can be expressed as:

$$d\epsilon_{ij}^{p} = \lambda \frac{\partial g}{\partial \sigma_{ij}} \tag{2.48}$$

in which $\lambda \geq 0$ is a scalar proportionality factor. For an associated flow rule, f is assumed to be equal to g (f=g), while for a non-associated flow rule, f is not considered to be equal to g. In practice, most of the materials are considered to follow non-associated flow rule of plasticity.

As mentioned earlier, before yielding, elasticity-based constitutive laws are used to express the stress-strain relationships. Beyond the initial yielding surface (see Figure 2.11), both initial yield and subsequent stress states must satisfy the following yield function, in the plastic loading range, (Chen and Chen, 1975; Chen, 1982)

$$f(\sigma_{ij}, \epsilon_{ij}^{p}, k) = 0 \qquad and \qquad f + df = 0 \tag{2.49}$$

where k is the material constant, and a function of the plastic strain tensor, ϵ_{ij}^{p}. From the above equation and using the variational calculus, the following consistency condition can be obtained

$$df = \frac{\partial f}{\partial \sigma_{ij}} d\sigma_{ij} + \frac{\partial f}{\partial \epsilon_{ij}^{P}} d\epsilon_{ij}^{P} + \frac{\partial f}{\partial k} dk = 0 \tag{2.50}$$

From this equation, and equations 2.47, 2.48 and 2.49, the following stress-strain relationship in the plastic region (the region enclosed by initial yielding surface and fracture surface in Fig. 2.11) is obtained

$$d\sigma_{ij} = D_{ijkl}^{ep} \, d\epsilon_{kl} = (D_{ijkl}^{e} + D_{ijkl}^{p}) \, d\epsilon_{kl} \tag{2.51}$$

where, D^{e}_{ijkl}, D^{p}_{ijkl} and D^{ep}_{ijkl} are the elastic, plastic and elasto-plastic tangential stiffnesses, respectively. The plastic-stiffness tensor, D^{p}_{ijkl}, for an elastic-strain hardening material has the form

$$D_{ijkl}^{p} = -\frac{D_{ijtu}^{e} \frac{\partial g}{\partial \sigma_{tu}} \frac{\partial f}{\partial \sigma_{rs}} D_{rskl}^{e}}{h + \frac{\partial f}{\partial \sigma_{mn}} D_{mnpq}^{e} \frac{\partial g}{\partial \sigma_{pq}}} \tag{2.52}$$

in which the scalar function, λ, and the hardening parameter, h, are being defined as

$$\lambda = \frac{\frac{\partial f}{\partial \sigma_{ij}} D^{e}_{ijkl} d\epsilon_{kl}}{h + \frac{\partial f}{\partial \sigma_{mn}} D^{e}_{mnpq} \frac{\partial g}{\partial \sigma_{pq}}} \tag{2.53}$$

and,

$$h = -\frac{\partial f}{\partial \epsilon^{p}_{ij}} \frac{\partial g}{\partial \sigma_{ij}} - \frac{\partial f}{\partial k} \frac{\partial k}{\partial \epsilon^{p}_{ij}} \frac{\partial g}{\partial \sigma_{ij}} \tag{2.54}$$

It is noticed that if non-associated flow rules are used, the tangent stiffness matrices, D^{p}_{ijkl}, become undesirably asymmetric, i.e.

$$f \neq g \qquad then \qquad D^{p}_{ijkl} \neq D^{p}_{klij} \tag{2.55}$$

Therefore, the finite element programs must have the capability of handling the unsymmetric stiffness matrix to incorporate this kind of models. On the other hand, the associated flow rules do not correctly capture the volumetric response of the concrete (Chen, 1982).

The isotropic-hardening model proposed by Chen and Chen (1975), the uniform hardening model developed by Han and Chen (1985) and the multiple hardening model suggested by Murray et al. (1979) are among the popular elastic-strain hardening plasticity models. None of these models can account for strain softening and degradation of the elastic modulus in the post-peak region.

2.2.2.2 Elastic-Perfectly Plastic Model

Under high levels of confinement, concrete is known to manifest significant ductile behaviour before fracturing. To model this ductility, the perfect plasticity concept was introduced as a reasonable first approximation. This model can be treated as a special case of the model discussed in the preceding section, in which the hardening parameter vanishes to zero (h=0) and the loading surface, f, is only a function of the state of stress and the plastic strain as:

$$f = f(\sigma_{ij}, \epsilon^{p}_{ij}) = 0 \tag{2.56}$$

Using this model, the incremental stress-strain relationship introduced in Eq. 2.51 is applicable in the plastic region. The plastic-stiffness tensor, D^{p}_{ijkl}, for an elastic-perfectly plastic material with an associated flow rule (f=g) can be introduced as

$$D^{p}_{ijkl} = - \frac{D^{e}_{ijtu} \frac{\partial f}{\partial \sigma_{tu}} \frac{\partial f}{\partial \sigma_{rs}} D^{e}_{rskl}}{\frac{\partial f}{\partial \sigma_{mn}} D^{e}_{mnpq} \frac{\partial f}{\partial \sigma_{pq}}} \tag{2.57}$$

As pointed out earlier, the classical theory of plasticity is based on the assumption that plastic deformation occurs without a corresponding change in the elastic moduli. But concrete is known to experience a degradation of the elastic moduli due to microcracking, especially in the softening regime (see Figure 2.10). The plastic-fracturing theory discussed in the next section, accounts for this behaviour of concrete by including the strain in the definition of plastic flow.

For moderate strain, mild steel behaves approximately like an elastic-perfectly plastic material in both compression and tension. For concrete, it is not realistic to treat it as an elastic-perfectly plastic material; but this assumption in conjunction with the limit theorems of plastic analysis and design reveals reasonable results in the response of reinforced concrete structures. From the view point of constitutive modelling, the hypoelastic-perfectly plastic model proposed by Ohtani and Chen (1987) can be considered as an elastic-perfectly plastic model. In this model, concrete is idealized by a hypoelasticity model before yielding and an elastic-perfectly plastic formulation in the post-yielding regime. This model suffers from its inability to describe the degradation of the elastic moduli and degradation of the strength leading to the strain-softening behaviour in the post-peak regime.

2.2.3 PLASTIC-FRACTURING MODELS

The plastic-fracturing theory appears to be an effective approach in modelling the behaviour of concrete materials. In this theory, the inelastic behaviour of concrete is attributed to microcracking in addition to plastic slip (Bazant and Kim, 1979). In other word, plastic

deformation is defined by the flow theory of plasticity in the usual manner, while the stiffness degradation is modeled by the fracturing theory of Dougill (1975). Thus, fracturing concepts are combined with the plasticity theory to derive the constitutive relations. In these relations, the plastic strain increments are obtained using the conventional plastic loading surfaces in the stress space, whereas the fracturing stress decrements are defined by a postulated potential function in the strain space:

$$\begin{aligned} f(\sigma_{ij}, H_k) &= 0 \\ \phi(\epsilon_{ij}, H'_k) &= 0 \end{aligned} \tag{2.58}$$

in which f and ϕ are the loading and the fracturing surfaces; and H_k and H'_k are the hardening parameters. The resulting constitutive equation from this theory is:

$$d\sigma_{ij} = D^t_{ijkl}\, d\epsilon_{kl} = (D^e_{ijkl} - D^p_{ijkl} - D^{fr}_{ijkl})\, d\epsilon_{kl} \tag{2.59}$$

where, D^e_{ijkl}, D^p_{ijkl}, D^{fr}_{ijkl} and D^t_{ijkl} are the elastic, plastic, fracturing and total tangential stiffnesses, respectively. Through the use of tedious algebraic calculations and six inelastic material parameters which are functions of stress and strain invariants, the above tensors can be evaluated.

It was mentioned earlier that this approach combines two loading surfaces, the yield surface in the stress space and the fracturing surface in the strain space. This causes difficulties in the definition of the loading criterion, which is specially serious for the softening regime in which the strains continue to increase with the decrease of stresses. To avoid this problem, a strain-space plasticity approach has been proposed by Han and Chen (1986) to formulate the plastic fracturing surface. More information about the formulation of this theory can be found in the paper by Bazant and Kim (1979), and in the book by Chen and Han (1988).

The plastic-fracturing models have been criticized in that the stress-strain relationship in the softening range is merely a nominal property, and not a material property as assumed by the model. In the post-peak regime, strain localization usually occurs and the descending branch of the load-deformation curve may not be interpreted as the strain-softening of the material. However, if the geometrical and structural effects are lumped together and considered by some means like the model of Frantziskonis and Desai (1987), the continuous description of the softening stress-strain relation may be reasonable. The plastic-fracturing models generally require a large number of functions and material parameters, and involve heavy computational iterations

in the finite element analysis. Therefore, the application of these models is very limited in practice.

2.2.4 ELASTIC-PLASTIC-DAMAGE MODELS

As mentioned perviously, the failure of concrete is attributed to the progressive propagation and concentration of microcracks in the material. This is defined as the damage of the material. The continuum damage mechanics (Kachanov, 1986) based on thermodynamics can be used to model this phenomenon. In this approach, the stiffness degradation behaviour is assumed to be caused by material damage. There are two types of material damage variables usually employed to represent the damage. One is the isotropic or scalar damage which is related to the collapse of micro-porous structure of the material. The other is the anisotropic or tensorial damage which is related to the creation of surfaces in the material due to de-cohesion. If a material is virgin isotropic elastic, the scalar damage preserves its property, while the tensorial damage induces anisotropy for the elastic behaviour of the material. This is called deformation-induced-anisotropy. The damage growth in the material can be described by either prescribing a damage evolution law (Mazars, 1986), or by using the concept of damage surface (Krajcinovic and Fonseka, 1981).

Two types of damage models, elastic-damage model and elastic-plastic-damage model for the concrete have been suggested. In the elastic-damage models, the inelastic behaviour of concrete materials is reflected only in the stiffness degradation, and there is no permanent deformation in the material after a complete unloading. Dougill's work belongs to this category. To describe the coupling between the plasticity of the concrete and its elastic stiffness degradation, the elastic-plastic-damage models have been suggested (Ortiz and Popov, 1982; Frantziskonis and Desai, 1987; Simo and Ju,1987; Lubliner et al., 1989; Oliver et al., 1990; Chen 1992). To prevent mesh-sensitiveness associated with the strain-softening in the finite element analysis, Bazant et al. (1988) adopted a modified nonlocal continuum approach in which the nonlocal averaging only is applied to the variables that control strain-softening or damage.

In summary, the elastic-plastic-damage model that combines the conventional plasticity theory with the continuum damage theory is very promising and should provide a reasonable modelling technique for describing the behaviour of concrete materials. Presently, it is under active development.

2.2.5 ENDOCHRONIC MODELS

The endochronic theory seems to be an attractive and comprehensive approach for modelling of concrete material behaviour such as nonlinear response, inelastic volume dilatancy, hydrostatic pressure sensitivity, damage accumulation, creep and cyclic behaviour. This theory was initially proposed by Valanis (1971) as a generalization of the theory of visco-elasticity for the description of metal behaviour. It attempts to improve the numerical efficiency by employing an inelastic continuous model without recourse to yield condition and hardening rules. Bazant et al. (1976, 1978, 1980) extended this theory to describe the behaviour of concrete materials. The basic concept of the endochronic theory is the introduction of an intrinsic time as a non-decreasing scalar variable used to measure the evolution of irreversible damage.

Although it appears that the endochronic models may become a potentially useful approach in the numerical analysis of concrete structures, a clear understanding of the theory is necessary because of its limitations in satisfying the principles of continuum mechanics. A thorough investigation of the accuracy , shortcomings and advantages of the endochronic theory was undertaken by Hanna (1983) at McGill University. One of the shortcomings reported by Hanna is the incrementally nonlinear nature of the model which makes it quite expensive in terms of computing costs. Moreover, a large number of material parameters are required to be defined which, in turn, require more intensive computations.

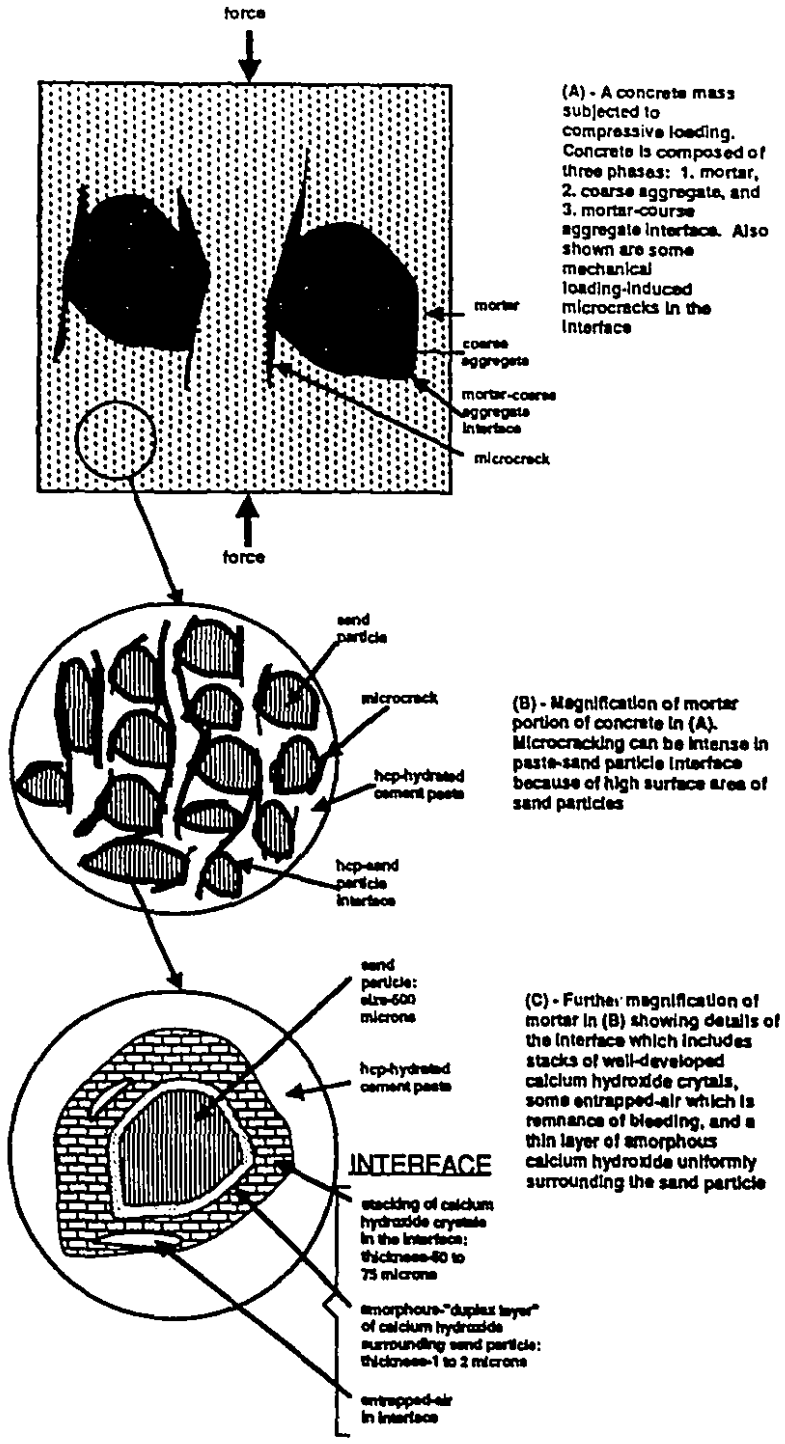

Figure 2.1: Details of concrete mass and magnification of its mortar portion for: (A) concrete, (B) mortar portion of concrete, and (C) further magnification of mortar (Chen and Cohen, 1992)

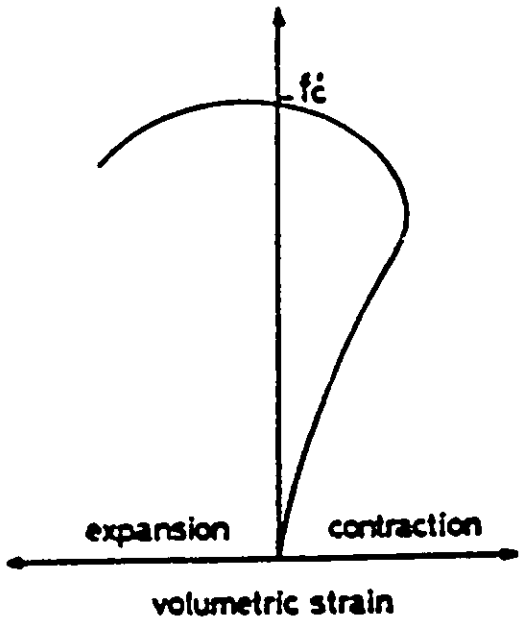

Figure 2.2: Volumetric strain versus uniaxial compressive stress (Kupfer et al., 1969)

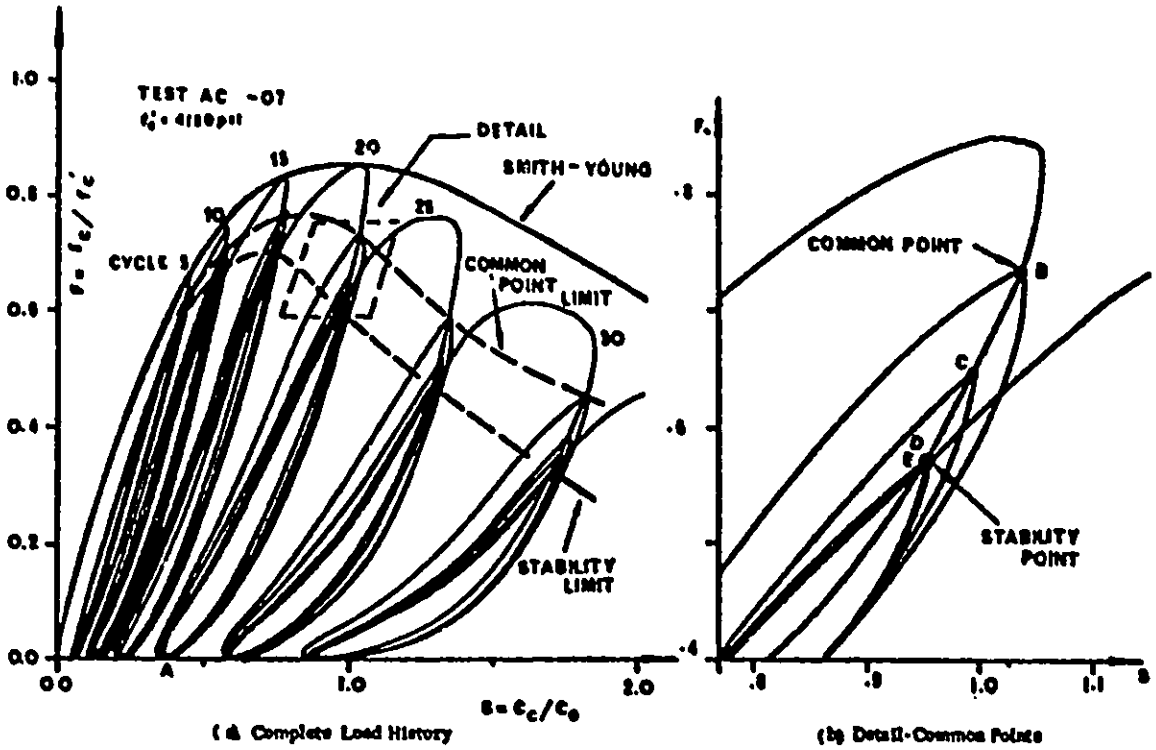

Figure 2.3: Variation of common and stability points under uniaxial compressive repeated loading (Karsan and Jirsa, 1969)

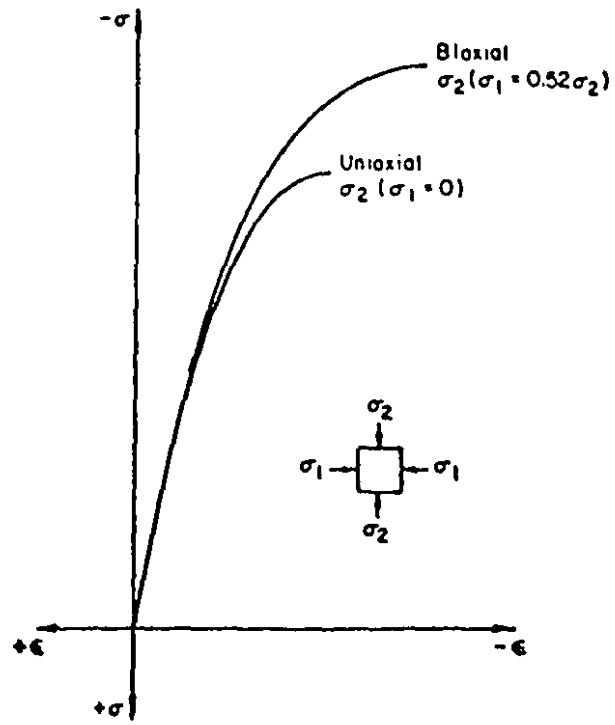

Figure 2.4: Effect of biaxial stress on concrete (Ghoneim, 1978)

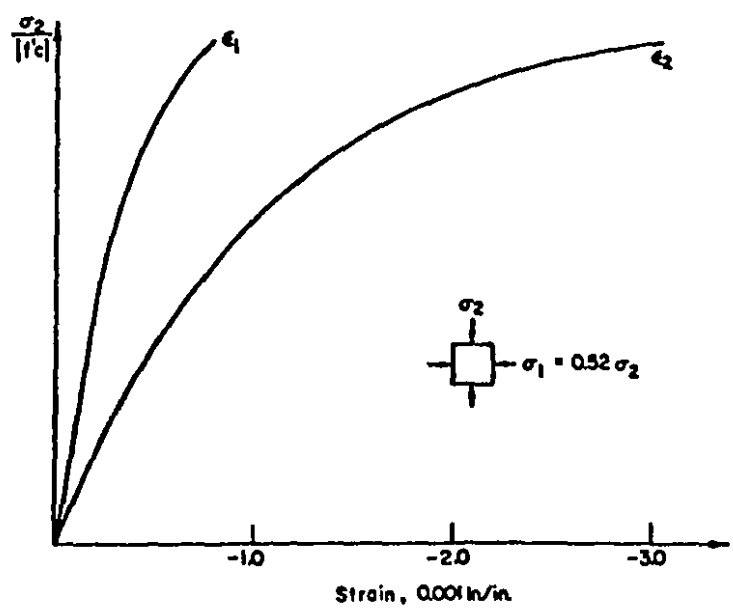

Figure 2.5: Stress-induced orthotropic behaviour of biaxially loaded concrete (Ghoneim, 1978)

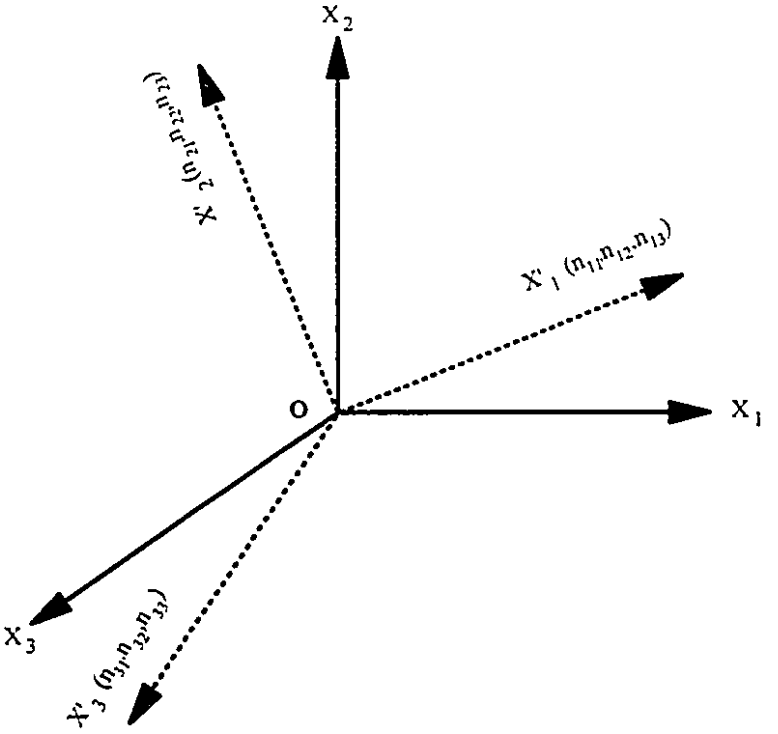

Figure 2.6: Systems of coordinate axes

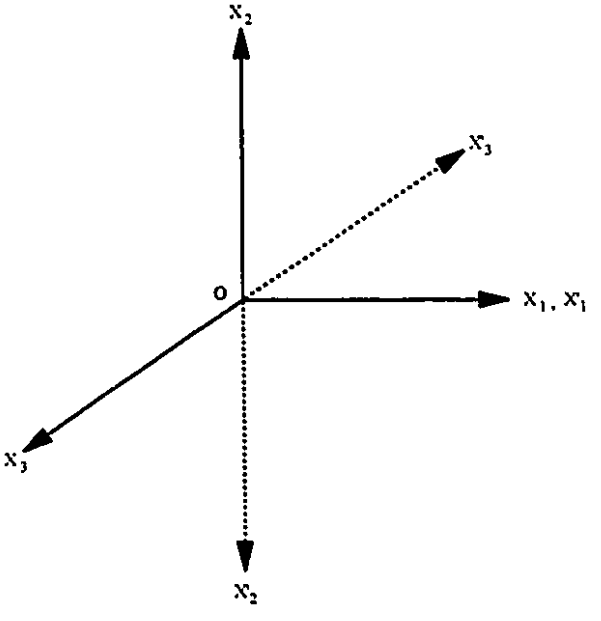

Figure 2.7: System of coordinates for orthotropic materials

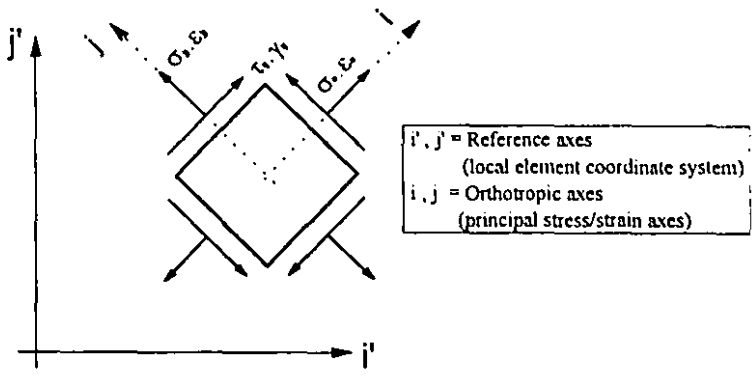

(a)

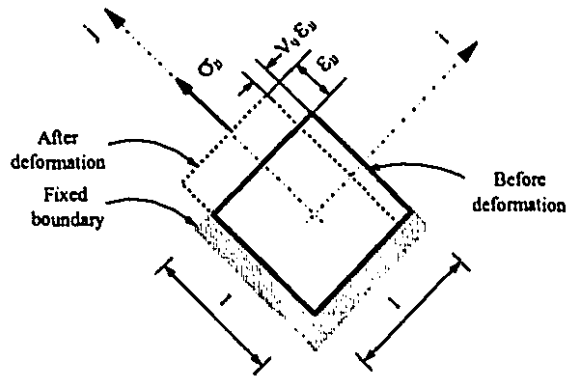

(b)

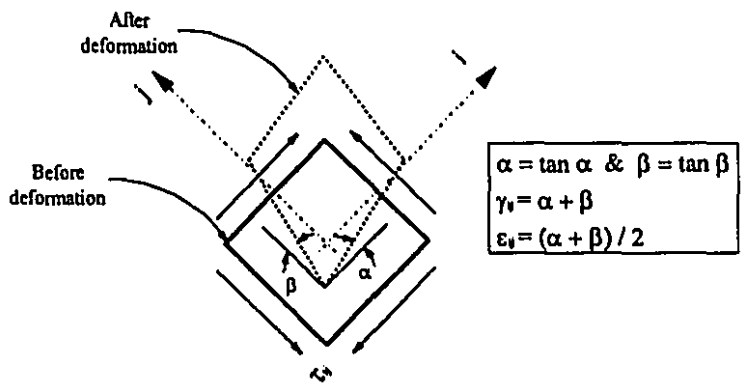

(c)

Figure 2.8: Definitions of: (a) positive stress/strain components in plane i-j, (b) Poisson's ratio in plane i-j, and (c) shear strain in plane i-j

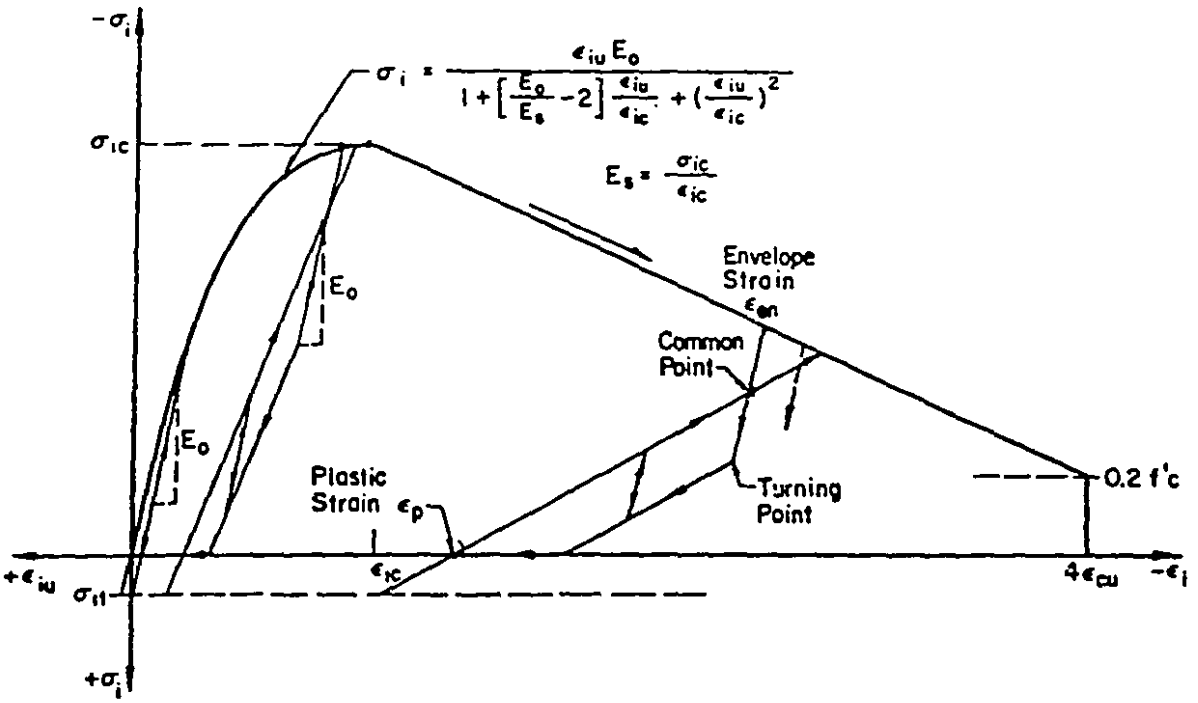

Figure 2.9: Stress-strain curve for plain concrete under monotonic and cyclic loading (Darwin and Pecknold, 1976)

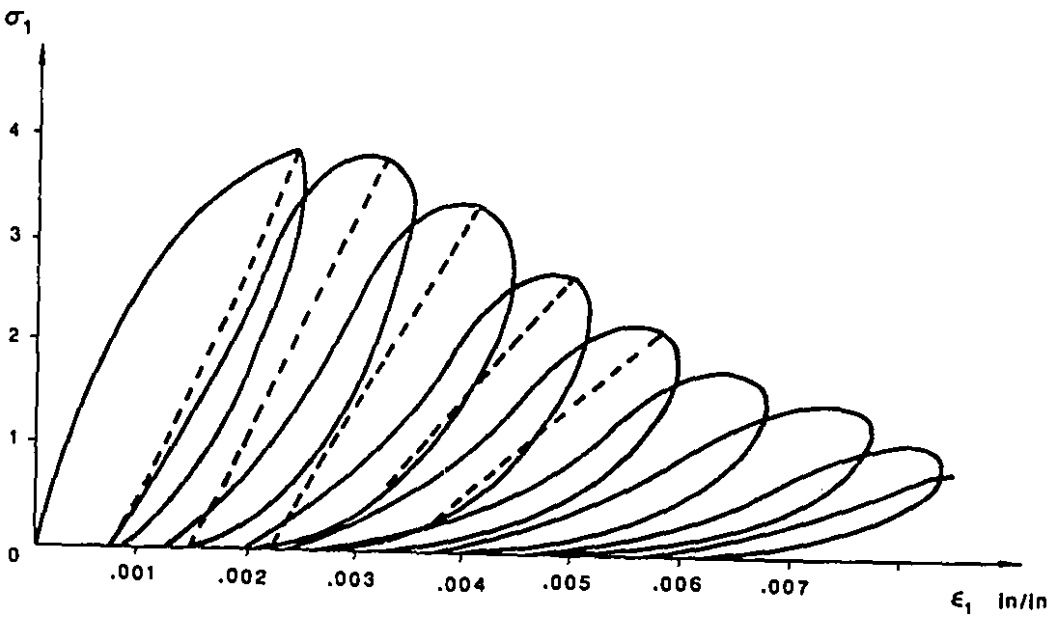

Figure 2.10: Stress-strain curve under cyclic uniaxial compressive loading (Sinha et al., 1964)

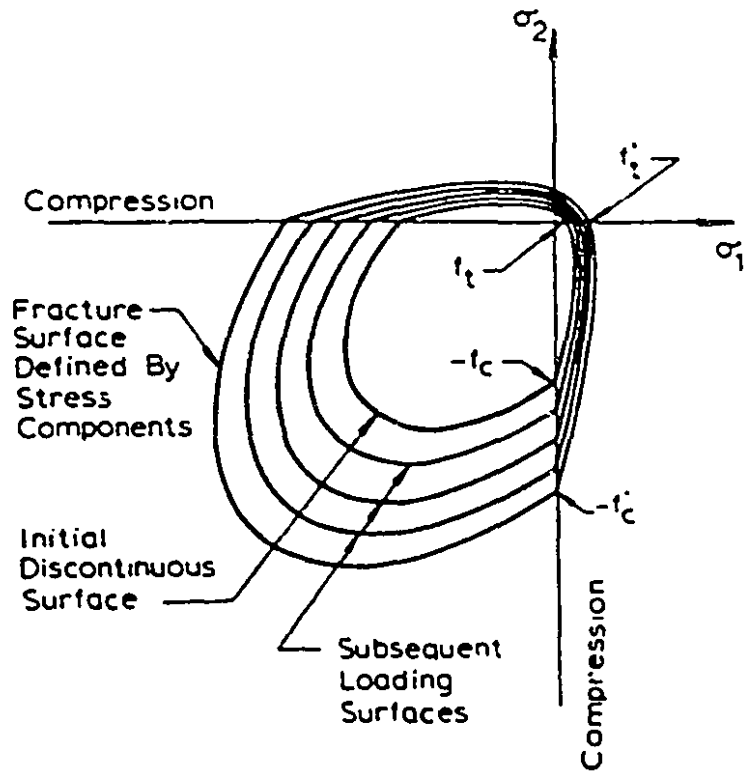

Figure 2.11: Loading surfaces of concrete in the biaxial stress plane (Chen, 1982)

CHAPTER 3

THE PROPOSED MATERIAL MODEL

This chapter presents the proposed constitutive model for concrete and the required material properties including, the stress-strain curve, the instantaneous modulus of elasticity, the Poisson's ratio, etc. The constitutive model for concrete is introduced for two distinct cases: the uncracked concrete and the cracked concrete. The uncracked concrete is modeled using a new hypoelasticity model which allows for the evaluation of the equivalent uniaxial strains in terms of the "real" strains in both pre- and post-compressive peak regions. With regard to the uncracked concrete two common types of crack modelling techniques (discrete and smeared crack models) are discussed and a brief discription of the different smeared crack models (fixed, rotating and multiple crack models) in connection with the proposed hypoelasticity model are presented (see Shayanfar and Mirza, 1994). The compressive strength-degradation of the concrete in the compression-tension state after cracking is also included as reported by Vecchio and Collins (1986). The monotonic and cyclic stress-strain curves which can be used effectively for both normal and high-strength concretes, the Poisson's ratio, the failure criteria for concrete and the constitutive model for steel reinforcement are presented in the last part of this chapter.

3.1 GENERAL

In recent years, a large number of constitutive models for concrete materials have been

developed, as presented in Chapter 2, but the models that are rational, reliable, practical and simple to implement in a general purpose finite element analysis program are very limited. A rational concrete model should be able to describe adequately the main characteristics of the complete stress-strain behaviour of concrete materials, ranging from a tension with a low confining pressure to a compressive state with very high confining pressure, besides dealing with both the pre-peak and the post-peak regimes. Furthermore, the reliability of an applicable model is closely related to its numerical stability, which in turn depends on its formulation and the numerical techniques adopted for its computer implementation. This practical application requires that the model should be as simple as possible, as long as the main characteristics of the constitutive behaviour of the concrete materials are "captured". The main characteristics of a proper model for concrete materials, as discussed in Chapter 2, can be summarized as follows:

1) The high nonlinearity of the stress-strain behaviour of concrete in the pre-peak regime, i. e. growing and propagation of microcracks resulting in a decrease in the material stiffness.

2) The softening behaviour of concrete in the post-peak regime resulting from the localization of macrocracks in narrow bands.

3) The elastic stiffness degradation caused by the extension of microcracks during subsequent unloadings and reloadings. (refer to Fig. 2.6).

4) The irrecoverable volume dilatation at high level of compressive load resulting in an increase in the Poisson's ratio.

All of the above features for concrete are included in the material model developed during this course of study. This model can be treated as a hypoelastic model which is very simple to implement in a nonlinear finite element analysis program. The incremental nature of the hypoelastic models along with the nonlinear stress-strain relationship utilized in the proposed model (see Section 3.4.1), capture the nonlinear stress-strain behaviour of concrete. The proposed constitutive model is applicable for the entire stress or strain history including the post-peak regions and can model the strain softening behaviour of concrete through the assumed nonlinear stress-strain curve. The proposed analytical stress-strain relationship for concrete, under cyclic loading, can account for the stiffness degradation during subsequent unloadings and reloadings (see Section 3.4.2). A variable Poisson's ratio is used to account for volume dilatation at high stress levels (see Section 3.5).

3.2 CONSTITUTIVE MODEL FOR UNCRACKED CONCRETE

Once again the generalized incremental Hooke's law for an orthotropic material under biaxial actions, Eq. 2.25, is modified according to the following assumptions:

1) To satisfy the energy conservation principle, the elastic material stiffness matrix should be symmetric, giving:

$$\nu_{21} E_1 = \nu_{12} E_2 \tag{3.1}$$

2) To define the Poisson's ratios (ν_{12}, ν_{21}), the following equation is imposed:

$$\frac{\nu_{12}}{E_1} = \frac{\nu_{21}}{E_2} = \frac{\nu}{E_o} \tag{3.2}$$

where E_o is the initial stiffness moduli and ν is the equivalent Poisson's ratio as described in Section 3.5.

3) Because of lack of information related to the shear modulus of elasticity of the concrete, G, it is also assumed to be independent of the axis orientation. This assumption accompanied with Eqs. (3.1) and (3.2) results in the following equation:

$$(1-\nu^2 \frac{E_1 E_2}{E_o^2}) G = \frac{1}{4}(E_1 + E_2 - 2\nu \frac{E_1 E_2}{E_o}) \tag{3.3}$$

With these assumptions, the incremental stress-strain relationship in Eq. 2.25 takes the following form:

$$\begin{Bmatrix} d\sigma_{11} \\ d\sigma_{22} \\ d\sigma_{12} \end{Bmatrix} = \frac{1}{1-\nu^2 \frac{E_1 E_2}{E_o^2}} \times \begin{bmatrix} E_1 & \nu E_1 E_2 / E_o & 0 \\ \nu E_1 E_2 / E_o & E_2 & 0 \\ 0 & 0 & \frac{1}{4}(E_1 + E_2 - 2\nu \frac{E_1 E_2}{E_o}) \end{bmatrix} \begin{Bmatrix} d\epsilon_{11} \\ d\epsilon_{22} \\ d\gamma_{12} \end{Bmatrix} \tag{3.4}$$

The above constitutive matrix contains four material constants which are the instantaneous tangent stiffness moduli in the principal directions 1 and 2, i. e. E_1 and E_2, the equivalent Poisson's ratio, ν, and the initial modulus of elasticity, E_o. The evaluation of these parameters at each load stage

is presented in Sections 3.4 and 3.5.

3.2.1 Equivalent Uniaxial Strains

For an increment of stress or strain, the material can be assumed to behave as a linear elastic material and the principle of superposition can be considered to be applicable. Thus, the state of "real" stress at any point of the element in its principal plane is composed of two distinct cases (see Fig. 3.1):

(1) Stress is applied only along the axis 1 ($d\sigma_1 \neq 0$ and $d\sigma_2 = 0$), and the resulting incremental strains in the principal directions 1 and 2 are ε_{1u} and $\varepsilon_{2,1u}$, respectively (see Fig. 3.1b);

(2) Stress is applied only along the axis 2 ($d\sigma_1 = 0$ and $d\sigma_2 \neq 0$), and the resulting incremental strains in principal directions 1 and 2 are $\varepsilon_{1,2u}$ and ε_{2u}, respectively (see Fig. 3.1c).

The condition for equivalence of the systems (a) and (b+c) is (see Fig. 3.1):

$$\begin{aligned} d\epsilon_1 &= d\epsilon_{1u} + d\epsilon_{1,2u} \\ d\epsilon_2 &= d\epsilon_{2u} + d\epsilon_{2,1u} \end{aligned} \tag{3.5}$$

Applying Eq. 3.4 for each stress state (b) and (c) separately, the following equations are obtained corresponding to the directions with no stress:

$$\begin{aligned} \nu \frac{E_1 E_2}{E_o} d\epsilon_{1u} + E_2 d\epsilon_{2,1u} &= 0 \qquad (Case\ \ b) \\ E_1 d\epsilon_{1,2u} + \nu \frac{E_1 E_2}{E_o} d\epsilon_{2u} &= 0 \qquad (Case\ \ c) \end{aligned} \tag{3.6}$$

The strains $\varepsilon_{2,1u}$ and $\varepsilon_{1,2u}$ can be expressed in terms of ε_{1u} and ε_{2u} as follows:

$$\begin{aligned} d\epsilon_{2,1u} &= -\frac{\nu E_1}{E_0} d\epsilon_{1u} \\ d\epsilon_{1,2u} &= -\frac{\nu E_2}{E_o} d\epsilon_{1u} \end{aligned} \tag{3.7}$$

Combining Eqs. (3.5) and (3.7) gives:

$$\begin{Bmatrix} d\epsilon_1 \\ d\epsilon_2 \end{Bmatrix} = \begin{bmatrix} 1 & -\frac{\nu E_2}{E_o} \\ -\frac{\nu E_1}{E_o} & 1 \end{bmatrix} \begin{Bmatrix} d\epsilon_{1u} \\ d\epsilon_{2u} \end{Bmatrix} \tag{3.8}$$

Solution of this equation for $d\varepsilon_{1u}$ and $d\varepsilon_{2u}$ gives the following results:

$$\begin{Bmatrix} d\epsilon_{1u} \\ d\epsilon_{2u} \end{Bmatrix} = \frac{1}{1-\nu^2 \frac{E_1 E_2}{E_o^2}} \begin{bmatrix} 1 & \frac{\nu E_2}{E_o} \\ \frac{\nu E_1}{E_o} & 1 \end{bmatrix} \begin{Bmatrix} d\epsilon_1 \\ d\epsilon_2 \end{Bmatrix} \tag{3.9}$$

Equation (3.9) is a general equation which can be used to evaluate the incremental equivalent uniaxial strains, $d\varepsilon_{iu}$, based on the current incremental "real" strains, $d\varepsilon_i$, (i = 1,2).

By following a similar procedure, Eq. 3.9 takes the following form based on Darwin's constitutive matrix (see Eq. 2.30):

$$\begin{Bmatrix} d\epsilon_{1u} \\ d\epsilon_{2u} \end{Bmatrix} = \frac{1}{1-\nu^2} \begin{bmatrix} 1 & \nu\sqrt{\frac{E_2}{E_1}} \\ \nu\sqrt{\frac{E_1}{E_2}} & 1 \end{bmatrix} \begin{Bmatrix} d\epsilon_1 \\ d\epsilon_2 \end{Bmatrix} \tag{3.10}$$

It is obvious that the use of Eq. 3.10 is limited to the case where the moduli of elasticity (E_1 and E_2) have positive non-zero values. This condition (non-zero value for the modulus of elasticity) occurs when the state of stress in two principal directions is located on the ascending branch of the stress-strain curves. Based on several analyses, it was noticed that when the tangential stiffness, E_i, becomes nearly zero, the error of the incremental equivalent uniaxial strain, $\Delta\varepsilon_{iu}$, resulting from Darwin's method ($\Delta\varepsilon_{iu} = \Delta\sigma_i / E_i$) becomes larger, and compression failure of the concrete occurs suddenly with a rapid increase of the equivalent uniaxial strain. On the other hand, the equivalent uniaxial strains evaluated using Eq. 3.9 do not suffer from the difficulty arising from the division by zero, or a very small value. Therefore, the incremental stress-strain relationship in Eq. 3.9 is applicable for the entire stress or strain history (in both pre- and post-

peak regions), while Eq. 3.10 can only be used for the pre-peak regime.

With the crucial assumption of concrete being an isotropic material, i.e., $E_1=E_2=E_0$, Eq. 3.9 takes the following form as proposed by Noguchi (Meyer and Okamura, 1985):

$$\begin{Bmatrix} d\epsilon_{1u} \\ d\epsilon_{2u} \end{Bmatrix} = \frac{1}{1-\nu^2} \begin{bmatrix} 1 & \nu \\ \nu & 1 \end{bmatrix} \begin{Bmatrix} d\epsilon_1 \\ d\epsilon_2 \end{Bmatrix} \tag{3.11}$$

3.2.2 Rotation of Material Axis

During the subsequent iterations/ load steps, because of the presence of shear stresses the principal and material axes rotate. The material axes are assumed to coincide with the principal axes. A schematic representation of the material principal axes during two subsequent iterations/ load steps is shown in Fig. 3.2. The orientation of each principal coordinate system is measured with reference to the local coordinate system of the element.

In each iteration/ load step, the angle between the current principal coordinate system and the previous coordinate system, $\Delta\theta_i=\theta_{new}-\theta_{old}$, is obtained and then the previous equivalent uniaxial strain vector, $\{\epsilon_{iu\ old}\}$, is transformed by the angle $\Delta\theta_i$ to obtain its projection in the new principal coordinate system, $\{\epsilon'_{iu\ old}\}$ which results in:

$$\{\epsilon'_{iu\ old}\} = \begin{Bmatrix} \epsilon'_{1u\ old} \\ \epsilon'_{2u\ old} \end{Bmatrix} = \begin{bmatrix} \cos^2(\Delta\theta_i) & \sin^2(\Delta\theta_i) \\ \sin^2(\Delta\theta_i) & \cos^2(\Delta\theta_i) \end{bmatrix} \begin{Bmatrix} \epsilon_{1u\ old} \\ \epsilon_{2u\ old} \end{Bmatrix} \tag{3.12}$$

The incremental strain vector in the local coordinate system, $\{\Delta\epsilon\}$, is obtained as:

$$\{\Delta\epsilon\} = \begin{Bmatrix} \Delta\epsilon_{xx} \\ \Delta\epsilon_{yy} \\ \Delta\epsilon_{xy} \end{Bmatrix} = \{\epsilon_{new}\} - \{\epsilon_{old}\} \tag{3.13}$$

where $\{\epsilon_{old}\}$ and $\{\epsilon_{new}\}$ are the previous and the current strain vectors in the local coordinate system, respectively. Then the incremental principal strain in the new coordinate system, $\{\Delta\epsilon'_i\}$, can be evaluated as follows:

$$\{\Delta \epsilon'_i\} = \begin{Bmatrix} \Delta \epsilon'_1 \\ \Delta \epsilon'_2 \end{Bmatrix} = \{\epsilon_{i\ new}\} - \{\epsilon'_{i\ old}\} \tag{3.14}$$

or,

$$\{\Delta \epsilon'_i\} = \begin{bmatrix} \cos^2(\Delta\theta_i) & \sin^2(\Delta\theta_i) & \cos(\Delta\theta_i)\sin(\Delta\theta_i) \\ \sin^2(\Delta\theta_i) & \cos^2(\Delta\theta_i) & -\cos(\Delta\theta_i)\sin(\Delta\theta_i) \end{bmatrix} \begin{Bmatrix} \Delta \epsilon_{xx} \\ \Delta \epsilon_{yy} \\ \Delta \epsilon_{xy} \end{Bmatrix} \tag{3.15}$$

where $\{\varepsilon'_{i\,old}\}$ and $\{\varepsilon_{i\,new}\}$ are the transformed old and the new principal strain vectors in the new coordinate system, respectively. From the above incremental transformed principal strain vector, $\{\Delta\varepsilon'_i\}$, the incremental equivalent uniaxial strain vector, $\{\Delta\varepsilon_{iu}\}$, is obtained using Eq. 3.9 as

$$\{\Delta \epsilon_{iu}\} = \begin{Bmatrix} \Delta \epsilon_{1u} \\ \Delta \epsilon_{2u} \end{Bmatrix} = \frac{1}{1-\nu^2 \dfrac{E_1 E_2}{E_o^{\,2}}} \begin{bmatrix} 1 & \dfrac{\nu E_2}{E_o} \\ \dfrac{\nu E_1}{E_o} & 1 \end{bmatrix} \begin{Bmatrix} \Delta \epsilon'_1 \\ \Delta \epsilon'_2 \end{Bmatrix} \tag{3.16}$$

Finally, the new equivalent uniaxial strain vector is calculated as

$$\{\epsilon_{iu}\} = \begin{Bmatrix} \epsilon_{1u} \\ \epsilon_{2u} \end{Bmatrix} = \{\epsilon'_{iu\ old}\} + \{\Delta \epsilon_{iu}\} \tag{3.17}$$

It is obvious that based on the above formulation, the equivalent uniaxial strain is obtained from the "real" principal strains and the material parameters (E_1, E_2, and ν) corresponding to the previous load stage. In Darwin's model, the material axes are not transformed if the principal axis rotates within ±45 degrees from their original position; beyond this limit, the material axes are transformed. This method introduces a discontinuity in the computed equivalent uniaxial strains and causes more errors in the computation process (Meyer and Okamura, 1985). The method adopted in this study as outlined earlier, ensures the continuity of the computed equivalent uniaxial strains and gives more reliable results.

3.3 CONSTITUTIVE MODEL FOR CRACKED CONCRETE

Cracking of concrete is one of the important aspects of material nonlinear behaviour of concrete. Intensive research effort has resulted in a large number of cracking models, which can be divided broadly into two categories, namely, discrete cracking models and smeared cracking models. Furthermore, within each category, these models can be applied either with a strength-based, or fracture mechanics based crack propagation criterion (See Fig. 3.3).

3.3.1 The Discrete Cracking Model

The discrete cracking model is based on the concept of displacement discontinuity across a crack. In a finite element analysis program, this can be achieved by disconnecting elements at the nodal points along their boundaries as shown in Fig. 3.4. The main problem with this approach is the difficulty resulting from the introduction of the additional nodal points required by the altered topology of the analytical model.These additional degrees of freedom have the effect of destroying the small band width of the global structural stiffness matrix, resulting in a much greater computational effort to solve the equilibrium equations.

The discrete cracking model was first used for the analysis of reinforced concrete beams by Ngo and Scordelis (1967). For problem involving a few dominant cracks, such as the diagonal-tension crack in a reinforced concrete beam, the discrete cracking model offers a more realistic representation, i. e., a crack represents a strain discontinuity. Moreover, the aggregate interlock and the dowel action can be modelled in the discrete-cracking representation by using special linkage elements that cross the crack and control its behaviour as it opens and slides. The stiffness of this linkage can be decreased as the crack opens, thereby decreasing the interlock forces with wider cracks. In practice, the discrete cracking model is not popular and the majority of the available computer programs in nonlinear finite element analysis of reinforced concrete are employing the smeared cracking model which is easier to implement and much less computationally demanding than the discrete model.

3.3.2 The Smeared Cracking Model

The smeared crack model developed by Rashid (1968) has been adopted by the majority

investigators in the area of nonlinear finite element analysis of reinforced concrete structures. This model offers automatic generation of cracks, without a redefinition of the finite element topology and complete generality in possible crack direction. Based on this procedure, the cracked concrete is represented as an orthotropic material with an infinite number of parallel fissures across that part of the finite element (see Fig. 3.5). After cracking has occurred (usually defined when the principal tensile stress or strain exceeds a predefined limiting value), the constitutive matrix is defined as:

$$\begin{Bmatrix} d\sigma_1 \\ d\sigma_2 \\ d\tau_{12} \end{Bmatrix} = \begin{bmatrix} E_1 & 0 & 0 \\ 0 & E_2 & 0 \\ 0 & 0 & \beta G \end{bmatrix} \begin{Bmatrix} d\varepsilon_1 \\ d\varepsilon_2 \\ d\gamma_{12} \end{Bmatrix} \tag{3.18}$$

in which E_1 ($E_1 = 0$) and E_2 are the tangential stiffnesses perpendicular and parallel to the crack direction, respectively. Once the second crack is detected in the direction perpendicular to the first crack, the tangential stiffnesses E_2 is also set to zero. The factor β ($0<\beta<1.0$) is the multiplier of the uncracked concrete shear stiffness, G, which accounts for the reduced shear stiffness after cracking has resulted from dowel action and aggregate interlock, and is called the shear retention factor. If the term βG is ignored in the above equation, it can cause numerical difficulties in some cases, and also cause distortion of the crack patterns obtained from the finite element analyses (Schnobrich, 1972; Hand et al., 1973; Lin and Scordelis, 1975). To model the tension-stiffening effect using the descending branch of the tensile stress-strain curve, E_1 may be set equal to zero, or determined as the secant modulus of elasticity as shown in Fig. 3.12. Table 3.1 summarises the key features of both discrete and smeared cracking models.

The cracking models employed in conjunction with the smeared crack procedure can be categorized into the following three groups:

1) Fixed crack models

2) Rotating crack models

3) Multiple non-orthogonal crack models

Table 3.1: Cracking Models (Bello, 1992)

Model	Base	Approach	Advantages	Disadvantages
Discrete Cracking	Fracture Mechanics	Based on energy release rate	Bond effects are more accurately represented. Crack width computation is more accurate Problems of non-objectivity do not arise.	Additional concrete properties, e.g. energy release rate, G_f, fracture toughness, K_c Redefinition of structure topology after crack formation. Extensive remeshing is required where crack direction is not known *a priori*.
	Strength based	Based on limiting tensile stress/ strain	More realistic when few cracks dominate behaviour. Can realistically represent aggregate interlock by use of linkage element. Useful in investigating stresses when crack location is predefined.	Same as above; but no additional concrete property is required. Often the predicted response is sensitive to the refinement of finite element mesh.
Smeared Cracking	Fracture Mechanics	Based on energy release rate	Problems of non-objectivity do not arise. Can handle problems involving few dominant cracks. In addition, it has the three advantages listed below for strength-based model.	Additional concrete properties required, eg. energy release rate, G_f, fracture toughness, K_c
	Strength based	Based on limiting tensile stress/ strain	Computationally efficient; no need to redefine structure topology after cracking. Crack direction is not restricted to element boundaries. Adequate in problems in which precise crack location is not important.	Inadequate when precise crack location/geometry is important. Prone to non-objectivity; dependence of solution on grid size. Inadequate in problems involving few dominant cracks.

3.3.2.1 Fixed Crack Models

In the fixed crack models, once one crack is formed, the principal directions are not allowed to rotate and a second crack can form only when the stress perpendicular to the first crack direction exceeds the tensile strength of concrete ($\sigma > f'_t$). In this model, the principal tensile stresses can be built up at angles that differ from those of the original two fixed-orthogonal directions. These stresses can eventually exceed the cracking stress; however, no corrective action can be taken with this model and as a consequence, the numerical solutions can be "too stiff" and can lead to collapse loads that are significantly too high (Cope et al., 1980; Milford and Schnobrich, 1984; Crisfield and Wills, 1987 and 1989; Kolleger and Melhorn, 1987). This model is adequate for elements reinforced in only one direction, or in two directions with almost the same amounts of reinforcement.

3.3.2.2 Rotating Crack Models

In rotating crack models (Cope et al., 1980; Gupta and Akbar, 1984; Vecchio, 1989), the shortcomings associated with the fixed crack models are eliminated by permitting the principal directions to rotate after one or two cracks are formed. The cracking direction is taken to be perpendicular to the current major principal strain at any stage of loading.

The stiff response resulting from fixing the principal directions is eliminated by using this model. This approach has been criticized by Bazant (1983) for not reflecting the physical nature of cracking. However, it has been argued by Crisfield and Wills (1989) that when a tangential shear modulus is chosen such that:

$$\beta G = \frac{(\sigma_1 - \sigma_2)}{2(\epsilon_1 - \epsilon_2)} \tag{3.19}$$

then the orthotropic rotating crack models become tensorially invariant and hence consistent.

3.3.2.3 Multiple Non-Orthogonal Crack Models

The multiple non-orthogonal crack models have the ability to duplicate more than two non-orthogonal crack at one point of the structure. These models are not popular and only a few

researchers have used them (Barzgar and Schnobrich, 1986; Rots, 1988; Barzgar and Ramaswamy, 1990). The detailed discussion of this model is beyond the scope of this thesis. In this study, both the fixed and rotating crack models have been formulated and used in conjunction with the R C nonlinear finite element formulation.

3.3.3 Compressive Strength Degradation After Cracking

While cracking takes place, the concrete parallel to the crack direction is still capable of resisting tensile or compressive stresses. If it is subjected to tension, a linear elastic behaviour for concrete is assumed up to a tensile stress level equal to the tensile strength of concrete, f'_t, which represents the onset of the linear softening branch of tensile stress-strain curve of concrete, as proposed by Kabir (1976).

However, when concrete is subjected to compression, experimental results reported by Vecchio and Collins (1986), and Feenstra and de Borst (1993) show that the damages caused to the concrete with the transverse post-cracking tensile strains, have a degrading effect not only on the compressive strength of the concrete, but also on its compressive stiffness. Based on the experimental results of the reinforced concrete panels tested at University of Toronto by Vecchio and Collins (1986), the following formulas are used to determine the degraded compressive strength of the concrete, σ_{2c}, and the associated compressive strain, ϵ_{2c}

$$\sigma_{2c} = \frac{f'_c}{\beta} \qquad \epsilon_{2c} = \frac{\epsilon_{cu}}{\beta} \tag{3.20}$$

where, $\beta = 0.8 + 0.34 \left(\frac{\epsilon_{1u}}{\epsilon_{cu}}\right) \geq 1.0$.

Here, ϵ_{1u} is the current tensile strain in principal direction 1 and ϵ_{cu} is the uniaxial concrete strain at the peak stress.

3.4 STRESS-STRAIN CURVE FOR CONCRETE

3.4.1 Monotonically Increasing Compressive Uniaxial Stress-Strain Curve

Based on the experimental findings of Sinha, Gerstle and Tulin (1964), and Karsan and Jirsa (1969) [see Figs. 2.3 and 2.10], the stress-strain curve for concrete under cyclic loading has an envelope curve identical with the curve for monotonically increasing compressive loads. Therefore, for the envelope curve of the compressive stress-strain curve under cyclic loading, an analytical expression which represents the stress-strain curve of a cylinder of concrete subjected to monotonically increasing compressive loads up to failure, can be employed. Generalization of the expression given by Popovics (1973) which has been found by Thorenfeldt et al. (1987) to accurately represent the family of stress-strain curves for different strength concretes including the high strength concrete (refer to Figures 3.6 and 3.7) is adopted. This expression relating the stress, σ_i, and the equivalent uniaxial strain caused by this stress, ε_{iu}, is introduced as:

$$\frac{\sigma_i}{\sigma_{ic}} = \frac{n_i \left(\frac{\epsilon_{iu}}{\epsilon_{ic}}\right)}{n_i - 1 + \left(\frac{\epsilon_{iu}}{\epsilon_{ic}}\right)^{n_i k_i}} \qquad (3.21)$$

where, σ_i = current compressive principal stress in principal direction i,

ε_{iu} = equivalent uniaxial strain resulted from σ_i,

σ_{ic} = compressive strength of biaxially loaded concrete resulting from the failure envelope curve,

ε_{ic} = equivalent uniaxial strain when σ_i reaches σ_{ic},

n_i = curve fitting factor in principal direction i, and

k_i = factor to increase the post peak decay in stress

Here, k_i is equal to 1 when $(\varepsilon_{iu}/\varepsilon_{ic})$ is less than 1, and it is a number greater than 1 when $(\varepsilon_{iu} / \varepsilon_{ic})$ exceeds 1. Collins and Porasz (1989) suggested the value of k_i for $(\varepsilon_{iu} / \varepsilon_{ic}) > 1$ as

$$k_i = 0.67 + \frac{\sigma_{ic}}{9000} \qquad (in\ psi\ Units)$$

or,

$$k_i = 0.67 + \frac{\sigma_{ic}}{62} \qquad (in\ MPa\ Units) \qquad (3.22)$$

The parameter n_i takes a value greater than 1 and is evaluated using the equation:

$$n_i = 0.8 + \frac{\sigma_{ic}}{2500} \qquad (in\ psi\ Units)$$

or,

$$n_i = 0.8 + \frac{\sigma_{ic}}{17} \qquad (in\ MPa\ Units) \qquad (3.23)$$

In the computer program if the calculated value for n_i is less than or equal to 1, it is assigned a value of 1.1.

Equation (3.21) makes the relationship between σ_i and ε_{iu} a function of four constants: σ_{ic}, ε_{ic}, n_i and k_i. These four constants can all be obtained from the compressive strength of the concrete, σ_{ic}, which is evaluated from the failure envelope curve suggested by Kupfer and Gerstle (1973) depending on the biaxial loading ratio ($\alpha=\sigma_1/\sigma_2$). For normal weight concrete, n_i can be estimated from Eq. 3.23 and k_i can be calculated using Eq. 3.22. If the initial slope E_o of the stress-strain curve (initial modulus of elasticity) is known, or it can be estimated, the strain at peak stress ε_{iu} can be found from the following equation:

$$\epsilon_{ic} = \frac{\sigma_{ic}}{E_o} \frac{n_i}{n_i - 1} \qquad (3.24)$$

The initial tangent stiffness of the concrete, E_o, lies between the stiffness of the aggregate and the stiffness of the paste. Its value can be estimated using the composite material modelling laws (Mills and Ono, 1972). One suggestion for E_o is (Carrasquillo et al., 1981):

$$E_o = 40000\sqrt{f'_c} + 1{,}000{,}000 \qquad (in\ psi\ Units)$$
$$(for \quad 3000 < f'_c < 12000)$$

or,

$$E_o = 3320\sqrt{f'_c} + 6900 \qquad (in\ MPa\ Units)$$
$$(for \quad 21 < f'_c < 83) \tag{3.25}$$

The values of E_1 and E_2 required in Eq. 3.4 for a given stress ratio ($\alpha = \sigma_1 / \sigma_2$) are found as the slopes of the σ_1-ε_{1u} and σ_2-ε_{2u} curves, respectively. The tangent to the ascending branch of the stress-strain curve, Eq. 3.21, is given by:

$$E_i = \frac{d\sigma_i}{d\epsilon_{iu}} = \frac{\dfrac{n_i\sigma_{ic}}{\epsilon_{ic}}\left(n_i - 1 + \left(\dfrac{\epsilon_{iu}}{\epsilon_{ic}}\right)^{n_i k_i}\right) - \dfrac{n_i k_i}{(\epsilon_{ic})^{n_i k_i}}\left(\epsilon_{iu}^{n_i k_i - 1}\right)\left(n_i \sigma_{ic}\dfrac{\epsilon_{iu}}{\epsilon_{ic}}\right)}{\left(n_i - 1 + \left(\dfrac{\epsilon_{iu}}{\epsilon_{ic}}\right)^{n_i k_i}\right)^2}$$

or,

$$E_i = \left(\frac{n_i\,\sigma_{ic}}{\epsilon_{ic}}\right)\left(\frac{n_i - 1 + (1 - n_i k_i)\left(\dfrac{\epsilon_{iu}}{\epsilon_{ic}}\right)^{n_i k_i}}{\left(n_i - 1 + \left(\dfrac{\epsilon_{iu}}{\epsilon_{ic}}\right)^{n_i k_i}\right)^2}\right) \tag{3.26}$$

From the above equation, the initial modulus of elasticity can be evaluated as a function of σ_{ic} and ε_{ic} at $\varepsilon_{iu} = 0.0$, namely,

$$E_o = \left(\frac{d\sigma_i}{d\epsilon_{iu}}\right)_{\epsilon_{iu}=0} = \frac{\sigma_{ic}}{\epsilon_{ic}}\left(\frac{n_i}{n_i - 1}\right) \tag{3.27}$$

On the other hand, this equation can be used to evaluate the strain at the peak point, ε_{ic}, as a function of σ_{ic} and E_o, as introduced in Eq. 3.24.

For the elastic tension region (ascending branch of tensile stress-strain curve), E_i is assumed to be equal to E_0 and for the descending branch of both the compression and the tension zones, E_i is set equal to zero to avoid computational difficulties associated with a negative value for E_i. in the computer program developed in this study. The value of E_i in these regions is given

by the user and the unbalanced stresses are released in a step-wise fashion.

3.4.2 Cyclic Uniaxial Compressive Stress-Strain Curve

Concrete under compression is assumed to behave elastically up to a certain stress level (0.30 σ_{ic}). A new analytical representation of the focal point model (Yankelevsky and Reinhardt, 1987) is used to construct the unloading and reloading curves under cyclic loading. In this formulation, it is assumed that in the uniaxial stress-strain plane, there exist five geometrical loci, which are called as "focal points". These focal points allow the construction of the unloading-reloading cycles using piece-wise linear curves (see Fig. 3.8). Four focal points (E, F, G and H) are located on the tangent to the ascending branch of the envelope curve at the origin, and the fifth focal point (I) rests on the strain axis as shown in Fig. 3.8.

To construct the unloading and reloading curves corresponding to point A(ε_{cn} , σ_{cn}) located on the envelope curve presented in the previous section, the following graphical procedure is followed (see Fig. 3.8):

(1) Define a stress-strain coordinate system.

(2) Plot the envelope curve in this coordinate system.

(3) Specify the focal points **E**, **F**, **G**, and **H**, which lie on the tangent at the origin to the envelope curve,with the following coordinates: σ_E = -3.0 σ_{ic}, σ_F = -σ_{ic}, σ_G = -0.75 σ_{ic}, and σ_H = -0.2 σ_{ic}; and the focal point **I** (-ε_{IC}, **0**) on the strain axis.

(4) Connect the starting point **A** with focal point **F** to intersect the ε axis at point **B**(ε_B, **0**), where ε_B is the residual strain which is termed the "plastic strain".

(5) Intersect the line connecting the focal point **G** and the point **B** with a vertical line passing through the starting point **A** to obtain point **C**, which is called the "common point".

(6) The line that connects the focal point **E** and the point **C** intersects with the line connecting the focal point **H** and the point **B** giving point **D** which is called "turning point".

(7) Connect the focal point **I** and the common point **C** and find the intersection of this line with the envelope curve which is point **J**.

At this stage the unloading branch **AC-CD-DB** and the reloading branch **BC-CJ** are completed. While partial unloading is occurring at point **R** which is below the common point (refer to Fig. 3.8), the partial reloading consists of three parts: **(1)** the line **RT**, which connects the reloading starting point, R, with point T, located on the global reloading curve BC (the slope of this line

is equal to the initial tangent, OE), (2) the line **TC** which is part of the line BC, and (3) the line **CJ**. If partial unloading occurs above the common point **C**, say at the point **R'**, then R' is projected on the envelope curve at **A'** and a new unloading-reloading curve corresponding to point A' will be constructed. This curve is shown by dashed line in Fig. 3.8.

A mathematical representation of this model is used to implement it into the nonlinear finite element formulation. According to the following representation, the unloading and reloading for each starting point $A(\varepsilon_{en},\sigma_{en})$ is generated automatically.

The point B is given by:

$$\epsilon_B = \frac{B_1\epsilon_F - \sigma_f}{B_1} \qquad \sigma_B = 0 \tag{3.28}$$

where $\varepsilon_F = \sigma_F/E_0$, and $B_1 = (\sigma_A-\sigma_F)/(\varepsilon_A-\varepsilon_F)$.

The point C is given by:

$$\epsilon_C = \varepsilon_A \qquad \sigma_C = B_2\,(\epsilon_A - \epsilon_G) + \sigma_G \tag{3.29}$$

where $\varepsilon_G = \sigma_G/E_0$, and $B_2 = -\sigma_G/(\varepsilon_B-\varepsilon_G)$.

The point D is given by:

$$\epsilon_D = \frac{B_3\epsilon_E - B_4\epsilon_H + \sigma_H - \sigma_E}{B_3 - B_4} \qquad \sigma_D = B_3\,(\epsilon_D - \epsilon_E) + \sigma_E \tag{3.30}$$

where $\varepsilon_H = \sigma_H/E_0$, $\varepsilon_F = \sigma_E/E_0$, $B_3 = (\sigma_C-\sigma_E)/(\varepsilon_C-\varepsilon_E)$, and $B_4 = -\sigma_H/(\varepsilon_B-\varepsilon_H)$.

Several uniaxial repeated test have been compared with the model predictions (see Shayanfar and Mirza, 1994), including the work of Sinha et al. (1964) as shown in Fig. 3.9. It is obvious that the proposed analytical model compares well with the test results and represents basic features of the concrete behaviour in cyclic compression. It can be seen that with an increase in the number of cycles, the stiffness of the concrete decreases, and the plastic strain increases. In general, as the residual strain increases, the concrete becomes increasingly softer. It should be

noted that high strength concretes normally exhibit lower residual strains.

3.4.3 Uniaxial Tensile Stress-Strain Curve

The formation of cracks, their propagation and widening have a major influence on the nonlinear behaviour of a concrete structure. It has effects on both the local behaviour, such as bond between reinforcement and concrete, and the global behaviour, such as flexural stress distribution. Therefore, the cracking process in concrete needs to be well understood and appropriately formulated for computational implementation.

Unconfined concrete under monotonic uniaxial tension exhibits linear elastic behaviour up to about 80% of its ultimate strength, and has a tangent modulus of elasticity which is comparable to that in compression (Gopalaratnam and Shah, 1985). When the stress is increased further, the behaviour is highly nonlinear. Concrete softens considerably as the peak stress is attained and then, as a result of increasing microcracks in the cement matrix and at the matrix-aggregate interface, a descending branch of the stress-strain curve is obtained.

A large part of the energy is absorbed in the descending zone and complete failure occurs sometimes at a strain 40 times the strain corresponding to the peak tensile stress (Gopalaratnam and Shah, 1985). In this study, concrete in tension is assumed to behave as a linearly elastic material up to a tensile stress level equal to the tensile strength of concrete, f'_t, which represents onset of the softening branch (see Fig. 3.11).

Detailed analyses of concrete beams and shear panels (Shayanfar et al., 1993) show that the size of finite elements has a significant effect on the computed results including the failure load. This phenomenon is called "finite element size effect". It was shown that if the value of ε_{tu} is adjusted appropriately according to the element size, it can help eliminate the mesh sensitivity drawback. In the present study, two models have been used to determine an appropriate value of ε_{tu} for a given finite element size: (a) crack band model, based on the fracture mechanics concepts, as a function of the fracture energy, mesh size and tensile strength of concrete, and (b) a new proposed model as a function of only the element size. More information is provided in this regard in Chapter 5 and in a report by Shayanfar et al. (1993).

In this investigation, it is assumed that the compressive stress can cause some damage in the concrete which affects its subsequent tensile strength. If the compressive strain, in the principal direction under consideration, equals or exceeds the equivalent uniaxial strain corresponding to

the maximum compressive strength of concrete, ε_{ic}, then the material is assumed to have no subsequent tensile capacity due to the extensive internal microcracking of the concrete. If the compressive stress has not exceeded this value, a linear variation for the tensile strength of concrete is adopted. The values 0 and f'_t have been set for the tensile strengths corresponding to the compressive strength, σ_{ic}, and the compressive elastic limit, respectively. The reduced tensile strength, σ_{it}, and its associated parameters are calculated as follows:

$$\sigma_{it} = \frac{\tan\alpha.\tan\beta}{\tan\beta - \tan\alpha}(\epsilon_p + \epsilon_{pp})$$

$$\epsilon_{it} = \frac{\sigma_{it}}{\tan\beta} \qquad (3.31)$$

$$\epsilon_{inu} = \frac{\epsilon_{tu}}{\epsilon_t}(\epsilon_{it})$$

where α and β have been defined in Fig. 3.11. For concrete in the elastic range, a full tensile strength capacity, $\sigma_{it}=f'_t$, is assumed.

To study the influence of various "tension-stiffening" models on the response of reinforced concrete structures, different descending branch shapes, as shown in Fig. 3.12, have been studied.

While cyclic loading in tension part, the unloading and reloading started from the ascending branch will follow the ascending branch (linear elastic behaviour). The unloading from the descending branch follows a straight line passing through the unloading point and the origin of the stress-strain coordinate system. In other word, in this case the secant modulus to the unloading point will be taken as the modulus of elasticity of concrete.

3.4.3.1 Tensile Strength of Concrete

It is difficult to test concrete in pure axial tension, therefore the tensile strength of concrete is usually evaluated by an indirect test. The different test procedures along with the equations used for determining the tensile strength are listed below (ACI, 1989). Depending on the type of the structure, one can follow the results of the following procedures to estimate an appropriate value for the tensile strength of concrete. For example, for structures failing in a flexural mode, the results of rupture test are recommended, while for the shear mode of failure, the strength values obtained from the direct tension test.

Direct Tension Test:

$$f'_t = 4\lambda \sqrt{f'_c} \qquad (in\ psi\ Units)$$

or,

$$f'_t = 0.33\lambda \sqrt{f'_c} \qquad (in\ MPa\ Units) \tag{3.32}$$

Modulus of Rupture Test:

$$f_r = 7.5\lambda \sqrt{f'_c} \qquad (in\ psi\ Units)$$

or,

$$f_r = 0.6\lambda \sqrt{f'_c} \qquad (in\ MPa\ Units) \tag{3.33}$$

Split Cylinder Test:

$$f'_t = 0.65\, f_{sp} \tag{3.34}$$

and,

$$f_{sp} = \frac{2P}{\pi LD}$$

where

λ = a factor which accounts for the density of the concrete

= 1.00, for normal weight concrete

= 0.85, for sand-light weight concrete

= 0.75, for all light weight concrete

P = the applied compressive load to cause failure

L = the length of the cylinder

D = the diameter of the cylinder

3.5 EQUIVALENT POISSON'S RATIO

As mentioned earlier in Section 2.1, concrete under uniaxial and biaxial compression first compacts and then dilatates due to the internal microcracking. To take this dilatancy of concrete into account the value of the equivalent Poisson's ratio is assumed to be of the following form (Ottoson, 1979):

$$\begin{aligned} \nu &= \nu_i && \text{for } \gamma_2 \le \gamma_a \\ \nu &= \nu_f - (\nu_f - \nu_i)\sqrt{1 - \left(\frac{\gamma_2 - \gamma_a}{1 - \gamma_a}\right)^2} && \text{for } \gamma_2 > \gamma_a \end{aligned} \qquad (3.35)$$

in which, ν_i is the initial Poisson's ratio; γ_2 is the nonlinear index which represents the ratio of the actual compressive stress, σ_2, to the corresponding value of that stress at failure (ultimate strength), σ_{2c}, ($\gamma_2 = \sigma_2 / \sigma_{2c}$); ν_f is the Poisson's ratio at failure and set equal to 0.36; and γ_a is the nonlinear index corresponding to the onset of dilatancy which is set to be 0.80. Because the Poisson's ratio starts to increase at the stress level corresponding to $\gamma_a = 0.80$ (Kupfer et al., 1969). In the model, an upper bound $\nu \le 0.45$ is set to eliminate problems associated with the Poisson's ratio approaching 0.5. For the tension-tension stress condition, $\nu = \nu_i$, is applicable.

The initial Poisson's ratio, ν_i, is assumed to be equal to 0.20. An examination of the available information shows that the initial Poisson's ratio of high-strength concrete is comparable with the expected range of values for the lower strength concretes. Shideler (1957) and Carrasquil et al. (1981) reported values for Poisson's ratio of light-weight, high-strength concrete having uniaxial compressive strength up to 10,570 psi (73 MPa) at 28 days to be 0.20 regardless of the compressive strength, age and the moisture content.

3.6 FAILURE CRITERIA FOR CONCRETE

Behaviour of concrete under biaxial stress states, as reported by a number of investigators is remarkably different from that under uniaxial conditions. Based on the experimental observation under biaxial compression, the compressive strength of the concrete increases because of the internal friction and aggregate interlock. Conversely, a lateral compressive stress decreases the tensile strength of the concrete because the compressive stress introduces tensile stresses at the

micro-level due to the heterogeneity of the material which increases the process of internal damage as reported by Vonk (1990). A lateral tensile stress has no major influences on the tensile strength of concrete. To account for these phenomena, the failure envelope proposed by Kupfer and Gerstle (1973), is employed to obtain the compressive and tensile strength of concrete under the biaxial stress state. The lateral tensile stress beyond cracking can also decrease the compressive strength of concrete as obtained by Vecchio and Collins (1986), and Feenstra and de Borst (1993). To account for this, the model proposed by Vecchio and Collins (1986) is used in the proposed formulation as discussed in Section 3.3.3. A slightly modified form of the biaxial strength envelope curve developed by Kupfer et al. (1969) is used in the program built up in the present study as shown in Fig. 3.13.

3.7 CONSTITUTIVE RELATIONSHIP FOR STEEL REINFORCEMENT

The behaviour of steel reinforcement is basically uniaxial and consequently modelling of its behaviour is relatively simple compared to that of the concrete. Two aspects of steel models are relevant here; the representation of steel in the finite element model and the constitutive relationship. The three most common methods used to represent reinforcing steel in finite element models (ASCE, 1982) are:

1. Distributed (smeared) model,
2. Embedded model, and
3. Discrete model

In a distributed representation, the steel is smeared over the concrete and a perfect bond is assumed between the concrete and the steel. An embedded representation treats steel as a uniaxial member built into the concrete, such that its nodal displacements are constrained by those of the "host" concrete element. A discrete representation is similar to an embedded representation, but in this case the nodal displacement of the steel bar are not constrained by those of the "host" element. Figure 3.14 illustrates the three common representations of steel bars in finite element models.

The stress-strain behaviour of steel is usually represented by a bilinear or a trilinear idealization identical in tension and compression. An elastic-perfectly plastic, or an elastic-strain hardening model utilizes a bilinear curve, while an elastic-plastic-strain hardening model is represented by a trilinear curve. Figure 3.15 shows these idealizations.

The steel reinforcement is treated in HODA program as an elasto-plastic-strain-hrdening material as shown in the figure. The Bauchinger effect or reduction of the steel yielding stress due to load reversal is also considered [see Fig. 3.15(c)]. The constitutive relationship for steel before yielding is given by:

$$\{\Delta\sigma\} = \begin{bmatrix} E_S & 0 & 0 \\ 0 & 0 & 0 \\ 0 & 0 & 0 \end{bmatrix} \{\Delta\epsilon\} \tag{3.36}$$

where E_s is the uniaxial elastic modulus of elasticity.

After the steel yields, the constitutive relationship is modified to reflect the change in the modulus. For example, in an elastic-strain hardening model, the modification is as:

$$\{\Delta\sigma\} = \begin{bmatrix} E_s^* & 0 & 0 \\ 0 & 0 & 0 \\ 0 & 0 & 0 \end{bmatrix} \{\Delta\epsilon\} \tag{3.37}$$

where E^*_s is the strain-hardening modulus (see Fig. 3.15).

It should be noted that perfect bond has been assumed between reinforcing steel and the concrete; this assumption holds for all the structural elements analyzed. The effect of dowel action is incorporated into the computer formulation through the parameter 6, the shear retention factor with values between zero and 1.0, which accounts for both dowel action at the steel-concrete interface and the aggregate interlock at the cracks. For the three models used to idealize steel, buckling of reinforcing bar has not been considered explicitly, however, these bars are embedded in concrete which provides the support to prevent any lateral instability of the reinforcing bars.

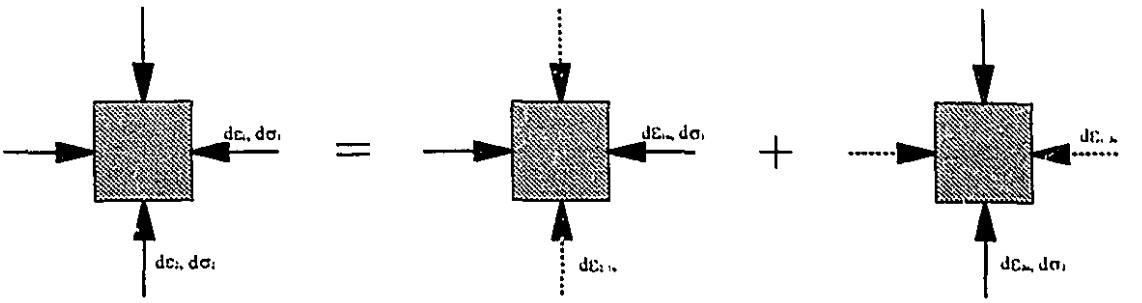

Figure 3.1: Schematic representation of real strains and equivalent uniaxial strains

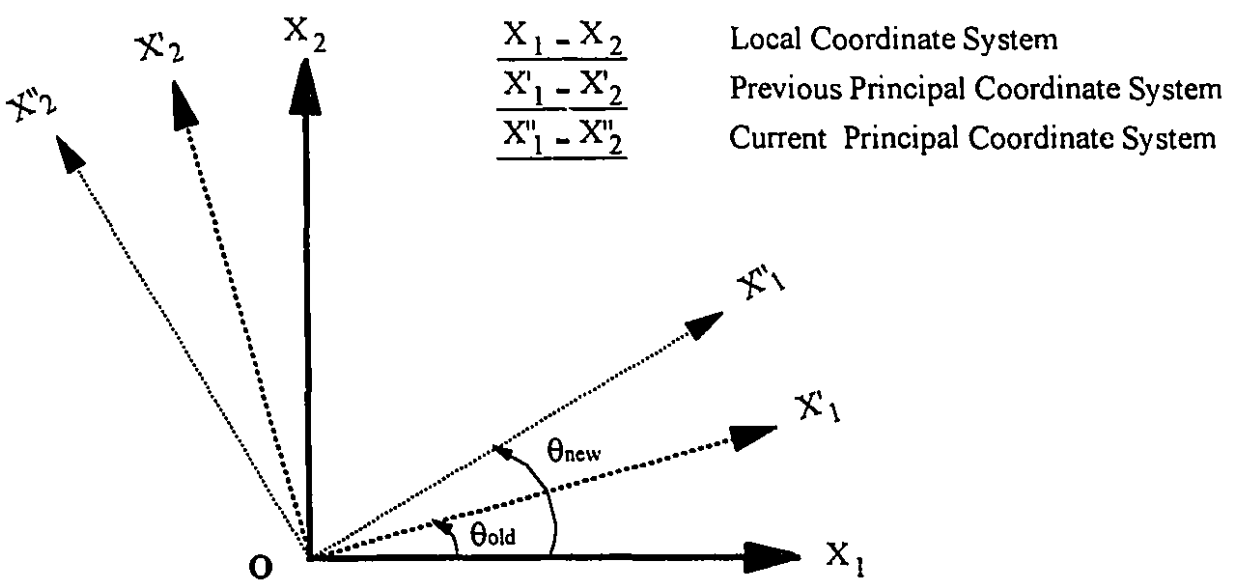

Figure 3.2: Schematic representation of different coordinate systems at any point of an element

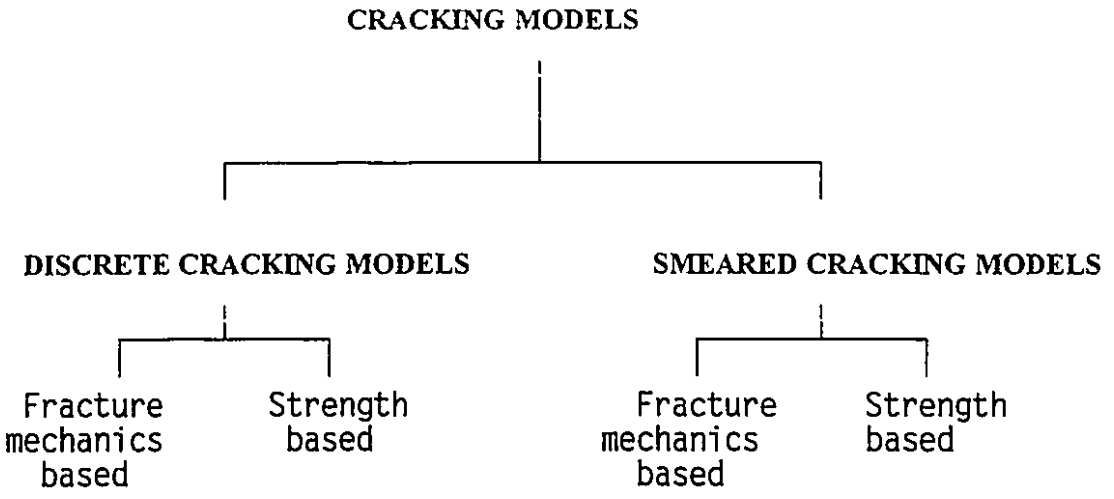

Figure 3.3: Classification of cracking models

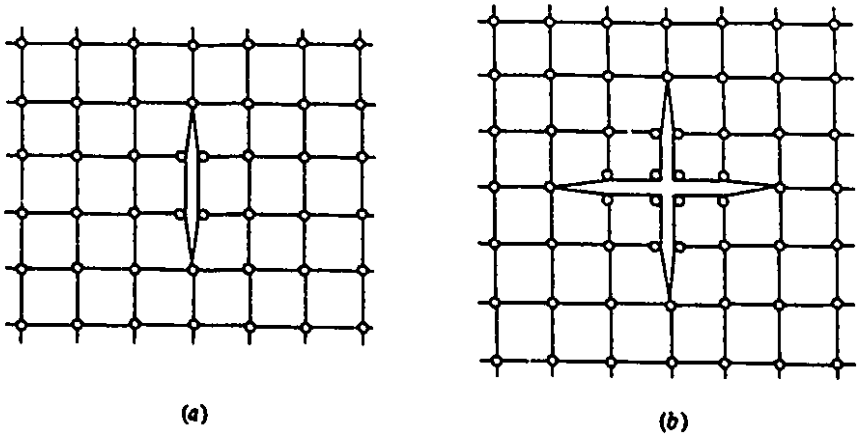

Figure 3.4: Nodal separating using two or four coincident nodes: (a) one-directional and (b) two-directional cracking

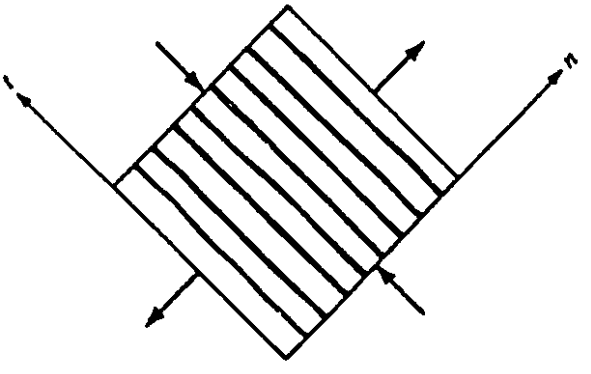

Figure 3.5: Idealization of a single crack

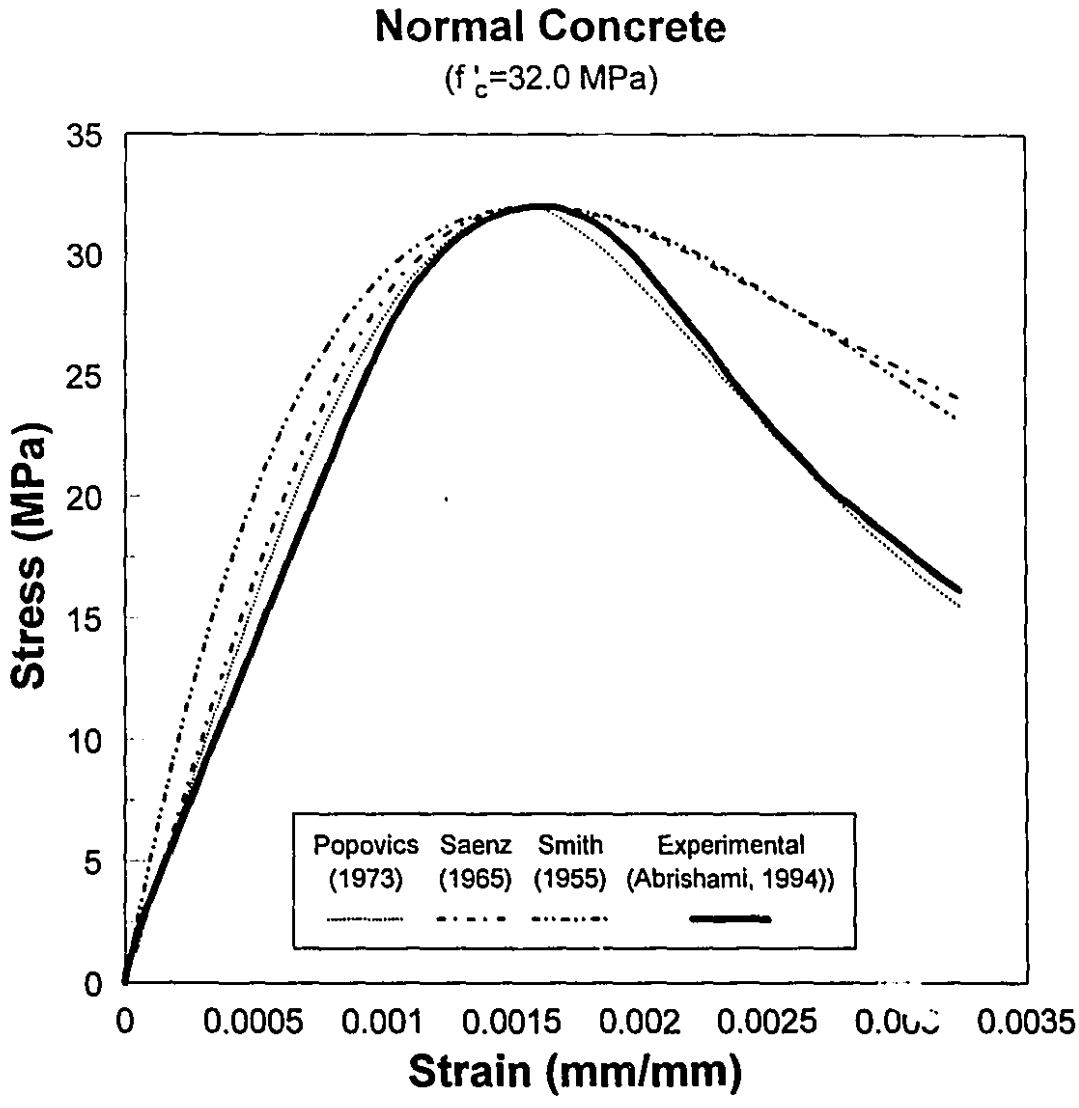

Figure 3.6(a): Comparison of different analytical stress-strain curves with the experimental results for normal concrete

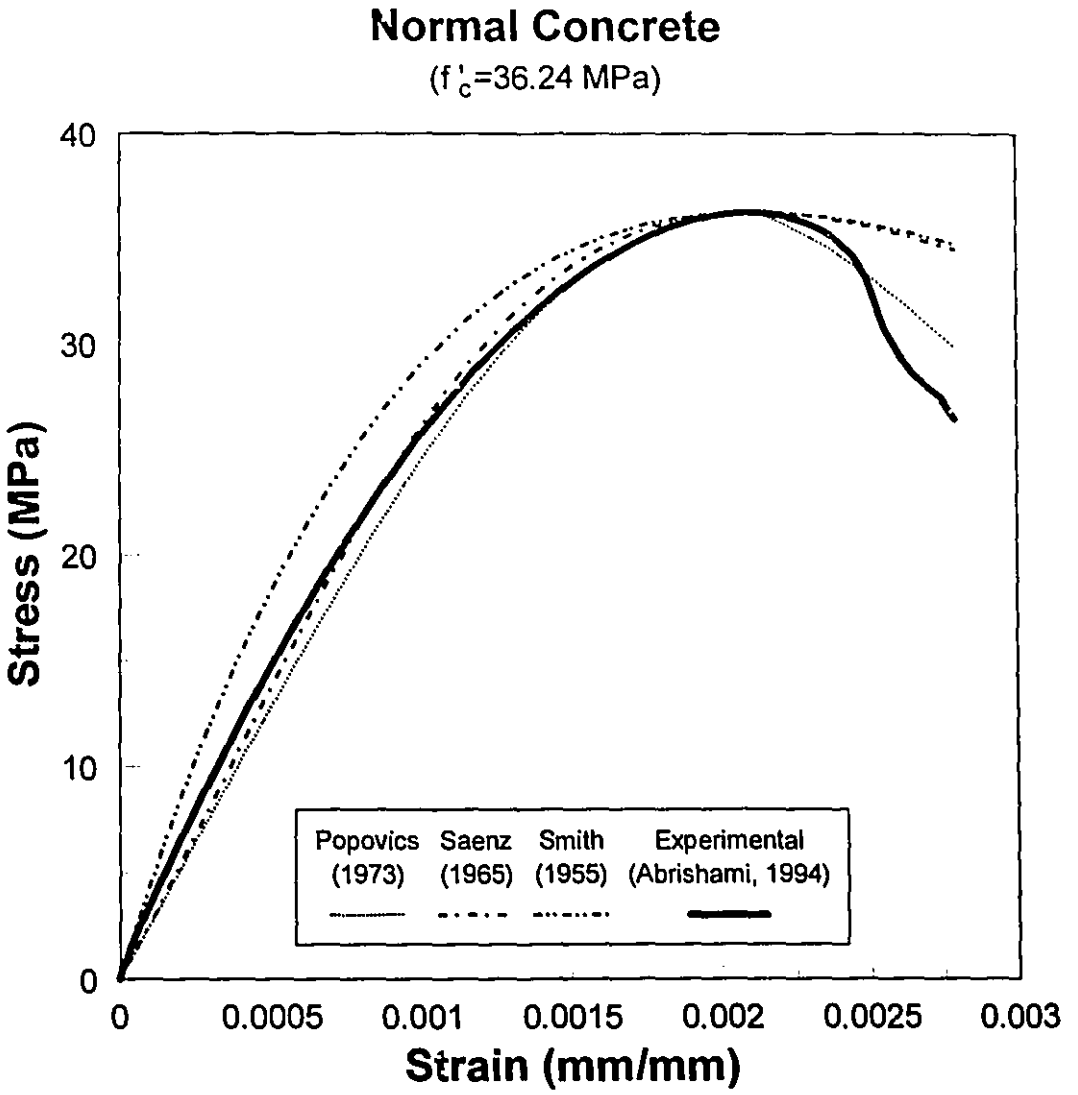

Figure 3.6(b): Comparison of different analytical stress-strain curves with the experimental results for normal concrete

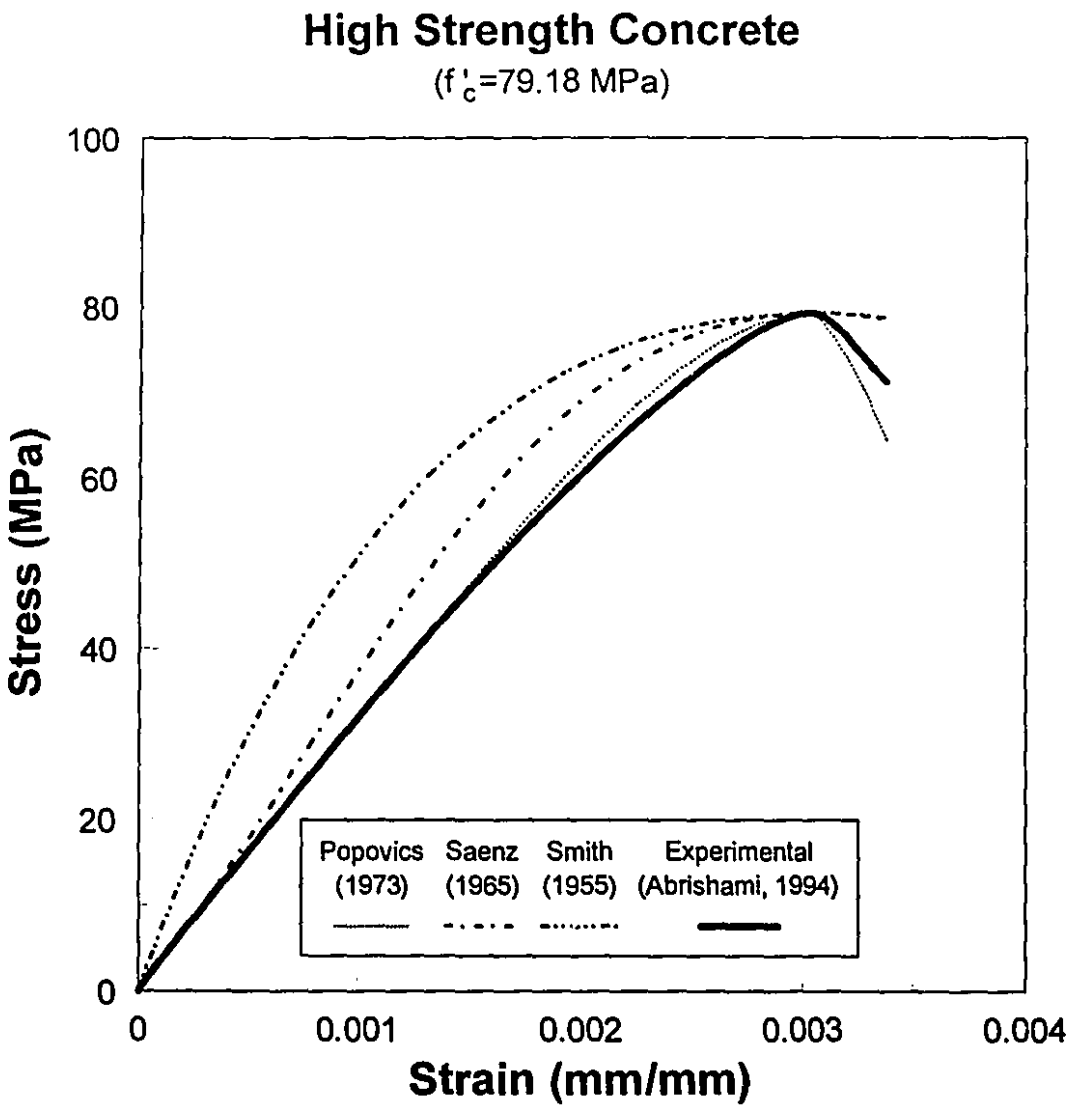

Figure 3.7(a): Comparison of different analytical stress-strain curves with the experimental results for high strength concrete

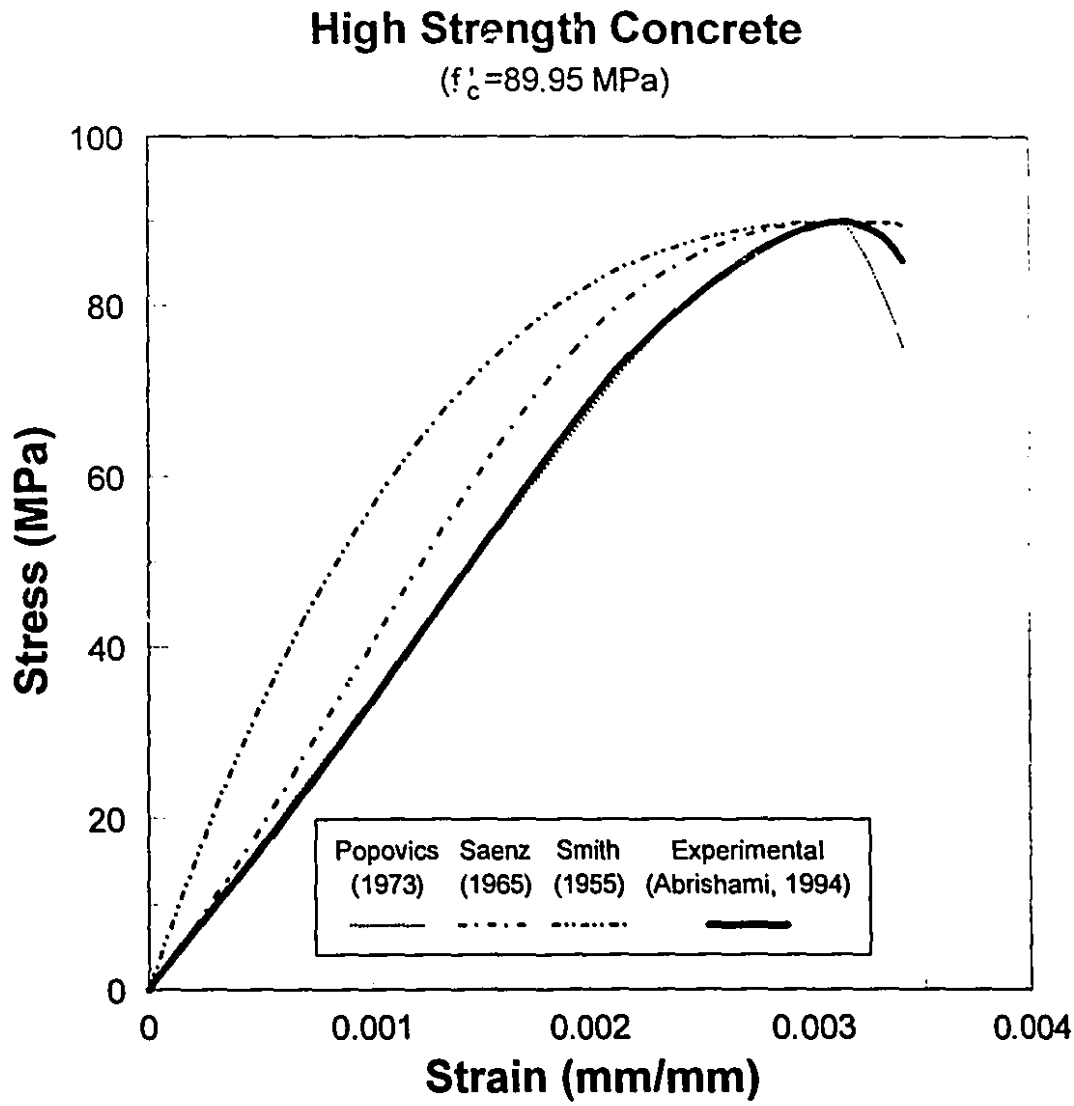

Figure 3.7(b): Comparison of different analytical stress-strain curves with the experimental results for high strength concrete

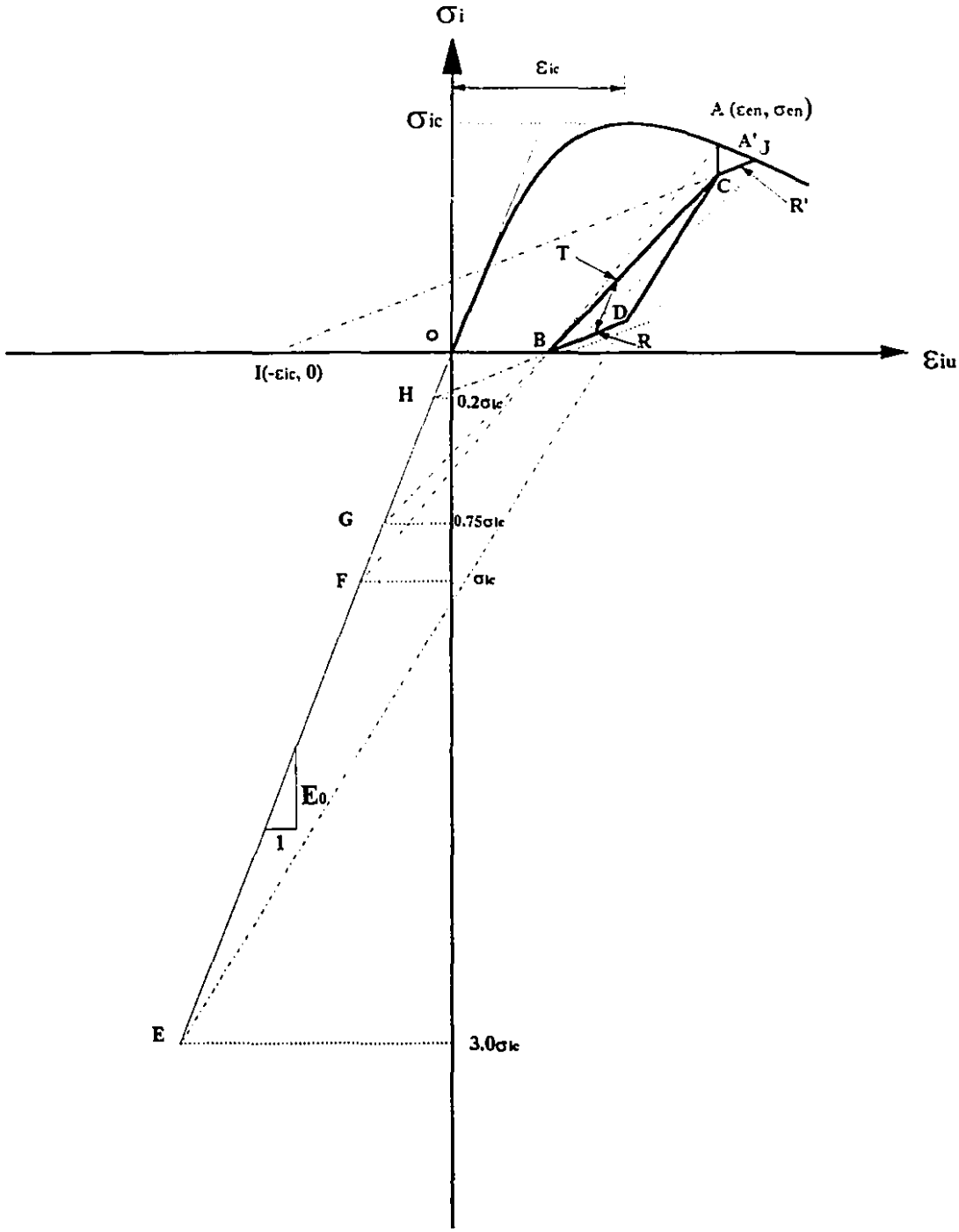

Figure 3.8: Scheme of the focal point model for uniaxial cyclic compression load

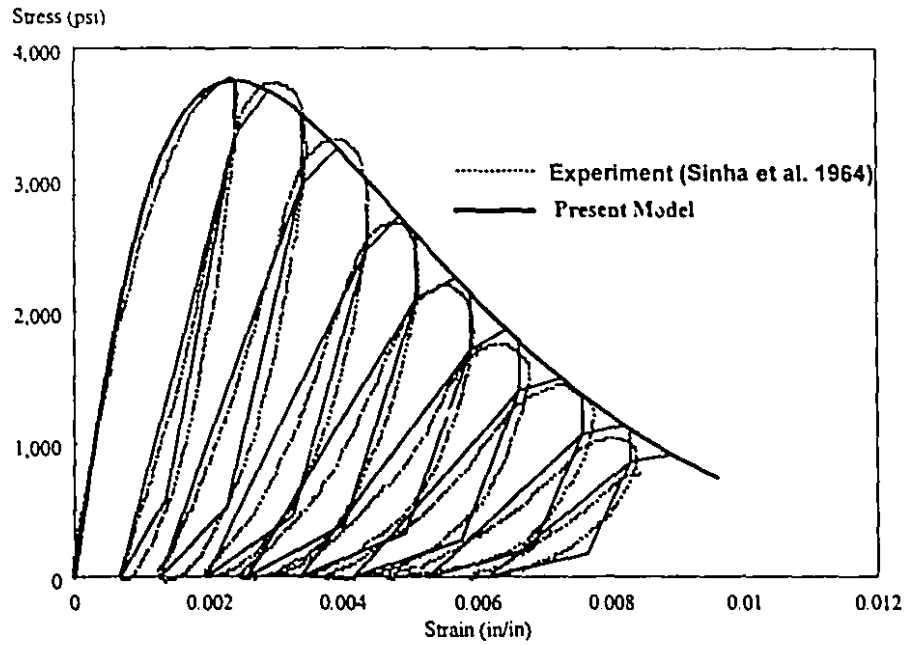

Figure 3.9: Comparison of the present model with the experimental cyclic compression stress-strain curve

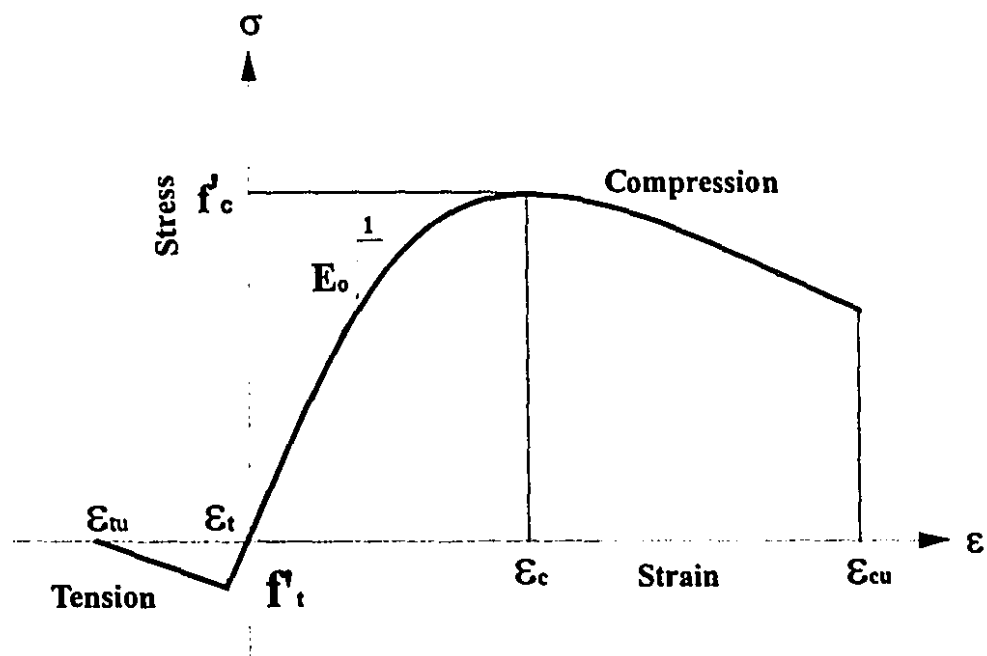

Figure 3.10: Analytical uniaxial stress-strain curve of plain concrete

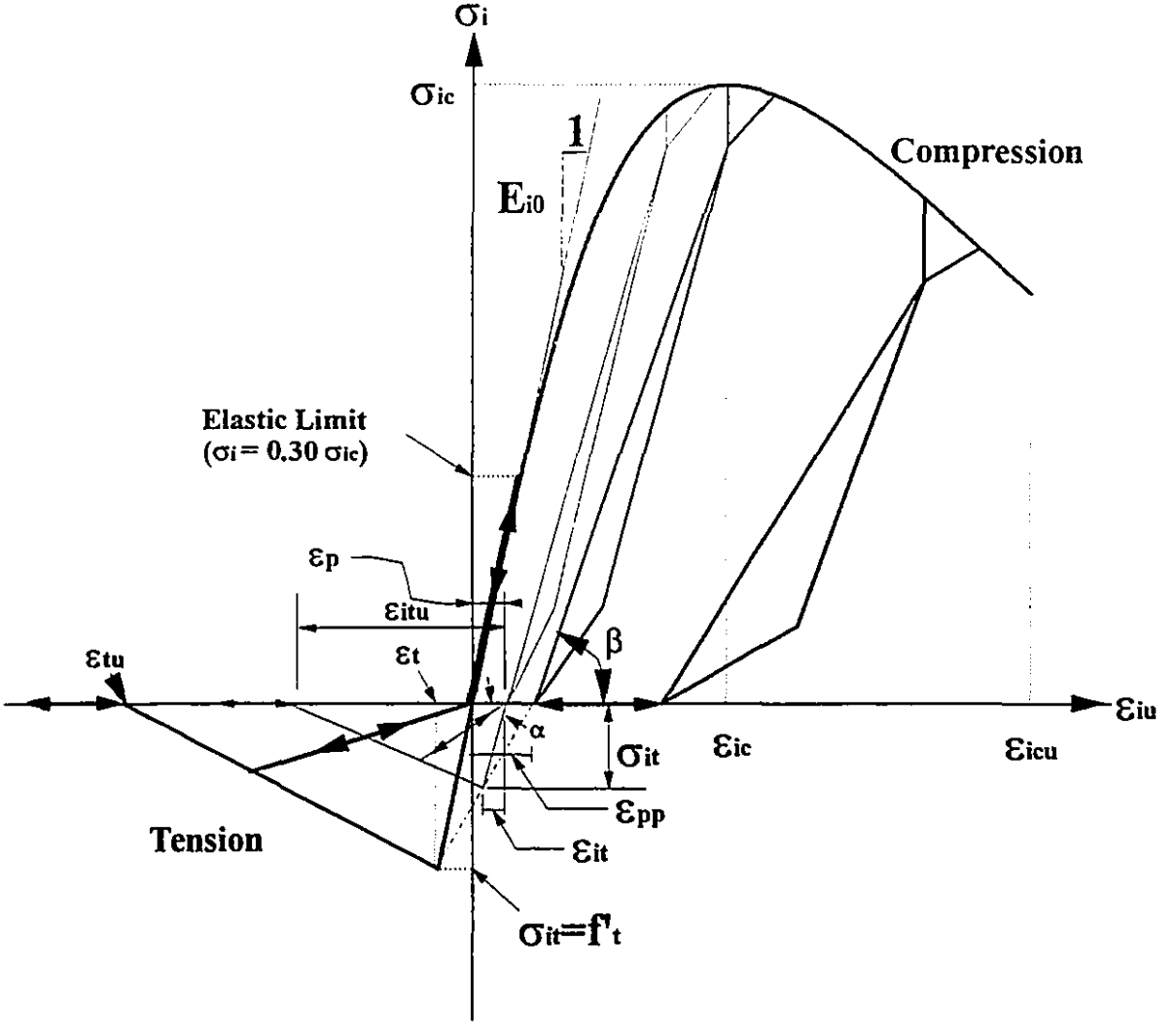

Figure 3.11: Proposed equivalent uniaxial stress-strain curve in ith direction.

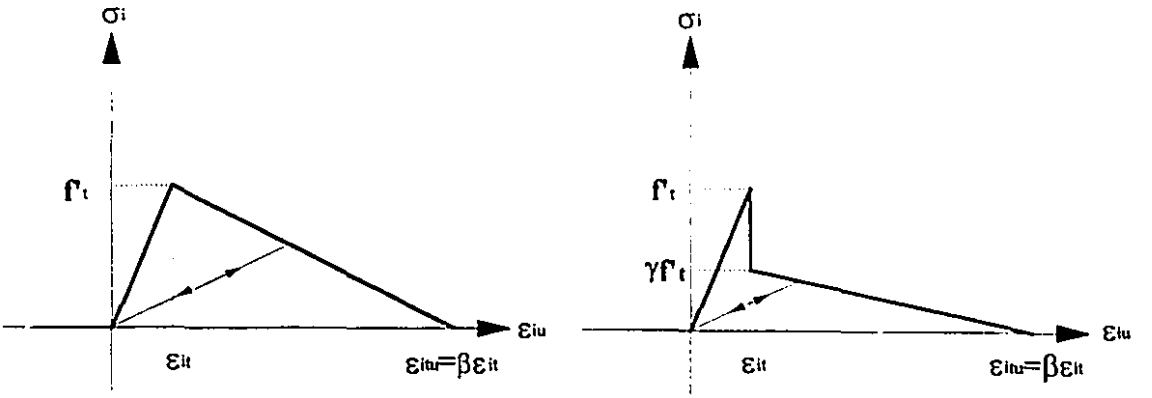

Figure 3.12: Concrete models in tension: (a) linear softening; (b) discontinuous softening

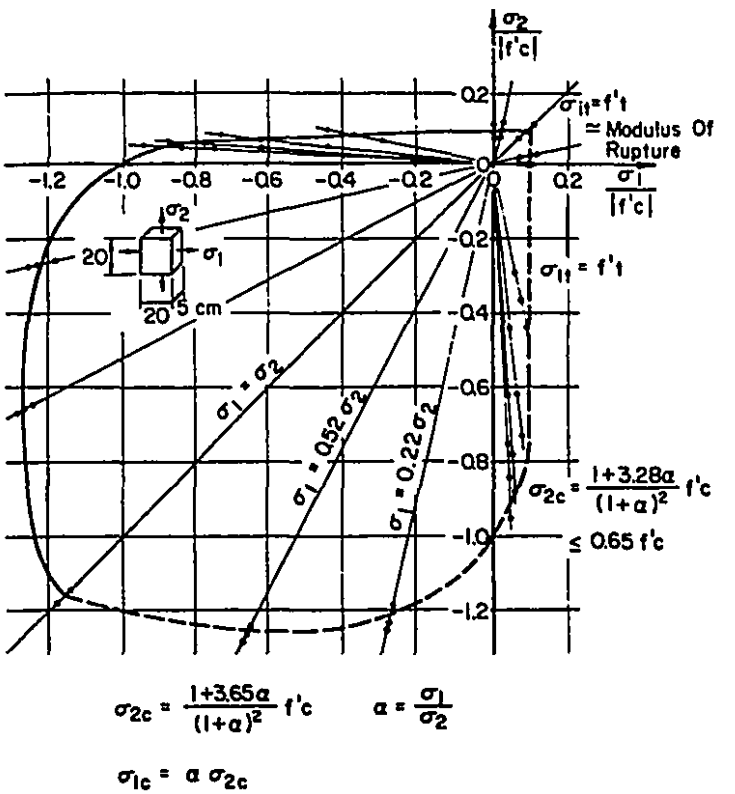

Figure 3.13: Typical biaxial failure envelope for concrete (Ghoneim, 1978)

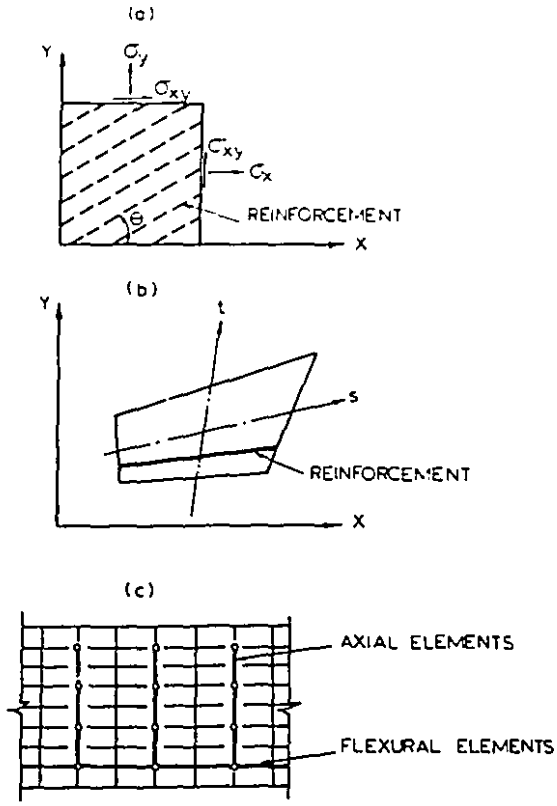

Figure 3.14: Typical steel representations in finite element models:of concrete structures, (a) distributed (b) embedded, and (c) discrete (ASCE, 1982)

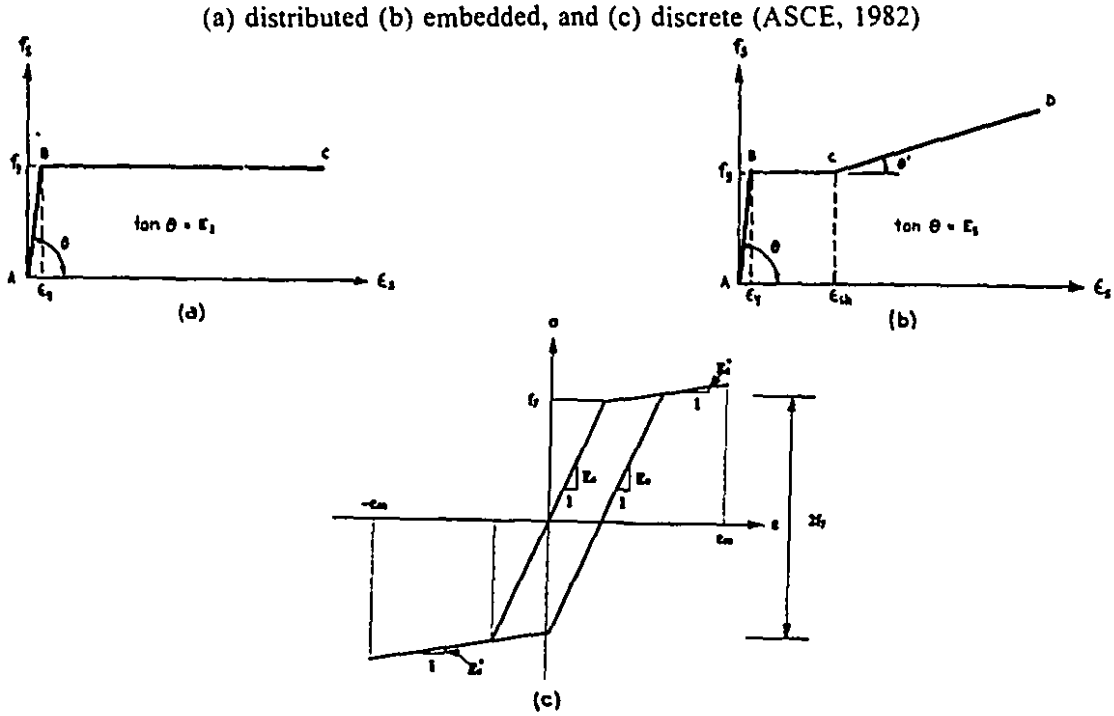

Figure 3.15: Idealized steel stress-strain curves: (a) elastic-perfectly plastic idealization, (b) elastic-strain hardening idealization, and (c) elastic-plastic-strain hardening idealization

CHAPTER 4

NONLINEAR FINITE ELEMENT FORMULATION

This chapter describes the key features of the nonlinear finite element program, HODA, developed during this course of study. The various program capabilities and its limitations are outlined, followed by the finite element displacement formulation based on energy considerations. The element library of the program including membrane, plate bending, facet shell , one dimensional bar, and boundary elements is discussed next, with a brief introduction to the finite element formulation of a special bar embedded within the shell element. The layer discretization technique which can provide very efficient tools in modelling the concrete and the steel as a composite material, and which can also facilitate the numerical integration within the body of the shell element, is also discussed in this chapter. The transformation of strain, stress, constitutive matrix and coordinates, the assembly process, and the numerical algorithms in nonlinear analysis including the solution process, the unbalanced forces, the convergence criteria and the divergence criteria are outlined thereafter.

4.1 GENERAL

Like most of the other nonlinear finite element analysis programs, the HODA program was developed within the university environment. The origin of the HODA program can be traced back to the earlier programs: NARCS, NOTACS, FELARC and NONLACS developed by Lin (1973), Kabir (1976), Ghoneim (1978) and Nofal (1988), respectively. The HODA program was developed using the existing version of the NONLACS program and differs from the previous

programs in terms of its ability to analyze both normal and high strength concretes, to utilize different cracking models including the fixed and the rotating crack models, to handle the elimination of mesh size dependency using the strength-based or fracture mechanics approaches, and to carry out structural analysis under reversed cyclic, as well as for monotonically increasing loads based on the model proposed in Chapter 3.

This program can capture the static response of any plain, reinforced and/ or prestressed three-dimensional concrete structure that is composed of thin plate members which are in plane stress condition subjected to monotonically increasing or cyclic loadings. This includes beams, slabs (plates), shells, folded plates, box girders, shear walls, or any combination of these structural elements. Time-dependent effects like creep and shrinkage can also be considered. The program, however, has its limitations; it cannot account for transverse shear deformations in the plate bending problem, fatigue type effects, geometric non-linearities, dynamic loads, and the slip between the concrete and the reinforcing steel. In the following sections some aspects of the finite element formulation used in the development of the HODA program are outlined. While the required mathematical model for this program can have a three-dimensional geometry, it must be ensured that each element is subjected to a plane stress condition.

4.2 FINITE ELEMENT DISPLACEMENT FORMULATION

In the classical theory of structural analysis two basic approaches exist: force (flexibility) and displacement (stiffness) methods. In the former the initial unknowns are forces but in the latter they are displacements. In the computer analysis of structural systems, the force method requires more manual input data than the displacement method and it is more user-dependent. On the other hand, the displacement method is fully capable of being automated and quite well suited for computer implementation. Most of the computer programs available in the practice for structural analysis, take advantage of the displacement based formulation for linear/ nonlinear finite element method (see Shayanfar, 1994).

In the finite element method, the structure is discretized into an assemblage of finite elements. The displacements at any point of the element, {u}, can be evaluated in terms of the displacements of the specific points within, or on the boundary of element called "nodes" or "joints" as,

$$\{u\} = [N]\{U\}_n \tag{4.1}$$

in which [N] is the matrix of shape functions and $\{U\}_n$ is the element nodal displacement vector in element local coordinate system. The vector of strains at any point of the element, $\{\varepsilon\}$, is related to the element nodal displacements, $\{U\}_n$, using the following equation

$$\{\epsilon\} = [B]\{U\}_n \tag{4.2}$$

where [B] is the strain-displacement matrix and can be obtained as:

$$[B] = [L][N] \tag{4.3}$$

in which [L] is the differential operator matrix and defined such that

$$\{\epsilon\} = [L]\{u\} \tag{4.4}$$

then the stresses at any point of the element, $\{\sigma\}$, can be found using the constitutive matrix, [C], as:

$$\{\sigma\} = [C](\{\epsilon\} - \{\bar{\epsilon}\}) + \{\bar{\sigma}\} \tag{4.5}$$

where $\{\bar{\varepsilon}\}$ and $\{\bar{\sigma}\}$ are the vectors of initial strains and stresses, respectively.

Suppose a structure in equilibrium condition having nodal displacements {D}, external applied loads {R}, body forces {P} and surface tractions {T}. Now, impose a system of virtual nodal displacement {δD} on this structure. This system of virtual nodal displacement results in elemental virtual displacements which are denoted by $\{\delta U\}_n$. The resulted virtual displacements, {δu}, and virtual strains, {δε}, at any point of the element can be expressed as:

$$\{\delta u\} = [N]\{\delta U\}_n \tag{4.6}$$

$$\{\delta \epsilon\} = [B]\{\delta U\}_n \tag{4.7}$$

The principle of virtual displacement for static analysis of a conservative system requires that the total internal work resulting from real stresses through the virtual strains is equal to the total external work due to the real external applied loads moving through the virtual displacements. This can be expressed mathematically as:

$$\sum_{\substack{all\\elements}} \int_{V^e} \{\delta\epsilon\}^T \{\sigma\}\, dV^e = \{\delta D\}^T \{R\} + \sum_{\substack{all\\elements}} \int_{V^e} \{\delta u\}^T \{P\}\, dV^e + \sum_{\substack{all\\elements}} \int_{A^e} \{\delta u\}^T \{T\}\, dA^e \tag{4.8}$$

where V^e and A^e are volume and surface area of any element, respectively. Substituting Eqs. (4.2), (4.5), (4.6) and (4.7) into Eq. 4.8 results in:

$$[K]\{D\} = \{F\} \tag{4.9}$$

with

$$[K] = \sum_{\substack{all\\elements}} [K_m]_n \tag{4.10}$$

and

$$\{F\} = \{R\} + \{F\}_P + \{F\}_T + \{F\}_{\bar{\epsilon}} + \{F\}_{\bar{\sigma}} \tag{4.11}$$

where [K] is the structure stiffness matrix, {D} is the structure nodal displacement vector and {F} is the equivalent nodal force vector of the structure, all in the global coordinate system. $[K_m]_n$ is the element stiffness matrix, {R} is the applied nodal external load vector; and $\{F\}_P$, $\{F\}_T$,, $\{F\}_{\bar{\epsilon}}$, and $\{F\}_{\bar{\sigma}}$ are equivalent nodal force vectors due to body forces, surface tractions, initial strains and initial stresses, respectively. The following relations are obtained for $[K_m]_n$, $\{F\}_P$, $\{F\}_T$,, $\{F\}_{\bar{\epsilon}}$, and $\{F\}_{\bar{\sigma}}$, respectively:

$$[K_m]_n = \int_{V^e} [B]^T [C]\ [B]\, dV^e \tag{4.12}$$

$$\{F\}_P = \sum_{\substack{all\\elements}} \int_{V^e} \{N\}^T \{P\}\, dV^e \tag{4.13}$$

$$\{F\}_T = \sum_{\substack{all \\ elements}} \int_{A^e} \{N\}^T \{T\}\, dA^e \tag{4.14}$$

$$\{F\}_{\bar{\epsilon}} = \sum_{\substack{all \\ elements}} \int_{V^e} [B]^T [C]\, \{\bar{\epsilon}\}\, dV^e \tag{4.15}$$

$$\{F\}_{\bar{\sigma}} = \sum_{\substack{all \\ elements}} \int_{V^e} [B]^T \{\bar{\sigma}\}\, dV^e \tag{4.16}$$

Equation (4.7) can be derived from Eq. 4.2, if the matrix [B] is independent of {U}, otherwise the problem would be geometrically nonlinear. In the above discussion, it is also assumed that in Eq. 4.5, [C] is independent of {ε} and consequently Eq. 4.9 represents a system of linear equations for equilibrium of the structure. If the [C] is dependent on {ε}, the problem involves material nonlinearities. In the present study, only the material nonlinearity is considered.

4.3 ELEMENT LIBRARY

The element library includes membrane, plate bending, facet shell , one dimensional bar, and boundary elements. Figure 4.1 shows some of the elements and their associated degrees of freedom. The two node, three degrees of freedom per node, one dimensional bar element [see Fig. 4.1(c)] is used to model uniaxial truss members (steel or concrete), unbonded prestressing tendons and shear connectors. The shear connector element is a specialized form of the standard bar element. This element is used to model the steel-concrete connection in composite construction (Razaqpur and Nofal, 1990).

There are two four node quadrilateral membrane elements RQUAD4 (Razaqpur and Nofal, 1987) and QLC3 (Sisodiya et al., 1972) [see Fig. 4.1(a)]. Both elements have three degrees of freedom per node (two in-plane translational, u and v, and one rotational, ω, degrees of freedom), but differ with respect to the assumed displacement fields (shape functions). The full development of the element RQUAD4, together with extensive performance tests, is given by Aziz (1988) and McNeal et al. (1988). The detailed derivation of QLC3 has been presented by

Ghoneim (1978). The element RQUAD4 is superior in its performance to the constant strain element and is comparable to the linear strain triangular element, but has fewer degrees of freedom than the latter. It also has the advantage of being easily connected to the standard beam elements when analyzing coupled shear walls, or shear wall and frame interaction problems. The strain-displacement relationship for a membrane element takes the following form:

$$\{\epsilon\} = [B_p]\{U_p\}_n \tag{4.17}$$

in which $\{\varepsilon\} = \{\partial u/\partial x,\ \partial v/\partial y,\ \partial u/\partial y + \partial v/\partial x\}^T = \{\varepsilon_x,\ \varepsilon_y,\ \gamma_{xy}\}^T$, $[B]_p$ is strain-in-plane displacement matrix and $\{U_p\}_n$ is the vector of nodal inplane displacements of the element.

The library also contains two four node plate bending elements: the rectangular plate bending element, RBE (Zienkiewicz, 1983), and the improved discrete Kirchhoff quadrilateral plate bending element, IDKQ (Chinniah, 1985) [see Fig. 4.1(b)]. Both elements have three degrees of freedom per node (normal rotations,θ_x and θ_y, and lateral displacement w). The strain-displacement relationship for a plate bending element is written as:

$$\{\chi\} = [B_b]\{U_b\} \tag{4.18}$$

in which $\{\chi\} = \{\partial^2 w/\partial x^2,\ \partial^2 w/\partial y^2,\ 2\partial^2 w/\partial x\partial y\}^T$ is the vector of curvatures and twists, $[B]_b$ is strain-bending displacement matrix and $\{U_b\}_n$ is the vector of nodal bending displacements of the element.

Two four node, six degree of freedoms per node, anisotropic facet shell elements are also available in the library [see Fig. 4.1(d)]. These elements are obtained by combining the plate bending elements with the quadrilateral membrane elements using Kirchhoff's assumptions. According to these assumptions, the straight fibers of the plate, which are perpendicular to a chosen reference surface before deformation, remain plane after deformation, and also the normal stresses acting on planes parallel to the reference surface are negligible, i. e. $\gamma_{xz} = \gamma_{yz} = \sigma_z = 0$. The strain-displacement relationship for a quadrilateral shell element is introduced as:

$$\{\epsilon\} = [\,[B_p] \quad -z[B_b]\,] \begin{Bmatrix} \{U_p\} \\ \{U_b\} \end{Bmatrix} = [B]\{U\}_n \tag{4.19}$$

where z is the distance of the point within the shell element from the reference surface and [B] is the strain-displacement matrix of the element. Since these elements are applied in problems

involving material nonlinearities, the coupling between the membrane and bending actions is considered. In other words, the stiffness matrix $[K_m]_n$ of the shell element, with six degree of freedoms per node shown in Fig. 4.1(d), is given by

$$[k_m]_n = \int_{V^e} [B]^T [C] [B] \, dV^e = \begin{bmatrix} [k]_{pp} & [k]_{pb} \\ [k]_{bp} & [k]_{bb} \end{bmatrix} \tag{4.20}$$

in which,

$$[k_{pp}] = \iint [B_p]^T [C_{pp}] [B_p] \, dx\,dy \tag{4.21}$$

$$[k_{pb}] = \iint [B_p]^T [C_{pb}] [B_b] \, dx\,dy = [k_{bp}] \tag{4.22}$$

$$[k_{bb}] = \iint [B_b]^T [C_{bb}] [B_b] \, dx\,dy \tag{4.23}$$

$$[C_{pp}] = \int_z [C] \, dz \tag{4.24}$$

$$[C_{pb}] = -\int_z z [C] \, dz \tag{4.25}$$

$$[C_{bb}] = \int_z z^2 [C] \, dz \tag{4.26}$$

where $[K_m]_n$ is a 24×24 element stiffness matrix and the subscripts "pp" and "bb" denote the membrane and bending elements, respectively. The subscripts "pb" and "bp" signify the coupling effects between the membrane and bending actions. The coupling matrices become null if the middle surface of the shell is an axis of material symmetry. The above integrations are carried out using the Gauss quadrature procedure at each layer and then the contributions of the various layers at each Gauss quadrature point are added by means of layer discretization technique as outlined

in the next section.

Shell element type I is obtained by combining the quadrilateral membrane element, QLC3, with the rectangular plate bending element, RBE. Shell element II is obtained by combining the quadrilateral membrane element, RQUAD4, with the discrete Kirchhoff quadrilateral plate bending element, IDKQ. The type of element to be employed during an analysis normally depends on the behaviour of the structure under consideration. The type I shell element is suitable for beam behaviour problems while the type II shell element is a more general element.

4.3.1 Bar Element

The bar elements are special one dimensional elements embedded within the shell elements that can be used for modelling the heavy/ concentrated reinforcements and bonded prestressing bars. Figure 4.2 indicates a typical bar element in local and natural coordinate systems of a shell element. The natural coordinates of the two ends of the bar element, i. e. (ξ_1, η_1) and (ξ_2, η_2), are given as data in the input file of the computer program [see Fig. 4.2(b)] and accordingly the length, L_i,and the coordinates of the two ends of the element with respect to the local coordinate system is calculated [see Fig. 4.2(a)]. This element bar is assumed to lie on the reference surface of the shell element, therefore it contributes only to the inplane stiffness matrix of the shell element, $[K_{pp}]$, and with the assumption of perfect bond, its strain-inplane displacement relationship can be defined as,

$$\epsilon_s = [t]\,[B_p]\,\{U_p\}_n \tag{4.27}$$

in which ϵ_s is the uniaxial strain at any point within the bar element and the strain transformation matrix, [t], is defined as,

$$[t] = [\cos^2\theta \quad \sin^2\theta \quad \cos\theta.\sin\theta] \tag{4.28}$$

where θ is the angle between the bar element and the x-axis in the local coordinate system [see Fig. 4.2(a)]. The stress at any point of the bar, σ_s,is obtained by:

$$\sigma_s = E_B \cdot \epsilon_s \tag{4.29}$$

where E_B is the tangent modulus of the bar element which can be equal to E_s or E^*_s, depending on the strain, ϵ_s, and the loading condition, monotonically increasing or cyclic, [see Fig. 3.15(c)].

The contribution of the bar elements within a typical shell element, $[K_{BP}]$, to the inplane stiffness matrix, $[K_{pp}]$, can be found using the Eq. 4.12 as:

$$[k_{Bp}] = \sum_{i=1}^{m} \int_{0}^{L_i} A_i [B_p]^T [t]_i^T E_{B_i} [B_p] \, ds \qquad (4.30)$$

where m indicates the number of bars in the element, i refers to the ith bar, and A_i, L_i and E_{B_i} are the cross-sectional area, the length and the tangent modulus of the ith bar, respectively. The above integration is evaluated using the Gauss quadrature procedure with three integration points.

4.4 LAYERED DISCRETIZATION TECHNIQUE

The program employs a layered finite element approach; the structure is idealized as an assemblage of thin constant thickness plate elements with each element subdivided into a number of imaginary layers as shown in Fig. 4.3. The number of layers depends on the behaviour of the structure being analyzed; for shell and plate bending problems, five to eight layers might be needed to capture the stress variation across the thickness, while for plane stress problems using more than one layer is not necessary. A layer can be either of concrete, smeared reinforcing steel and/ or a continuous steel plate. Each layer is assumed to be in a state of plane stress, and can assume any state - uncracked, partially cracked, fully cracked, non-yielded, yielded, crushed, loaded and unloaded - depending on the stress/ strain level. These are indicated by indices KC = 1 to 6 for monotonically increasing loads and indices LRC = 1 to 10 for reversed cyclic loads, as shown in Fig. 4.4. Each of these indices designates a specific part of the stress-strain curve for loading condition in both figures 4.4(a) and (b) and unloading condition in Fig. 4.4(b). These indices have been appropriately implemented in the HODA program.

Steel can be idealized as a smeared layer or as a bar element embedded in concrete at the reference surface. Smeared steel representation is suitable for representing distributed reinforcement as in slabs and structural walls, while the bar representation is appropriate for isolated large reinforcing bars or tendons such as beams with heavy longitudinal reinforcement. The stiffness matrix of a shell element is obtained using Eq. 4.20 in which the integration of Eqs. 4.21 to 4.23 is evaluated using the Gauss quadrature procedure and that of Eqs. 4.24 to 4.26 is performed by means of layered discretization technique as (see Fig. 4.3):

$$[C_{pp}] = \int_z [C]\, dz$$
$$= \sum_{i=1}^{n_c} (z_{i+1} - z_i)\, [C_c]_i + \sum_{i=1}^{n_s} [C_s]_i t_{s_i} + \sum_{i=1}^{n_{sp}} (z_{i+1} - z_i)\, [C_{sp}]_i \tag{4.31}$$

$$[C_{pb}] = -\int_z z\, [C]\, dz$$
$$= -\frac{1}{2}\sum_{i=1}^{n_c} (z_{i+1}^2 - z_i^2)\, [C_c]_i - \sum_{i=1}^{n_s} [C_s]_i z_{s_i} t_{s_i} - \frac{1}{2}\sum_{i=1}^{n_{sp}} (z_{i+1}^2 - z_i^2)\, [C_{sp}]_i \tag{4.32}$$

$$[C_{bb}] = -\int_z z^2\, [C]\, dz$$
$$= \frac{1}{3}\sum_{i=1}^{n_c} (z_{i+1}^3 - z_i^3)\, [C_c]_i + \sum_{i=1}^{n_s} [C_s]_i z_{s_i}^2 t_{s_i} + \frac{1}{3}\sum_{i=1}^{n_{sp}} (z_{i+1}^3 - z_i^3)\, [C_{sp}]_i \tag{4.33}$$

in which $[C_c]_i$, $[C_s]_i$ and $[C_{sp}]_i$ are constitutive matrices for concrete, smeared steel and steel plate at each Gauss quadrature point in layer i for the respective materials. Using the layered discretization as outlined above, the integrations in Eqs. 4.21 to 4.23 involve functions of x and y only and the integrands are evaluated at the Gauss quadrature points and are added to obtain the element stiffness matrix in local coordinate system. The procedure similar to that for Eq. 4.20, as outlined above, can be employed to perform the numerical integrations in Eqs. (4.15) and (4.16). The detailed information has been presented by Ghoneim (1978).

4.5 TRANSFORMATIONS

In any finite element formulation, it is necessary to have references to describe the magnitude and/ or direction of the structural quantities including displacements, forces, stresses, strains, constitutive relations, etc., so that the required numerical calculations can be handled as conveniently as possible. The most common coordinate systems in computer structural analysis

are: local, global, natural, and principal (referred to as "material axis" in some models) coordinate systems. The transformation of the quantities from one system to the other is of vital importance and it must be well understood. Transformation from the natural coordinate system to any other system and vice versa can be implemented using the mapping technique as discussed in any standard finite element text book. Transformations from the local, global and principal coordinate systems to each other are discussed in this section. In this regard, the transformation of the stress and the strain vectors, constitutive matrix and coordinates (nodal displacements, nodal forces, element stiffnesses) are discussed separately.

The global coordinate system consists of a set of right-hand orthogonal axes: X, Y, and Z, which are oriented as shown in Fig. 4.5(a). The orientation of the global coordinate system is arbitrary, but the relative directions of the axes are conveniently represented by orienting the thumbs and the fingers of the right hand as shown in Fig. 4.5(b). The nodal forces, nodal displacements and the stiffness components of the structure are referenced to the global coordinate system.

The local coordinate system for a quadrilateral element is shown in Fig. 4.6 and denoted by: $X^*Y^*Z^*$ system. The X^* axis passes through the mid-points of the two sides: 1-4 and 2-3, and is directed as shown in Fig. 4.6(b). The Z^* axis is obtained by the cross product of the two vectors composed of the diagonals 1-3 and 2-4 as shown by dashed lines in Fig. 4.6(b). The Y^* axis is then obtained as the cross product of X^* and Z^*. The nodal forces, nodal displacements and the stiffness components of the elements are referenced to this local coordinate system (see Shayanfar, 1994). The principal coordinate system is a system of right-hand orthogonal, $X'Y'Z'$, whose axes are parallel to the principal stresses/ strains. The constitutive matrix at any point within the element, is first developed in this coordinate system and then transformed to the local coordinate system.

In the following discussion, the transformation is between a new system which is denoted with superscript "'" and an old coordinate system with no superscript. The new or old coordinate system can consist of any of the local, global or material coordinate systems. The discussion starts with a two dimensional state of stress/ strain, and finally, it is expanded to a general form of the three dimensional state.

4.5.1 Transformation of the Strain Vector

Consider the plane strain condition shown in Fig. 4.7. By geometric considerations, as stated in any classical text book for strength of materials, the following equation can be used to transform the strain vector in the old coordinate system, $\{\varepsilon\} = \{\varepsilon_x, \varepsilon_y, \gamma_{xy}\}^T$, to the strain vector in the new coordinate system, $\{\varepsilon'\} = \{\varepsilon_{x'}, \varepsilon_{y'}, \gamma_{x'y'}\}^T$:

$$\{\epsilon'\} = [T_\epsilon]\{\epsilon\} \tag{4.34}$$

where

$$[T_\epsilon] = \begin{bmatrix} \cos^2\theta & \sin^2\theta & \sin\theta\cos\theta \\ \sin^2\theta & \cos^2\theta & -\sin\theta\cos\theta \\ -2\sin\theta\cos\theta & 2\sin\theta\cos\theta & \cos^2\theta-\sin^2\theta \end{bmatrix} \tag{4.35}$$

where $[T_\epsilon]$ is the strain transformation matrix. For a general three-dimensional strain state, if the direction cosines of the new coordinate system, x'y'z', with respect to the old coordinate system, xyz, are defined as (see Fig. 4.8),

$$\begin{array}{lll} l_1 = \cos(x',x) & m_1 = \cos(x',y) & n_1 = \cos(x',z) \\ l_2 = \cos(y',x) & m_2 = \cos(y',y) & n_2 = \cos(y',z) \\ l_3 = \cos(z',x) & m_3 = \cos(z',y) & n_3 = \cos(z',z) \end{array} \tag{4.36}$$

It can be shown that the strain transformation matrix, $[T_\epsilon]$, for engineering strains, $\{\varepsilon\} = \{\varepsilon_x, \varepsilon_y, \varepsilon_z, \gamma_{xy}, \gamma_{xz}, \gamma_{yz}\}^T$, takes the following form:

$$[T_\epsilon] = \begin{bmatrix} l_1^2 & m_1^2 & n_1^2 & l_1m_1 & l_1n_1 & m_1n_1 \\ l_2^2 & m_2^2 & n_2^2 & l_2m_2 & l_2n_2 & m_2n_2 \\ l_3^2 & m_3^2 & n_3^2 & l_3m_3 & l_3n_3 & m_3n_3 \\ 2l_1l_2 & 2m_1m_2 & 2n_1n_2 & (l_1m_2+l_2m_1) & (n_1l_2+n_2l_1) & (m_1n_2+m_2n_1) \\ 2l_1l_3 & 2m_1m_3 & 2n_1n_3 & (l_1m_3+l_3m_1) & (n_1l_3+n_3l_1) & (m_1n_3+m_3n_1) \\ 2l_2l_3 & 2m_2m_3 & 2n_2n_3 & (l_2m_3+l_3m_2) & (n_2l_3+n_3l_2) & (m_2n_3+m_3n_2) \end{bmatrix} \tag{4.37}$$

4.5.2 Transformation of the Stress Vector

Consider the plane stress condition shown in Fig. 4.9. By satisfying the equation of equilibrium, the following equation can be used to transform the stress vector in the old coordinate system, $\{\sigma\} = \{\sigma_x, \sigma_y, \tau_{xy}\}^T$, to the stress vector in the new coordinate system, $\{\sigma'\} = \{\sigma_{x'}, \sigma_{y'}, \tau_{x'y'}\}^T$:

$$\{\sigma'\} = [T_\sigma]\{\sigma\} \tag{4.38}$$

and

$$[T_\sigma] = \begin{bmatrix} \cos^2\theta & \sin^2\theta & 2\sin\theta\cos\theta \\ \sin^2\theta & \cos^2\theta & -2\sin\theta\cos\theta \\ -\sin\theta\cos\theta & \sin\theta\cos\theta & \cos^2\theta - \sin^2\theta \end{bmatrix} \tag{4.39}$$

where $[T_\sigma]$ is called stress transformation matrix. By comparing Eq. 4.39 and Eq. 4.35, it is obvious that if the strain transformation matrix is partitioned as:

$$[T_\varepsilon] = \begin{bmatrix} T_Q & T_R \\ T_S & T_T \end{bmatrix} \tag{4.40}$$

then the stress transformation matrix in Eq. 4.39 can be defined as:

$$[T_\sigma] = \begin{bmatrix} T_Q & 2T_R \\ \frac{1}{2}T_S & T_T \end{bmatrix} \tag{4.41}$$

For a general three-dimensional stress state, the strain matrix introduced in Eq. 4.37 can be partitioned into 3×3 matrices (T_Q, T_R, T_S, T_T) and the stress transformation matrix, $[T_\sigma]$, is obtained using Eq. 4.41.

4.5.3 Transformation of the Constitutive Matrix

The preceding discussions shows that the strains and stresses in the new coordinate

system, X'Y', can be expressed in terms of the old coordinate system, XY, using Eqs. (4.34) and (4.38), respectively. Also the strains and stresses in the old coordinate system, XY, can also be expressed in the new coordinate system, X'Y', by simply replacing the (θ) by (-θ) in Eqs. (4.35) and (4.39). The results take the following forms:

$$\{\epsilon\} = [T_\sigma]^T\{\epsilon'\} \tag{4.42}$$

$$\{\sigma\} = [T_\epsilon]^T\{\sigma'\} \tag{4.43}$$

The stress-strain relationships in old and new coordinate systems can be written, respectively, as:

$$\{\sigma\} = [C]\{\epsilon\} \tag{4.44}$$

and

$$\{\sigma'\} = [C']\{\epsilon'\} \tag{4.45}$$

By considering Eq. 4.44 and substituting the vectors {ε} and {σ} by their equivalents obtained from Eqs. (4.42) and (4.43), the following equation results:

$$[T_\epsilon]^T\{\sigma'\} = [C][T_\sigma]^T\{\epsilon'\} \tag{4.46}$$

Per-multiplication of the two sides of the above equation with $[T_\sigma]$, knowing that $[T_\sigma][T_\epsilon]^T$ is equal to the identity matrix, results in:

$$\begin{aligned}\{\sigma'\} &= [T_\sigma][C][T_\sigma]^T\{\epsilon'\} \\ &= [C']\{\epsilon'\}\end{aligned} \tag{4.47}$$

where,

$$[C'] = [T_\sigma][C][T_\sigma]^T \tag{4.48}$$

The above equation represents the transformation of constitutive matrix from the old coordinate system to the new coordinate system. By following the same procedure using Eqs. (4.34), (4.38) and (4.45), the transformation of constitutive matrix from new coordinate system to the old coordinate system can be carried out using:

$$[C] = [T_\epsilon]^T[C'][T_\epsilon] \tag{4.49}$$

For example, the proposed constitutive matrix in principal (or material) coordinate system is

represented by Eq. 3.4. If the angle between the local coordinate system (old system) and the principal coordinate system (new system) is denoted by (θ), the constitutive matrix in local coordinate system can be obtained using Eq. 4.49 as:

$$[C] = \frac{1}{1-\nu^2\frac{E_1E_2}{E_o^2}} \times \begin{bmatrix} E_1\cos^2\theta + E_2\sin^2\theta & \nu E_1E_2/E_o & \frac{1}{2}(E_1 - E_2)\sin\theta\cos\theta \\ & E_1\sin^2\theta + E_2\cos^2\theta & \frac{1}{2}(E_1 - E_2)\sin\theta\cos\theta \\ sym & & \frac{1}{4}(E_1 + E_2 - 2\nu\frac{E_1E_2}{E_o}) \end{bmatrix} \quad (4.50)$$

4.5.4 Transformation of the Coordinates

This includes the transformation of the element nodal displacements, element nodal forces and element stiffness matrices from the local to the global axes, or vice versa. If the direction cosines of the new (local) coordinate system, x'y'z', with respect to the old (global) coordinate system, xyz, are as defined in Eq. 4.36, the transformation matrix from global to local can be defined as:

$$[T] = \begin{bmatrix} l_1 & m_1 & n_1 \\ l_2 & m_2 & n_2 \\ l_3 & m_3 & n_3 \end{bmatrix} \quad (4.51)$$

where each row consists of the direction cosines of the local (new) coordinate system axis with respect to the global (old) coordinate system. The relations between the element nodal displacements and the element nodal forces from the global to the local coordinate systems can be written, respectively as:

$$\{U\}_n = [T]\{D\}_n \quad (4.52)$$

$$\{S\}_n = [T]\{F\}_n \quad (4.53)$$

and the transformation of the element stiffness matrix from the local to the global axes is

performed by:

$$[k]_n = [T]^T[K_m]_n[T] \tag{4.54}$$

in which $\{U\}_n$, $\{S\}_n$, and $[K_m]_n$ are the element nodal displacement, element nodal force and element stiffness matrices in local coordinate system, respectively; and $\{D\}_n$, $\{F\}_n$, and $[K]_n$ are the element nodal displacement, element nodal force and element stiffness matrices in global coordinate system, respectively.

4.6 THE ASSEMBLY PROCESS

The transformed element stiffness matrices, $[K]_n$, which were just generated (refer to Eq. 4.54), can now be used to generate the global stiffness matrix of the structure, [K]. The elements in [K] are the global load components at the joints which are required to produce unit global displacement components at the joints. The elements in $[K]_n$ are the global load components at the joints of element n which are required to produce unit global displacement components of the joints of that individual element. Since the total load required at any joint, to produce a displacement of the joint, is the sum of the loads required to displace the joints of all of the elements connected to that joint, it should be possible to generate the elements in the global stiffness matrix, [K], for any joint by simply summing the loads required to produce global unit joint displacements in each element connected to the joint. This merely corresponds to summing the elements in the individual transformed element stiffness matrices. This operation can be represented symbolically by

$$[K] = \sum_{n=1}^{N} [K]_n \tag{4.55}$$

where N is the number of elements in the structure. Care must be exercised in summing the elements of each $[K]_n$ into the correct rows and columns in [K], since [K] and $[K]_n$ are not the same size matrices. This becomes a book-keeping problem which is dependent upon the numbering scheme in {F} and {D}. This total operation is known as "the assembly process" or "the direct stiffness method" (see Shayanfar, 1994).

4.7 NUMERICAL ALGORITHMS FOR NONLINEAR ANALYSIS

4.7.1 Solution Procedure

In the nonlinear finite element method, the change in the material stiffness matrix during loading, necessitates an incremental solution procedure. Techniques have been developed (Desai and Abel, 1972) for solution of nonlinear problems by the finite element method using piece-wise linearization. Three basic techniques are in use: (1) Incremental or Stepwise procedures, (2) Iterative or Newtonian methods, and (3) Incremental-Iterative or Mixed procedures. The latter combines the advantages of both the incremental and iterative methods and tends to minimize their disadvantages (for more information on the advantages and disadvantages of these methods, see Desai and Abel, 1972).

The incremental-iterative procedure with a tangent stiffness scheme (see Fig. 4.10) has been adopted in the HODA program. In this method the total load is divided into some load increments and during each load increment the analysis is carried out through subsequent iterations until the required force/ displacement convergence criteria (see Section 4.7.3), or the maximum number of iterations allowed within each load increment are achieved. At the beginning of each load increment, the total load increment is applied and the stiffness matrix of the structure, $[K_i]$, is evaluated according to the tangent constitutive matrices computed at the end of the previous iteration, $[C_{i-1}]$, and the unbalanced nodal forces are obtained using the initial stress method introduced in Section 4.7.2. Therefore, the equilibrium equation (Eq. 4.9) takes the following form (see Fig. 4.10):

$$[K_{i-1}]\{\Delta D_i\} = \{\bar{F}_i\} \tag{4.56}$$

and the total displacement after the ith iteration is given by:

$$\{D_i\} = \sum_{i=1}^{i} \{\Delta D_i\} \tag{4.57}$$

where $[K_{i-1}]$ is the stiffness matrix of the structure at the end of iteration number (i-1), $\{\bar{F}_i\}$ is the unbalanced force vectors during the iteration i and $\{D_i\}$ is the total nodal displacement vector of the structure within the iteration i.

4.7.2 Unbalanced Forces

The unbalanced forces after each iteration are calculated using the initial stress method due to Zienkiewicz et al. (1969). The method is based on the fact that a unique increment of stress corresponding to an increment of strain is available. After the iteration i, the unbalanced stress vector, $\{\bar{\sigma}_i\}$, is given by:

$$\{\bar{\sigma}_i\} = \{\Delta\sigma_i\} - [C_{i-1}]\{\Delta\varepsilon_i\} \tag{4.58}$$

where $[C_{i-1}]$ is the tangent constitutive matrix at the beginning of the iteration i, $\{\Delta\varepsilon_i\}$ is the strain increment vector during iteration i, and $\{\Delta\sigma_i\}$ is the "true" stress increment obtained from the stress -strain relationship. The equivalent unbalanced forces, $\{\bar{F}_{i+1}\}$, to be applied in the next iteration are then given by

$$\{\bar{F}_{i+1}\} = -\sum_{\substack{all \\ elements}} \int_{V^e} [B]^T \{\bar{\sigma}_i\} dV^e \tag{4.59}$$

4.7.3 Convergence Criteria

Convergence criteria are utilized to stop the iterations in each load step as soon as a required degree of accuracy has been attained. In the HODA program, two convergence criteria developed by Lin (1973) and Kabir (1976) are adopted. Lin used absolute values of input convergence/ divergence data, but Kabir added convergence/ divergence criteria that uses input percentage factors to be multiplied by the solutions computed in the first iteration of each load step. For any of these procedures, two possible convergence criteria are used:

(1) How small are the unbalanced forces after the ith iteration $\{\bar{F}_{i+1}\}$? or

(2) How small are the displacement increments $\{\Delta\delta_i\}$?

The method based on criterion (1) is called "the force convergence criterion" and the one based on (2) is termed "the displacement convergence criterion".

In the HODA program, the convergence in iteration i, for example, is checked as follows:

(1) Evaluate the maximum absolute value of unbalanced force/ displacement components in the six global directions at all nodes and establishes the norm vector $\{F_0\}^i_{6\times1}$.

(2) If all components of the norm vector $\{F_0\}'$ are less than the permissible convergence values, convergence is assumed to have occurred and no more iterations are performed. Otherwise another iteration is executed unless i is greater than n where n is the maximum number of iterations allowed per load step specified in the input data file. At the end of each load step (where either convergence criteria are satisfied, or i > n), the remaining unbalanced forces are added to the next load increment to avoid the accumulation of error over the load steps.

4.7.4 Divergence Criteria

As for the convergence criteria, two possible divergence criteria are available in the HODA program:

(1) Displacement divergence criterion or,

(2) Force divergence criterion.

If any of the norm vector components $\{F_0\}'$ exceeds the corresponding maximum force/ displacement values input as the divergence values, the solution will be terminated because of the excessive unbalanced forces or displacements.

If during an incremental increase of load, the resulting displacement increments or unbalanced forces do not decrease during the iterations, divergence is said to have occurred indicating structural collapse. If this happens, zero values will appear on the main diagonal of the structural stiffness matrix which becomes singular and the equilibrium equations can not be solved, stopping the execution of the program. A message stating " Zero on Diagonal of Stiffness Matrix, Solution is Stopped." will appear on the output file.

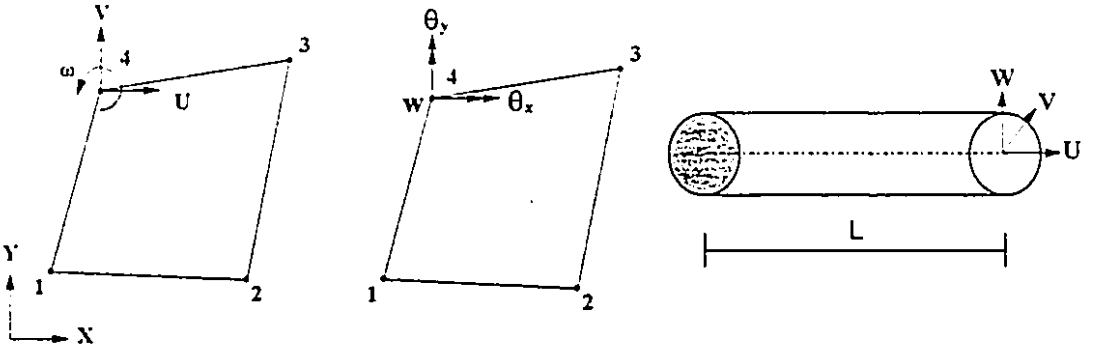

a) Membrane Element

b) Plate Bending Element

c) One Dimensional Element

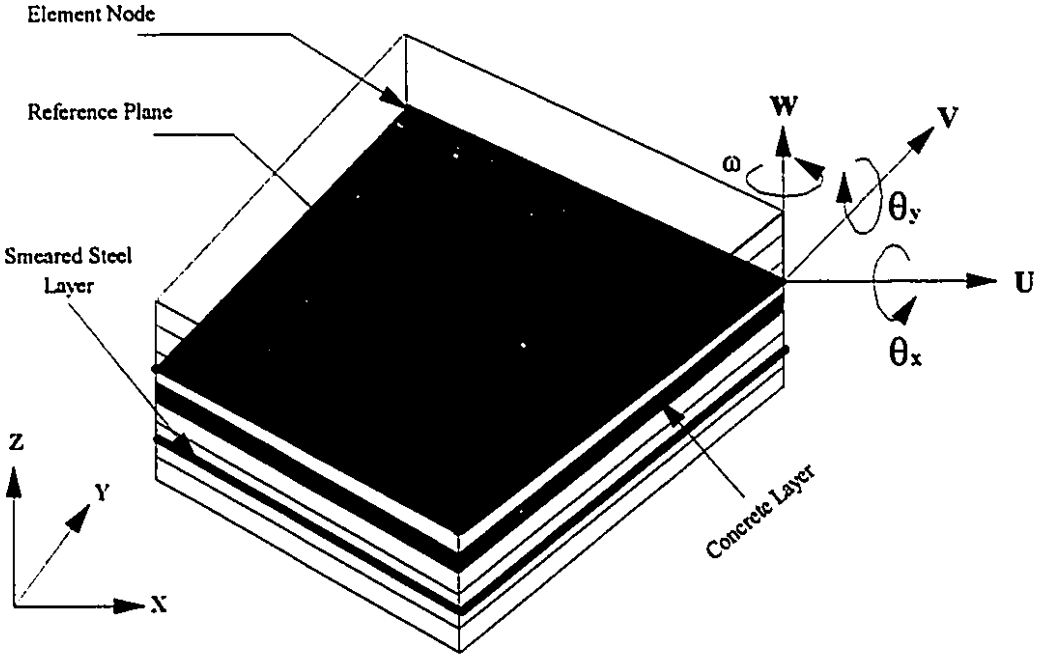

d) Facet Shell Element

Figure 4.1: Some typical finite elements in the HODA program and the associated degrees of freedom.

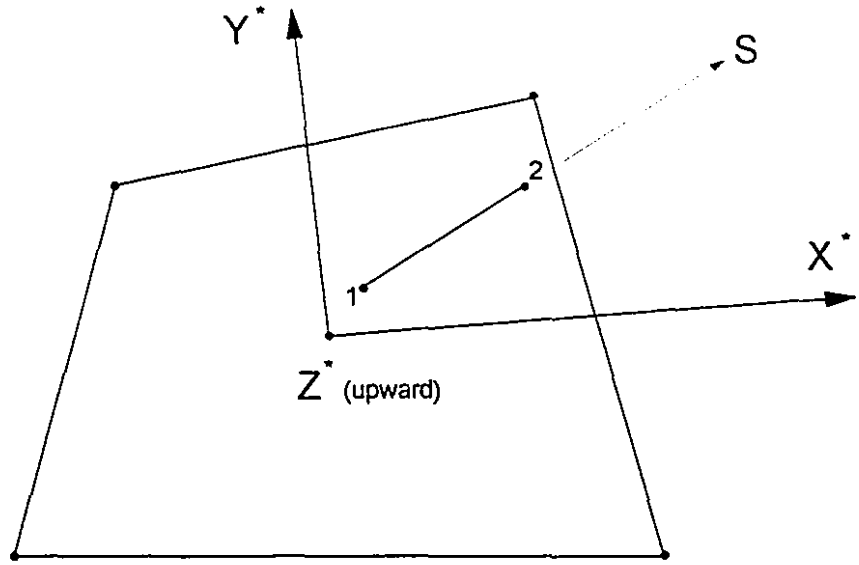

(a) In element local coordinate system

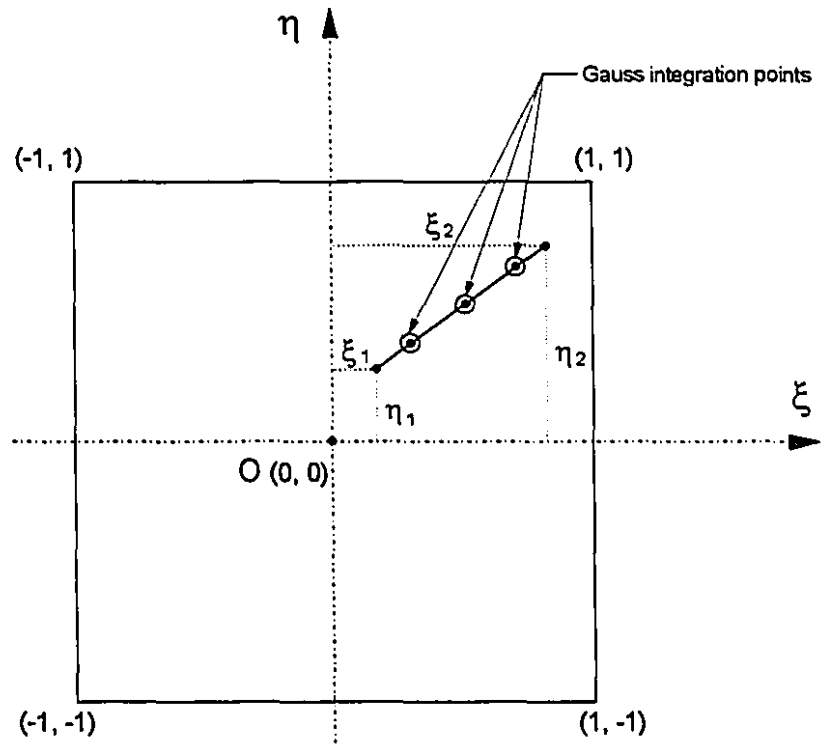

(b) In natural coordinate system

Figure 4.2: A typical bar element (after Ghoneim, 1978)

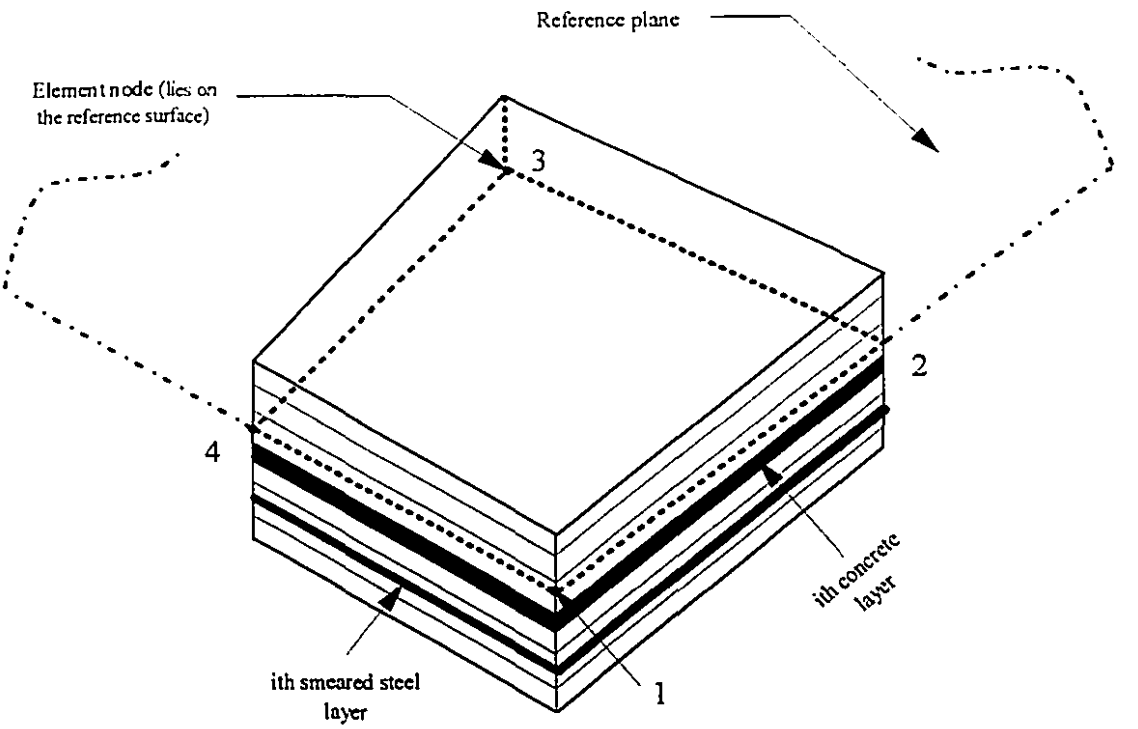

(a) Facet shell element

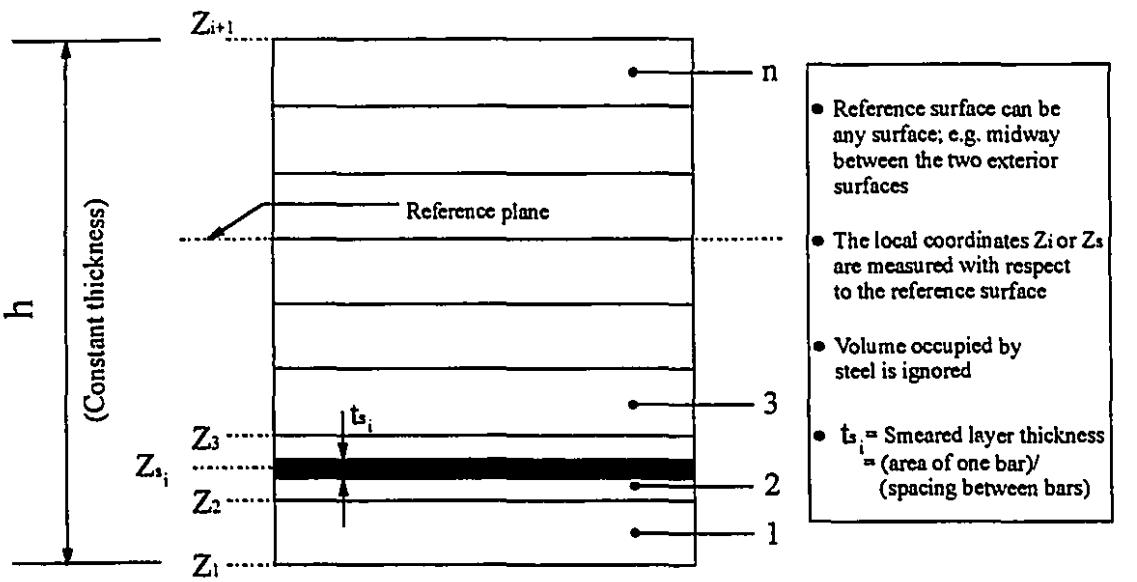

(b) Representation of different layers

Figure 4.3: Layered finite element (after Ghoneim, 1978)

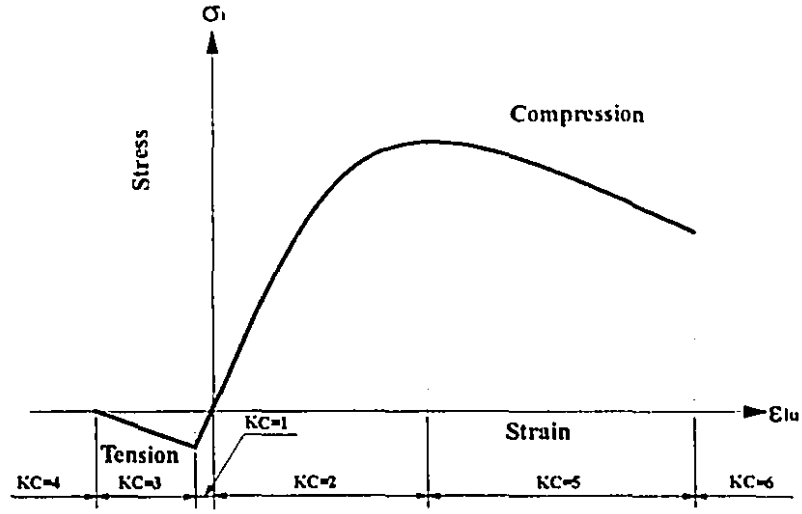

(a) Indices (KC) for montonically increasing load

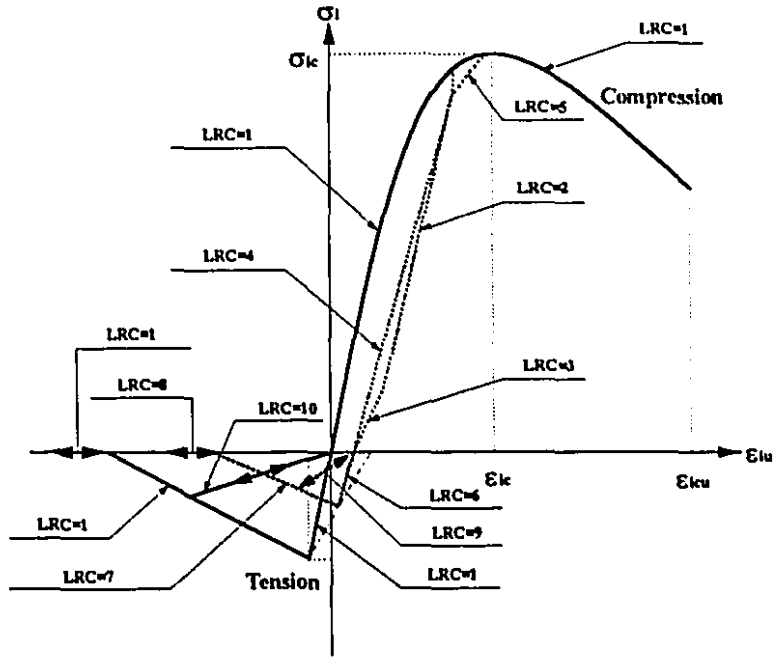

(b) Indices (LRC) for reversed cyclic load

Figure 4.4: Indices indicating states of stresses for concrete

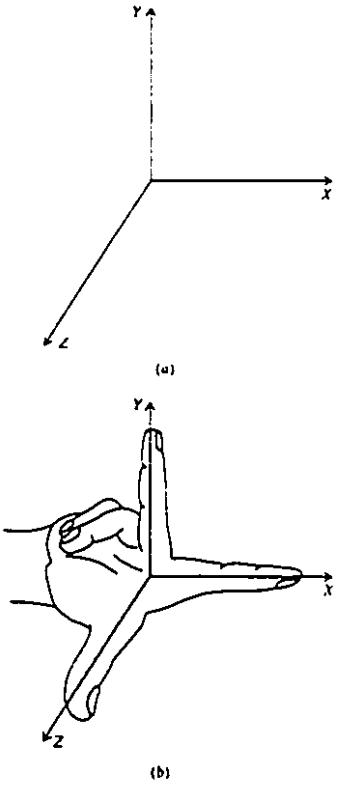

Figure 4.5: The global coordinate system

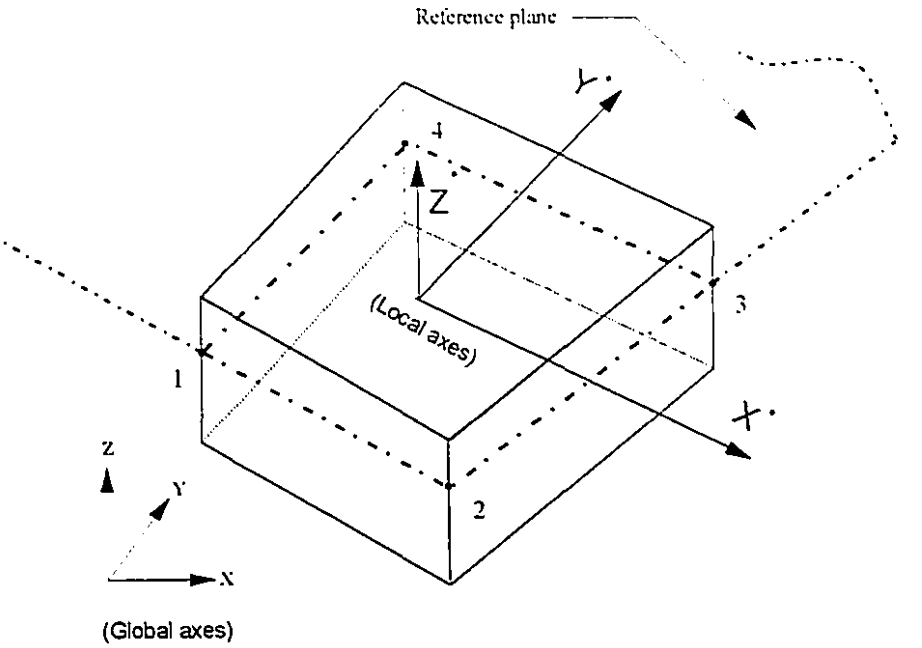

(a) Local coordinates within a shell element

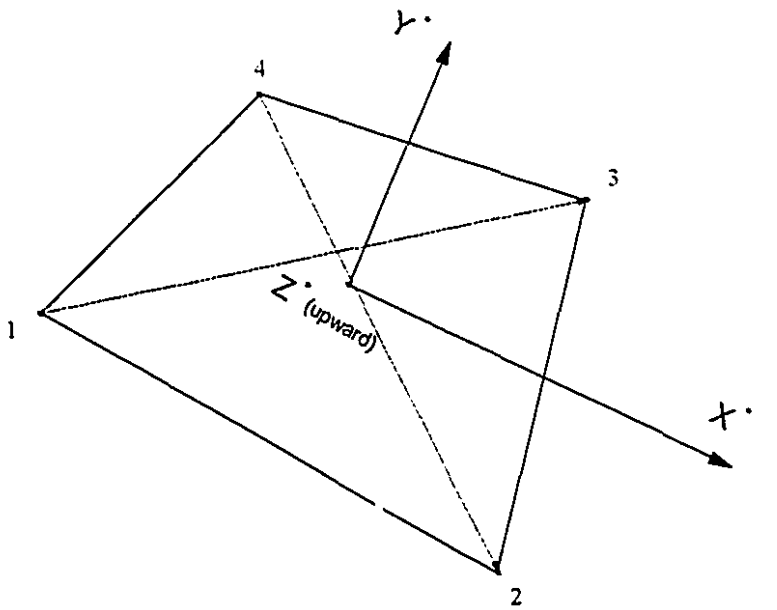

(b) Local axes on the reference surface

Figure 4.6: The local coordinate system

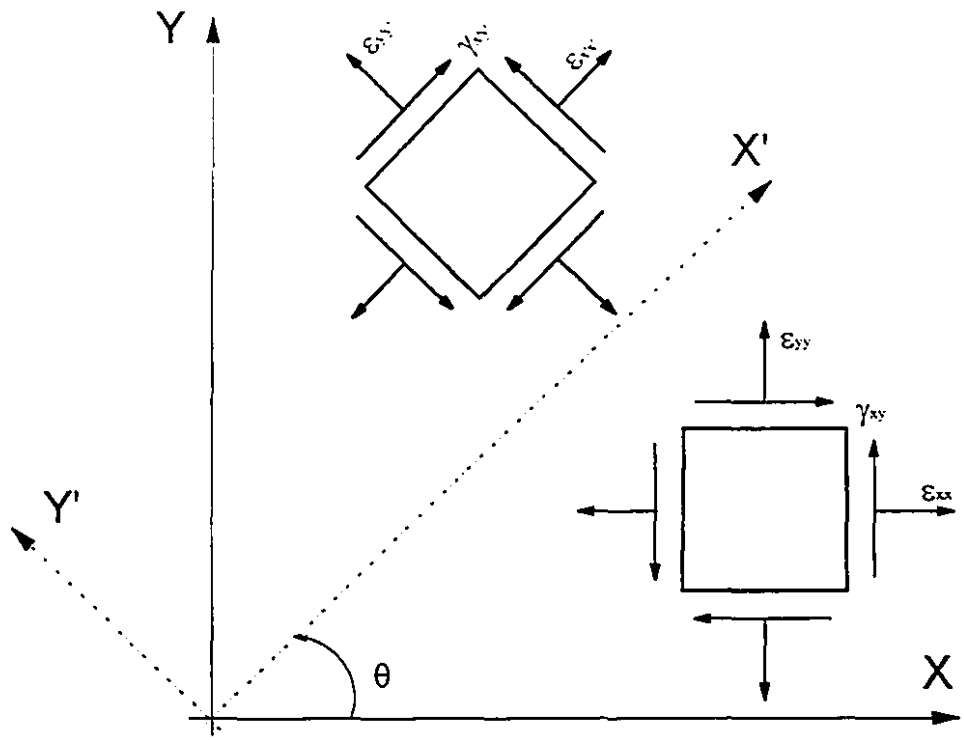

Figure 4.7: Transformation of plane strains

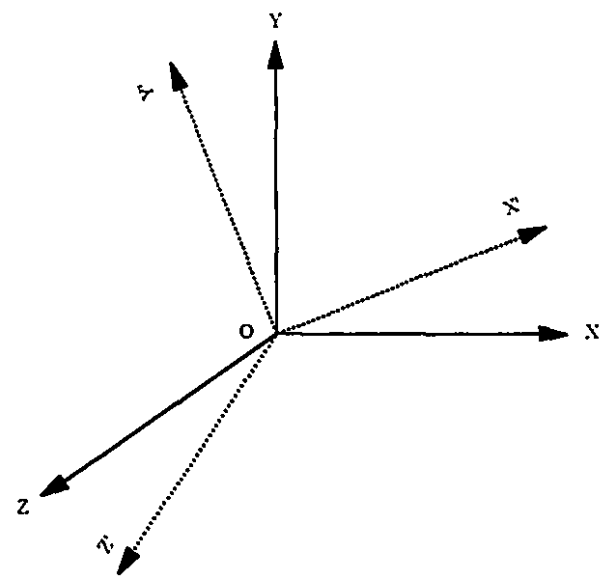

Figure 4.8: old and new coordinate systems

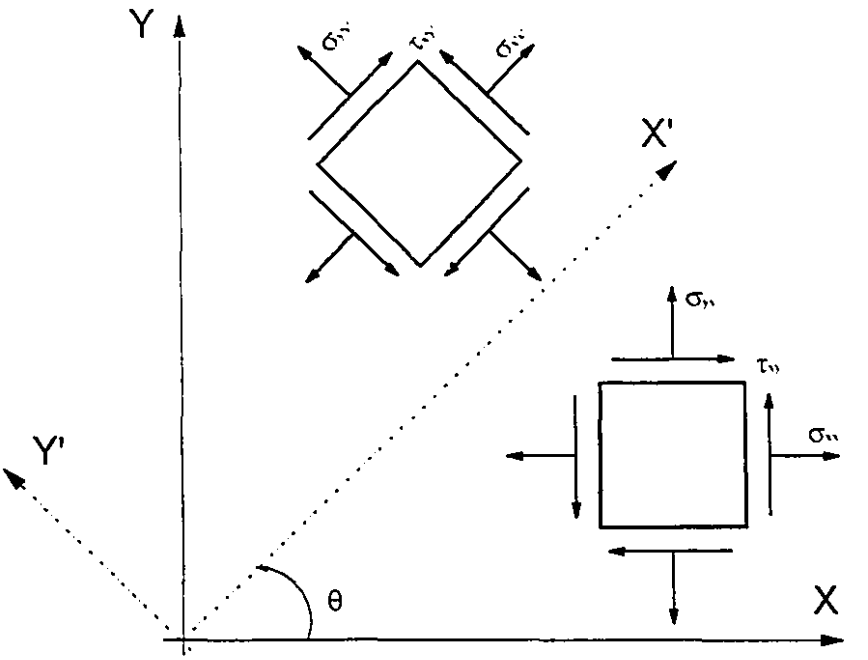

Figure 4.9: Transformation of plane stresses

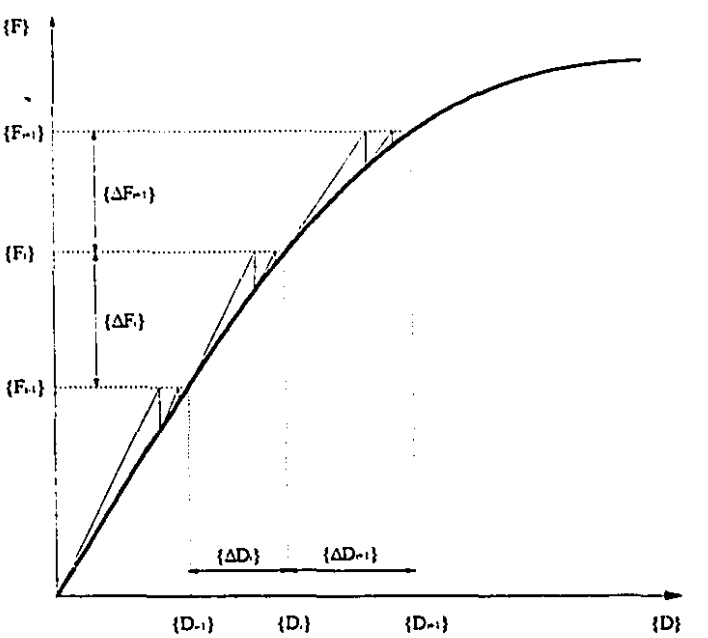

Figure 4.10: A Schematic Representation of the Incremental-Iterative Tangent Stiffness Method

CHAPTER 5

ELEMENT SIZE EFFECT PHENOMENON

This chapter presents the results of an investigation into the effect of finite element size in nonlinear finite element analysis of concrete structures. The influence of element size on different behavioural aspects of reinforced concrete structures including the load-displacement and load-strain characteristics, crack pattern and ultimate load are discussed along with a comparison with the experimental data where available. To eliminate the dependence of the computed results on the finite element size, two models have been used: a) crack band model, based on the fracture mechanics concepts, as a function of fracture energy, mesh size and tensile strength of concrete, and b) a new proposed model as a function of only the element size. These models have been implemented into the nonlinear finite element analysis program HODA. The analytical results obtained using the different models are compared; the proposed model gives good agreement with the experimental results and can be used effectively with relatively large finite element mesh sizes with reasonable accuracy.

5.1 GENERAL

Realization of the full potential of the finite element method to study the nonlinear behaviour of structural concrete elements requires an extensive verification to establish the accuracy of the responses of a variety of structural members, by comparing their computed responses under a variety of loadings with the available experimental results, including load-displacement, load-strain characteristics, cracking patterns and ultimate loads. In this respect, the

influence of the "numerical" effects, such as the element size, load steps, integration order, etc., on the various classes of structures needs to be studied. Despite the extensive research effort, there exists a need to determine a simple material model that best represents the behaviour of the various classes of structural elements and their assemblages. Such an extensive verification will result in improving the level of confidence in the nonlinear finite element analysis of structural concrete, while at the same time pointing out areas that need further research and development.

According to the smeared crack model (as introduced in Section 3.3.2), the tensile stress in a finite element is limited by the tensile strength of the material, f'_t, and after reaching this strength limit, the stress in the finite element decreases. As practised initially, the stress was assumed to decrease suddenly to zero, with a vertical drop in the stress-strain curve at the maximum stress [see Fig 5.1(a)], however it was realized that improved and more realistic results are usually obtained if the stress is reduced gradually, i.e., the material is assumed to exhibit strain-softening (Lin and Scordelis, 1975) [see Fig. 5.1(b)]. However, the concept of strain-softening proved to be a mixed blessing. After strain-softening had been implemented in large finite element analysis programs and widely applied, it was discovered that the computed results are not the same with regard to the element size used, i.e., the results change significantly if the mesh is refined (Bazant, 1976; Gilbert and Warner, 1978; Bazant and Cedolin, 1979, 1980 ,and 1983; Bazant and Oh, 1983a; Darwin, 1985; Rots et al., 1985; Balakrishnan et al., 1988). Similar problems are encountered when cracking is idealized using the discrete cracking model, based on the strength concept (Bazant, 1992).

The responses of selected reinforced concrete members were studied using the HODA finite element analysis program, and it was found to be strongly dependent on the size of the finite element in the mesh. This is termed the "element size dependency phenomenon". This chapter is aimed at finding and properly evaluating the key parameters that can help to remedy this drawback (for more detailed information, refer to Shayanfar et al., 1993).

5.2 INFLUENCE OF FINITE ELEMENT SIZE ON COMPUTED RESPONSES

Two beams (an under-reinforced beam and an over-reinforced beam) and a shear panel are analyzed using different finite element meshes to study the influence of the element size. These specimens were analyzed using the HODA program with "no mesh size dependency analysis" option (or for brevity "no mesh dependency"). The experimental results for load-

displacement and load-strain characteristics, cracking patterns and the ultimate loads are compared with the corresponding computed values.

Table 5.1: Gaston's beams, T2LA & T5L and Cervenka's shear panel W-2 (material properties)

Material property	Beam T2LA	Beam T5L	Shear panel
f'_c (psi)	2120	2500	3650
E_0 (psi)	2624500	2880000	2900000
ε_{cu}	0.0027	0.0027	0.0025
ε_u (*)	0.004	0.004	0.0035
f'_t (psi)	345	500	530
ν (*)	0.17	0.17	0.17
F_y (psi)	44000	40200	51200
E_s (psi)	2750000	2880000	2730000
E_s^*(psi)	1060000	822000	251160
ε_{su}	0.036	0.036	0.036

(*) Assumed values

5.2.1 Example 1: Reinforced concrete beams

Two simply supported reinforced concrete beams tested by Gaston et al. (1952), with two concentrated third-point loads, are investigated. The details of reinforcement and the geometry of the beams are shown in Fig. 5.2. The properties of materials for the beams are given in Table 5.1. The beam T2LA is under-reinforced, while the beam T5L is over-reinforced. The reinforcement is symmetrical with respect to the mid-span section for both beams.

To study the influence of the element size on the response of the beams, six types of mesh configurations with 4, 20, 30, 80, 120, and 320 elements were used for idealizing beams T2LA and T5L. The element size varied from 1.5 in to 18 in. Due to the symmetric configuration of the beam and the loading, only one-half of the beam was modeled for the finite element analyses and half of the total load was applied to the structure in 30 load steps varying from large to very small

Table 5.2: Effect of mesh size on the ultimate failure load for the beam T2LA (ε_{tu}=0.0007)

Number of elements	Size of element (in x in)	Finite element aspect ratio	Failure load (lb)	P_{Hoda}/P_{Exp}
4	18 x 12	1.50	19,500	1.24
10	6 x 12	2.0	16,500	1.05
30	6 x 4	1.50	16,000	1.02
80	3 x 3	1.0	15,000	0.96
120	3 x 2	1.50	14,500	0.93
320	1.5 x 1.5	1.0	14,000	0.89
Experimental result	-	-	15,666	-

increments as the ultimate load was approached. Figure 5.3 shows a typical finite element model of the beams with 20 elements.

The load-deflection curves for the under-reinforced beam T2LA are shown in Fig. 5.4, which presents the results for the models with five different meshes. The concrete ultimate tensile strain, ε_{tu}, was assumed to be constant for all mesh sizes and was arbitrarily selected to be 0.0007. As can be seen from Fig. 5.4, in the case of the coarsest mesh with 4 elements, the ultimate load is overestimated (19,500 lb), compared with the experimental ultimate load of 15,666 lb. When a coarse mesh is used, the structure is a little stiffer and behaves in a relatively more ductile manner. With a decrease in the size of the elements, the ultimate load decreases and the load-deflection response is less ductile.

Variation of the computed ultimate load with the number of elements for beam T2LA is presented in Table 5.2 and in Fig. 5.5, which shows that the ultimate load for the beam is dependent on the mesh size used in the analysis. It can be noted that for the same ultimate tensile strain, the ultimate load for this under-reinforced beam decreases with an increase in the number of elements. To show the effect of element size on the prediction of the concrete strain, for three

mesh configurations with 4, 80, and 320 elements, the computed load-concrete compressive strain curve at the beam mid-span top is presented in Fig. 5.6. Once again, the results are influenced by the element size and it emphasizes the sensitivity of the computed responses to the mesh characteristics.

For the beam T5L, which is over-reinforced, a similar analysis procedure was followed. The results show that the effect of the element size on the ultimate load is not significant, i. e., the beam response is not dependent on the mesh characteristics. Because of the high ratio of tensile reinforcement, cracking of the concrete does not have a significant effect on the material nonlinearity of the concrete. Also, as the value of ε_{tu} was varied with all other parameters maintained constant, the ultimate load remained approximately constant and relatively close to the experimental ultimate load, (see Table 5.3).

5.2.2 Example 2: Reinforced concrete shear panel W-2

The shear panel W-2, tested by Cervenka (1970) under monotonically increasing load, is investigated in this example. The panel consists of orthogonally reinforced square plates, 30 in x 30 in in size, and 3 in in thickness. Two panels are combined to form one beam, like the specimen shown in Fig. 5.7. The material properties of the shear panel are summarized in Table 5.1. Because of symmetry, only one-half of the specimen is idealized for the finite element analysis. The total load is applied at the two points on the outer rib as shown in Fig. 5.8.

Table 5.3: Effect of element size on the ultimate load of bea T5L

Number of elements	Size of elements (in x in)	ε_{cr}	ε_{tu}	Ultimate load (lb)	P_{Hoda}/P_{Exp}
4	18 x 12	0.00013	0.001	17000	0.96
20	6 x 6	0.00013	0.001	17000	0.96
80	3 x 3	0.00013	0.001	16500	0.94
80	3 x 3	0.00013	0.0021	16500	0.94
80	3 x 3	0.00013	0.0031	16500	0.94
320	1.5 x 1.5	0.00013	0.001	16500	0.94
Experimental result	-	-	-	17666	-

To study the influence of the mesh size, three different meshes with 35, 120, and 460 elements are examined. The ultimate tensile strain, ε_{tu}, is assumed to be constant and arbitrarily selected to be 0.002. Figure 5.8 illustrates a typical mesh layout for the shear panel with 35 elements.

The load-deflection curves for this panel for the different meshes are plotted in Fig. 5.9. As in Example 1, it can be observed that the element size has a significant effect on the load-deflection curve. Once again, it was noted that with an increase in the number of finite elements idealizing the system, the ultimate load decreases. In each case, the deflection response before cracking is identical, however, after cracking there are deviations from the experimental response and the deflection at the ultimate load decreases with a decrease in the element size.

The effect of different mesh configurations on the analytical crack pattern at Gauss quadrature points at a selected load level (P=24000 lb) for the shear panel is shown in Fig. 5.10. Here, thick lines represent fully opened cracks ($\varepsilon > \varepsilon_{tu}$), while thin lines indicate partially opened cracks ($\varepsilon_{cr} < \varepsilon < \varepsilon_{tu}$). It can be noted from Fig. 5.10 that the crack patterns are different and are influenced considerably by the element size. With a decrease in the element size, the progress of fully opened cracks increases, resulting in wider crack patterns. It is also evident that the penetration of the fully opened cracks in a finer mesh configuration is greater than that for the coarse mesh, and consequently it leads to a lower ultimate load for the finer mesh.

5.2.3 QUALITATIVE REPRESENTATION OF MESH SIZE DEPENDENCY

The problem of spurious mesh sensitivity can be also illustrated, for example, by qualitative consideration of the rectangular panel in Figures. 5.11(a) and (b), which is subjected to a uniform vertical displacement at the top boundary. A small region near the centre of the left side is assumed to have a slightly smaller strength than the rest of the panel, and consequently a smeared crack band starts growing from the left to the right. The solution is obtained by incremental loading with two finite element meshes of very different mesh sizes as shown. By stability checks, it is found that the cracking must always localize into a band of single element width at the cracking front [see Fig. 5.11(a) and (b)]. Typical qualitative results for this, and other responses such as load-deflection, load-crack length and energy released versus the number of elements are illustrated in Fig. 5.11(c), (d) and (e). In the load-deflection diagram [Fig. 5.11(c)], it is seen that the peak load as well as the post-peak softening is strongly dependent on the

element size. In other words, with an increase in the element size [Fig. 5.11(a)], the ultimate load increases and the structure behaves in a stiffer manner compared with a model with smaller size element. Plotting the load (reaction) versus the length of the crack band, again large differences are found [Fig. 5.11(d)]. This implies that if a very fine mesh is used (case B) to obtain a specific, it requires lower load than that for the coarse mesh (Case A).

The energy which is dissipated due to cracking decreases with the refinement of the finite element mesh [solid line in Fig. 5.11(e)] and converges to 0 as h tends to 0. This gives unreliable results. With accommodation of the fracture mechanics concepts or the proposed model presented in Section 5.3.2, the energy release rate can be ensured to be constant [dashed line in Fig. 5.11(e)].

5.3 ELIMINATION OF ELEMENT SIZE DEPENDENCY

Cracking of concrete is one of the important aspects of the material nonlinear behaviour. Intensive research effort has resulted in a large number of cracking models, which can be divided broadly into two categories, namely, discrete cracking models and smeared cracking models. Furthermore, within each category, these models can be applied either with a strength-based, or fracture mechanics-based crack propagation criterion. The problem of mesh sensitivity is encountered when cracking is idealized using the smeared or discrete cracking models based on the strength concept (Bazant and Cedolin, 1979; Bazant, 1992). The main objective of this chapter is to develop a solution to eliminate this drawback from the strength-based criterion with an appropriate adjustment of the value of the ultimate tensile strain, ε_{tu}, as a function of only the element size, h.

Fracture mechanics concepts can be used to deal with propagation of cracks, and are based on the concept of energy dissipation in the structure undergoing the fracture process. It should be noted that if the computed response is to correlate with the experimental response, then the energy dissipated in the process should be independent of the type of mesh. This implies that irrespective of the finite element size selected, the area under the experimental and the computed load-deflection curves should be equal. Therefore, the energy release rate should be constant in both the experimental and the computer model irrespective of the finite element size used. For the sake of comparison, the "crack band model" proposed by Bazant (1976) is also implemented in the computer program HODA and some key features of this model are presented in the following

section.

5.3.1 Crack Band Model

The basic characteristics of this model are (Bazant, 1992):

(1) to characterize the material behaviour in the fracture process zone in a smeared manner through a strain-softening constitutive relationship, and

(2) to impose a fixed width w_c of the front of the strain-softening zone (crack band), representing a material property.

The imposition of constant w_c is required to avoid spurious mesh sensitivity and objectivity, assuming that the energy dissipation due to fracture per unit length (and unit width) is constant, and equal to the fracture energy of the material, $G_f=0.5\varepsilon_{tu}f'_t w_c$. The width of the crack band front, w_c, can be assumed to be approximately three times the maximum aggregate size, d_a (i. e., $w_c=3d_a$) (Bazant and Oh, 1983). However, w_c-values ranging from d_a to $6d_a$ gave almost equally good results (Bazant, 1992). Once the shape of the softening branch of the stress-strain relationship is fixed, the crack band model is fully characterized by three material parameters: f'_t, G_f and w_c.

The finite element size, $h=w_c$, required by the crack band model, may be too small in the case of very large structures. In this case, it is possible to enlarge the element size, provided that the softening branch of the stress-strain relationship is adjusted to obtain the same energy dissipation, G_f. The given stress-strain curve OPA in Fig. 5.12 for the strain-softening crack band needs to be replaced for increasing element size, h, by curves OPB, OPC, OPD, etc., such that when the areas under any of these curves is multiplied by h, the same fracture energy value, G_f, is obtained.

One can also use elements with $h < w_c$, provided that the post-peak slope is decreased such that a constant fracture energy, G_f, is obtained, as shown in curve OPF.

As the element size is increased, the slope of the strain-softening branch gets steeper, until for a certain element size, h_0, a vertical stress drop, as represented by the curve OPC is obtained. For a still larger element size, the diagram OPD would exhibit snapback, which would cause computational difficulties. The point of vertical drop is determined again from the condition that the area under the curve OGE must be the same as the area under the curve OPD (PC and GE in Fig. 5.12 represent f'_t and f_{eq}, respectively). This consideration indicates that the equivalent

tensile strength, f_{eq}, of the large finite element of size $h > h_0$ is given by

$$f_{eq} = f_t' \sqrt{\frac{h_0}{h}} \tag{5.1}$$

in which $h_0 = (2EG_f/f_t'^2)$ is the element size for which a vertical stress drop is obtained.

5.3.2 The Proposed Model

Different structural elements, including the under-reinforced beam T2LA and the shear panel W-2, were analyzed using the HODA program with different mesh sizes. Various analyses using the program indicated that the shape and the length of the descending branch of the tensile stress-strain curve of concrete have significant effects on the computed responses. These characteristic parameters are controlled by the values of the ultimate tensile strain, ε_{tu}, and the tensile strength of concrete, f_t'. It was shown (see Shayanfar et al., 1993) that the value of f_t' does not have a considerable influence on the value of the ultimate load, as compared with the value of ε_{tu}.

For each mesh configuration, the value of ε_{tu} was adjusted so that the computed ultimate load was close to the experimental ultimate load. The results of analyses for beam T2LA and shear panel W-2 are presented in Tables 5.4 and 5.5, respectively. The best values of ε_{tu} for the beam and the shear panel for different mesh sizes are presented in Table 5.6. The results confirm that there is a unique value of ε_{tu} corresponding to each mesh size regardless of the type and detailing of the structure. After determining the best value of ε_{tu} for each mesh size (element width), h, the variation of ε_{tu} with respect to the element width is plotted in Fig. 5.13. A regression analysis of the results leads to the following exponential equation:

Table 5.4: Effect of ε_{tu} on ultimate load, for under-reinforced beam T2LA

Number of elements	Size of elements (in x in)	ε_{cr}	ε_{tu}	Ultimate load (lb)	P_{Hoda}/P_{Exp}
4	18 x 12	0.00013	0.0007	19500	1.24
4	18 x 12	0.00013	0.00018	16000	1.02
20	6 x 6	0.00013	0.0007	14000	0.90
20	6 x 6	0.00013	0.001	14500	0.93
20	6 x 6	0.00013	0.0013	15500	0.99
80	3 x 3	0.00013	0.0007	15000	0.96
80	3 x 3	0.00013	0.00013	13500	0.86
80	3 x 3	0.00013	0.0021	15500	0.99
80	3 x 3	0.00013	0.0028	16500	1.053
80	3 x 3	0.00013	0.005	17000	1.085
320	1.5 x 1.5	0.00013	0.0007	14000	0.90
320	1.5 x 1.5	0.00013	0.0031	15500	0.99
Experimental result	-	-	-	15666	-

Table 5.5: Effect of ε_{tu} on ultimate load of shear panel W-2

Number of elements	Size of elements (in x in)	ε_{cr}	ε_{tu}	Ultimate load (lb)	P_{Hoda}/P_{Exp}
35	6 x 6	0.00018	0.0002	26000	0.98
35	6 x 6	0.00018	0.0018	28500	1.08
35	6 x 6	0.00018	0.002	28700	1.083
35	6 x 6	0.00018	0.00125	26500	1.00
120	3 x 3	0.00018	0.0002	25500	0.96
120	3 x 3	0.00018	0.005	30500	1.15
120	3 x 3	0.00018	0.0006	25500	0.96
120	3 x 3	0.00018	0.0021	26250	0.991
460	1.5 x 1.5	0.00018	0.0002	24000	0.91
460	1.5 x 1.5	0.00018	0.002	24500	0.925
460	1.5 x 1.5	0.00018	0.0013	24500	0.925
460	1.5 x 1.5	0.00018	0.0031	26700	1.008
Experimental result	-	-	-	26500	-

Table 5.6: Optimum value of ε_{tu} for different mesh sizes for beam T2LA and shear panel W-2

Size of element (in inches)	The optimum value of ultimate tensile strain (ε_{tu})	
	Beam T2LA	Shear panel
1.5 x 1.5	0.0031	0.0031
3 x 3	0.0021	0.0021
6 x 6	0.0013	0.00125
18 x 12	0.00018	--

$$\epsilon_{tu} = 0.004\, e^{-0.2h} \qquad (\epsilon_{tu} \geq \epsilon_{cr}) \tag{5.2}$$

If ε_{tu} is smaller than ε_{cr}, then

$$\epsilon_{tu} = \epsilon_{cr} \tag{5.3}$$

where h is the width of the element in inches (for non-square elements: $h = \sqrt{A}$, in which A is the element area), and ε_{tu} is the concrete ultimate tensile strain.

This formula is empirical and is obtained by a trial and error procedure. Based on this formula, the value of ε_{tu} decreases with an increase in the value of h, and vice versa, so that the energy dissipation capacity and the ultimate load of the structure remain constant irrespective of the size of finite element used in the mathematical model. If the element size, h, is too large so that the ε_{tu} is less than ε_{cr}, then ε_{tu} is considered to be equal to ε_{cr}. This is because of the numerical difficulties in the snapback of the tensile stress-strain curve of concrete. It should be pointed out that using this formula, a coarse mesh can be selected for finite element analysis with an acceptable degree of confidence in the computed results and considerable saving in the computational effort.

However, it should be noted that Eq. 5.2 was derived for the case of beams and shear panels, and its validity for other systems need to be investigated.

5.4 IMPLEMENTATION OF THE MODELS INTO THE HODA PROGRAM

The algorithms employed for implementation of the crack band theory and the new proposed model are presented in this section. With the imposed modifications, the program can handle the nonlinear finite element analysis of the structures based on "no mesh dependency analysis", "the crack band theory" and "the proposed model".

5.4.1 Crack Band Model

The crack band theory algorithm is summarized for implementation into the HODA program as follows:

Case (1): If the size of the element is equal to the crack band width, i. e. $h = w_c$, then the ultimate tensile strain of concrete is evaluated as (see curve OPA of Fig. 5.12)

$$\epsilon_{tu} = \frac{2G_f}{f_t' W_c} = \overline{OA} \tag{5.4}$$

where h is the element size, G_f is the fracture energy, w_c is the crack band width which is approximately equal to three times the maximum aggregate size ($3d_a$), and f'_t is the direct tensile strength of concrete evaluated using Eq. 3.32.

Case (2): If the size of the element is less than the crack band width, i. e. $h < w_c$, then the ultimate tensile strain is calculated using (see curve OPF of Fig. 5.12)

$$\epsilon_{tu} = \frac{2G_f}{f_t' h} = \overline{OF} \tag{5.5}$$

Case (3): If the size of the element is greater than the crack band width, i. e. $h > w_c$, first the mesh size, h_0, is determined for the case for which a vertical drop in stress is encountered. From curve OPB of Fig. 5.12 it can be found that: $G_f = 1/2\ \epsilon_{cr}\ f'_t(h_0) = 1/2\ (f'_t / E_0)\ f'_t(h_0)$, and then,

$$h_0 = \frac{2E_0G_f}{f_t^{'2}} \tag{5.6}$$

Now, if $w_c < h < h_0$ then,

$$\varepsilon_{tu} = \frac{2G_F}{f_t' h} = \overline{OB} \tag{5.7}$$

and if $w_c < h > h_0$ is governed, an equivalent curve OGE is used by modifying the tensile strength of concrete, f_{eq}, to avoid a snapback part (curve OPD). Thus, $G_f = h_0 f_t'^2/2E_0 = h f_{eq}^2 /2 E_0$, and

$$f_{eq} = f_t' \sqrt{\frac{h}{h_0}} \tag{5.8}$$

where f_{eq} is the equivalent tensile strength of concrete for large finite element size with $h > h_0$. Finally, the ultimate tensile strain of concrete, ε_{tu}, is obtained as,

$$\epsilon_{tu} = \frac{f_{eq}}{E_0} = \overline{OE} \tag{5.9}$$

5.4.2 The Proposed Model

As explained in Section 5.3.2, the following equation can be used to evaluate the concrete ultimate tensile strain, ε_{tu}, corresponding to each element size, h:

$$\epsilon_{tu} = 0.004e^{-0.20h} \qquad (\epsilon_{tu} \geq \epsilon_{cr}) \tag{5.10}$$

where h is the element size in inches. If h is large so that the Eq. 5.10 gives a value less than the cracking strain, ε_{cr}, to avoid numerical difficulties associated with a snapback portion on the tensile stress-strain curve, the value of ε_{tu} is set equal to that of ε_{cr}. For more information on how this model and crack band model were implemented in the HODA program, refer to the flow chart in Fig. 5.14.

5.5 COMPARISON OF RESULTS AND DISCUSSIONS

The proposed model and the "crack band model" proposed by Bazant (1976) are implemented in the HODA computer program as discussed in the previous section. The detailed analysis of the beam T2LA and the shear panel W-2 is presented in this section along with a comparison of the results.

5.5.1 Beam T2LA

Beam T2LA is examined using 4 and 320 elements for the computer models. The value of ε_{tu} for the program with "no mesh dependency analysis" (MDEP=1) is assumed to be equal to 0.0007 for all beam idealizations. For the beam idealized using 4 elements, the results are shown in Fig. 5.15. The ultimate load computed using the with "no mesh dependency analysis" is 19,500 lb which is 24% higher than experimental value of 15,666 lb. At load levels higher than 14,000 lb, the beam response is stiffer than the other models with yielding of steel reinforcement occurring at a load of 16,500 lb which is higher than the experimental yield load of 14,000 lb. The ultimate load obtained using the crack band model is 18,100 lb, which overestimates the ultimate load by 16%, while the value based on the proposed model is 16,100 lb, which is quite close to the experimental value with a discrepancy of only 2%. The yield load from both the crack band and the proposed models are the same as the experimental result of 14,000 lb. The load-deflection curve for these two models follow the same general pattern and are quite close to the experimental response. It is obvious that the proposed formulation can be used effectively with relatively large size finite elements. With this approach, the required computational times can be reduced considerably.

As can be seen from Fig. 5.16, the ultimate loads for the beam idealized using 320 elements obtained from both the crack band model and the proposed model are the same, 15,500 lb, and quite close to the experimental result. It shows that the application of these two models gives similar results with reasonably accurate prediction of the ultimate load. Use of the HODA program with "no mesh dependency analysis" underestimates the value for the ultimate load at 14,000 lb with an 11% discrepancy. A summary of the ultimate loads for the various mesh sizes computed for the different models for beam T2LA is presented in Tables 5.6.

5.5.2 Shear panel W-2

The shear panel W-2 is examined for the models with 35 and 120 elements to show the effect of fineness of the mesh on the computed results. The values of ε_{tu} for the analysis with the program with "no mesh dependency analysis" (MDEP=1) are assumed to be equal to 0.002 and 0.005, respectively. The load-deflection curves for 35 element using the different models are shown in Fig. 5.17. The ultimate load obtained from the model with no mesh dependency is equal to 28,700 lb with a difference of +8.3% from the experimental result of 26,500 lb. The load-deflection curves computed for the different models are quite close to the experimental response up to load level of 12,000 lb. Beyond this load level the program with "no mesh dependency analysis" exhibits stiffer response compared with the experimental response (see Fig. 5.17). The load-deflection curves resulting from both the crack band model and the proposed model agree quite well with the experimental curve and predict the ultimate load quite accurately with a value of 26,700 lb which represent a deviation of only +0.7% from the experimental result.

The results for the shear panel idealized using 120 elements are presented in Fig. 5.18. The ultimate load resulting from the program with "no mesh dependency analysis" gives a value of 30,500 lb, with a difference of 15% from the experimental value of 26,500 lb. The ultimate

Table 5.7: Ultimate load for the beam T2LA and the shear panel W-2 for different models

Type of structure	Number of elements	Size of elements (in x in)	Ultimate tensile strain (ε_{tu})	Ultimate Load (lb)			
				No mesh dependency analysis	Crack band model	Proposed model	Experimental values
Beam T2LA	4	18 x 12	0.0007	19500	18100	16100	15666
	80	3 x 3	0.0007	15000	15000	15500	15666
	320	1.5 x 1.5	0.0007	14000	15500	15500	15666
Shear panel W-2	35	6 x 6	0.002	28700	26700	26500	26500
	120	3 x 3	0.002	26500	25700	26500	26500
	460	1.5 x 1.5	0.002	24500	26700	26700	26500
	120	3 x 3	0.005	30500	25700	26500	26500

load for the crack band model is 25,700 lb, representing a discrepancy of -3%, while the ultimate load for the proposed model is 26,500 lb which is exactly the same as the experimental result. A summary of the ultimate loads for various mesh sizes computed for the different models for shear panel W-2 is presented in Tables 5.7. Excellent agreement between the computed values obtained using the proposed model and experimental values is obvious from a comparison of the last two columns.

5.5.3 Crack patterns

One of the most significant factors involved in the prediction of the behaviour of reinforced concrete structures is the formation and propagation of cracks with increasing load. The cracks in the concrete are the major source of material nonlinearity. The ability of the different models to predict the crack propagation in concrete is examined in this section. For this purpose, the crack pattern for only one mesh configuration of the shear panel is presented with thick lines representing fully opened cracks ($\varepsilon > \varepsilon_{tu}$) and thin lines showing partially opened cracks ($\varepsilon_{cr} < \varepsilon < \varepsilon_{tu}$). The predicted crack patterns for beam T2LA using different models at different load stages are presented in the report by Shayanfar et al. (1993).

The ability of the models to simulate the experimental cracking pattern for shear panel is demonstrated in Figures 5.19 through 5.21. Figures 5.19 and 5.20 compare the crack patterns for the program with "no mesh dependency analysis" (Case a), the crack band model (Case b) and the proposed model (Case c) with the experimental cracking patterns (Case d) at two load levels: 24,000 lb and 25,500 lb, respectively. In comparing the cracking patterns, the following terminology has been used with reference to Fig. 4.4(a). The concrete is assumed to crack at the end of tension stress-strain branch KC = 1. These cracks widen partially along the branch KC = 3 and become much wider or "fully opened" along the branch KC = 4. The comparison of the different configurations show that the progress of fully opened cracks for both the crack band and the proposed model is wider than for the no mesh dependency model and fits better the experimental crack pattern. Figure 5.21 compares the crack patterns at ultimate load stage using the different models. The patterns obtained for the crack band and the present models are the same and considerably wider than those obtained using the program with "no mesh dependency analysis". The experimental cracking pattern at failure stage was not available (Cervenka, 1970).

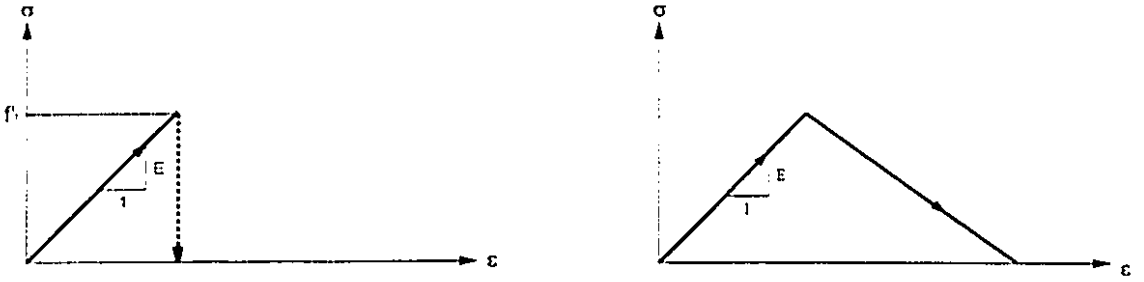

(a) (b)

Figure 5.1: Tensile stress-strain curve

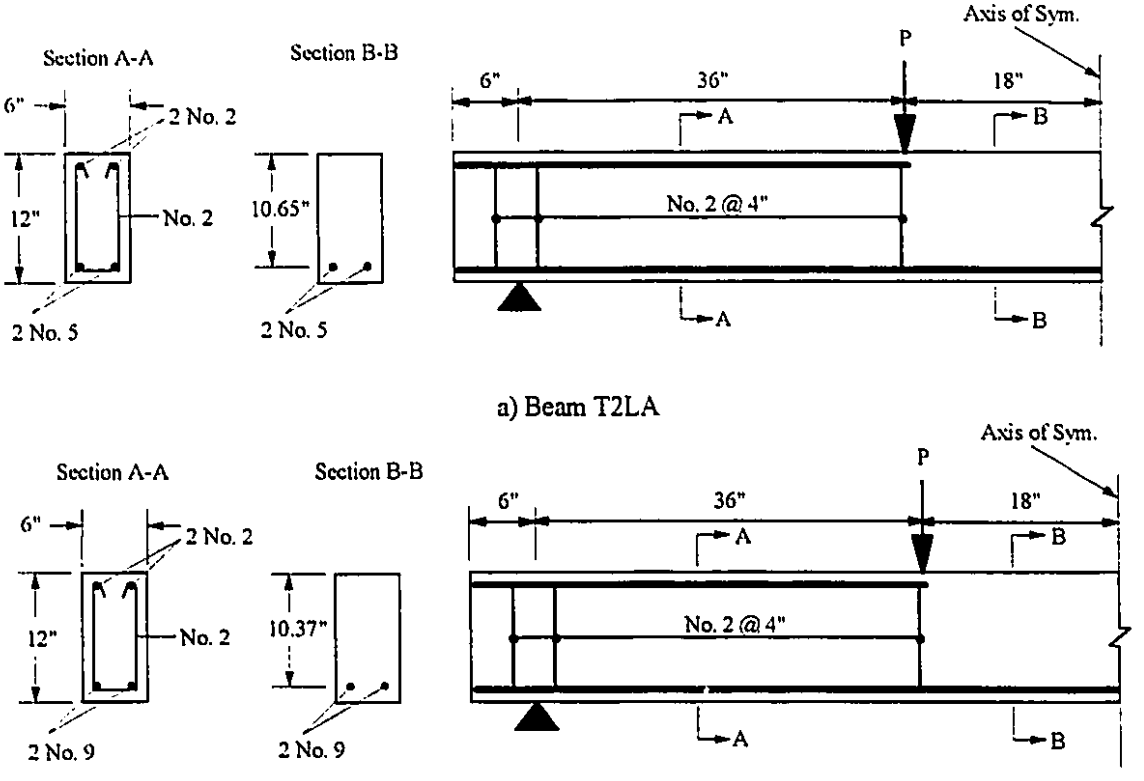

a) Beam T2LA

b) Beam T5L

Figure 5.2: Geometry and reinforcement details of the beams

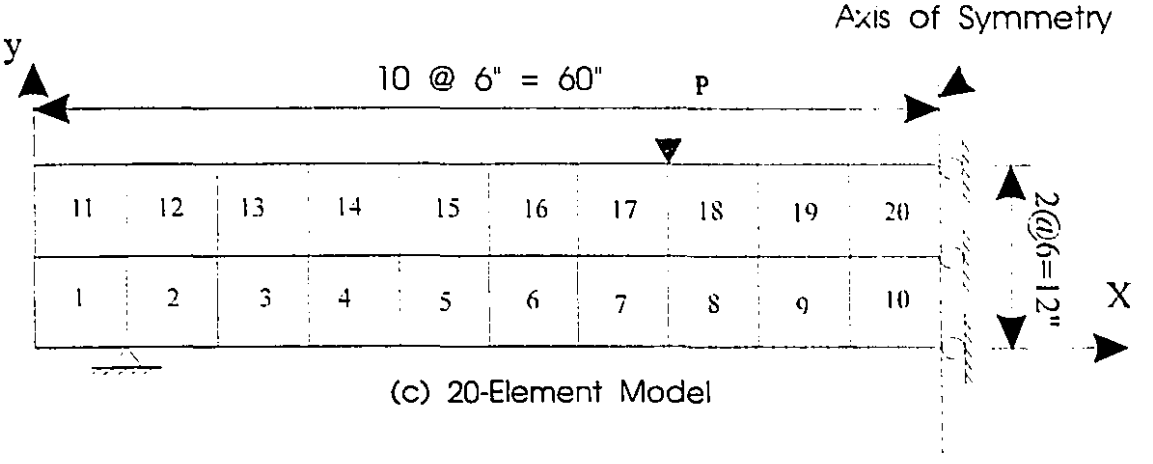

Figure 5.3: Typical mesh layout for beams T2LA and T5L

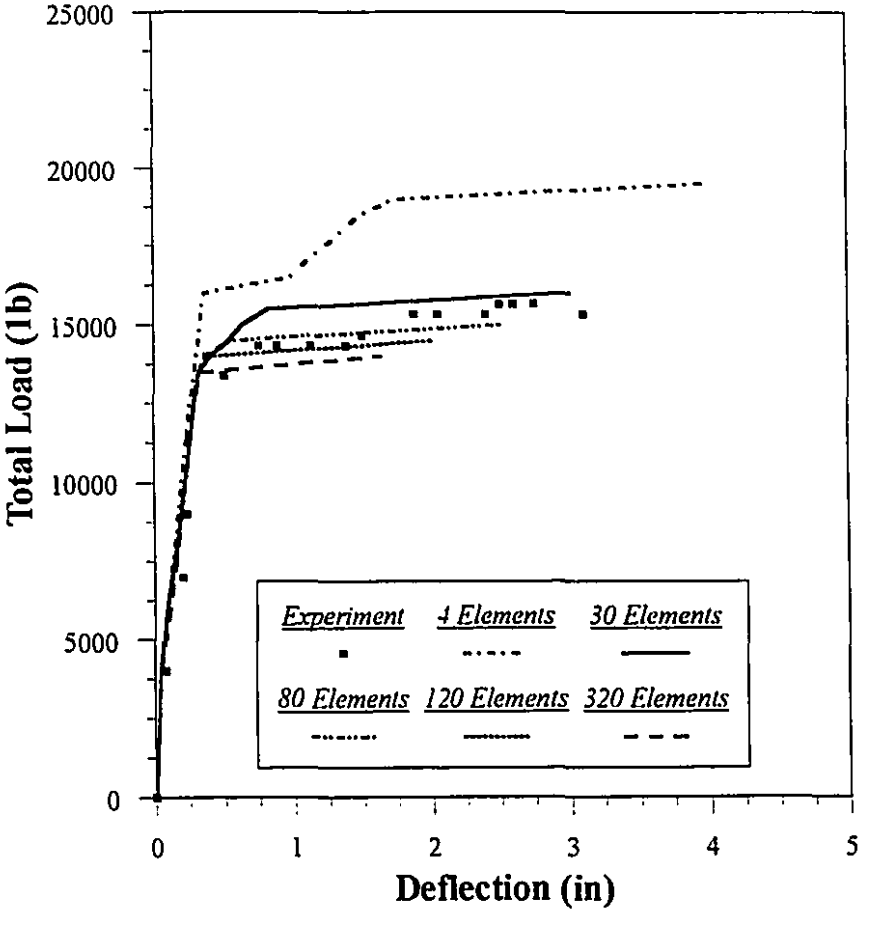

Figure 5.4: Load-deflection curve at mid-span for beam T2LA (ε_{lu} = 0.0007)

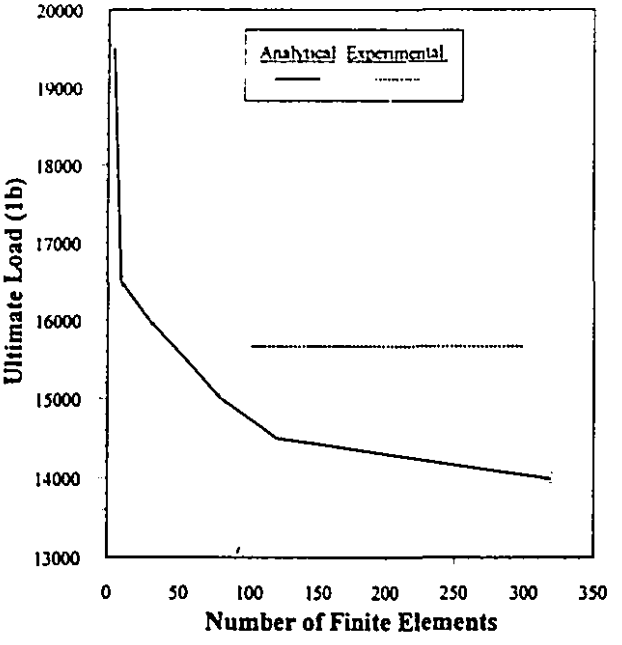

Figure 5.5: Effect of mesh size on computed ultimate load for beam T2LA (ε_{tu}=0.0007)

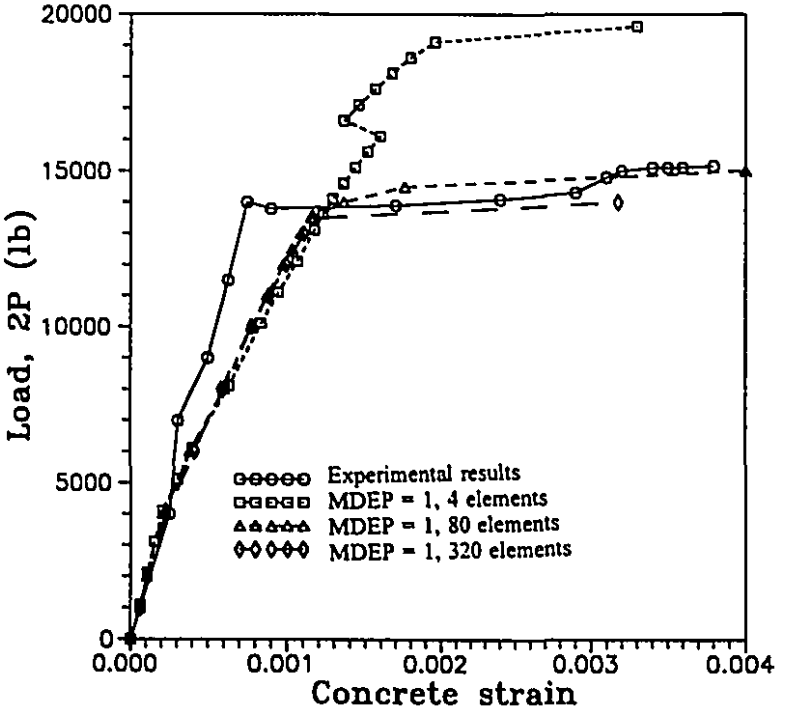

Figure 5.6: Load-concrete strain at mid-span top for beam T2LA (ε_{tu}= 0.0007)

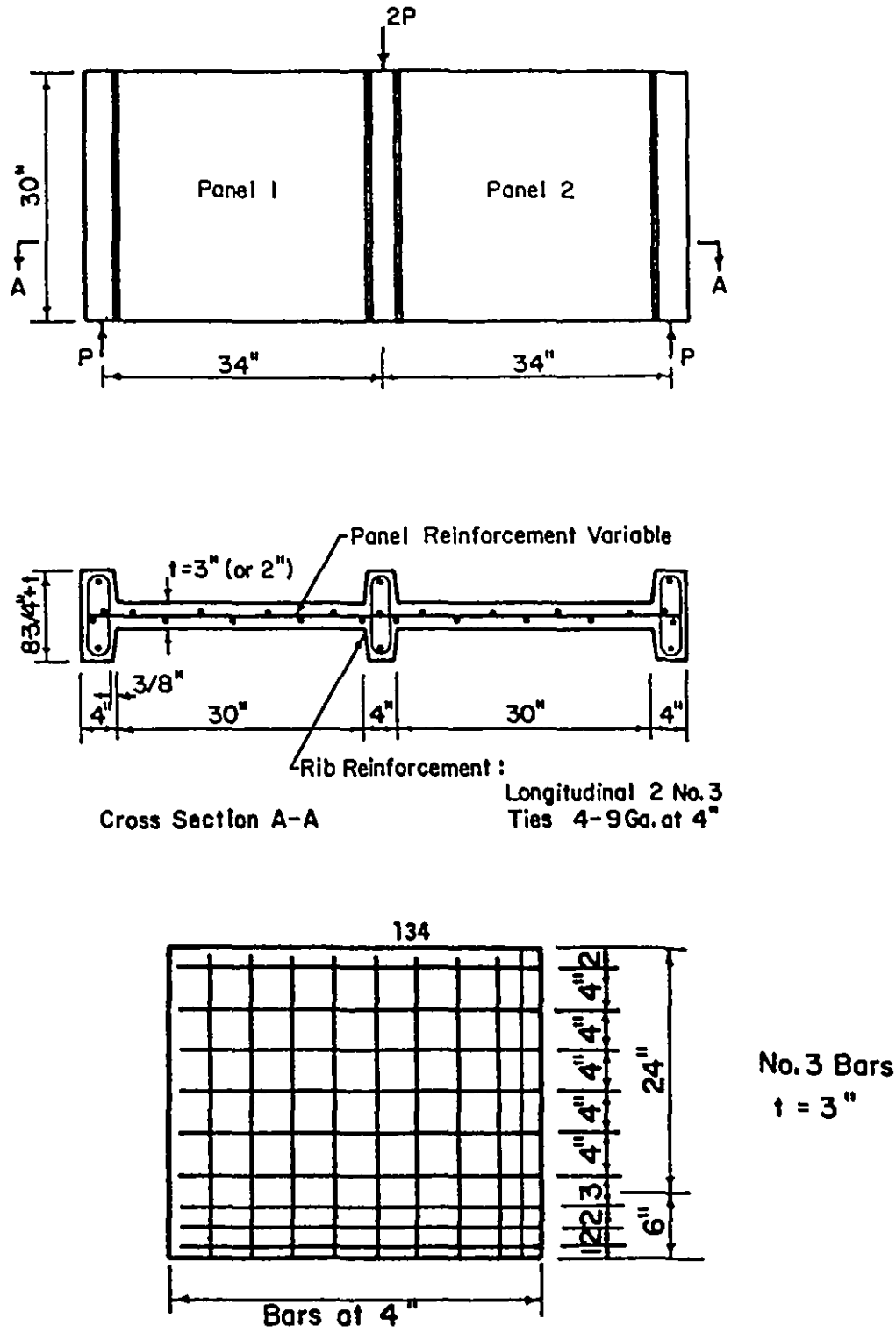

Figure 5.7: Details of reinforcement and geometry for shear panel W-2 (Cervenka 1970)

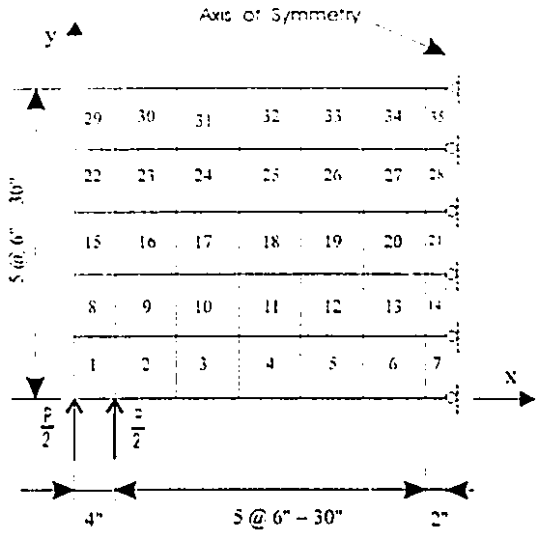

(a) 35-Element Model

Figure 5.8: Typical mesh configuration for shear panel W-2

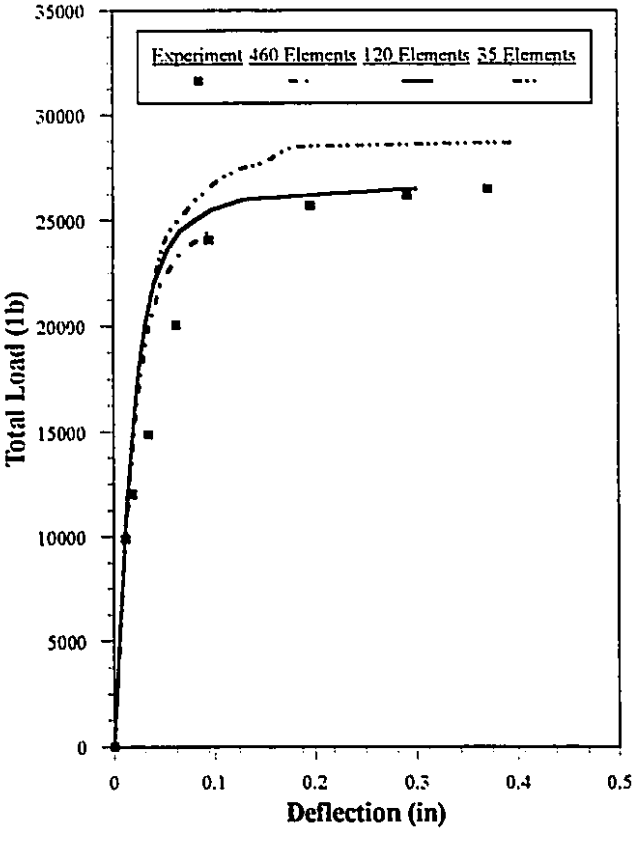

Figure 5.9: Load-deflection curve for shear panel W-2 (ε_{tu} = 0.002)

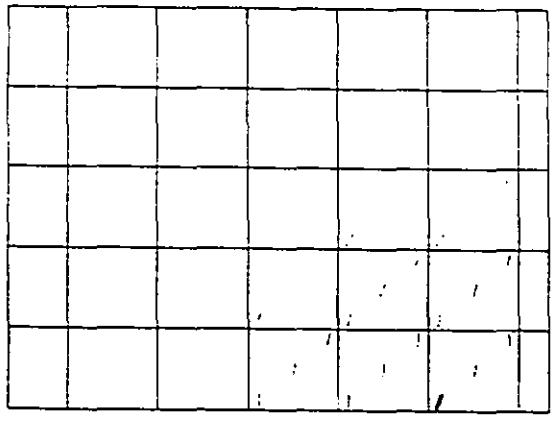

a) 35-Element Model

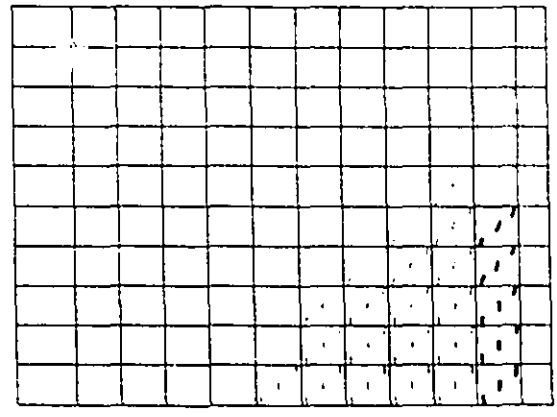

b) 120-Element Model

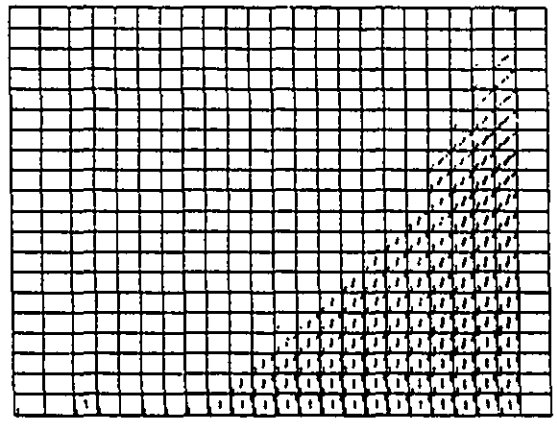

c) 460-Element Model

Figure 5.10: Effect of mesh size on crack pattern of shear panel W-2

(P=24,000 lb, ε_{tu}=0.002)

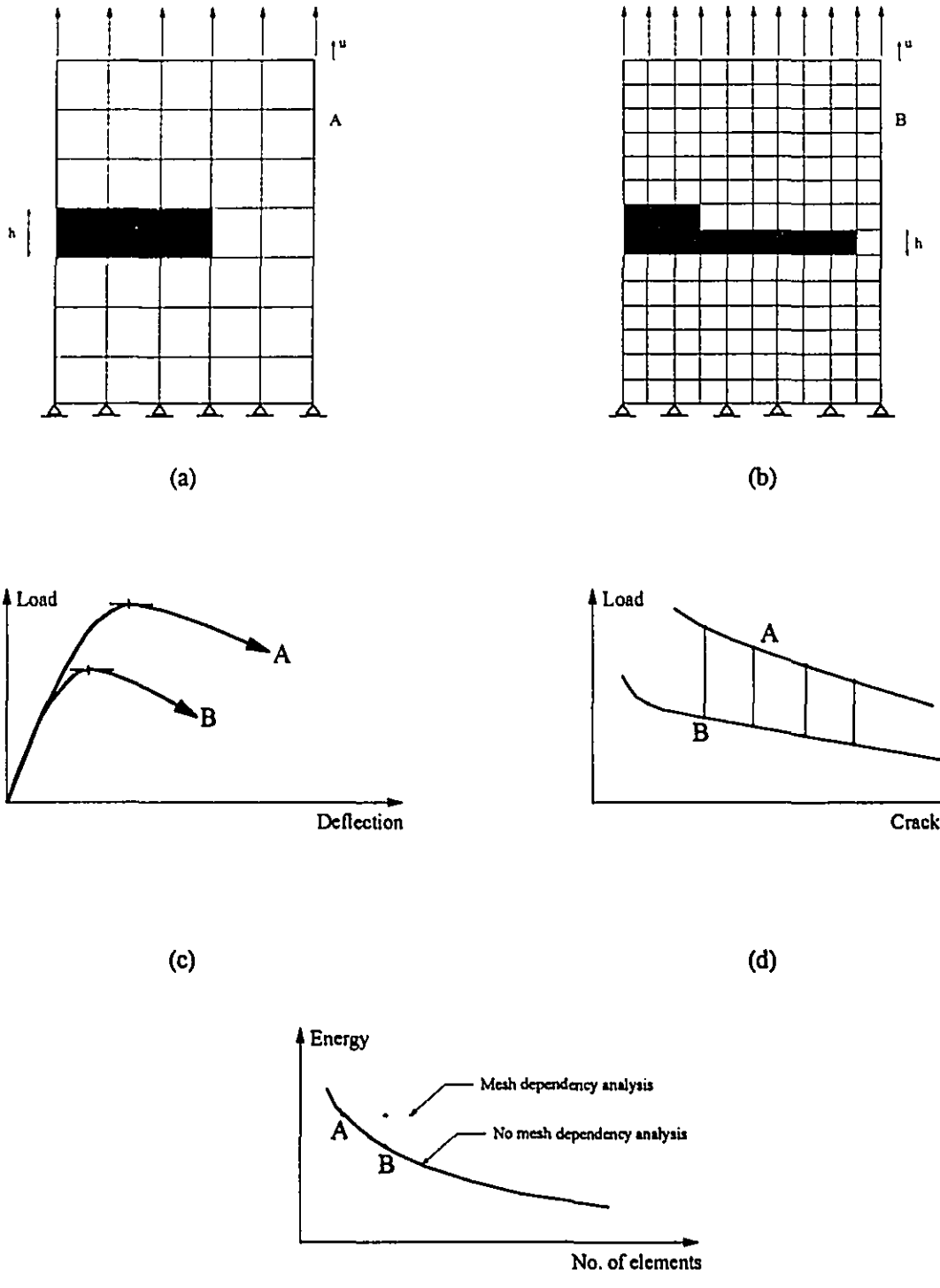

Figure 5.11: Qualitative influence of mesh size on the response of a tension member

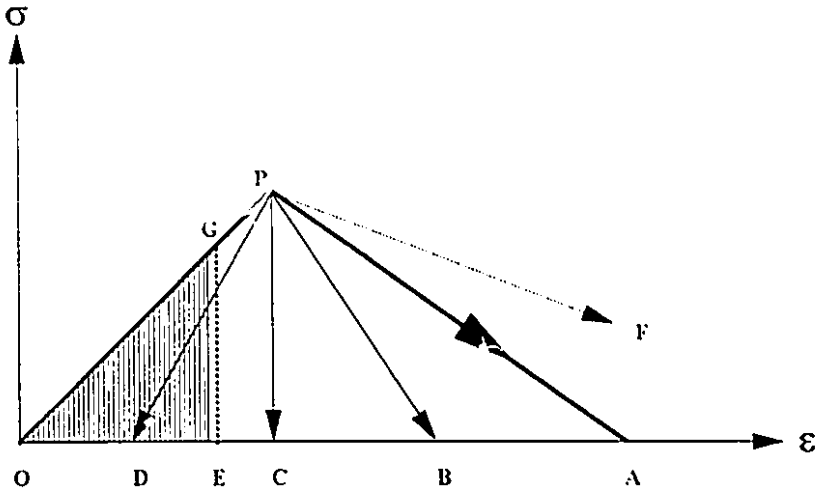

Figure 5.12: Effect of size on post-peak softening

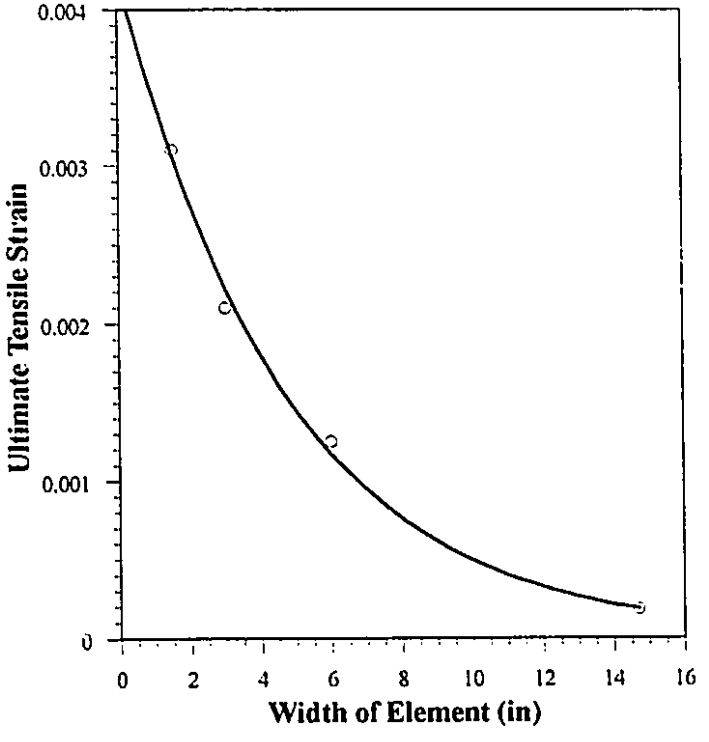

Figure 5.13: Ultimate tensile strain of concrete, ε_{tu}, versus width of element, h

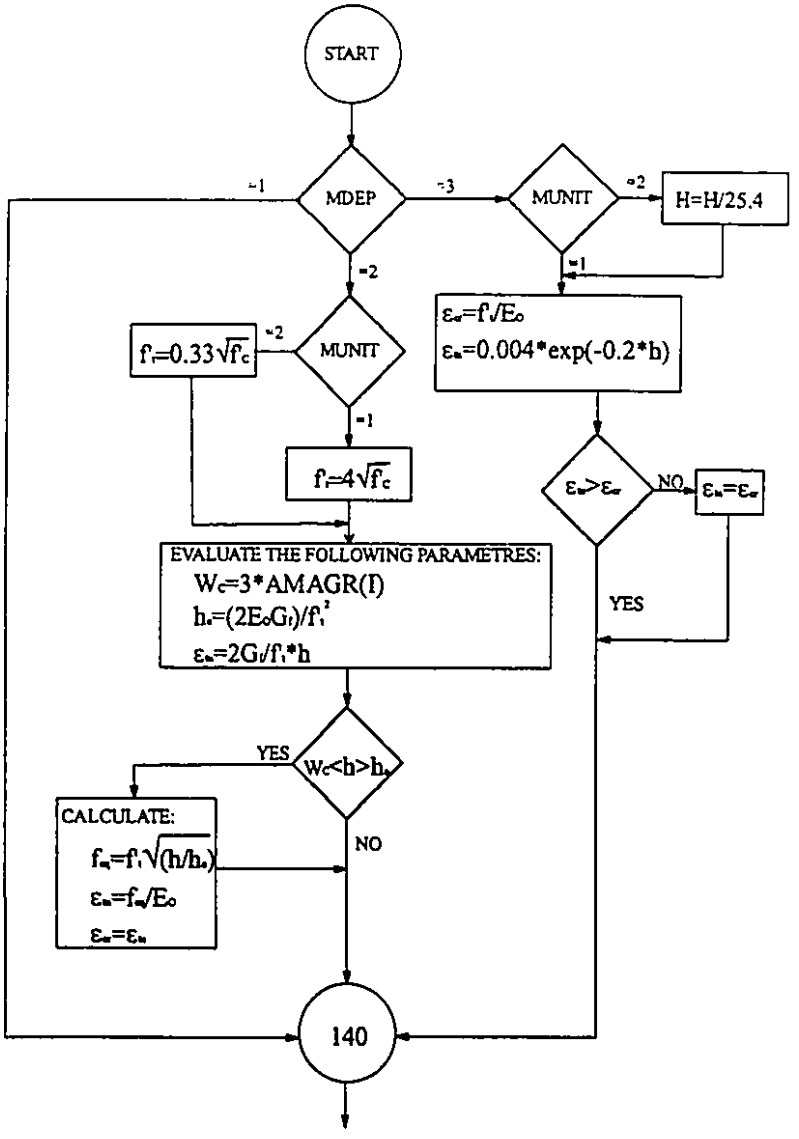

Required input data:

MDEP= Mesh dependency analysis factor
- --1 No mesh dependency analysis
- --2 Mesh dependency analysis based on the crack band theory
- --3 Mesh dependency analysis based on the proposed model

MUNIT= Unit system option
- --1 Imperial units
- --2 SI Units

GF(I)= Fracture energy for concrete type number I
- --Recommended value of 0.5 lb/in (0.1 N/mm)

AMAGR(I)= Maximum aggregate size for concrete system type number I
- --Recommended value of 1.0 in (25.4 mm)

Figure 5.14: A flow chart for the changes on subroutines: TENSION and CYCMAT

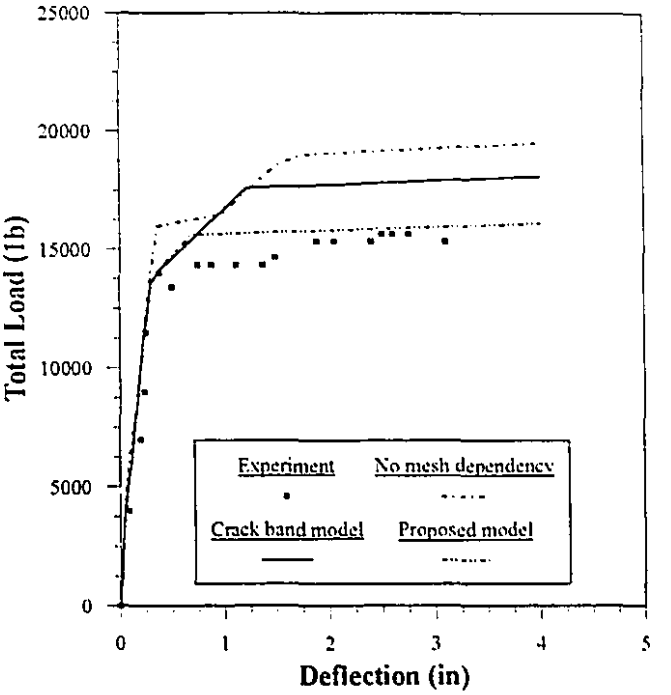

Figure 5.15: Load-deflection curves for beam T2LA with 4 elements

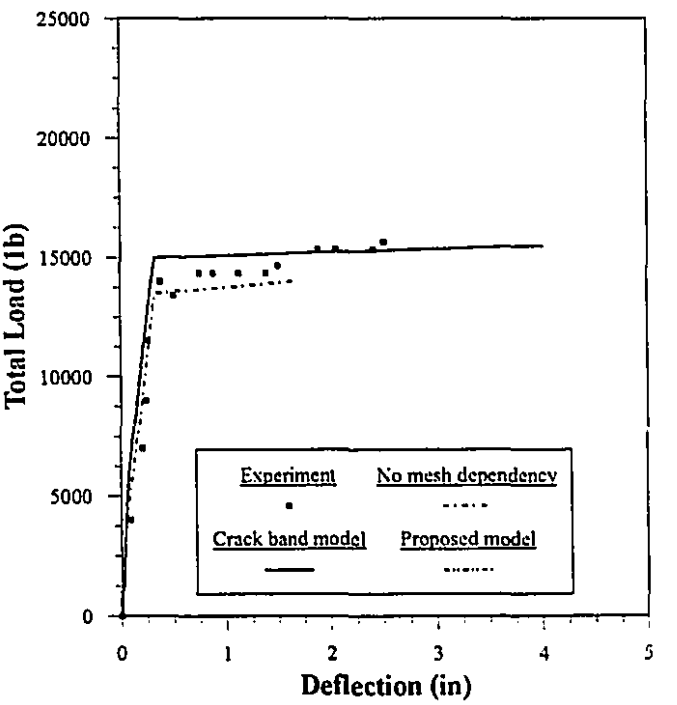

Figure 5.16: Load-deflection curves for beam T2LA with 320 elements

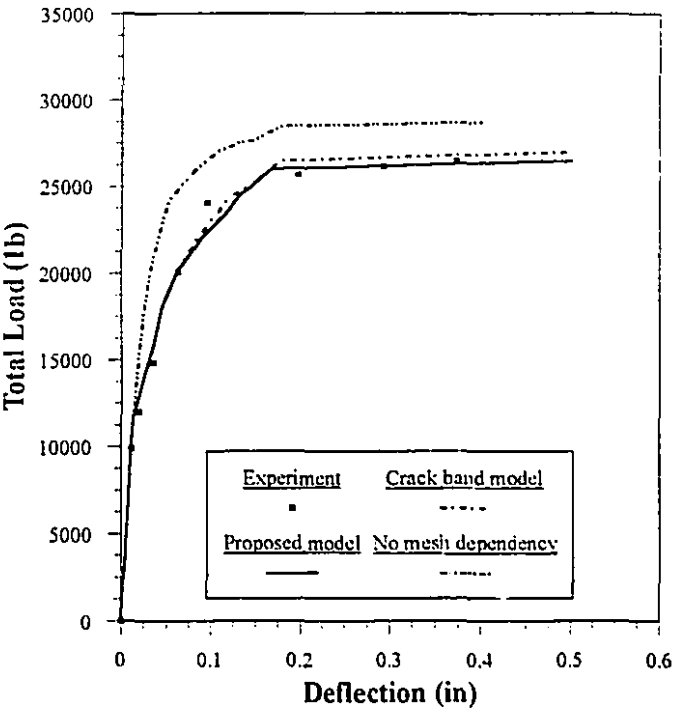

Figure 5.17: Load-deflection curves for shear panel W-2 with 35 elements

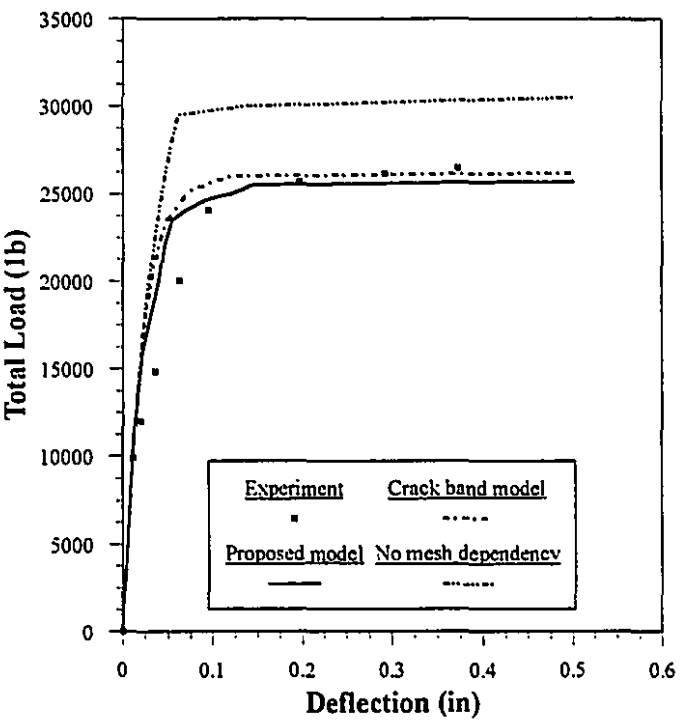

Figure 5.18: Load-deflection curves for shear panel W-2 with 120 elements

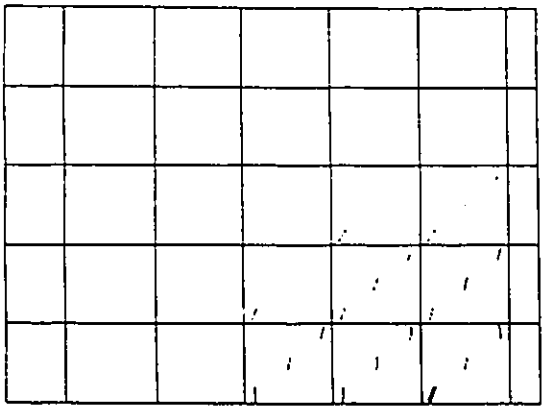

(a) No mesh dependency analysis
(ε_{tu}=0.002)

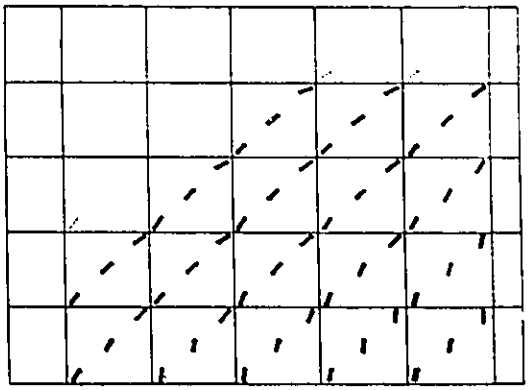

(b) Crack band model

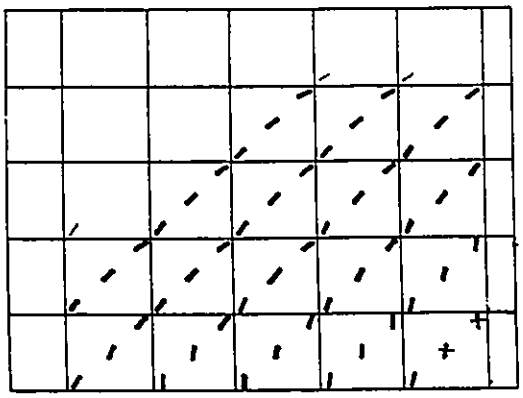

(c) Proposed model

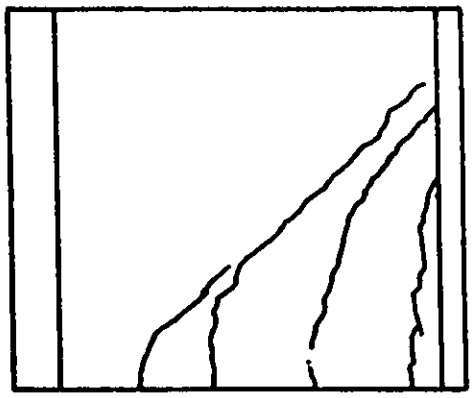

(d) Experimental

Figure 5.19: Comparison of analytical and experimental cracking patterns at load P=0.9 P_{Exp}=24,000 lb

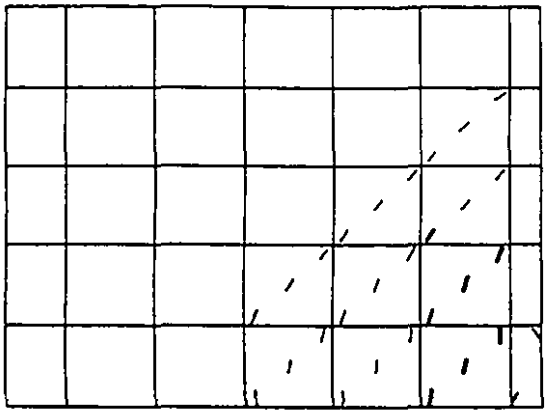

(a) No mesh dependency analysis
(ε_{tu}=0.002)

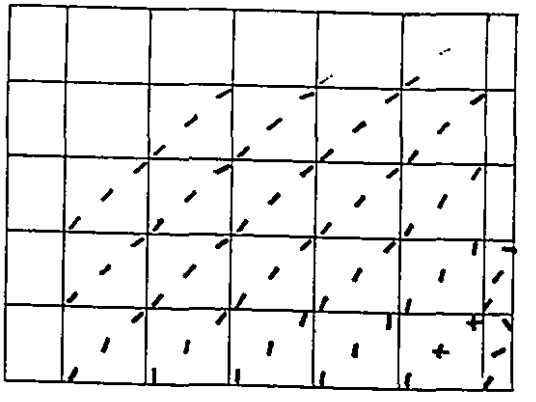

(b) Crack band model

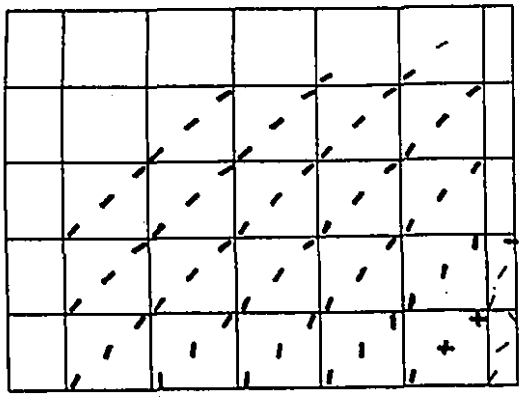

(c) Proposed model

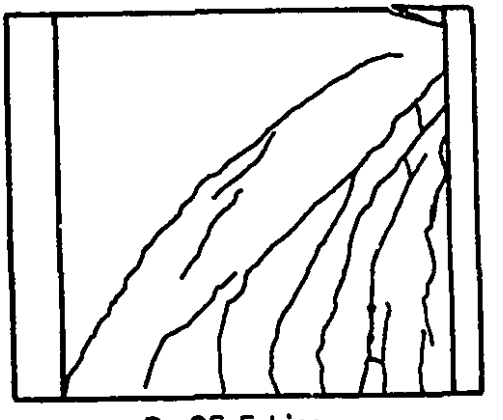

(d) Experimental

Figure 5.20: Comparison of analytical and experimental cracking patterns at load P=0.96 P_{Exp}=25,500 lb

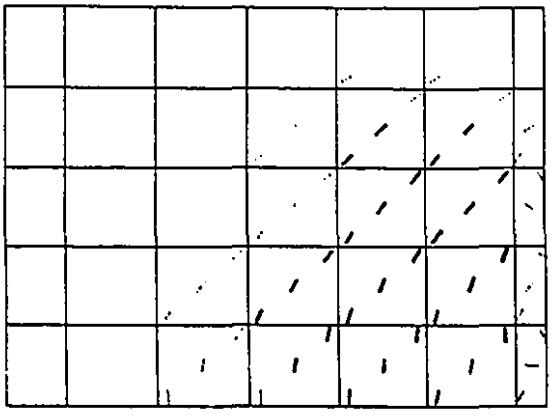

(a) No mesh dependency analysis (ε_{tu}=0.002)

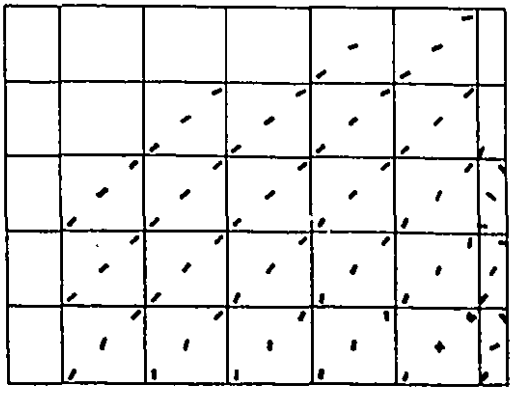

(b) Crack band model

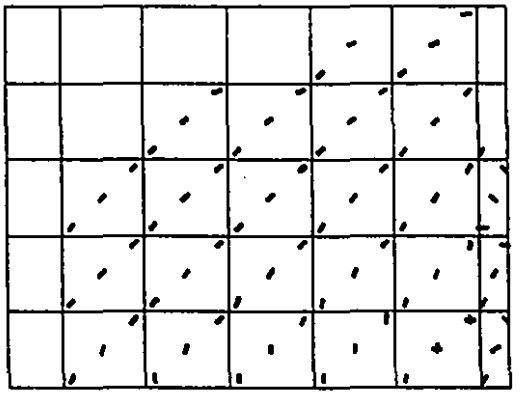

(c) Proposed model

Figure 5.21: Comparison of analytical cracking patterns at the ultimate stage

CHAPTER 6

ANALYSIS OF EXPERIMENTAL SPECIMENS

This chapter compares the computed and the experimental responses of several specimens using the HODA program. These include a total of five panels tested at University of Toronto under monotonically increasing inplane loadings (Vecchio, 1981; Vecchio and Collins, 1982), a squat shear wall tested by Cardenas et al. (1980) under monotonically increasing load up to the ultimate load carrying capacity of the structure, two high strength concrete beams, LS1 and HUCB, tested by Leslie et al. (1976) and Abrishami et al. (1995), respectively, and a shear panel (W-4) tested by Cervenka (1970) under reversed cyclic loading. Along with the analysis of each specimen, the effect of different nonlinear characteristics of reinforced concrete (tension-stiffening, failure criteria, cracking model, etc) are examined.

6.1 GENERAL

The computer program HODA is an ideal research-oriented tool to study the behaviour of reinforced concrete structures using nonlinear finite element analysis and hypoelasticity models. It provides several options for the user as follows:

Mesh size dependency analysis,

--1 mesh size dependency not considered

--2 mesh size dependency analysis based on the crack band theory

--3 mesh size dependency analysis based on the proposed model

Concrete stress-strain curve selection option

--1 Saenz and Smith's equations

--2 Popovics' equation

Constitutive matrix selection option

--1 Darwin's constitutive matrix

--2 Proposed constitutive matrix utilizing the transformation of equivalent uniaxial strains during the subsequent iteration

Tension-compression failure criteria option

--1 Kupfer and Gerstle

--2 Vecchio and Collins

Cracking model option

--1 Fixed crack model

--2 Rotating crack model

Loading option

--1 Monotonically increasing loading

--n Cyclic loading with n cycles

Tensile loading-unloading option

--1 Horizontal unloading

--2 Secant unloading

Tensile-softening branch option

--1.0 Continuous curve (no dropping at all)

--0.0 Sudden drop to zero after cracking with no tension-stiffening capability

--1.0-0.0 Dropping after cracking with tension-stiffening capability

For more information on the various options in the HODA program, refer to Appendix A.

To verify the reliability of the HODA program in predicting the nonlinear behaviour of reinforced concrete structures, its corroboration with well established experimental data is needed. Some specimens including the beams T2LA and T5L and the shear panel W-2 were analyzed earlier in Chapter 5, and good agreement was noted with the experimental results. The following sections deal with the analysis of the above structural elements in which the analytical results for each specimen are compared with the experimental findings.

6.2 PANELS TESTED AT THE UNIVERSITY OF TORONTO

In an international competition to predict the load-deformation response of the R C elements using the nonlinear finite element method, four of the R C panels tested at the University of Toronto by Vecchio and Collins (1982), were used by researchers from 13 different countries. The results showed wide scatter (Collins and Vecchio, 1985) and for one of the panels the ratio of the highest to the lowest prediction of strength was six to one. This was a clear indication that the current models for analyzing R C elements need much improvement. In the following sections the responses of five panels (from this set) are obtained using the HODA program and compared with the experimental results.

6.2.1 Description of the Panels

Five panels PV11, PV16, PV17, PV19 and PV23 were selected from the 30 specimens tested at the University of Toronto by Vecchio and Collins (1982). These five specimens were selected because of the varying reinforcement contents and loadings. The dimensions of the panels were 890×890×70 mm. They were reinforced with wires running parallel to the edges of the panel referred to as longitudinal and transverse reinforcements. The wire meshes had a typical grid spacing of 50 mm and were heat-treated to ensure a ductile response. The concrete and reinforcement properties along with the load pattern of each specimen are summarized in Table 6.1.

These panels were loaded by forces applied to 20 steel "shear keys", which were anchored into the perimeter edges of the specimens as shown in Fig. 6.1(a). Each shear key was attached to two "links" oriented at 45° with respect to the normal to the edge of the panel as illustrated in Fig 6.1(b). The links, in turn, were connected to a series of 220 kN double-acting hydraulic jacks. Only three links were rigid to stabilize the panel within the test rig. By varying the magnitude and the direction of the forces applied to the links, any combination of shear, tension and compression stresses can be applied to the edges of the test specimen. For example, Fig. 6.1(b) shows the required load arrangement to provide pure shear in which one link would apply a tensile force while the other would apply an equal compressive force. The normal force components would cancel, leaving only the shear force components.

Table 6.1: Material properties and loading patterns for the Panels*

Specimen	Concrete			Longitudinal steel		Transverse steel		Load Pattern
	ε_{cu}	f'_c (MPa)	f'_t (MPa)	ρ_l (%)	F_{yl} (MPa)	ρ_t (%)	F_{yt} (MPa)	
PV17	0.00200	18.6	1.4	0.740	255	0.740	255	Uniaxial compression
PV16	0.00200	21.7	1.0	0.740	255	0.740	255	Pure shear
PV11	0.00260	15.6	1.3	1.785	235	1.306	235	Pure shear
PV19	0.00215	19.0	1.9	1.785	458	0.713	299	Pure shear
PV23	0.00200	30.5	2.6	1.785	518	1.785	518	Shear and biaxial compression (H / V = -0.39)

* E_s = 200,000 MPa; $E_0 = 5000\sqrt{f'_c}$ MPa; ρ_l = Percentage of longitudinal steel; ρ_t = Percentage of transverse steel; H = Applied normal force; V = Applied shear force

6.2.2 Finite Element Modelling

The panels are modeled using only one shell element type I (QLC3+RBE) in which one layer of concrete and four smeared steel layers are used to represent concrete material and steel reinforcement meshes, respectively. Figure 6.2(a) shows a panel under shear and biaxial tensile forces. Any other loading type is a special case of this general loading condition. Since three rigid links were provided to stabilize the panel within its plane, the panel is modeled by a simply supported beam as shown in Fig. 6.2 (b). In the mathematical model, the load should be applied at the joints (nodal forces). From equilibrium considerations, the nodal forces corresponding to this load pattern can be obtained as represented in Fig. 6.2(b). The use of only one shell element saves a lot of computational time and reveals the efficiency of the finite element formulation employed in the HODA program.

The panels were analyzed using the HODA program and some of the computational and experimental responses are summarized in Table 6.2. Additional information concerning the behaviour of each panel is presented in the following sections.

Table 6.2: Results for Vecchio-Collins specimens*

Description	PV11	PV16	PV17	PV19	PV23
θ_{exp} (Deg.)	45-45	45-45	-	46-38	45-45
θ_{HODA} (Deg.)	45-46	45-45	-	45-39	42-48
τ_{exp} (MPa)	3.56	2.14	21.4	3.95	8.87
τ_{u1} (MPa)	4.17	2.09	-	5.79	8.02
τ_{u2} (MPa)	4.17	2.09	20.87	4.97	8.02
τ_{u3} (MPa)	3.69	2.05	-	4.17	8.42
τ_{u4} (MPa)	4.17	2.09	20.87	4.97	7.62
τ_{u1} / τ_{exp}	1.17	0.98	-	1.47	0.90
τ_{u2} / τ_{exp}	1.17	0.98	0.98	1.26	0.90
τ_{u3} / τ_{exp}	1.03	0.96	-	1.05	0.95
τ_{u4} / τ_{exp}	1.17	0.98	0.98	1.26	0.85
Failure mode (Experiment)	Yielding long. & trans. steels	Yielding long. & trans. steel	concrete crushing	yielding trans. and concrete crushing	concrete crushing, and bond failure
Failure mode (HODA)	Yielding long. & trans. steels	Yielding long. & trans. steel	concrete crushing	yielding trans. and concrete crushing	concrete crushing, and bond failure

* τ_{exp}= Experimental ultimate shear stress

τ_{u1} = Ultimate shear stress evaluated using the fixed crack model

τ_{u2} = Ultimate shear stress evaluated using the rotating crack model

τ_{u3} = Ultimate shear stress evaluated using the rotating crack model along with Vecchio-Collins failure criterion

τ_{u4} = Ultimate shear stress evaluated using the rotating crack model ignoring tension-stiffening

θ = average orientation of the principal strain/ stress directions for cracked concrete, measured counter-clockwise from the transverse axis

6.2.3 Panel PV11

This panel was heavily reinforced in both the longitudinal and the transverse directions

and subjected to pure shear. This large percentage of steel reinforcement places heavy demands on the concrete and reveals the adequacy of the concrete constitutive model employed. The panel was analyzed using the HODA program by utilizing 25 load steps and a maximum of 15 iterations in each load step. Four different analyses were carried out to examine the effect of each model on the response of the specimen. This includes: fixed crack model, rotating crack model, rotating crack model along with Vecchio-Collins failure criterion in the post cracking regime, and ignoring the tension-stiffening.

It should be noted that one of the assumptions made in developing the HODA program is that perfect bond exists between the concrete and the reinforcing steel. Therefore, under plane stress condition, the local strains and deformations at any point common to both the concrete (in one or more layers) and steel (smeared or idealized embeded bars) are identical. The tension-stiffening phenomenon occuring in reinforced concrete after cracking is taken into consideration using a strain-softening descending branch of the concrete stress-strain curve in tension.

The resulting longitudinal, transverse and shear strains versus the applied shear stress are plotted in Figures 6.3(a), (b) and (c), respectively. The cracking of the specimen initiated at a shear strength of 1 .6 MPa which is very close to the experimental result of 1.66 MPa. The first three models are very close to each other and to the experimental results. Because of slightly different steel reinforcement in longitudinal and transverse directions, the rotation of principal axis after cracking of concrete has a very slight deviation from 45° (45°-46°), which is the same as what was reported from the experiment. This is the main reason why the results of the fixed and rotating crack models are very close to each other. The model with no tension-stiffening capability for concrete, exhibits more flexible response after the initiation of cracking and is far from the experimental response. This shows that the bond between steel and concrete plays an important role in the response of this panel.

Finally, the panel failed because of yielding of both the longitudinal and the transverse reinforcements which is in complete agreement with the results reported by Vecchio and Collins (1982). After yielding of the reinforcement at a shear stress of 3.42 MPa, the model with no tension-stiffening exhibits the same response as the other models, because up to that stage of loading for all models, concrete undergoes large strains and the specimen develops a considerable number of cracks so that the bond between the concrete and the steel reinforcement is almost completely lost and the response is governed by the steel reinforcement which is the same for all of the models. The ultimate load resulting from the fixed, rotating and no tension-stiffening

models are identical and show a deviation of +17% from the experimental ultimate load, while the accommodation of the Vecchio-Collins failure criterion in the post-cracking region results in a brittle failure with an ultimate load which is +3% different from the experimental value (see Table 6.2).

6.2.4 Panel PV16

The panel PV16 is reinforced isotropically in the two directions with relatively small amounts of reinforcement ($\rho_l = \rho_t = 0.74$ %). This specimen is also subjected to pure shear. It is analyzed using the HODA program using 20 load steps and a maximum of 15 iterations in each load steps to meet the convergence requirements. Four different analyses as outlined for panel PV11 are carried out and the corresponding load-strain curves are shown in Fig. 6.4(a), (b) and (c).

The initial cracking is observed at a shear strength of 1.09 MPa which is quite close to the experimental value of 1.07 MPa as shown in Fig. 6.4. The first three models (fixed, rotating, and rotating & Vecchio-Collins) exhibit the same responses, but the model employing the Vecchio-Collins failure criterion in the post-cracking regime failed earlier in a brittle manner. If the tension-stiffening is ignored, a portion of strength of the structure resulting from bond action between concrete and steel is destroyed and the structure behaves in a more flexible manner. This, in turn, leads to yielding of the reinforcement at an early stage of loading as can be seen in Fig. 6.4 for the model with no tension-stiffening. The steel reinforcement in both directions yielded at an applied shear stress of 2.01 MPa for the models with tension-stiffening, and at a shear stress of 1.9 MPa for the model with no tension-stiffening.

Since the steel contents in both directions are the same, no rotation of principal axis after cracking of concrete is seen, and the principal angle remains constant at a value of 45°. Therefore, no difference between the results using the fixed and rotating crack models was noted (see Fig. 6.4). The panel failed by yielding of the steel reinforcements in both longitudinal and transverse directions which is in perfect agreement with the experimental observation. The analytical ultimate load resulting from all models are very close to the experimental value of 2.14 MPa. The ultimate loads predicted by the fixed, rotating and no tension-stiffening models are identical and deviate by only -2% from the experimental value, while the use of the Vecchio-Collins failure criterion gives an ultimate load which differs by -4% from the experimental value.

6.2.5 Panel PV17

The panel reinforcement pattern was identical to that of the panel PV16, but it was subjected to the uniaxial compression in the longitudinal direction. The panel was analyzed using 20 load steps and a maximum of 15 iterations in each load step. Only two models were used for the analysis, i. e., rotating crack and no tension-stiffening models. During the analysis, no tensile cracking was observed, thus the use of other models would have exhibited no difference in the results.

The variation of the longitudinal compressive strain is plotted against the applied normal stress in Fig. 6.5. This figure clearly shows the capability of the HODA program to analyse this specimen. Up to an applied normal stress of 17.2 MPa, the analytical response follows exactly the experimental response and beyond that a small deviation from the experiment is observed. The response is linear up to a compressive stress of 13 MPa.

Since no crack develops in the specimen, ignoring the tension stiffening has no effect on the response of the structure as can be seen in Fig. 6.5. The panel failed by crushing of concrete in the longitudinal direction which is the same as the experimental finding. The ultimate compressive stress is 20.87 MPa which is slightly different from the experimental value (21.4 MPa), with the discrepancy being -2%.

6.2.6 Panel PV19

Panel PV19 was reinforced heavily in the longitudinal direction (ρ_l=1.78%) and lightly in the transverse direction (ρ_t=0.713%) and it was subjected to pure shear. The panel was analyzed using the HODA program using 25 load steps. The variation of transverse and shear strains versus the applied shear stress are plotted using the four different models along with the corresponding experimental results in Fig. 6.6(a) and (b), respectively.

Cracking in the panel initiated at an applied shear stress of 1.93 MPa which is reasonably close to the corresponding experimental value of 2.07 MPa. After cracking of the concrete, no noticeable change in the crack direction is observed up to a load of 3.2 MPa which is very close to the experimental value of 3.11 MPa. At a load of 3.2 MPa, cracks begin to change direction considerably and the responses resulting from the fixed and the rotating crack models deviate from each other as can be seen in Fig. 6.6(a) and (b). The rotation of principal axis is located within

the interval (45°-39°) which is very close to the experimental interval of (46°-38°).

In the fixed crack model, the principal tensile stresses can be developed at angles not coincident with the original two fixed-orthogonal directions. These stresses can eventually exceed the cracking stress, but no corrective action can be taken using this model and consequently, the numerical solution is usually stiffer than the rotating crack model and the ultimate load is also higher (see Fig. 6.6). The analytical failure load obtained from the fixed crack model deviates by +47% from the experimental value, while the rotating crack model predicts the ultimate load with a discrepancy of +26% (see Table 6.2). If the rotating crack model is combined with the Vecchio-Collins failure criterion in the post-cracking regime, the overall response, more and less, is the same as the rotating crack model, except that the specimen fails earlier in a brittle manner and gives an ultimate load of 4.17 MPa which deviates by only +5% from the experimental value of 3.95 MPa. The rotating crack model predicts the yielding of transverse reinforcement at a load of 3.5 MPa, correlating extremely well with the experimental value of 3.45 MPa. The crushing of concrete is also observed at this stage of loading, followed by stiffening of the response resulting from steel strain-hardening phenomenon. This specimen finally collapses by the crushing of the concrete and the yielding of the transverse reinforcement.

The model with no tension-stiffening reveals more flexible results, but after yielding of reinforcement at a load of 3.5 MPa, it follows generally the response pattern of the model which considers tension-stiffening, because after yielding of the reinforcement, the bond between the concrete and steel is almost completely destroyed, and the response is governed by the tension /compression behaviour of steel reinforcement and/ or the compression behaviour of concrete. The computed ultimate load for this model is the same as for the model which accounts for tension-stiffening (see Fig. 6.6).

6.2.7 Panel PV23

This panel was heavily reinforced in both longitudinal and transverse directions (ρ_l=ρ_t=1.785%) and subjected to a combination of shear and biaxial compression. Four models were used in conjunction with the HODA program to analyze this specimen. The concrete longitudinal, transverse and shear strains are plotted versus the applied shear stress in Figures 6.7(a), (b) and (c), respectively. Because of the high percentage of steel reinforcement in both directions, great demand is placed on the concrete and the general behaviour of the specimen is

governed by the concrete as can be seen in Fig. 6.7.

The panel experiences relatively little tensile straining and the initial cracking occurs at an applied shear stress of 3.2 MPa which is comparable with the experimental value of 3.73 MPa. Since the longitudinal and transverse steel contents are identical, no change in the direction of the principal strain axes and consequently, as expected no difference between the "fixed crack" response and the "rotating crack" response is observed (see Fig. 6.7). The model employing the Vecchio-Collins failure criterion, responds in the same manner as the above-mentioned models up to a shear stress of 6.8 MPa and beyond that it gives a stiffer response which is closer to the experimental response and provides a better prediction for the ultimate load of the structure.

The model with no tension-stiffening, differs significantly from the models which incorporate tension-stiffening. This reveals the importance of the bond between the steel and the concrete on the overall response of this specimen. As mentioned earlier, because of the reinforcement arrangement, as expected, the steel is not dominant in the response of the panel, and it undergoes very small tensile strains which are very far from the yielding strain of 0.0026 [see Fig. 6.7(a) and (b)].

The panel failed by the failure of the concrete in compression which is very close to the experimental observation. The ultimate load predicted by both the fixed and the rotating crack models are under-estimated by -10% from the experimental value (Table 6.2). The use of the Vecchio-Collins failure criterion results in an ultimate load of 8.42 MPa with a difference of only -5% from the experimental value. Eliminating tension-stiffening under-estimates the ultimate load by -15%.The computed longitudinal and transverse strain responses are softer than the experimental response, while the shear strain response is stiffer.

In summary, analysis of the above five panels indicates the effect of the steel reinforcement details in different directions and the type of external applied load on the general behaviour of the structure and its mode of failure. If small amounts of reinforcement are provided in the specimen, more demand is placed on the steel and it undergoes large strains and dominates the final response of the structure. If the same amounts of reinforcement is placed in the two orthogonal directions, the rotation of principal strain axis after cracking is negligible and the results of fixed and rotating crack model are the same. On the other hand, if these two sets of reinforcements are considerably different from each other, the responses of the two models are quite different. The former exhibits a stiffer response and a higher ultimate load than the latter. Generally, the rotating crack model is more realistic than the fixed crack model in predicting the

load-strain relations and the ultimate load of the structure. Use of the Vecchio-Collins failure criterion in the post-cracking regime for all of these panels provides the best response and therefore it is important that it be incorporated in any finite element program to predict the post-cracking response.

6.3 THE SQUAT WALL TESTED BY CARDENAS ET AL. (1980)

6.3.1 Description of the Squat Wall

The rectangular squat wall SW9 with a height-width ratio of one, was tested by Cardenas et al. (1980) to investigate the basic behaviour of reinforced concrete walls under monotonically increasing lateral forces. The overall wall dimensions were 1905mm x 1905mm x 76 mm as shown in Fig. 6.8. The 457mm thick rigid concrete block at the base of the wall was post-tensioned to the laboratory test floor to simulate a rigid foundation. Horizontal loads were applied through an enlarged monolithic section, 305mm x 305mm, which acted as the rigid floor slab. Vertical and horizontal reinforcements were uniformly distributed over the wall. The ratios of the vertical and the horizontal reinforcements were 0.03 and 0.01, respectively. The bar sizes and their spacings are indicated in Fig. 6.9. All reinforcing steel consisted of straight bars and no special hoop reinforcement was provided.

6.3.2 Finite Element Modelling

The wall is divided into 100 rectangular finite elements for analysis using the HODA program (see Fig. 6.10). The enlarged section is represented by 20 elements and the fixed base is modelled by restraining the six degrees of freedom at the nodes along the wall base as shown in Fig. 6.10(a). Plane stress conditions are assumed, and therefore, a finite element consisting of one layer of concrete is sufficient. The horizontal loads are applied at the centre of the enlarged block as horizontal traction along the nodes as indicated in Fig. 6.10 (a). The horizontal and vertical reinforcements are represented by smeared steel layers with thicknesses as indicated in Fig. 6.10 (b) in which t_x and t_y are the thicknesses of smeared steel layers in the x and the y directions, respectively. The material properties of the concrete and the reinforcing steel used are the same as those used in the experiment and are presented in Table 6.3. However, no data was

available for the concrete tensile strength, f'_t, maximum compressive strain, ε_{cu}, ultimate compressive strain, ε_u, steel strain hardening modulus of elsticity, E_s^*, and steel ultimate strain, ε_{su}. The value of ε_{tu} for each mesh size is calculated by the program using the proposed model discussed in Chapter 5 to eliminate the mesh size dependency draw back (Shayanfar et al., 1993).

6.3.3 Response of the Squat Wall SW9

The analytical and experimental load-deflection curves for the squat wall SW9 are presented in Fig. 6.11. The ultimate load predicted by the HODA program is 645 kN, which is only 5% lower than the experimental ultimate load of 678 kN. The initiation of cracks predicted by the analytical model occurs at a load of 140 kN. Unfortunately, the experimental cracking load is not available for comparison.

The elastic response of the wall using the SAP90 program is also presented in Fig. 6.11. It is obvious that the elastic analysis can only predict the load-deflection behaviour of the wall before the initiation of cracks. After cracking, the elastic load-deflection curve deviates significantly from the experimental results.

Table 6.3: Material properties for squat wall SW9

SW9	f'_c (MPa)	E_o (MPa)	f'_t (*) (MPa)	ε_{cu}(*)	ε_u(*)
Concrete	43.02	30,000	2.17	0.002	0.003

Steel	f_y (MPa)	E_s (MPa)	E_s^*(*) (MPa)	ε_{su}(*)
Horizontal	448	200,000	4000	0.12
Vertical	413	200,000	4000	0.12

(*) assumed values

Analytical results obtained by Lefas et al. (1990) using nonlinear finite element analysis are also plotted in Fig. 6.11. Although their analysis yields an ultimate load of 670 kN which is very close to the experimental result, the overall response is much stiffer than the experimental results. The initial response of the wall is, in fact, very close to the response obtained by the HODA program. But after initiation of cracking at a load level of 190 kN, it deviates considerably from the experimental results and the computed results using the HODA program.

It can be observed from the load-deflection curves shown in Fig. 6.11 that the analytical responses exhibit stiffer behaviour than the experimental response at load levels below 140 kN which is the cracking load. It is very difficult to attribute this increased stiffness to any single parameter, but it is likely to be caused by the higher initial tangent modulus for the concrete assumed in the analysis. Since the initial modulus of elasticity of the concrete was not reported in the experiment, the initial tangent modulus is obtained from the empirical formula in the CSA Standard A23.3-M84, which is an approximation to scattered experimental results, and the accuracy of the values cannot be ascertained. However, upon the initiation of cracks, the stiffness of the wall decreases significantly and the load-deflection curve follows the experimental response closely until the failure of the wall.

The propagation of the cracks in the wall obtained from the HODA program is presented in Fig. 6.12. The first set of cracks appear, with a slight inclination, at the outermost tension fibres of the wall at a load level of 140 kN as shown in Fig. 6.12 (a). Unfortunately, the experimental crack pattern is not available for this load stage. Further loading caused cracking to continue to spread at a small inclination toward the compression zone near the base of wall. The crack pattern at load level 610 kN, which is one load stage before the failure of the wall, is presented in Fig. 6.12(b). The compressive forces transmitted through the diagonal concrete struts can also be visualized from the crack patterns. Local crushing of the concrete occurs eventually in the compression zone under the diagonal compression struts at a load of 645 kN. The experimental crack pattern at failure is also presented in Fig. 6.12(c). As can be observed, the analytical crack pattern agrees quite well with the experimental crack pattern. Generally, the analytical response of the squat wall analyzed using the HODA program, including the load-deflection characteristics, the ultimate load carrying capacity and the crack pattern of the structure agree quite closely with the experimental response.

6.4 HIGH STRENGTH CONCRETE BEAMS

6.4.1 Description of the High Strength Concrete Beams

Twelve under-reinforced rectangular beams with f'_c ranging between 64 to 81 MPa were tested by Leslie et al. (1976) to examine the use of a triangular stress block in preference to the currently used rectangular stress block (from the ACI Building Code) for concrete strengths exceeding 55 MPa. Among these beams, a simply supported high-strength reinforced concrete beam, LS1 (designated as "9.0-1" in the paper in which the first number indicates the cement contents in sacks/cu. yd. and the second number shows the nominal percentage of the longitudinal reinforcement) is investigated in this study. The beam was 203 × 305 mm in cross-section and it was supported over a clear span of 2134 mm (see Fig. 6.13). It was subjected to two concentrated third-point loads. The details of the reinforcement layout and the geometry of the beam are shown in Fig. 6.13. The material properties of the concrete and the steel reinforcement are given in Table 6.4.

In another research program conducted at McGill University, six normal and high strength concrete beams were tested by Abrishami et al. (1995) to investigate the effect of epoxy-coated reinforcement on the flexural behaviour of the normal and high strength concrete beams. The high strength reinforced concrete beam HUCB with no epoxy coating on the steel reinforcement is used in this study to investigate the basic behaviour of high-strength reinforced concrete beams. It is a simply supported beam subjected to two monotonically increasing applied concentrated loads as shown in Fig. 6.14. Both beams were 400 mm deep, 200 mm wide and have a clear span of 4500 mm. The beams were simply supported, singly reinforced and without any shear reinforcement. The details of reinforcement layout and the geometry of the beams are shown in Fig. 6.14. The material properties of the concrete and the steels are given in Table 6.4.

6.4.2 Finite Element Modelling

Because of symmetry of load and geometry of the beam LS1, only one-half of the beam is modelled in the finite element idealization. The beam LS1 is discretized into 14 shell elements as illustrated in Fig. 6.15. The Quadrilateral shell element (QLC3), an inplane membrane element, with 3 degrees of freedom per node (u, v, θ_z), and the rectangular bending element (RBE) with

3 degrees of freedom per node (θ_x, θ_y, w) are used. Plane stress conditions are assumed, and therefore, only one layer of concrete is sufficient. The longitudinal reinforcements are modelled using discrete bar elements and are lumped in single bars at the reference surfaces. The shear reinforcement in the shear spans is modelled as smeared steel layers.

The vertical loads are applied in 30 load steps with smaller increments of loads being applied just before the beam reaches its ultimate load stage. This would improve the rate of convergence of the solution and the accuracy in predicting the failure load.

Table 6.4: Sectional Details and Material Properties

Dimension and Material Property	Beam LS1	Beam HUCB
h (mm)	305	400
b (mm)	210	200
d (mm)	270	340
L (mm)	2280	4500
A_s (mm^2)	570	600
f'_c (MPa)	73.2	90.0
E_o (MPa)	30,000	34,000
ε_{cu}	0.002	0.0031
ε_u (*)	0.004	0.0034
f'_t (MPa)	2.82	3.13
f_y (MPa)	415	400
E_s (MPa)	200,000	200,000
ε_{sy}	0.0021	0.002
ε_{su}	0.06	0.075

* Assumed value

Since both the load and geometry of the beam HUCB are symmetric, only one-half of the beam is modelled using 20 quadrilateral shell elements as shown in Fig. 6.16. Plane stress conditions are assumed, and therefore, only one layer of concrete element is sufficient. The longitudinal reinforcement is lumped in a single discrete bar at the reference surface. The vertical loads are applied in 30 load steps with smaller increments of loads being applied just before the beam reaches its ultimate load stage. During the analyses in this section, the Popovics' equation is used to represent the uniaxial concrete stress-strain curve and the rotating crack model is also used for crack modelling.

6.4.3 Computed Response of High Strength Beam LS1

The analytical and experimental load-deflection curves for the beam LS1 are plotted in Fig. 6.17. The model, with no mesh dependency, in which the ultimate tensile strain of the concrete, ε_{tu}, is set to a constant value of 0.003, exhibits very stiff response, however, it predicts the ultimate load capacity of the specimen very accurately with a difference of only 0.1%. The model incorporating the proposed model to eliminate the mesh dependency gives a relatively softer response closer to the experimental results but it under-estimates the ultimate load carrying capacity of the structure by 10% (see Fig. 6.17).

Incorporation of a sudden drop of the stress after the tensile strength of concrete has been exceeded [see Fig. 3.12(b)], has a strong effect on the load-deflection response of the beam at early stage of loading after initial cracking of concrete. The various load-deflection, load-concrete compressive strain and load-steel tensile strain curves for beam LS1 are given in Figures 6.18, 6.19 and 6.20, respectively. These curves reveal the effect of the change in the softening branch parameter, γ, on the analytical response of the beam. As can be seen from Fig. 6.18, the load-deflection curves are closer to the experimental results when a smaller value of γ is used. Decreasing the value of the softening branch parameter, γ, is acceptable up to a value of 0.4, but further decrease of γ leads to a softer response than the experimental results at an early stage of loading and under-estimates the ultimate load of the beam significantly, which is not acceptable.

A summary of the response of the beam LS1 at yielding and ultimate stages of loading is given in Table 6.5, which shows the load and the corresponding mid-span deflections at yielding and ultimate stages of loading as well as the ductility ratio and the predicted mode of failure for each model. The displacement ductility ratio is defined as the maximum deflection at

Table 6.5: Summary of the response of beam LS1 at yielding and ultimate stages of loading *

Model	Yielding load		Ultimate load		Ductility ratio ($\mu_\Delta=\Delta_u/\Delta_y$)	Mode of failure
	P_y, kN	Δ_y, mm	P_u, kN	Δ_u, mm		
Experiment	152	6.2	200	27.1	4.36	F
MDEP=1, γ=1.0	188	5.5	196	26.4	4.76	F
MDEP=3, γ=1.0	168	5.8	180	30.0	5.17	F
MDEP=3, γ=0.6	164	5.6	180	25.2	4.40	F
MDEP=3, γ=0.4	172	5.7	176	23.1	4.04	F
MDEP=3, γ=0.0	160	5.8	164	5.8	1.00	F-B

* MDEP= Mesh dependency option, γ= Softening branch parameter, F= Flexural failure, F-B=Flexural yielding followed by diagonal tension and bond failure

failure, Δ_u, divided by deflection at first yielding of reinforcement, Δ_y ($\mu_\Delta=\Delta_u/\Delta_y$). It can be observed that by decreasing the value of softening parameter, γ, the ductility ratio, μ_Δ, decrease and for values of γ, less than 0.4, it does not match with the experimental findings.

In the experimental program, the shear or/ and bond failures were precluded by use of heavy stirrups in the shear spans (Fig. 6.13). This reinforcement detailing led to a flexural failure in which the steel reinforcement yielded first, followed by the crushing of the concrete. Variation of the applied load versus the concrete compressive strain at the outermost compression fibre at the mid-span section is plotted in Fig. 6.19, while the load-steel tensile strain curve at this section is given in Fig. 6.20. These figures show clearly that in the first three models (γ=1.0, 0.6 and 0.4), the yielding of the steel reinforcement is followed by the crushing of the concrete, leading to final failure of the beam. This is a clear evidence of flexural failure of these three models, which is in complete agreement with the experimental results. The model with no tension-stiffening (γ=0.0) exhibits a sudden brittle failure after a nearly linear response as soon as steel reinforcement yields (Figures 6.18, 6.19 and 6.20).

Figures 6.21, 6.22 and 6.23 show the crack patterns for the beam LS1 at the initiation of flexural cracking at a load of 40 kN, at the yielding of the steel reinforcement and at the ultimate load, corresponding to γ values of 1.0, 0.6, 0.4 and 0.0 in the concrete tension stress-strain curve. The values of yielding and ultimate loads are shown in Table 6.5 for different mesh dependency options and different values of γ, the strain softening parameter. For all values of γ, as expected, the cracks initiate at the outer-most tension fiber of the beam and these are oriented vertically. While there are very minor differences in the crack patterns at the yielding and the ultimate loads except near the support region, there are considerable differences in the cracking patterns at the initial cracking load (40 kN). It must be pointed out that the principal stresses are computed at each of the nine Gauss quadrature points in each finite element and if the principal strain exceeds the cracking strain, ε_{cr}, the computer program output indicates cracking at the appropriate Gauss quadrature point(s). Thus the formation of cracks occurs at the cracking strain- the peak point on the tensile stress-strain curve. With the value of γ = 1.0, the tensile strain continues to increase with the value of the tensile stress decreasing linearly. For a tension stress-strain curve with γ=0.0, the tensile stress drops suddenly to zero after cracking. Therefore, there is a maximum dissipation of energy with γ = 1.0, while it is a minimum with γ = 0.0, which explains why with γ = 1.0, the number of cracks at the initial cracking load (40 kN) is a minimum [Fig. 6.21(a)], while with γ = 0.0, this number is a maximum. [Fig. 6.21(d)]. For values of γ = 0.6 and 0.4, the number of cracks is between the two extremes (γ = 1.0 and γ = 0.0) [Figures 6.21(a), (b) and (c)]. Unfortunately, the experimental cracking pattern was not available, and therefore a direct comparison is not possible.

An examination of Table 6.5 and Figures 6.22 and 6.23, shows that consideration of tension-stiffening with increasing values of γ, results in a gradual increase in the energy dissipated at the ultimate load. Consequently, the ultimate load and the maximum deflection at this stage are considerably higher for γ = 1.0 than for γ = 0.0 with intermediate values for γ = 0.6 and γ = 0.4. As discussed earlier, the model with γ = 0.0 exhibited a sudden brittle failure when the steel reinforcement just yielded, resulting in a ductility ratio of only 1.0.

6.4.3 Computed Response of High Strength Beam HUCB

The load-deflection curves for the beam HUCB are plotted in Fig. 6.24. The proposed model for mesh dependency analysis is incorporated for all of the analyses presented in this section. The model with no stress drop after cracking ($\gamma = 1.0$) exhibits a very stiff response but predicts the ultimate load carrying capacity of the structure with a discrepancy of -7%. This figure shows again that decreasing the value of the softening branch parameter, γ, introduces softer response which is close to the experimental result and this decrease is acceptable up to a value of $\gamma = 0.4$. Further decrease of γ leads to softer response than the experimental one at early stage of loading and also under-estimates the ultimate load by 18% for the model with no tension-stiffening ($\gamma = 0.0$).

A summary of the responses of the beam HUCB is provided in Table 6.6. Based on the results presented in this table, the loads and the ductility ratios for the first three models ($\gamma = 1.0$, 0.6 and 0.4), are very close to the experimental observations. It can be concluded that as the value of γ is decreased, the ductility ratio decreases, and at lower value of γ ($\gamma < 0.4$), it does not correlate properly with the experimental findings.

As pointed out in Section 6.4.1, no shear reinforcement (stirrups) was provided in this specimen to prevent the formation of diagonal cracking in the shear spans (see Fig. 6.14). Therefore, in the experiment, this detailing led to the flexural yielding of reinforcement followed by diagonal tension cracking and bond-splitting failure as reported by Abrishami et al. (1995). Figures 6.25 and 6.26 show the load-concrete compressive strain and the load-steel tensile strain curves for the beam HUCB for the model with γ=0.4. The figures show that steel reinforcement yields first and at failure the concrete compressive strain at outermost compression fibre does not exceed the maximum compressive strain of concrete, ε_{cu}. This is a clear evidence that after the yielding of the steel reinforcement, the concrete does not crush and the failure of the specimen can be attributed to the bond failure as observed in the experiment.

Figure 6.27 presents the crack patterns for the model with γ=0.4 at initial cracking,yielding of the steel reinforcement, and near the ultimate load stage. Almost all of the cracks remain vertical and a few inclined cracks are observed. This is in close agreement with the experimental crack pattern at failure as shown in Fig. 6.27 (d). If the crack patterns shown in Fig. 6.27 are compared with their counter-parts in Figures 6.21(c), 6.22(c) and 6.23(c), it is observed that the crack patterns corresponding to beam HUCB are much narrower than their corresponding

crack patterns for beam LS1. This shows that energy dissipation capacity of the beam LS1 is higher than of the beam HUCB. This conclusion is supported by the fact that no shear reinforcement was provided in beam HUCB.

Table 6.6: Summary of the response of beam HUCB at yielding and ultimate stages of loading *

Model	Yielding load		Ultimate load		Ductility ratio ($\mu_\Delta=\Delta_u/\Delta_y$)	Mode of failure
	P_y, kN	Δ_y, mm	P_u, kN	Δ_u, mm		
Experiment	44.5	21.0	50.8	72.3	3.44	F-B
MDEP=3, γ=1.0	46	16.1	47	60	3.73	F-B
MDEP=3, γ=0.6	42	14.1	47	51.2	3.63	F-B
MDEP=3, γ=0.4	42	14.8	45	44.5	3.01	F-B
MDEP=3, γ=0.0	40	15.3	42	23.6	1.54	F-B

* MDEP= Mesh dependency option, γ= Softening branch parameter,
F-B=Flexural yielding followed by diagonal tension and bond failure

6.5 SHEAR PANEL SUBJECTED TO CYCLIC LOADING

6.5.1 Description of the Shear Panel

The reliability of the proposed material model for cyclic load condition (see Chapter 3) is examined in this section. For this purpose the shear panel W-4 tested by Cervenka (1970) under reversed cyclic loading is undertaken. the panel consisted of of isotropically and orthogonally reinforced square plates 30 x 30 in (764 x 764 mm), and 3 inches (76 mm) in thickness. This shear panel is similar to the shear panel W-2 analyzed in Chapter 5. The details of the reinforcement and the geometry of the panel are shown in Fig. 6.28. As can be seen, these two panels were combined to form one deep beam like specimen. This arrangement enabled easy testing of the beam specimen as a simply supported beam with a central concentrated load. Two square panels were tested simultaneously, although each panel acted independently of the other because of the statically determinate supports. The concentrated forces at the supports and at the

Table 6.7: Material Properties for the Shear Panel W-4

Material Property	Panel W-4 (Imperial Units)	Panel W-4 (SI Units)
f'_c	3,544(psi)	24.5(MPa)
f'_t	512(psi)	3.5(MPa)
E_o	2,900,000(psi)	20,000(MPa)
ε_{cu}	0.0025	0.0025
ε_u (*)	0.004	0.004
f_y	51,200(psi)	353(MPa)
E_s	27,300,000(psi)	188,000(MPa)
ε_{sy}	0.0019	0.0019
ε_{su}(*)	0.10	0.10

* Assumed value

load point were transmitted to the panels by three vertical ribs as shown in Fig. 6.28. These ribs also helped to maintain the lateral stability of the specimens during the testing program. The material properties of the concrete and the steel reinforcement are given in Table 6.7.

In the following discussion, a cycle consists of loading and then unloading in a single direction. For vertical loading, if the direction of the load is up-ward, the corresponding cycle is called "positive", and if it is down-ward, the cycle is referred to as "negative". During the test program, for the positive cycles, the support at mid-rib was fixed and the load was applied by the load cells at the the two end-ribs, while for the negative cycles the supports at the two end-ribs were fixed and the load was applied by the load cell at mid-rib.

6.5.2 Finite Element Modelling

Because of symmetry of load and geometry of the shear panel W-4, only one-half of the specimen is considered in the finite element idealization. The panel is discretized into 24 shell elements as shown in Fig. 6.29. The shell element type II which is a combination of the inplane membrane element RQUAD4 with 3 degree of freedoms per node (u, v, Θ_z), and the rectangular

bending element IDKQ with 3 degrees of freedom per node (Θ_x, Θ_y, w) is used to idealize the structure for analysis using the HODA program.

Plane stress conditions are assumed for the panel, therefore, only one layer of concrete is sufficient. The concentrated reinforcement in the ribs is modelled as embeded bar elements and the distributed reinforcement in the web is idealized as two smeared steel layers. The total load is applied at the two points on the outer rib of the structure as shown in Fig. 6.29. The loads are applied in four cycles and each cycle is composed of 30 load steps with a maximum of 15 iterations in each load step. The first cycle is positive and it alternatively becomes positive and negative.

6.4.3 Computed Response of the Shear Panel W-4

During the experimental program (Cervenka, 1970), the panel was initially cycled four times at relatively low load levels. Then it was cycled between ±23 kips (±102 kN) until failure. The load of 23 kips (102 kN) is 90% of the estimated monotonic load carrying capacity of the panel. Finally it failed at a load equal to 88% of the "monotonic" load limit (22.5 kips or 99.7 kN). The first two and a half cycles of the experimentally observed load-deflection response are given in Fig. 6.30.

The load-deflection response of the panel using the proposed cyclic load model, is plotted in Fig. 6.30. The model fails, if it is cycled at a peak load of 23 kips (102 kN) as was the case in the experiment. Darwin and Pecknold (1975) and Rule and Rowlands (1992) also encountered the same problem in their numerical model. This discrepancy could be due to the approximations associated with the constitutive model, under-estimation of the compressive strength of the concrete, f'_c, obtained from the uniaxial testing, and the different curing environments, etc.

For the sake of comparison with the experimental results, the load on the numerical model was cycled between 22.7 kips (100.7 kN) and -18.5 kN (-82 kips). The numerical results for the first two and a half cycles are given in Fig. 6.30. The numerical model exhibit stiffer response at the beginning of the first cycle, but after the initial cracking at the load level of 12 kips (53.2 kN), it softens and match better the experimental response. The displacement corresponding to the peak point in this cycle is 0.14 in (3.6 mm) which is the same as the experimental value. The stiff response at the beginning of the first cycle can be attributed to the initial cycling of the specimen during the experiment as mentioned earlier. Because this initial cycling can dissipate some of the

energy absorbing capacity of the specimen due to cracking and consequently make it softer. In the unloading regime, the stiffness of the model is comparable with the experimental results and it reveals less plastic deformation than the experimental results.

During the second cycle in which the peak point is -18.5 kips (-82 kN), the model traces very closely the experimental response and the yielding of the reinforcement and excessive cracking thereafter is observed at a load of -18.3 kips (81.2 kN). This situation prevented from further increase of loading beyond a value of 82 kN (-18.5 kips) leading to the failure of the specimen. The loading and unloading branches in the second cycle exhibit softer response than their counter-parts in the first cycle. The model shows softer response during the third cycle than the first cycle and follows the experimental curve closely.

The analytical crack patterns of the panel at the peak point of the first three cycles are shown in Figures 6.31(a), (b), and (c). The experimental crack pattern is also given in Fig. 6.31(d). A comparison of the analytical crack patterns with the experimental crack pattern shows that the direction and the position of the computed cracks at positive and negative cycles are very closely correlating with the experimental cracks.

The results presented for the shear panel W-4 verify the reliability of the computer program in handling the nonlinear finite element analysis under reversed cyclic loading. It is obvious that the behaviour of RC structures under cyclic loading involves very complex situations and the models accounting for this condition must be verified versus several specimens. This is beyond the scope of this research program and as a future research program one can concentrate on this aspect of the computer program HODA and examine the proposed cyclic model more comprehensively, and improve its performance by some modifications.

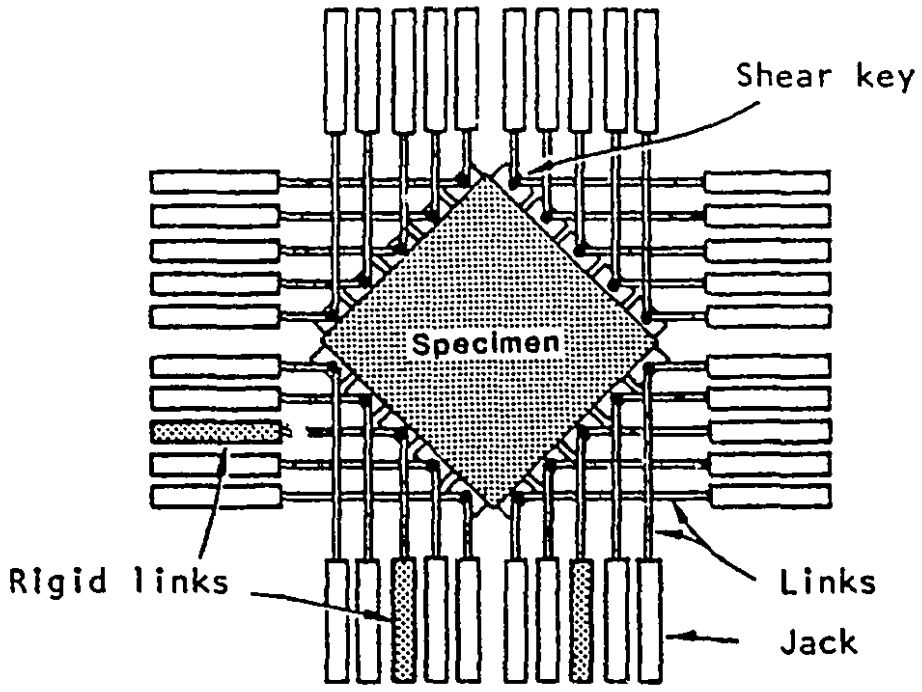

(a)

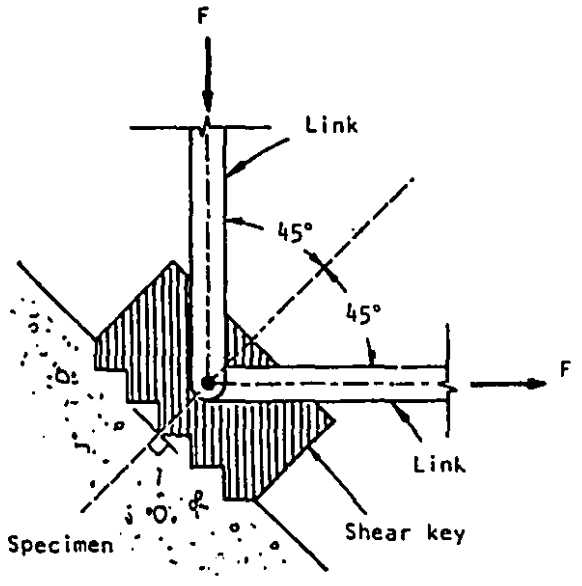

(b)

Figure 6.1: Test set-up for the Vecchio-Collins Panels (Vecchio, 1981)

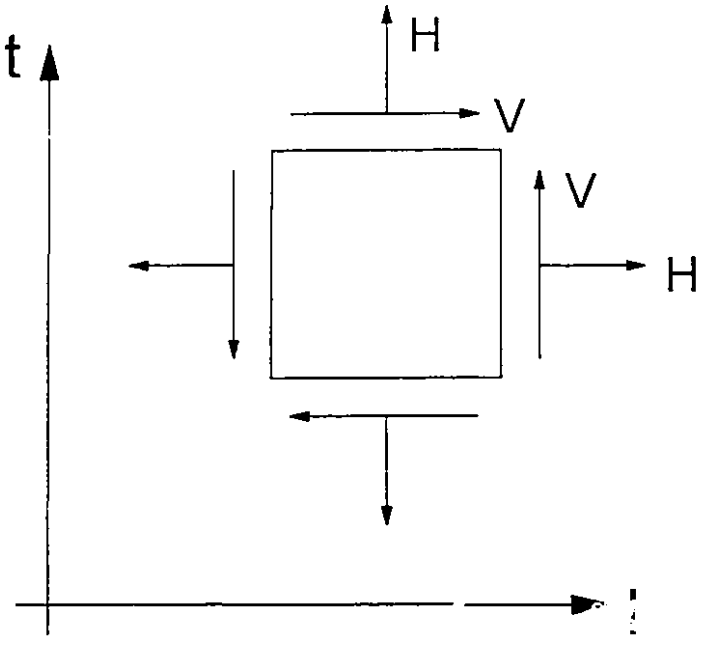

(a)

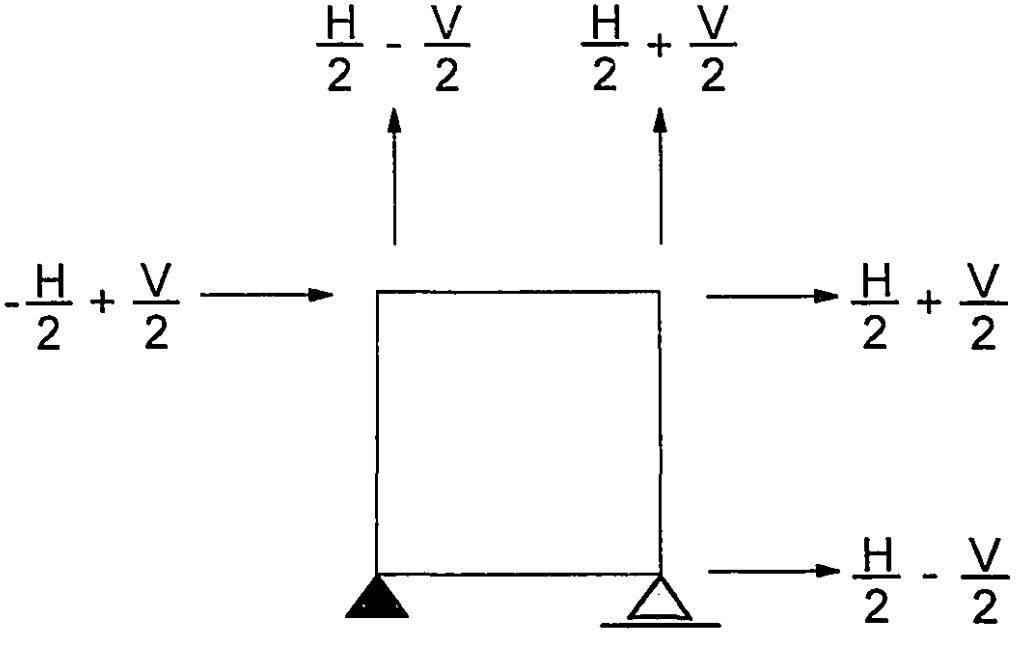

(b)

Figure 6.2: Finite element model for the Vecchio-Collins Panels

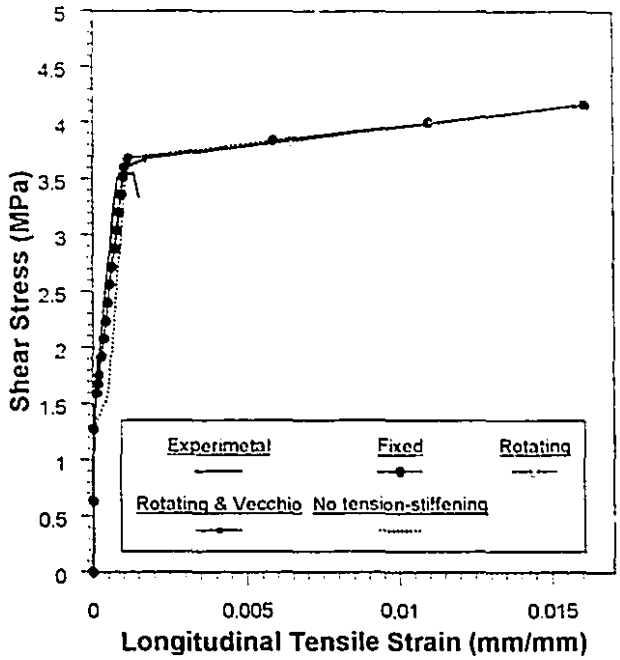

(a)

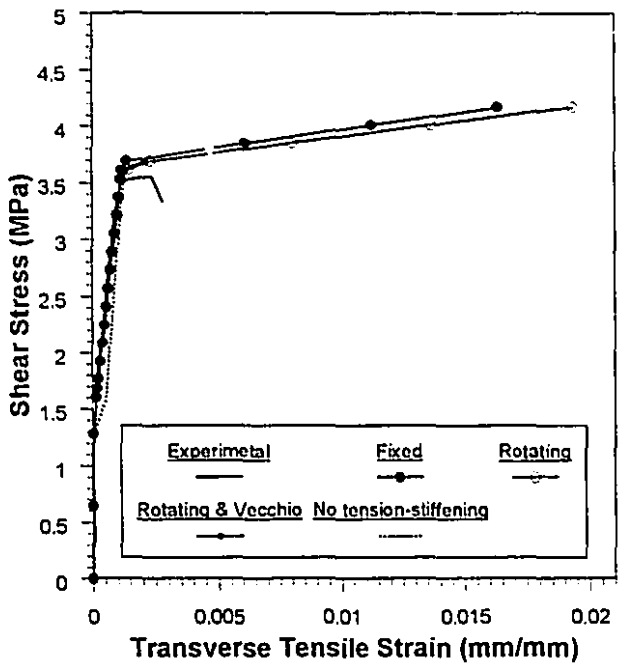

(b)

Figure 6.3: Load-concrete strain curves for panel PV11

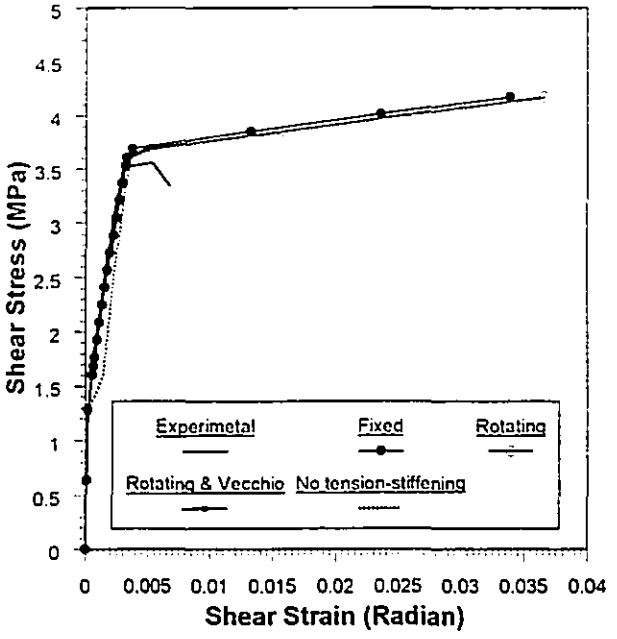

(c)

Figure 6.3(Continued): Load-concrete strain curves for panel PV11

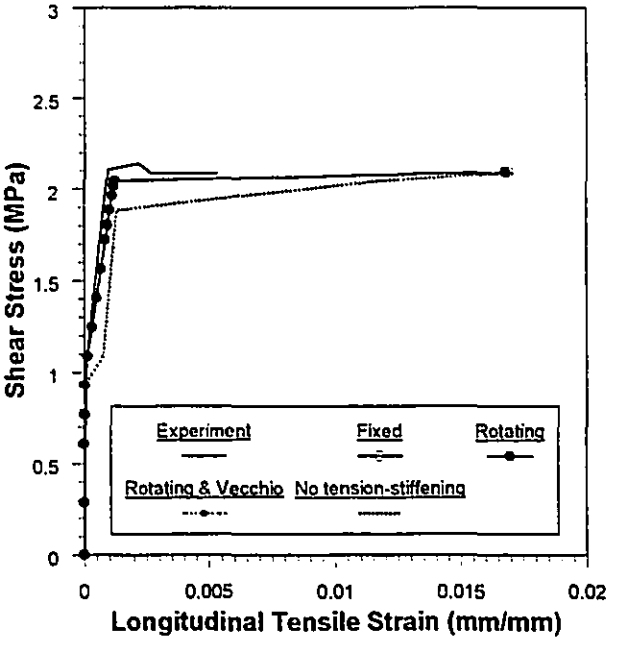

(a)

Figure 6.4: Load-concrete strain curves for panel PV16

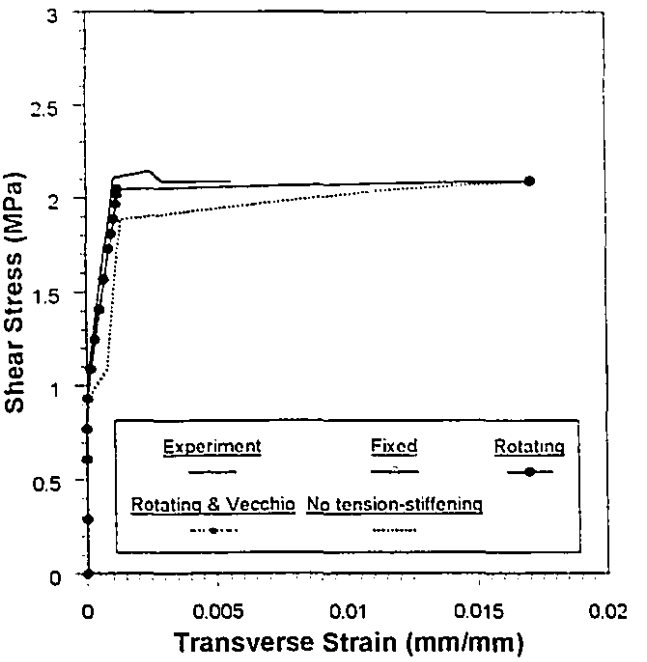

(b)

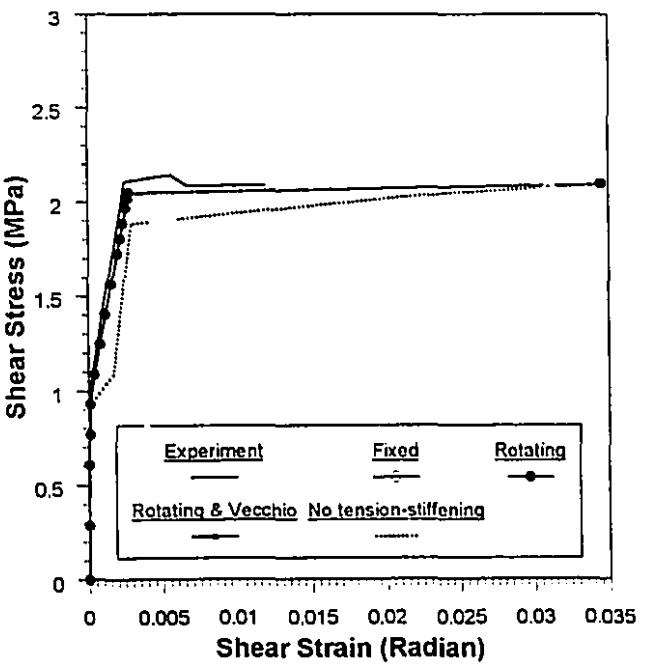

(c)

Figure 6.4(Continued): Load-concrete strain curves for panel PV16

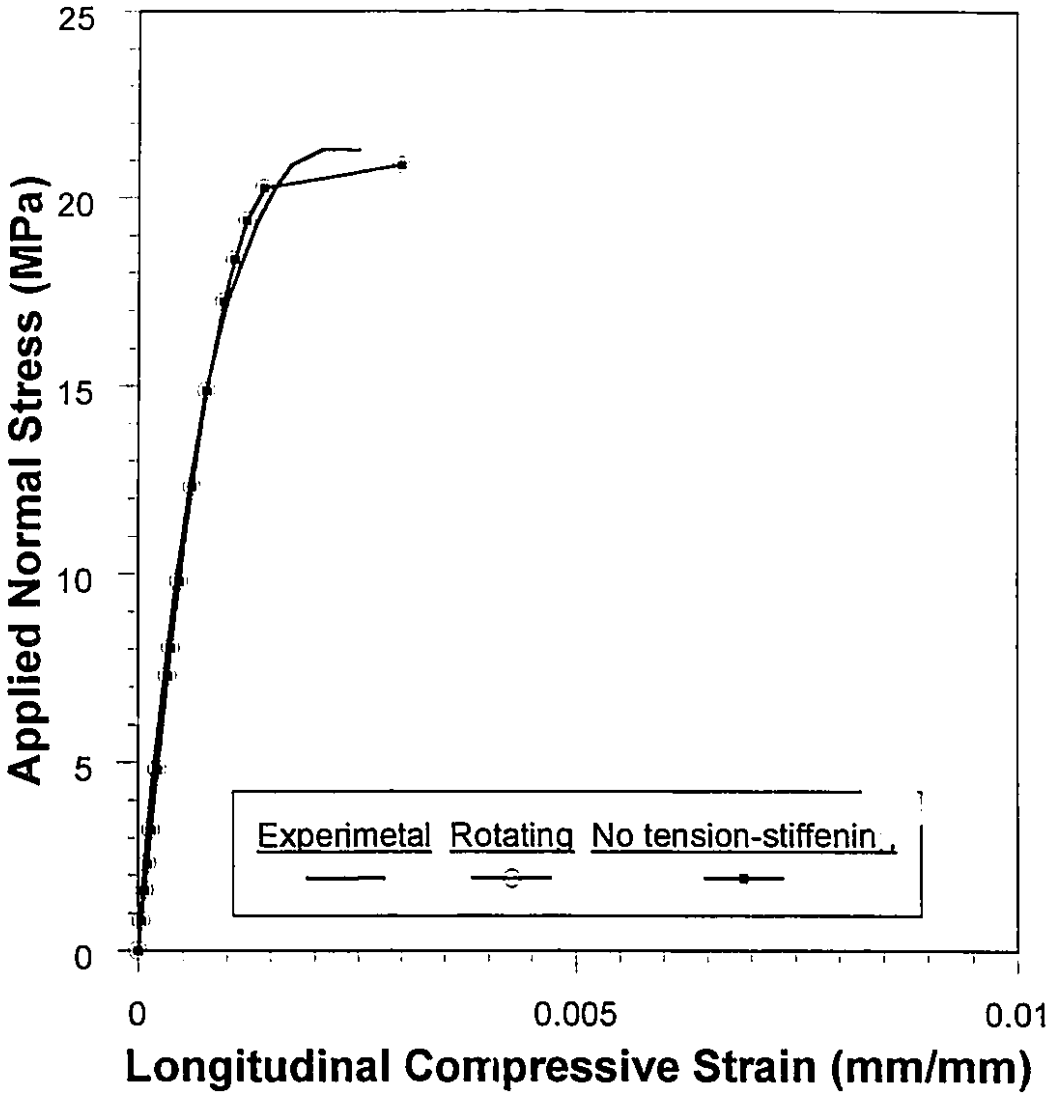

Figure 6.5: Load-concrete compressive strain curve in longitudinal direction for panel PV17

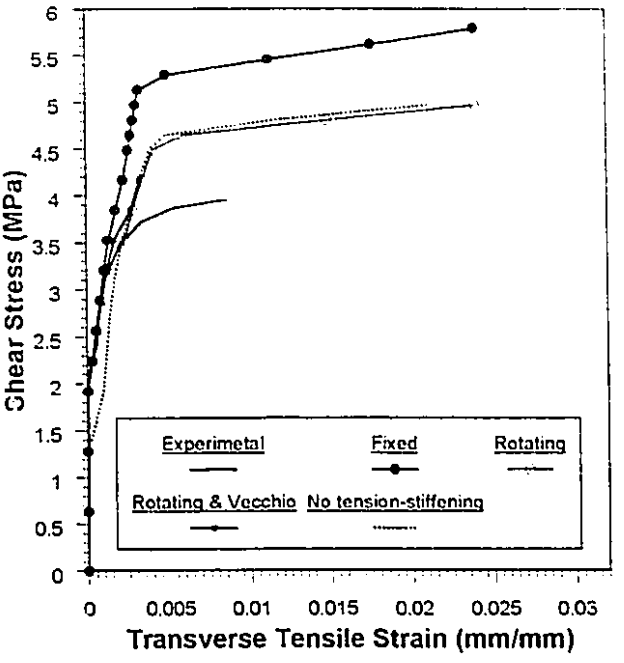

(a)

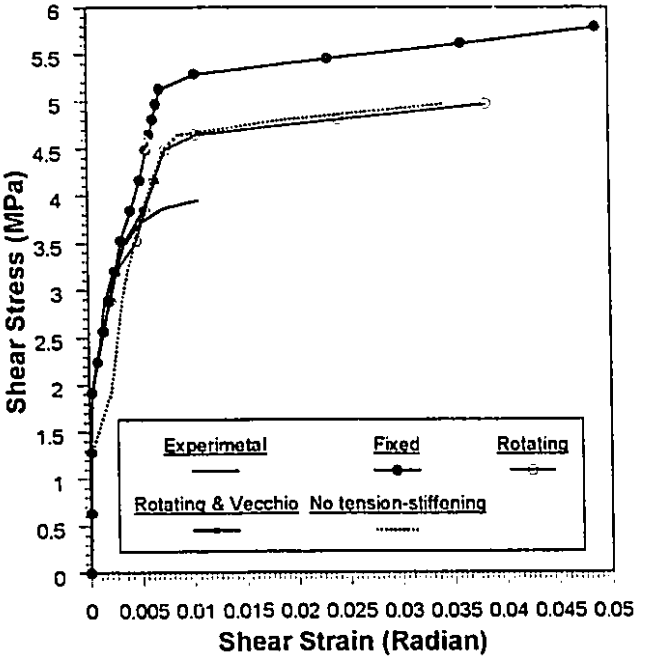

(b)

Figure 6.6: Load-concrete strain curves for panel PV19

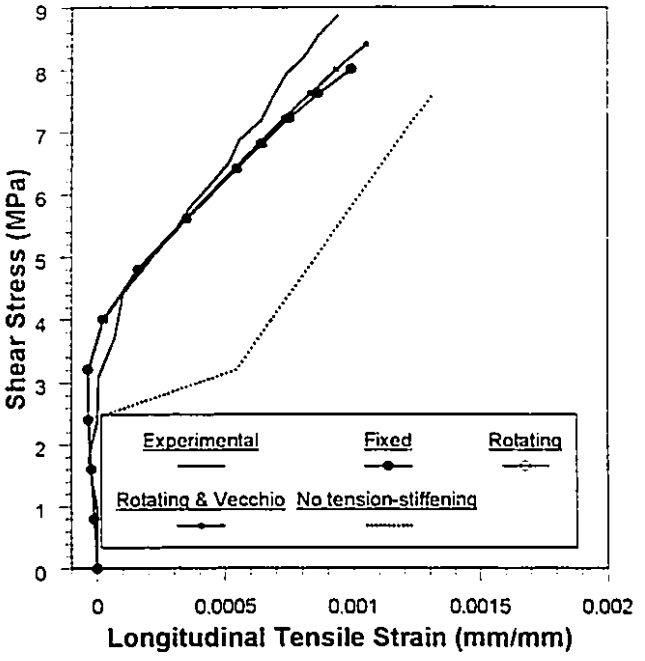

(a)

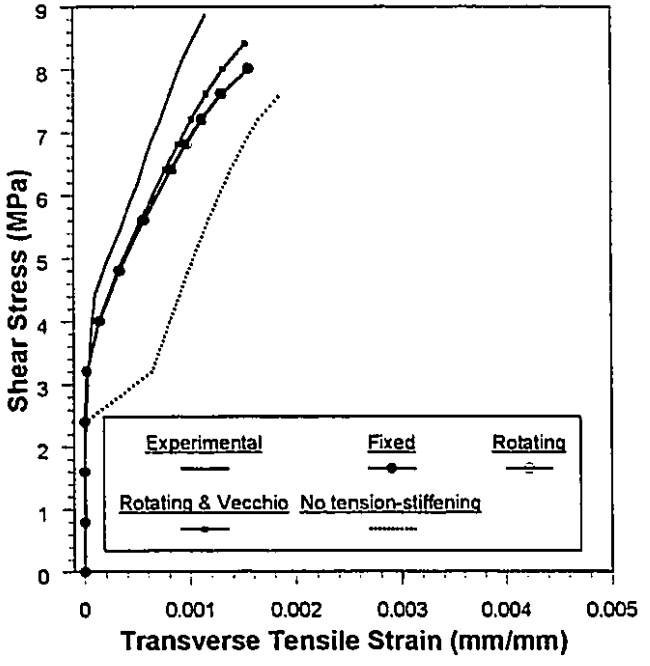

(b)

Figure 6.7: Load-concrete strain curves for panel PV23

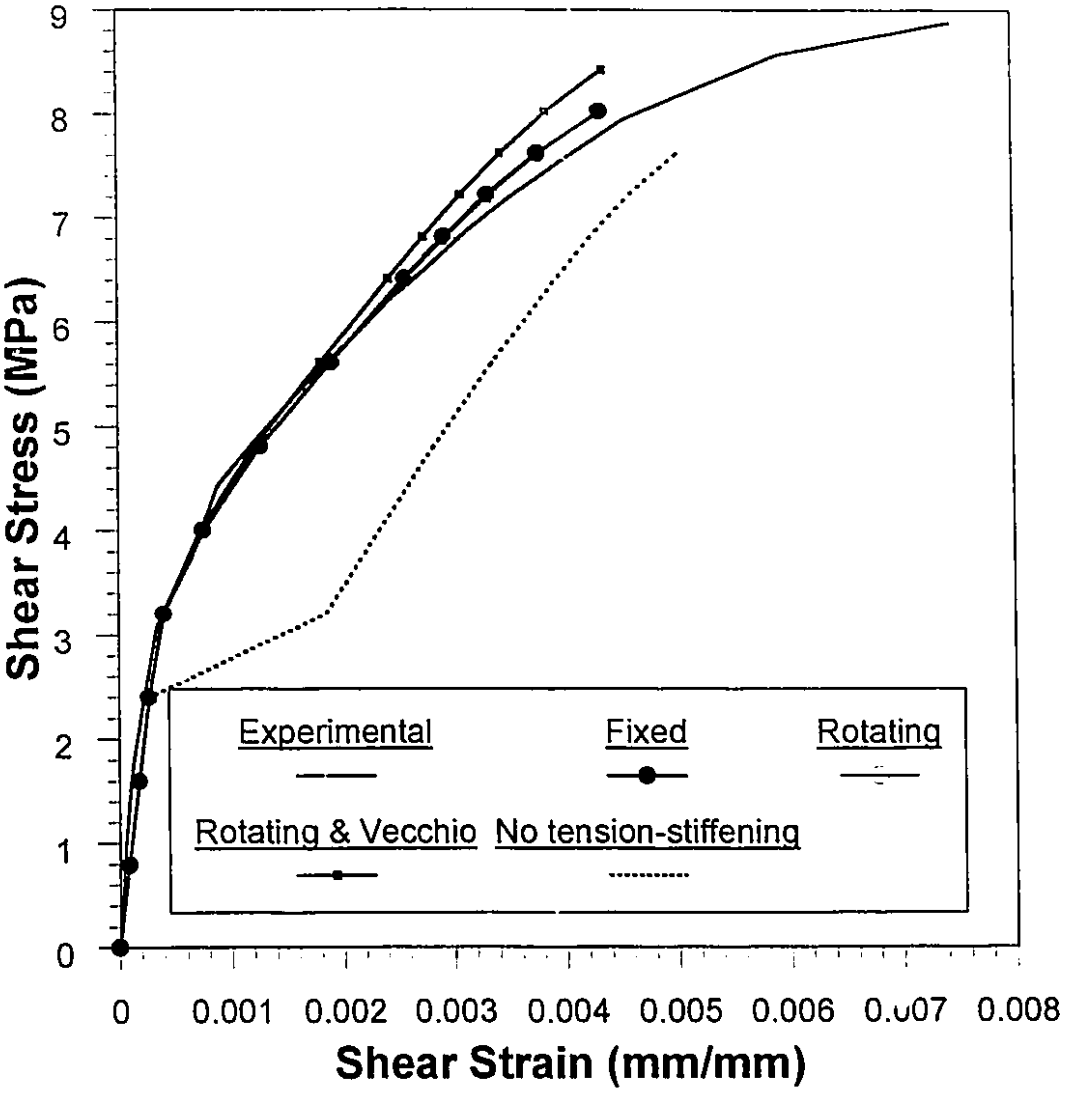

(c)

Figure 6.7(Continued): Load-concrete strain curves for panel PV23

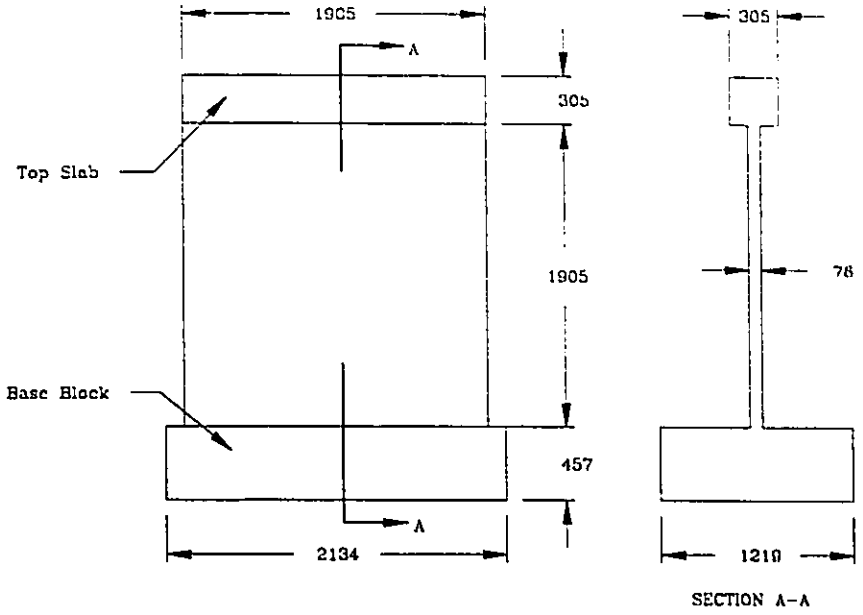

Figure 6.8: Overall dimensions of the squat wall, SW9

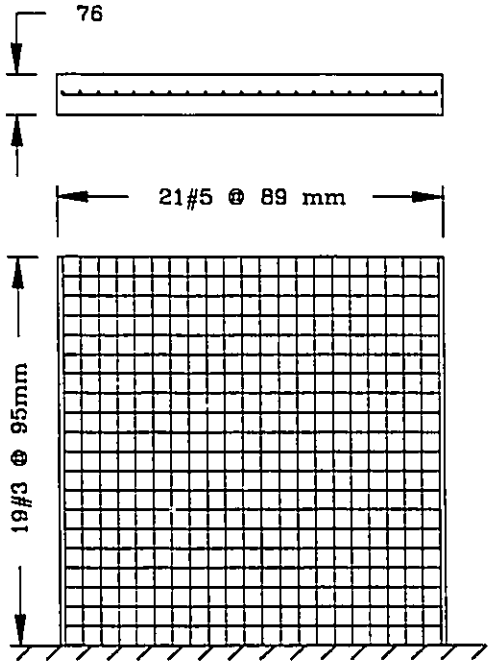

Figure 6.9: Reinforcement arrangement for the squat wall, SW9

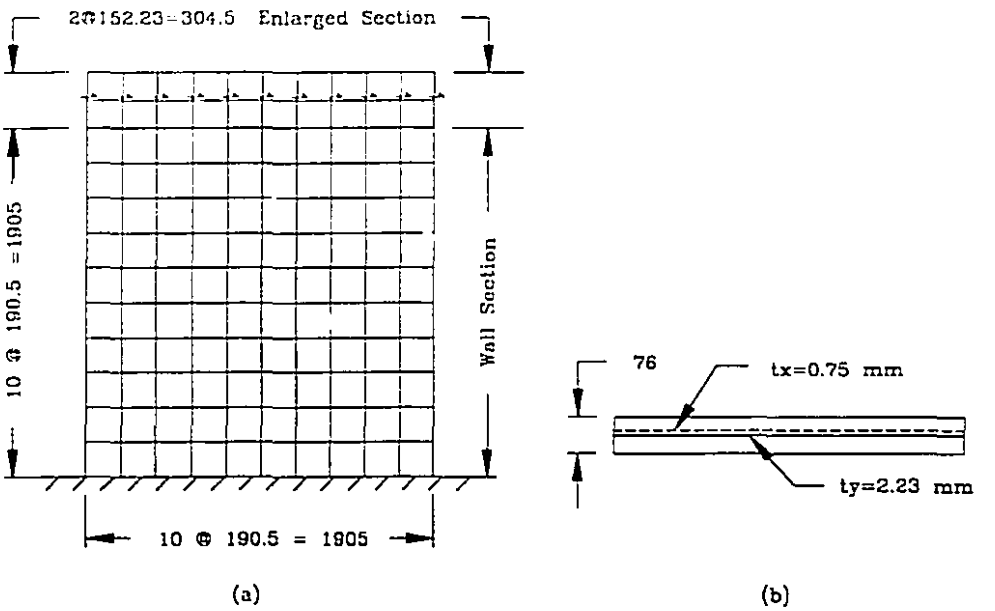

Figure 6.10: Idealization of the squat wall, SW9:
(a) Finite element idealization, (b) Smeared steel idealization

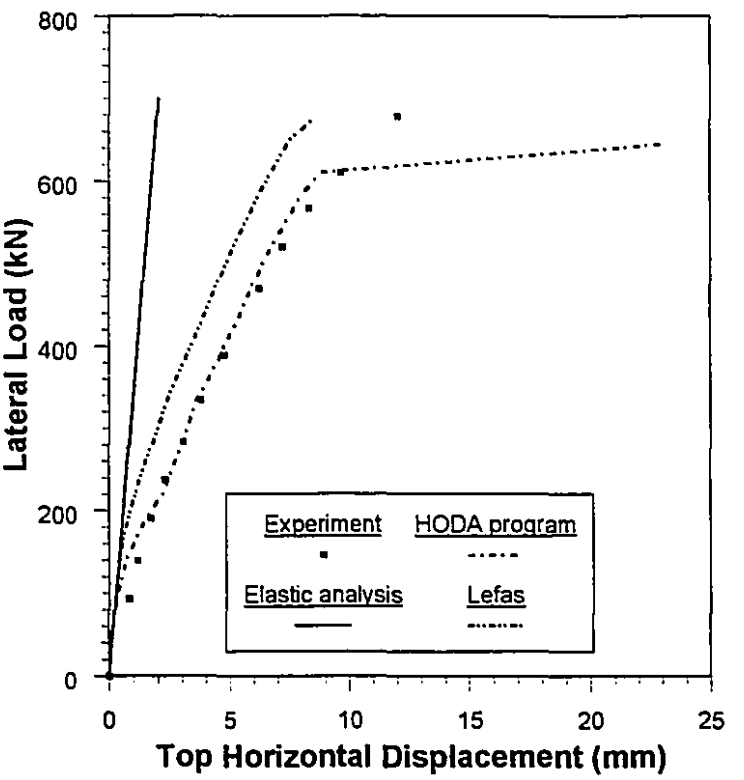

Figure 6.11: Load-deflection curves of the squat wall, SW9

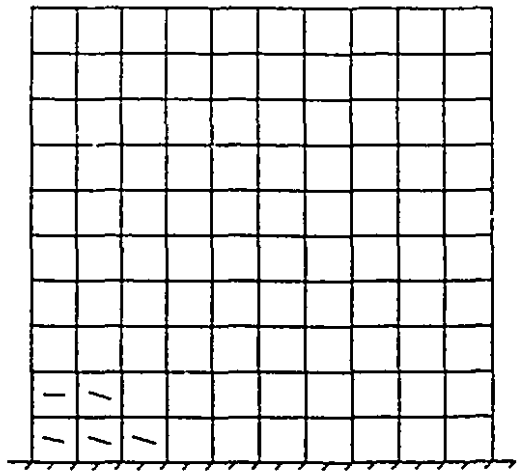

(a) Load Level of 140 kN (Analytical)

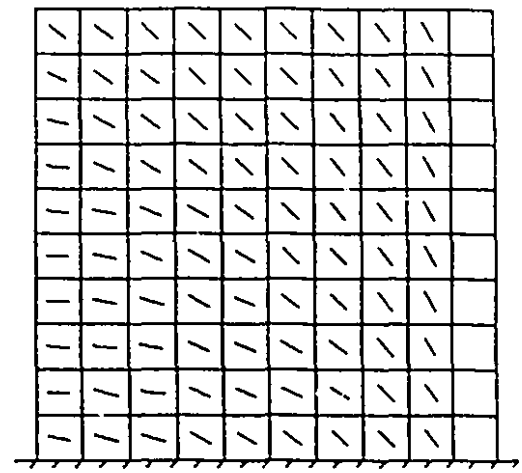

(b) Load Level of 610 kN (Analytical)

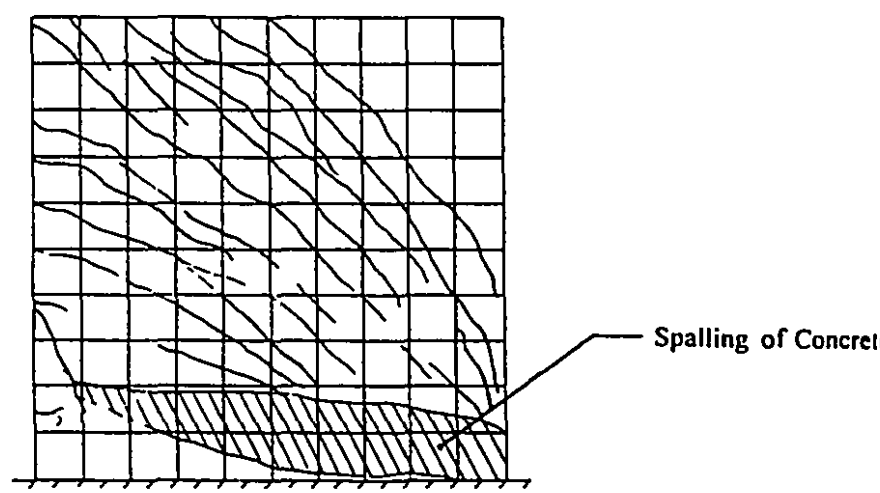

(c) At Failure Load (Experimental)

Figure 6.12: Comparison of the analytical and the experimental crack patterns of the squat wall, SW9

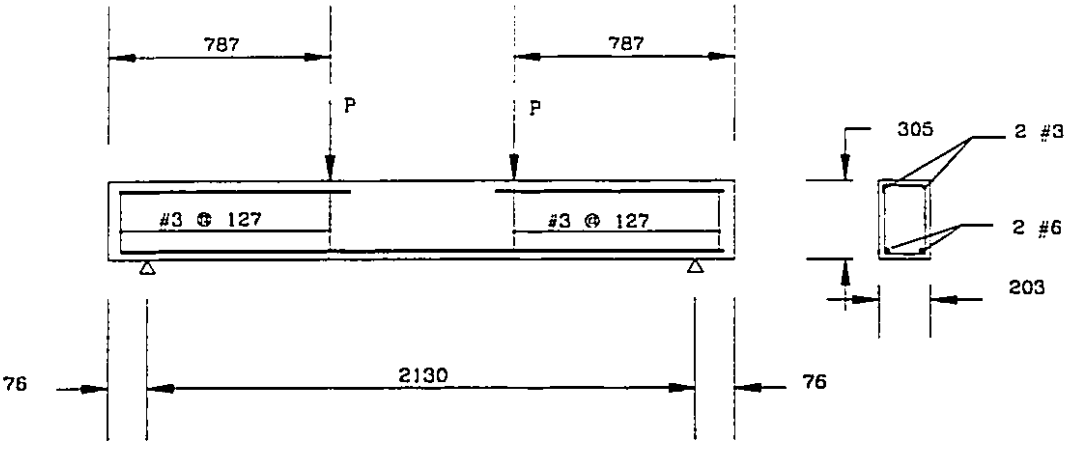

Figure 6.13: Geometry and Reinforcement Details of Beam LS1

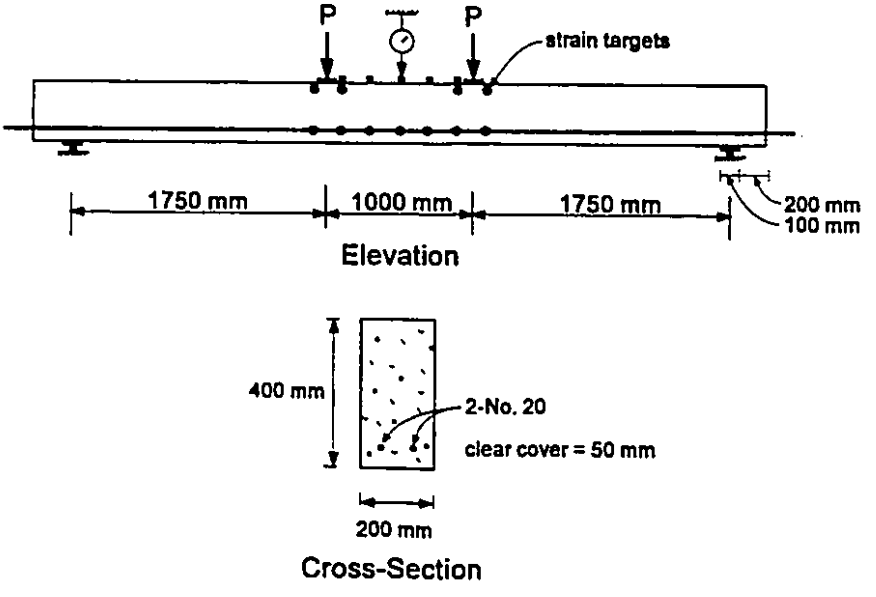

Figure 6.14: Geometry and Reinforcement Details of Beam HUCB (Abrishami et al., 1995)

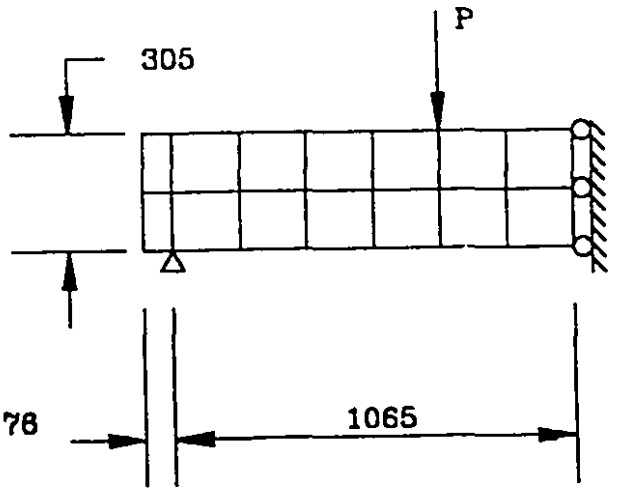

Figure 6.15: Finite element configuration for beam LS1 with 14 elements

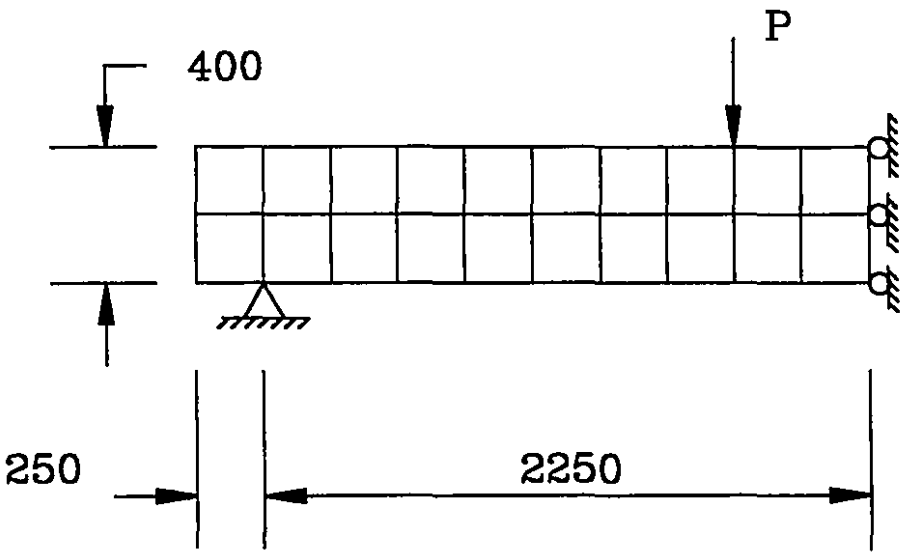

Figure 6.16: Finite element configuration for beam HUCB with 20 elements

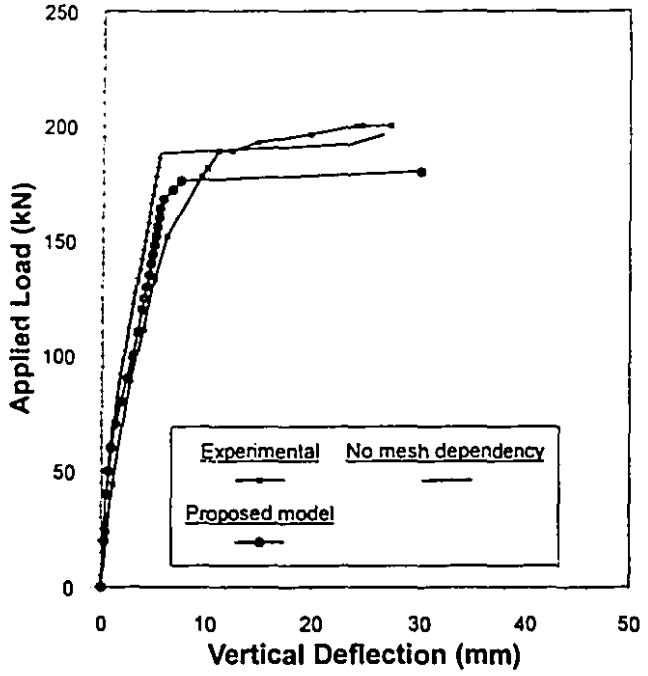

Figure 6.17: Load-deflection curves for beam LS1

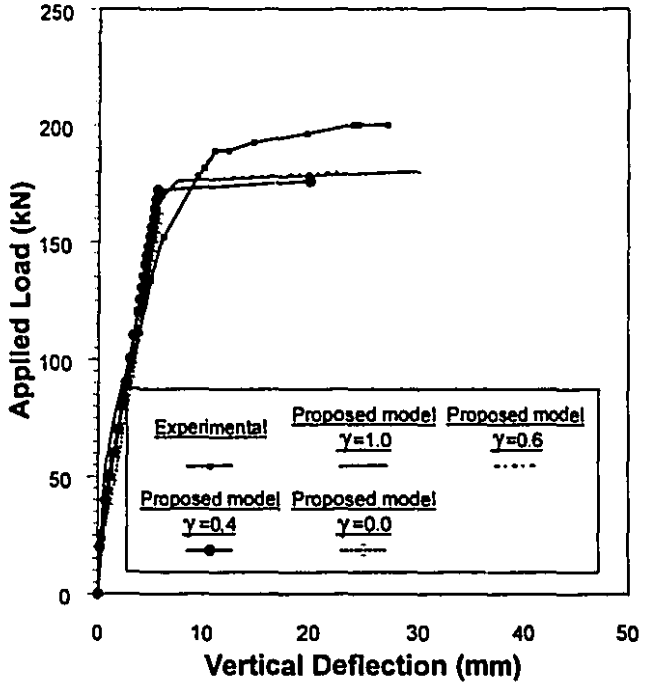

Figure 6.18: Load-deflection curves for beam LS1 using different tensile softening branch models

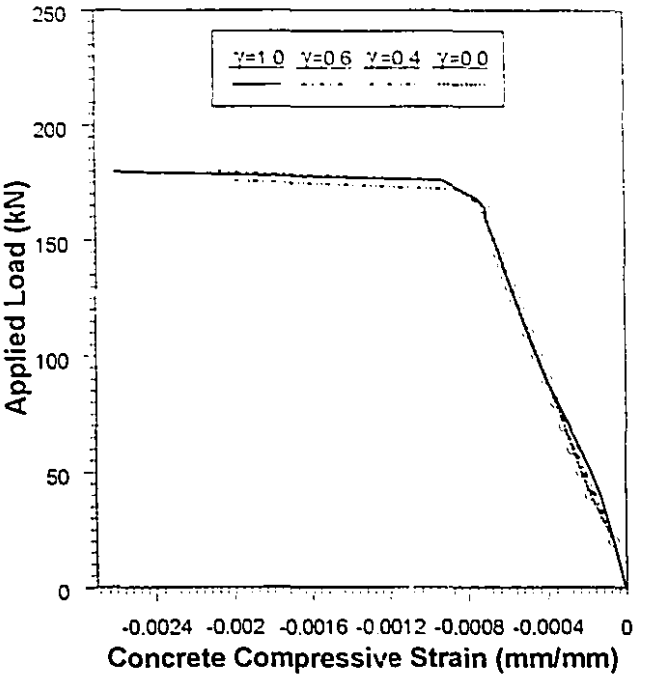

Figure 6.19: Load-concrete compressive strain curves for beam LS1

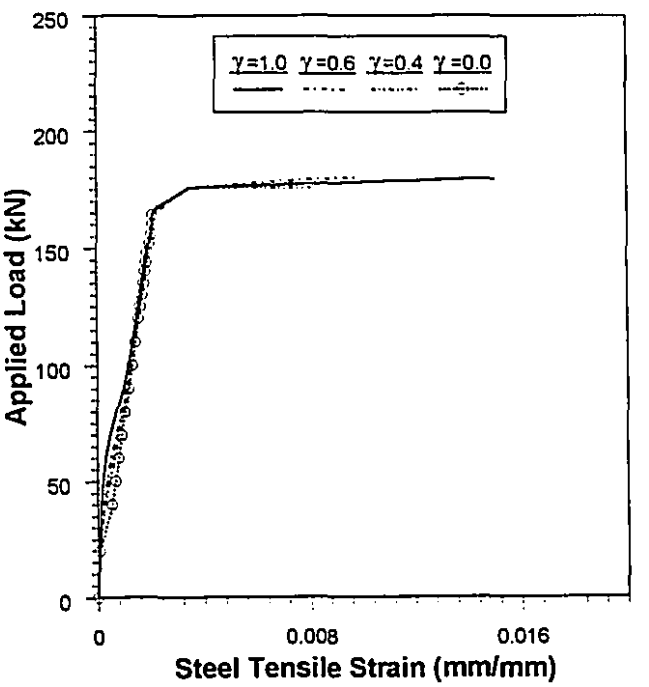

Figure 6.20: Load-steel tensile strain curves for beam LS1

(a) γ=1.0

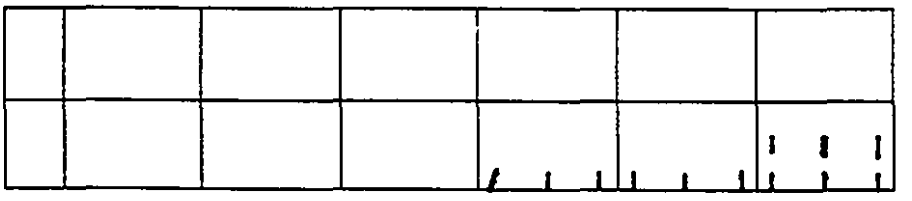

(b) γ=0.6

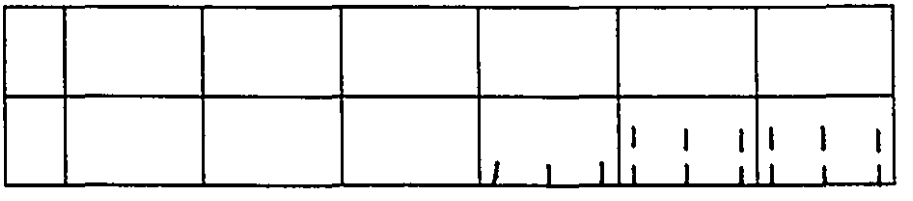

(c) γ=0.4

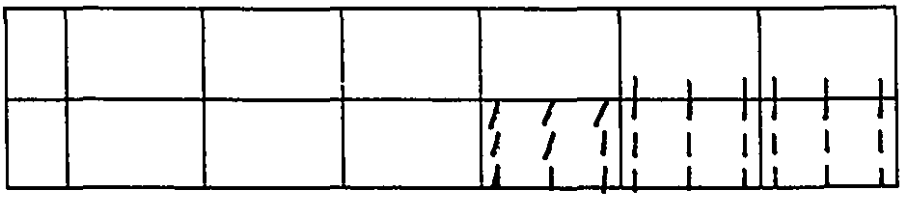

(d) γ=0.0

Figure 6.21: Crack patterns for beam LS1 at initial cracking using different models

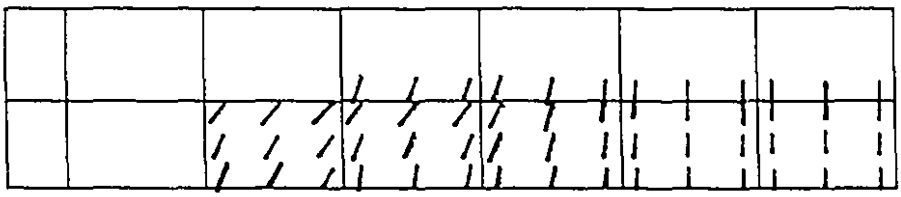

(a) γ=1.0

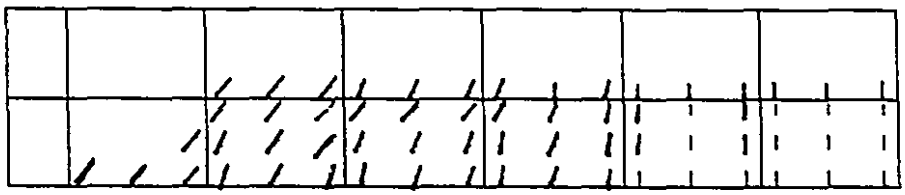

(b) γ=0.6

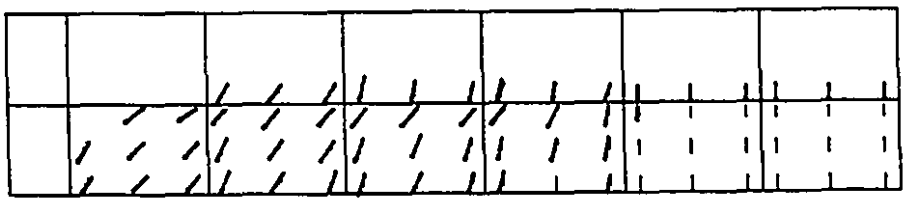

(c) γ=0.4

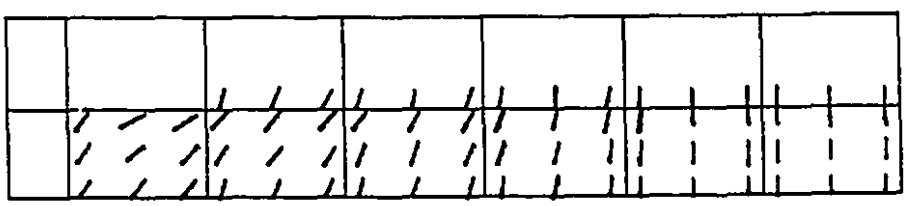

(d) γ=0.0

Figure 6.22: Crack patterns for beam LS1 at initial yielding using different models

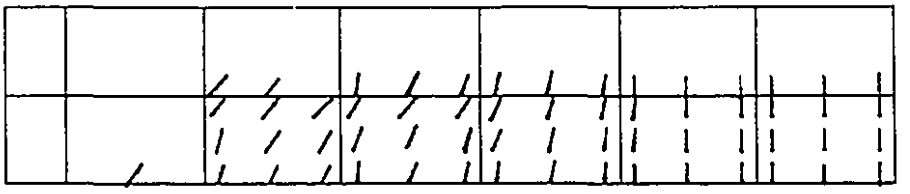

(a) γ=1.0

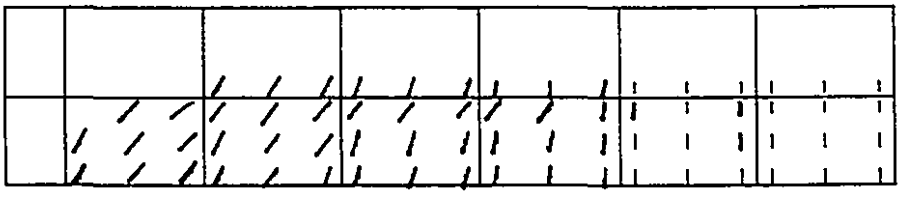

(b) γ=0.6

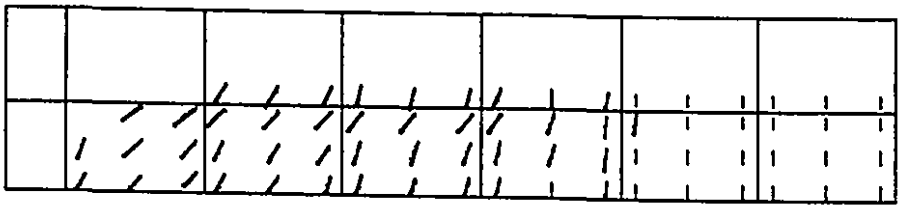

(c) γ=0.4

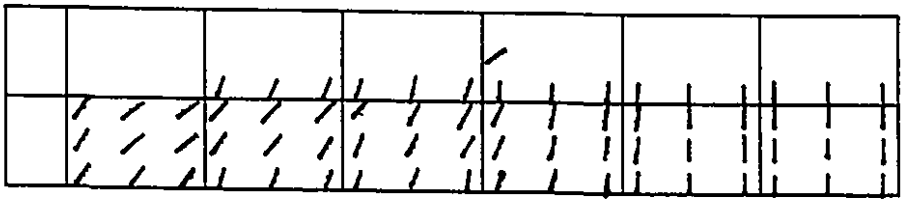

(d) γ=0.0

Figure 6.23: Crack patterns for beam LS1 at failure using different models

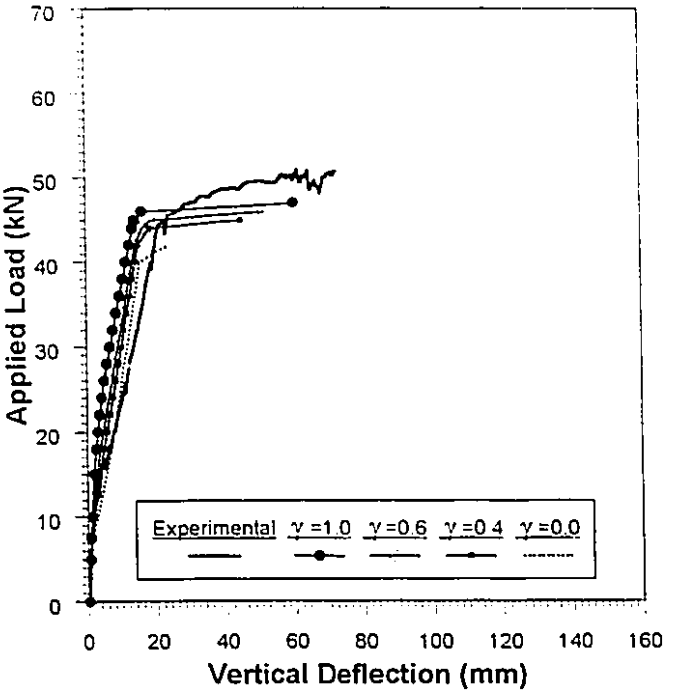

Figure 6.24: Load-deflection curves for beam HUCB using different tensile softening branch models

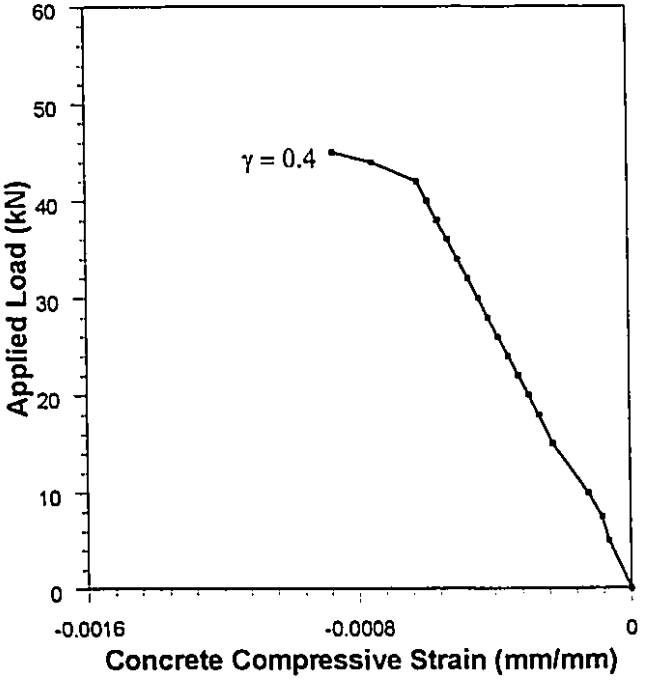

Figure 6.25: Load-concrete compressive strain curves for beam HUCB

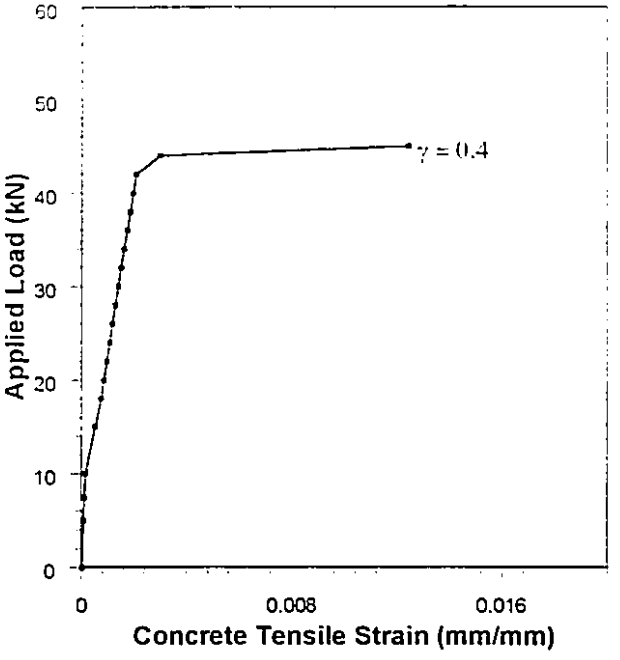

Figure 6.26: Load-steel tensile strain curves for beam HUCB

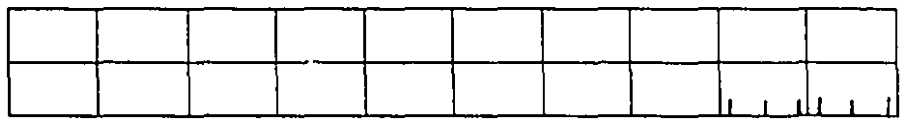

(a) Initial cracking

(b)Initial yielding

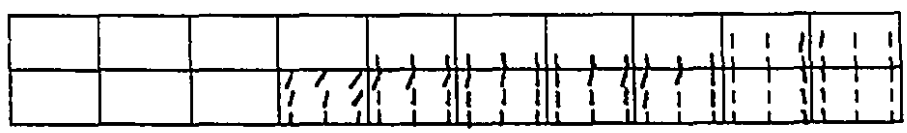

(c) Failure

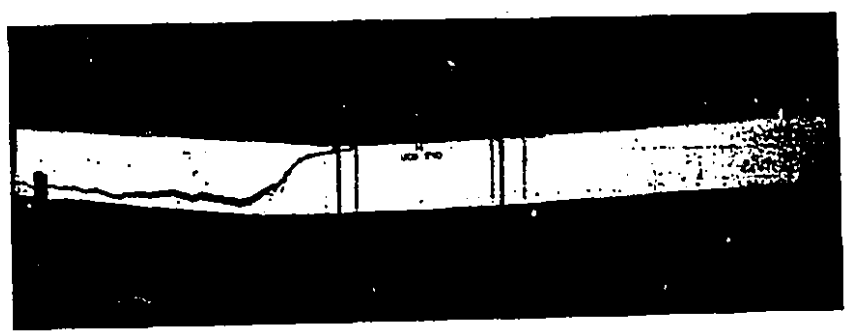

(d) Experiment

Figure 6.27: Crack patterns for beam HUCB with γ=0.4 at different load stages

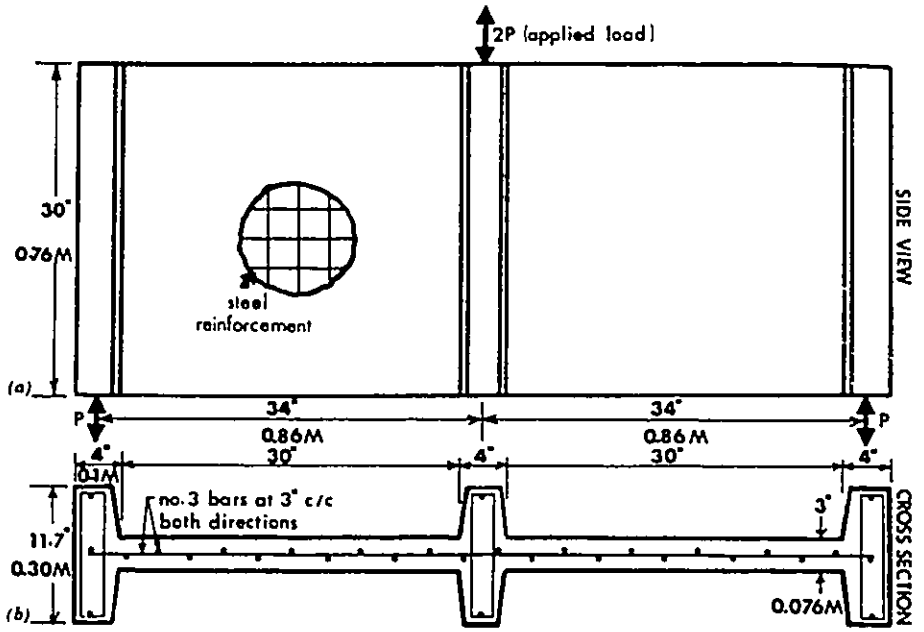

Figure 6.28: Geometry and reinforcement details of the shear panel W-4 (Rule and Rowlands, 1992)

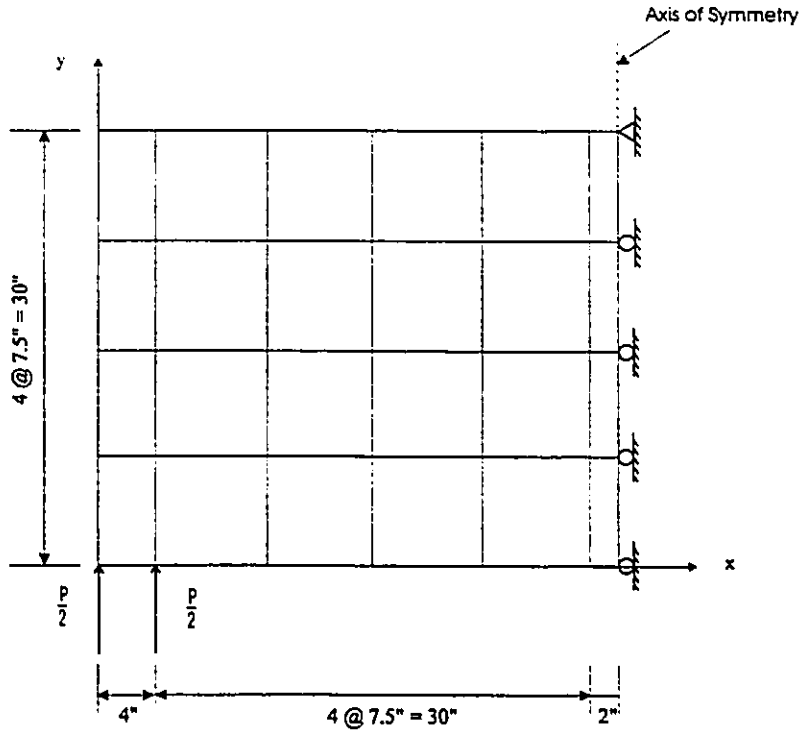

Figure 6.29: Finite element configuration for the shear panel W-4 with 24 elements

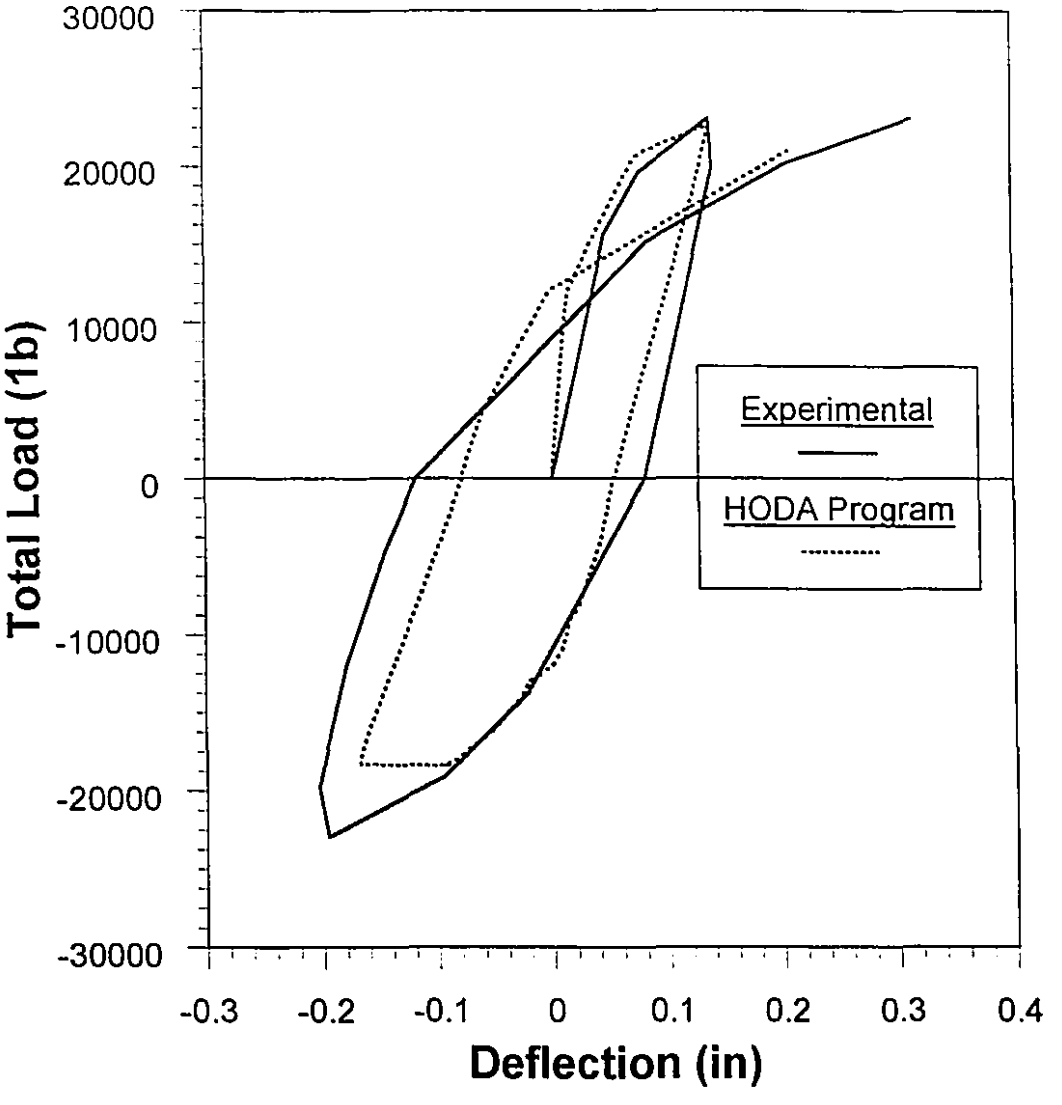

Figure 6.30: Experimental and analytical cyclic Response of the Shear panel W-4

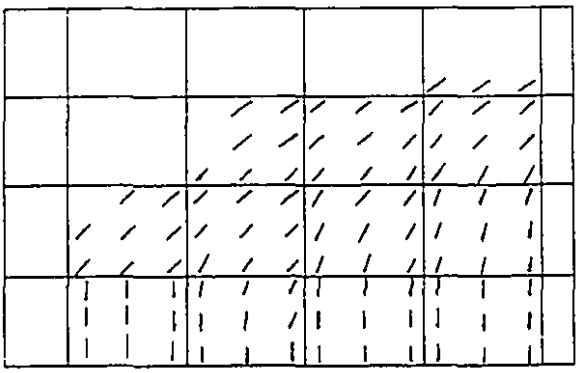

(a) First cycle

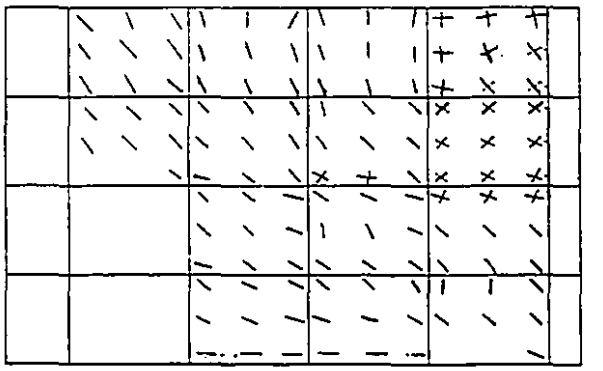

(b) Second cycle

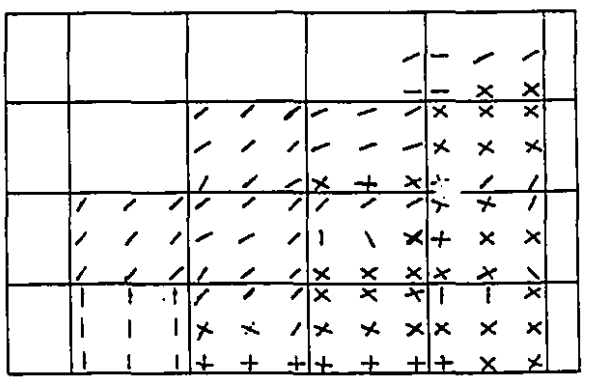

c) Third cycle

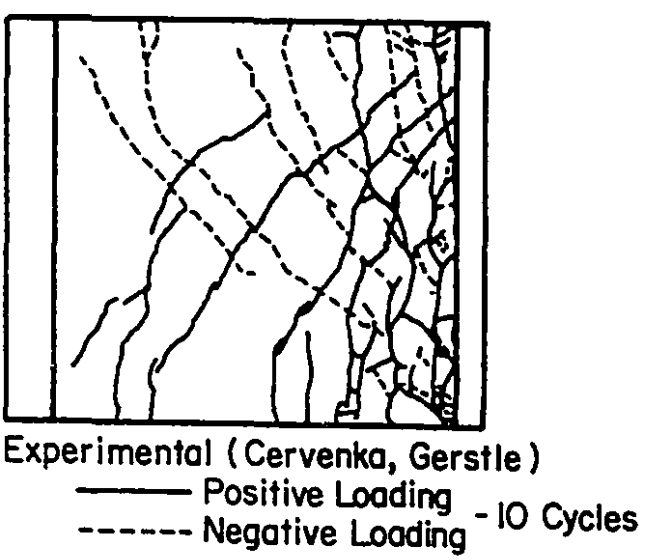

d) Experimental

Figure 6.31: Comparison of the analytical and the experimental crack patterns at peak points for shear panel W-4

CHAPTER 7

ANALYTICAL STUDY OF STRUCTURAL WALLS

This chapter presents the computed responses of three structural walls subjected to distributed lateral loads using the HODA program. These include a rectangular wall, an L-shaped wall and a C-shaped wall constituting the lateral load resisting system of a 4-storey building (Manatokas, 1989). Some parametric studies are also carried out on the three walls to show the effect of tension-stiffening of the concrete and strain-hardening of the steel reinforcement along with the type of steel idealization on the analytical response of these walls. No experimental results are available for these walls, however in each case the computed results are compared with the wall strength calculated using the CSA standard A23.3-M84. This chapter establishes the usefulness of the finite element analysis program HODA in the analysis of fairly complex structures where the experimental demands are quite time-consuming, expensive and often cumbersome.

7.1 DESCRIPTION OF THE STRUCTURAL WALLS

The 4-storey flat slab building (Fig. 7.1) with a structural wall system consisting of two L-shaped walls, a C-shaped elevator core and a rectangular wall was analyzed by Manatakos (1989). The storey heights for the first and the second storeys are 3.86m each, 3.56m for the third storey and 3.96m for the fourth storey. The columns support the gravity loads and their contributions to the lateral load resistance are assumed to be negligible; the entire lateral loads are resisted by the wall system. The 216mm thick flat slab is assumed to be a rigid diaphragm that

introduces the inertia forces at each floor level to the structural walls. The foundations of the building are considered to be fixed and transmit the forces to the ground without allowing the walls to rock. The building layout and the walls dimensions are illustrated in Fig. 7.1.

The lateral seismic forces are calculated based on the equivalent static loads according to the provisions of the National Building Code of Canada (1990). An approximate elastic analysis of the wall forces is based on the assumptions that the floors act as rigid diaphragms and thus walls deflect by the same magnitude at each floor. Torsional forces are also taken into account. The distribution of the lateral forces acting on the individual walls at the various floor levels was calculated by Lim (1994) and the results are summarized in Table 7.1.

The design of the walls is carried out based on the seismic design provisions of the CSA Standard CAN3-A23.3-M84. Detailed design of these three walls is presented by Lim (1994). The reinforcement details of the rectangular wall (with and without the concentrated reinforcement), the L- and the C-shape walls are shown in Fig. 7.2. It should be noted that no experimental results are available for the response of these walls and only their computed responses are presented in the following sections.

Table 7.1: Seismic lateral forces distributed to each wall (Lim, 1994)

Level	Rectangular wall (kN)	L-shaped wall (kN)	C-shaped wall (kN)
4	520	290	81
3	413	215	60
2	264	147	41
1	133	74	21

7.2 THE RECTANGULAR WALL

7.2.1 Finite Element Modelling

The rectangular wall is divided into 200 rectangular finite elements. Shell element I, which combines the quadrilateral inplane element (QLC3) and the rectangular bending element RBE,

is used. As the bending behaviour of the rectangular wall is essentially a plane stress problem, a single layer of concrete is sufficient. In order to provide a realistic description of the fixed foundation conditions at the wall base, all of the nodes along the lowest boundary of the wall are restrained for all 6 degrees of freedom as illustrated in Fig. 7.3. The model is loaded with equally divided horizontal loads at the nodes along the floor levels. This is to simulate the lateral forces applied to the wall through the floor slab diaphragm actions. The wall is also subjected to constant vertical loads due to the dead and live gravity loads from the structural system. The lateral loads are applied in 20 or 30 load steps with smaller increments of loads being applied just before the wall reaches its ultimate load stage. This improves the rate of convergence of the solution and the accuracy in predicting the ultimate load. The entire vertical load is applied in one load step at the beginning. The material properties of the wall are the same as those used in the design. Suitable assumptions have been made for the modulus of elasticity and the ultimate concrete strain in

Table 7.2: Material Properties of the Walls

Material properties	Rectangular wall	L-shaped wall	C-shaped wall
f'_c (MPa)	30	30	30
E_0 (MPa)	30120	30120	30120
f'_t (MPa)	3.29	3.29	3.29
ε_{cu}	0.002	0.002	0.002
ε_u	0.003	0.003	0.003
f_y (MPa)	400	400	400
E_s (MPa)	200000	200000	200000
E_s^* (MPa)	4800	4800	4800
ε_{sy}	0.002	0.002	0.002
ε_{su}	0.10	0.10	0.10

compression based on empirical formulas. The properties of the concrete and the reinforcing steel used in the analysis are presented in Table 7.2.

Two types of reinforcing bar arrangements are studied. These are: a) uniformly distributed reinforcement, the vertical and horizontal uniformly distributed reinforcement [see Fig. 7.2(a)] being represented by smeared steel layers as shown in Fig. 7.4, and b) concentrated reinforcement by keeping the total reinforcement ratio almost the same as for the uniformly distributed case, with concentrated vertical reinforcement being placed at the two ends of the wall with the remaining steel uniformly distributed between the two ends [see Fig. 7.2(b)]. Two types of steel idealizations are investigated for the concentrated steel. The first idealization uses a smeared steel model for the concentrated reinforcement, and the horizontal and vertical distributed reinforcements as illustrated in Fig. 7.5(a). The second idealization uses discrete bar elements to represent the concentrated reinforcement and smeared steel model for the distributed reinforcements as given in Fig. 7.5(b).

7.2.2 Computed Versus Predicted Ultimate Load

The analytical load-deflection curve at the top of the wall with distributed reinforcement detailing is presented in Fig. 7.6. A comparison of the computed ultimate load and the ultimate capacity of the rectangular wall calculated using the CSA Standard CAN3-A23.3-M84 is shown in Table 7.3. The result shows that the computed capacity for the distributed reinforcement detailing with smeared steel model is 1.25 times the nominal capacity with ϕ_c=1.0 and ϕ_s=1.0, while it is 1.58 times the design capacity calculated according the current CSA standard with ϕ_c=0.6 and ϕ_s=0.85.

When the concrete tensile strength and strain hardening of steel are ignored, i. e. $f'_t = 0$ and $E_s^* = 0$ (see Fig. 7.7), the computed ultimate load is reduced to 1850 kN which is only 10% higher than the nominal capacity predicted using the CSA Standard CAN3-A23.3-M84 (see also Table 7.4). It represents a model closest to the present design assumptions in the CSA Standard CAN3-A23.3-M84 where the recommended equation for ultimate capacity does not take into account the concrete tensile strength, tension stiffening and strain-hardening of the steel reinforcement. Although the validity of the assumptions is questionable, it yields a conservative value for the ultimate load which is quite acceptable for design purposes. As can be observed in Fig. 7.7, the stiffness of the wall without the concrete tensile strength, deteriorates significantly

upon the initiation of the cracks at a load level of 600 kN. When the concrete tensile strength is incorporated in the model, the computed ultimate load increases to 1950 kN despite ignoring the tension-stiffening, which is 5.4% higher than for the case when the tensile strength is ignored (1850 kN). The load-deflection curve also indicates that with consideration of the concrete tensile strength, the wall exhibits a much stiffer behaviour after cracking. Although both curves in Fig. 7.7 deviate from each other immediately after cracking, they gradually approach each other at load levels close to the ultimate load. The difference in the displacements for the two models becomes smaller after a load of 1600 kN. This observation is not surprising because as the wall approaches failure, most of the tensile "fibres" in the concrete would have cracked. As a result, the behaviour of the wall, with the concrete tensile strength considered, near failure is similar to the case without the tensile strength. This can also explain the reason for only a slight increase in the ultimate strength for the two cases.

Table 7.3: Comparison of the computed and predicted ultimate load for the rectangular wall

Detailing	Steel model	Computed ultimate load[1] P_u (kN)	Design capacity[2] P_r (kN)	Nominal capacity[3] P (kN)	Ratio of P_u/P
Distributed reinforcement	Smeared model	2100	1330	1681	1.25
Concentrated reinforcement	Bar element model	2050	1470	1710	1.23
Concentrated reinforcement	Smeared model	2550	1470	1710	1.52

[1] - Computed using the HODA program
[2] - Calculated using the CSA Standard CAN3-A23.3-M84 (ϕ_c=0.6, ϕ_s=0.85)
[3] - Calculated using the CSA Standard CAN3-A23.3-M84 (ϕ_c=1.0, ϕ_s=1.0)

7.2.3 Effect of Strain-Hardening of Steel

Figure 7.8 illustrates the influence of strain-hardening of steel on the load-deflection curves of the rectangular wall with distributed reinforcement detailing. As can be observed, the ultimate load increases only slightly from a value of 2025 kN for the case without strain-hardening (E_s^*=0) to a load of 2100 kN when strain-hardening is considered (E_s^*=4800 MPa). The load-deflection curves essentially coincide with each other until at load of 1500 kN where the curves

start to deviate. Variation of the lateral load versus the concrete strain at the outermost tension fibre for the two cases with and without steel strain-hardening is plotted in Fig. 7.9. Because of the assumption of perfect bond between the steel and the concrete, the strain in the concrete and the reinforcing steel at a given location are identical. An examination of the concrete strain reveals that the deviation of curves occurs after the yielding of steel reinforcement has taken place (at which the strain in steel reinforcement reaches the yielding strain of ε_{sy} as presented in Table 7.2). The change of the strain-hardening modulus does not appear to affect the load-deflection curves and the ultimate load significantly. This can be attributed to the fact that failure occurs due to the crushing of the concrete before more of the uniformly distributed steel reinforcement is stressed into the strain-hardening zone.

For the case of steel strain-hardening with E_s^*=4800 MPa, Fig. 7.8 shows that the first crack occurs at a load of 800 kN at the extreme tension "fibre" of the wall. Because of the redistribution of forces, there is a sudden increase in the concrete strain at the outer most tension elements as shown in Fig. 7.9. The neutral axis of the wall moves gradually towards the extreme compression fibre, thereby reducing the area of concrete in compression leading to the failure of the wall because of the crushing of the concrete.

Table 7.4: Comparison of the computed and predicted ultimate load for the walls

Type of wall	Detailing	Computed ultimate load[1] P_{u1} (kN)	Computed ultimate load[2] P_{u2} (kN)	Computed ultimate load[3] P_{u3} (kN)	Design capacity[4] P_r (kN)	Nominal capacity[5] P (kN)	Ratio of P_{u3}/P
Rectangular	Distributed reinforcement	2100	2000	1850	1330	1681	1.10
L-Shaped	Distributed reinforcement	1500	1300	1200	726	950	1.26
C-Shaped	Distributed reinforcement	580	500	420	240	315	1.25

[1] - Computed using the HODA program (E_s^*=4800 kN, with concrete tension-stiffening)
[2] - Computed using the HODA program (E_s^*=4800 kN, without concrete tension-stiffening)
[3] - Computed using the HODA program (E_s^*=0.0 kN, with no concrete tensile strength)
[4] - Calculated using the CSA Standard CAN3-A23.3-M84 (ϕ_c=0.6, ϕ_s=0.85)
[5] - Calculated using the CSA Standard CAN3-A23.3-M84 (ϕ_c=1.0, ϕ_s=1.0)

7.2.4 Effect of Steel Idealization for Concentrated Steel Reinforcement

The influence of idealizing the concentrated steel reinforcement using smeared steel and bar elements to represent the concentrated reinforcing steel at the two wall ends is studied using $E_s^* = 4800$ MPa. A comparison of the load-deflection curves for both smeared steel model and the bar element model for the rectangular wall with concentrated reinforcement detailing is shown in Fig. 7.10. The ultimate load obtained for the bar element model is 2050 kN, which is higher than the nominal capacity calculated using the CSA Standard CAN3-A23.3-M84 by about 20%. The ultimate load obtained for the smeared steel model is 2550 kN which is 49% higher than the nominal capacity calculated using the CSA Standard A23.3-M84 (see Table 7.3). Thus, the ultimate load using the smeared steel model is 24% higher than the ultimate load computed using bar element model. It can be observed that both load-deflection curves compare favourably until reaching a load of 2050 kN where both curves start to deviate (Fig. 7.10). Failure occurs at a load of 2050 kN for the bar element model while the smeared steel model continues to carry further load until a load of 2550 kN.

Comparison of the concrete strains at the outermost tensile fibre and the outermost compressive fibre in Figures 7.11 and 7.12, respectively, gives a closer picture of the behaviour between the bar element model and the smeared steel model. Both curves in each of the figures, essentially coincide with each other for load levels below 2000 kN. The steel reinforcement yields at a load of 1800 kN, and thereafter for the case of bar element model, the wall becomes softer and a rapid increase of strain results in the crushing of the concrete at the right-hand bottom of the structure, with the subsequent failure of the wall at a load level of 2050 kN. For the smeared steel model, the structure becomes softer after yielding of the reinforcement at load level of 1800 kN, but it stiffens thereafter at load level of 2000 kN because of strain hardening of the steel reinforcement. However, for this model the strains do not increase rapidly until a load level of 2500 kN. Clearly, the results of the concrete strain for the smeared steel model after a load of 2050 kN (with a sudden increase in load without any appreciable increase in strains) are contrary to expectation, indicating that the smeared steel representation is not suitable to represent heavy concentrated reinforcing steel in a structural wall. A more realistic representation should be using the bar element model.

Figures 7.13 and 7.14 illustrate the crack patterns of the rectangular wall at the various load levels for both bar element and smeared steel models. The cracking is initiated for both models at a load of 1000 kN [see Figures 7.13(a) and 7.14(a)]. The crack patterns at load level of 1800 kN at which yielding of steel reinforcement occur, are given in Figures 7.13(b) and 7.14(b). The crack patterns for both models

at one load step before failure are presented in Figures 7.13(c) and 7.14(c). These figures show that cracking which initiates at a low load level, spreads progressively towards the compression zone with increasing load. These cracks show a pattern of struts radiating from the compression zone at the right corner in Figures 7.13(c) and 7.14(c). A typical flexural failure of the wall where the failure is caused by yielding of steel reinforcement followed by crushing of concrete, is observed.

7.3 THE L-SHAPED WALL

7.3.1 Finite Element Modelling

The L-shaped wall is divided into a mesh consisting of 240 rectangular elements. Shell element I is used in the analysis, since the assumption of a plane stress condition is no longer valid for this structure. Each concrete element is subdivided into 7 layers to provide a more realistic model. Fixed foundation conditions are modelled at the wall base by restraining the nodes along the base for all 6 degrees of freedom as illustrated in Fig. 7.15. The model is loaded with horizontal loads at the web in Fig. 7.15. The wall is also subjected to a constant vertical axial loads due to the dead and live gravity load from the structural system. Horizontal loads are applied in 20 load steps, with smaller increments of loads being applied just before the wall reaches its ultimate load stage. The entire vertical load is applied in one load step at the beginning. The finite element idealization is shown in Fig. 7.15. The uniformly distributed reinforcement is represented by smeared steel layers. The material properties are given in Table 7.2.

7.3.2 Computed Response of the L-Shaped Wall

Figure 7.16 illustrates the load-deflection curves for the L-shaped wall. It can be noted that with tension stiffening, the ultimate load is 1500 kN, which is 15% higher than that for the case where tension-stiffening is ignored (1300 kN). The stiffness of the wall without tension-stiffening reduces significantly after the initiation of cracking at a load of 800 kN when compared with the model which considers tension-stiffening. As can be observed from Fig. 7.16, inclusion of the tension-stiffening increases the ultimate load and the stiffness of the wall. To provide a mathematical model closer to the assumptions of the current CSA standards for design of reinforced concrete structures, the concrete tensile strength and the steel strain hardening were neglected and the corresponding load-deflection curve is also presented in Fig 7.16. The cracking initiates at a much lower load level of 400 kN and the structure displays lower

stiffness than in the previous cases, i. e., with and without tension-stiffening. The ultimate load reduces to 1200 kN which is still 26% higher than the nominal capacity calculated using the CSA Standard CAN3-A23.3-M84 (see Table 7.4).

Variation of the lateral load versus the concrete strain at the outermost web tension fibre at the base of the wall is also plotted in Fig. 7.17. In the absence of tension-stiffening, at a given load level, the concrete strain is larger than the model which considers tension-stiffening.

The crack patterns for the L-shape wall with tension-stiffening at the various load levels are shown in Fig. 7.18. The cracking initiates at a load level of 800 kN with nearly horizontal cracks at the left-hand of the wall base. The steel reinforcement yields at a load level of 1100 kN and the corresponding crack pattern is shown in Fig. 7.18(b). At this load stage only one crack appeared in the flange of the wall. With further increase of the load, the cracks progress toward the compression zones in the wall. The crack pattern of the wall at one load step before ultimate load is shown in Fig. 7.18(c). The cracks in the wall web are similar to those for the rectangular wall except that they are more extensive for the L-shaped wall. Because the distributed load is assumed to be applied along the web center line, it passes through the shear center at the web-flange junction and therefore no twisting moment acts on the section. The compressive struts radiate into the web from the web-flange junction. The flexural cracks appear at the free end of the flange. As can be noted from Fig. 7.18(c), these cracks which appear first near the flange base, increase in number along the flange free edge and propagate towards the junction as the applied load is increased.

6.4 THE C-SHAPED WALL

7.4.1 Finite Element Modelling

The C-Shaped wall is divided into 80 rectangular finite elements. As for the L-shaped wall, each concrete element is subdivided into 7 layers. The boundary and loading conditions are similar to those in the L-shaped wall. The finite element idealization is shown in Fig. 7.19. The material properties are given in Table 7.2.

7.4.2 Computed Response of the C-Shaped Wall

Figure 7.20 illustrates the load-deflection curves for the C-shaped wall. The ultimate load of the model which considers tension-stiffening is 580 kN which is 16% higher than the value for the model

without tension-stiffening (500 kN). This observation is again consistent with the earlier findings for the rectangular and L-shaped walls that consideration of tension-stiffening increases the ultimate load and stiffens the load-deflection response of the structure. First cracking of the wall occurs at a lateral load level of 300 kN after which the stiffness of the model without tension-stiffening reduces significantly. The computed ultimate load without considering the concrete tensile strength and the steel strain-hardening decreases to 420 kN which is still 25% higher than the nominal capacity calculated using the CSA Standard CAN3-A23.3-M84 (see Table 7.4). In this case, the structure exhibits a response with a much smaller stiffness after initial cracking at a load level of 100 kN (see Fig. 7.20).

Figure 7.21 shows the load-concrete strain curves at the outermost tension flange "fibre" at the base of the wall. Again, the concrete strain after cracking for the case without tension-stiffening is larger than the model which considers tension-stiffening. The steel reinforcement yields at load level of 410 kN for the model considering concrete tension-stiffening, and at load level of 350 kN for the model without tension-stiffening.

Figure 7.22(a) illustrates initiation of horizontal cracks at a load level of 300 kN at the left-hand of the wall flange and wall web near the base. The crack pattern of the wall at yielding stage of the steel reinforcement is also shown in Fig. 7.22(b). The crack pattern at a load step just before failure is shown in Fig. 7.22(c). The cracks show the formation of a series of inclined struts radiating into the web from the web-flange junction. As for the L-shaped wall, the lateral load is assumed to be applied along the web center line at some eccentricity from the shear center of the C-shaped section, thereby causing a twisting moment to act on the section. This, in turn, causes torsional cracks in both flanges of the section. These expected torsional cracks are more dominant on the tension flange of the section than on the compression flange.

The preceding discussions of the analytical responses of the various structural walls exhibits the power of the nonlinear finite element program HODA in predicting the response of fairly complex structural systems. This study clearly establishes that the HODA program can be used to carry out detailed parametric studies to study the effect of different parameters on the behaviour of complex structural concrete elements.

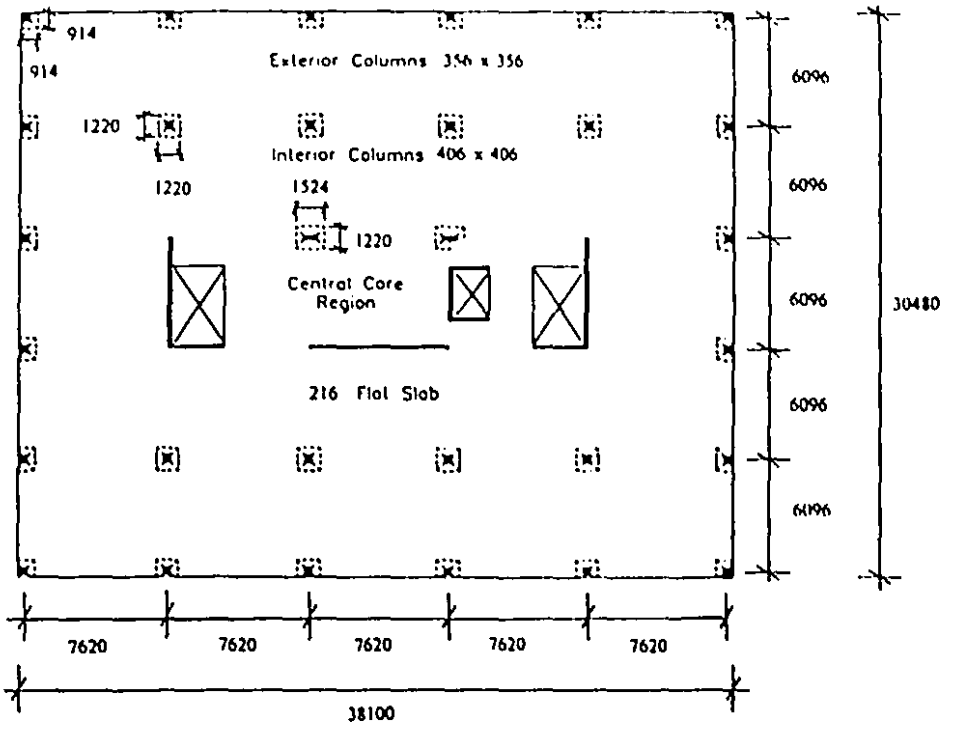

(a) Building layout

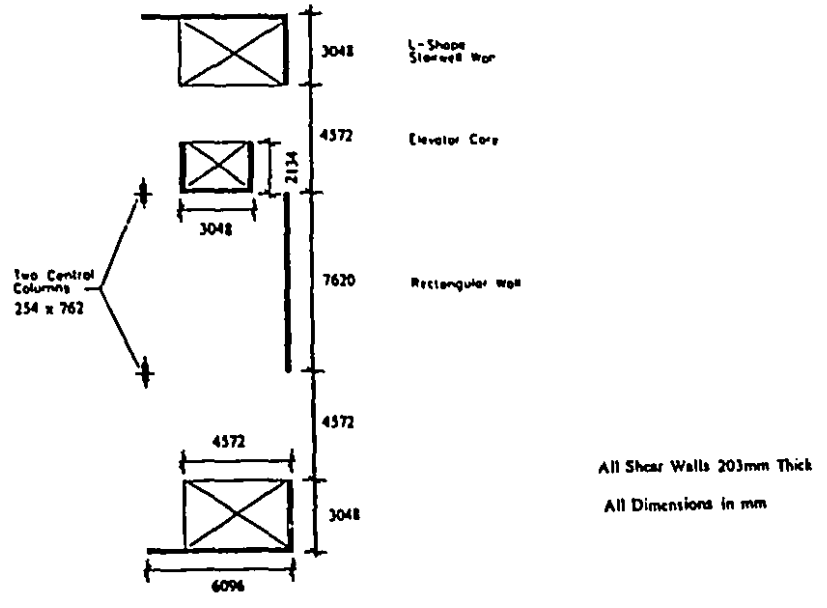

(b) Structural wall system

Figure 7.1: Layout of the low-rise building and the walls dimensions (Manatakos, 1989)

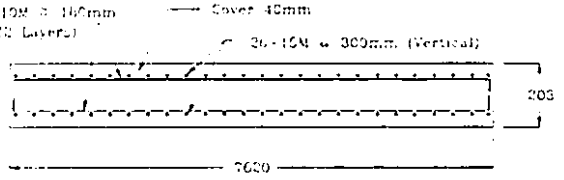

(a) Distributed reinforcement details for the rectangular wall

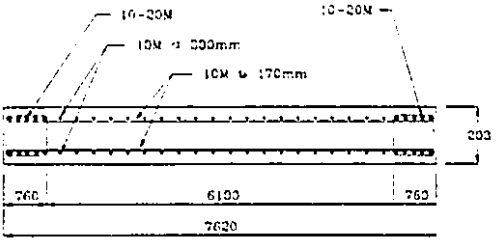

(b) Concentrated reinforcement details for the rectangular wall

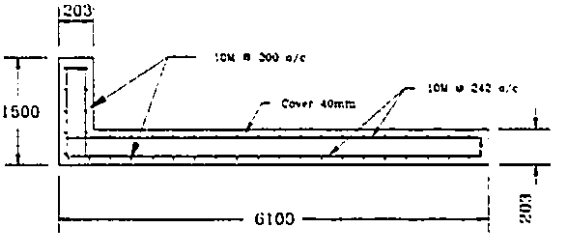

(c) The L-shaped wall

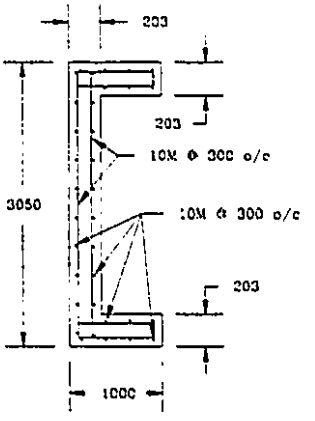

(d) The C-shaped wall

Figure 7.2: Reinforcement details of the walls

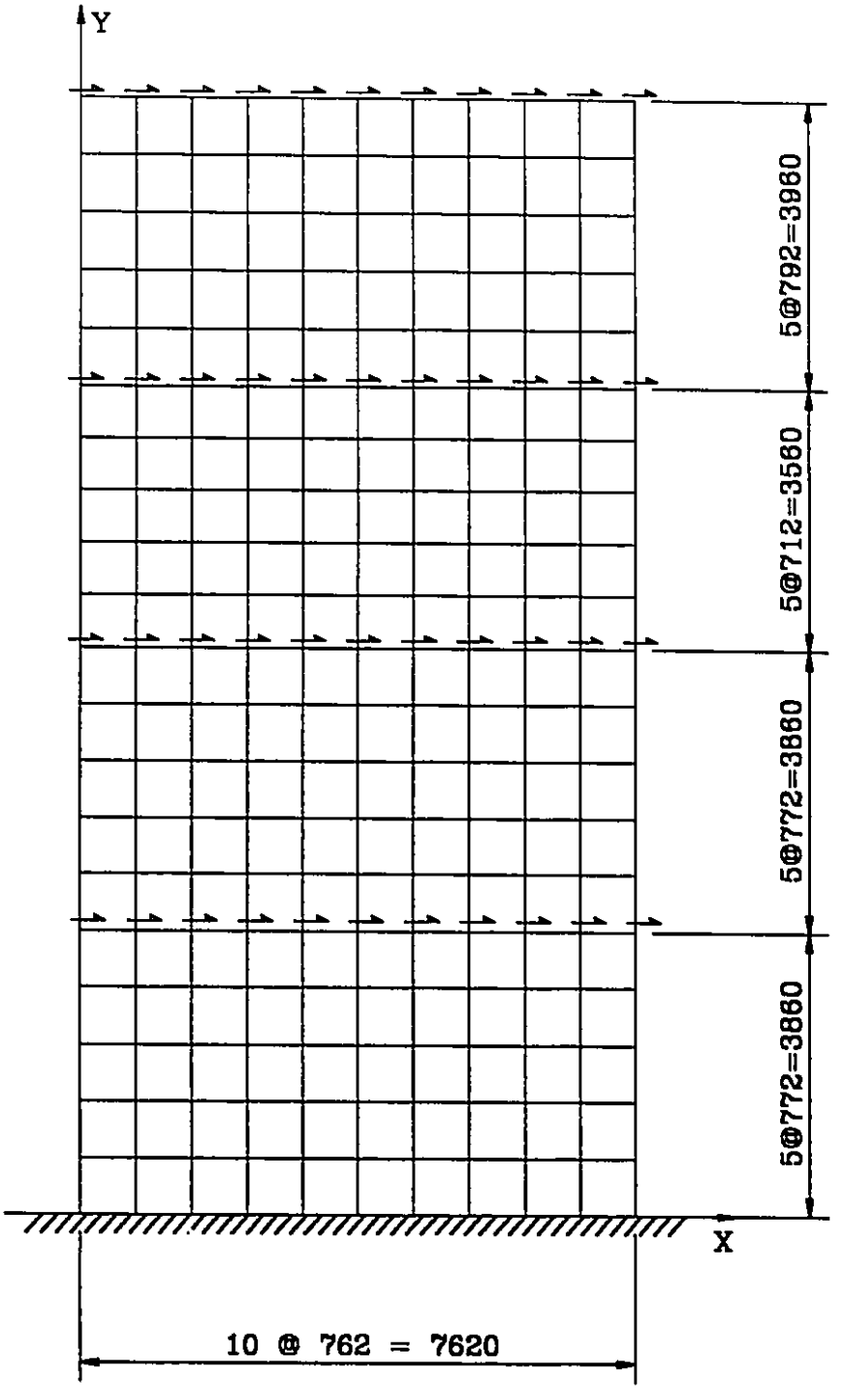

Figure 7.3: Rectangular wall finite element idealization

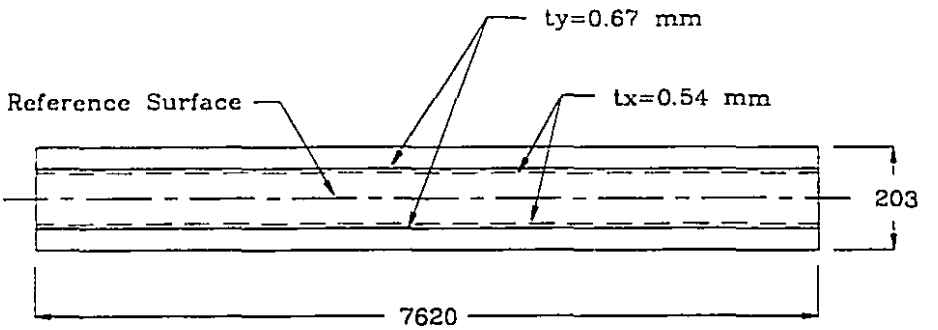

Figure 7.4: Idealization of distributed reinforcement for the rectangular wall

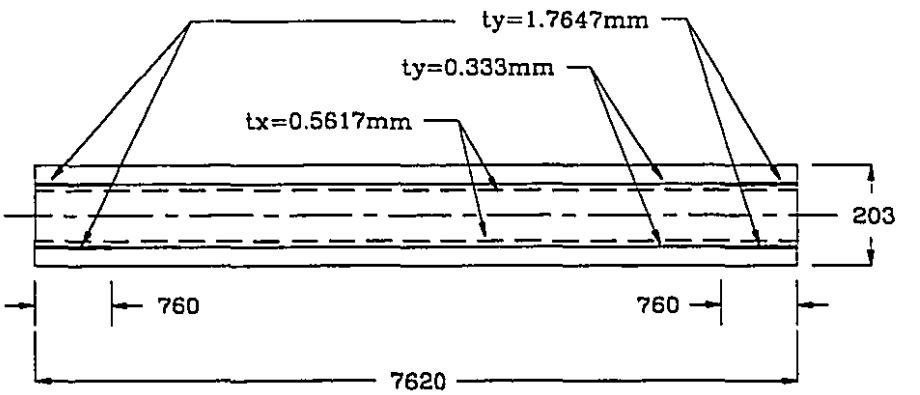

(a)

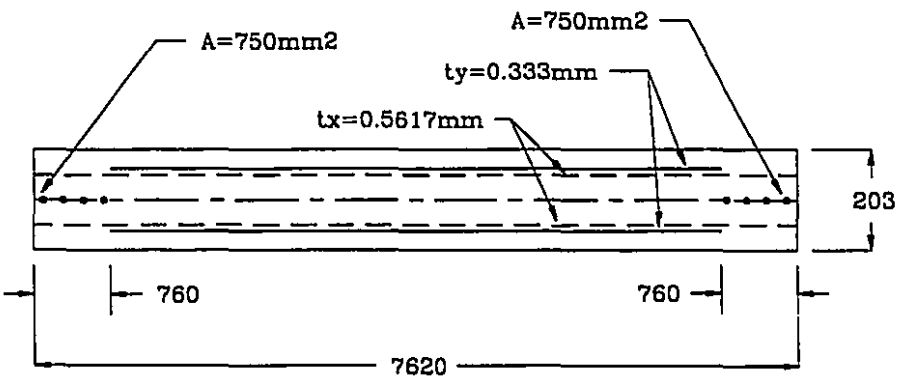

(b)

Figure 7.5: Steel idealization: (a) Smeared steel for all reinforcement
(b) Bar element for the concentrated reinforcing steel

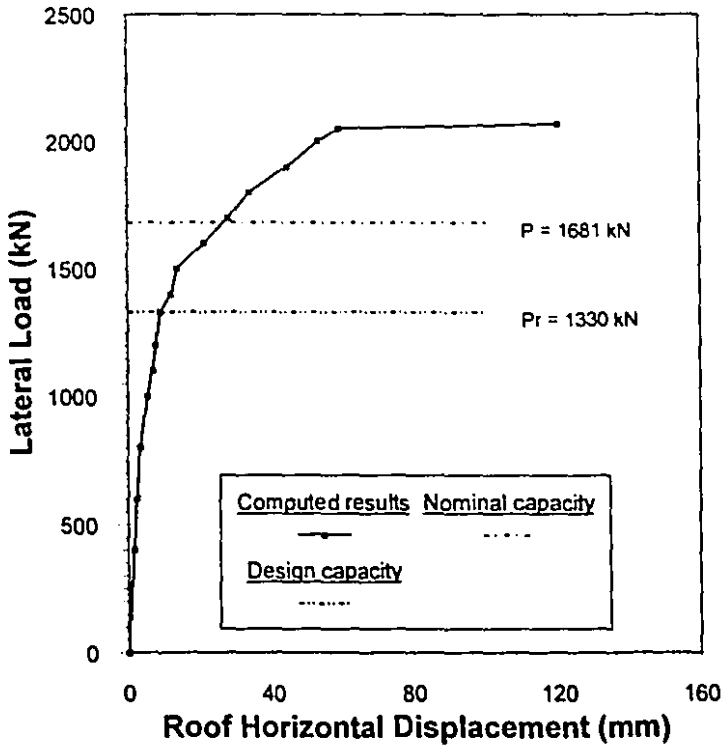

Figure 7.6: Load-deflection curves of the rectangular wall ($E_s^* = 4800$ MPa)

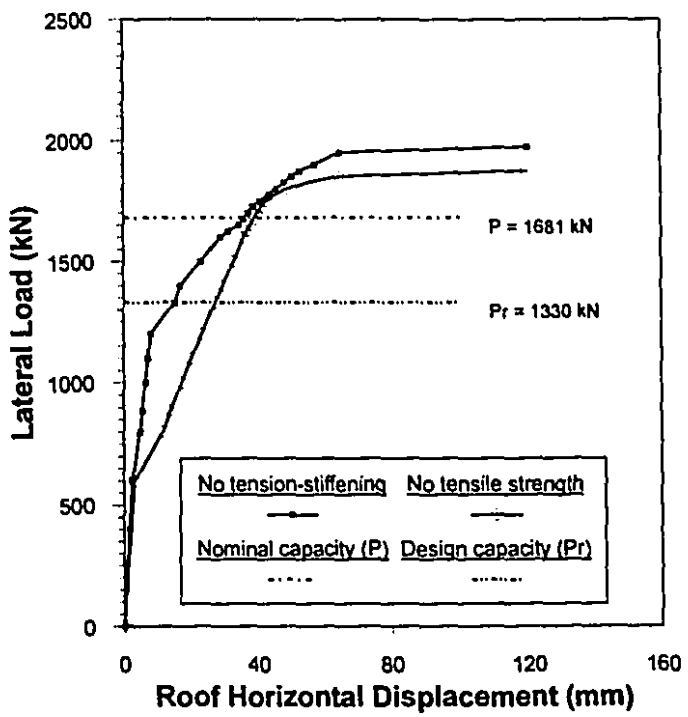

Figure 7.7: Load-deflection curves of the rectangular wall with no tension-stiffening and no concrete tensile strength ($E_s^* = 0$)

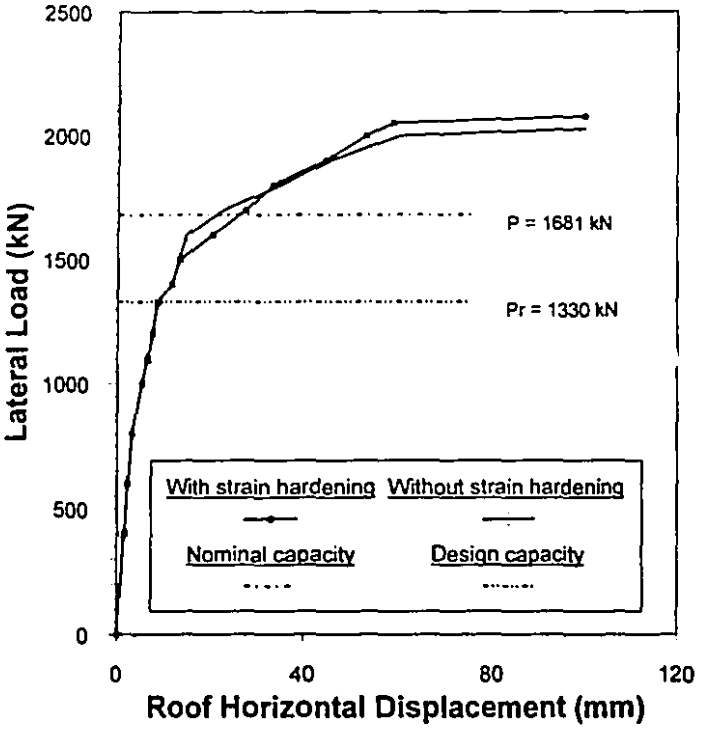

Figure 7.8: Load-deflection curves for rectangular wall with and without strain-hardening

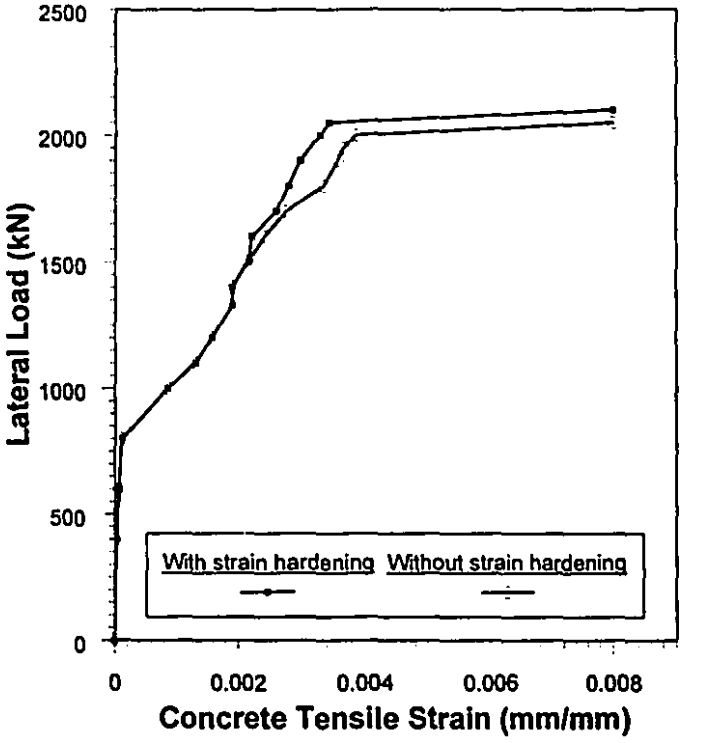

Figure 7.9: Load-concrete strain curves for rectangular wall with and without strain-hardening

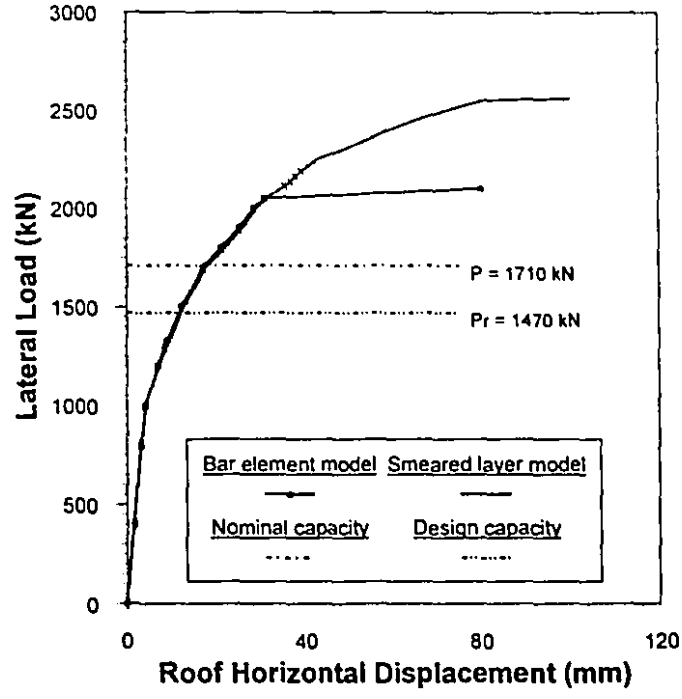

Figure 7.10: Load-deflection curves for bar element and smeared layer idealizations ($E_s^* = 4800$ MPa)

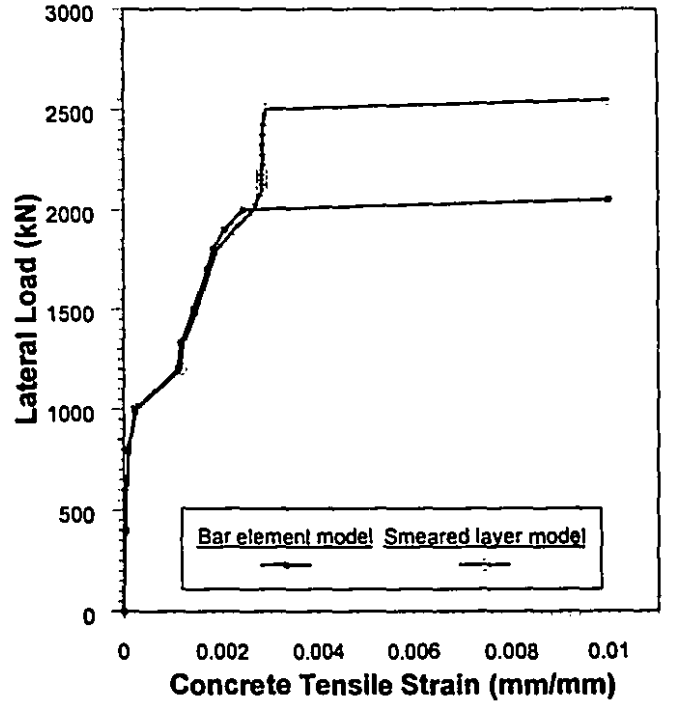

Figure 7.11: Load-concrete strain curves for bar element and smeared idealizations ($E_s^* = 4800$MPa)

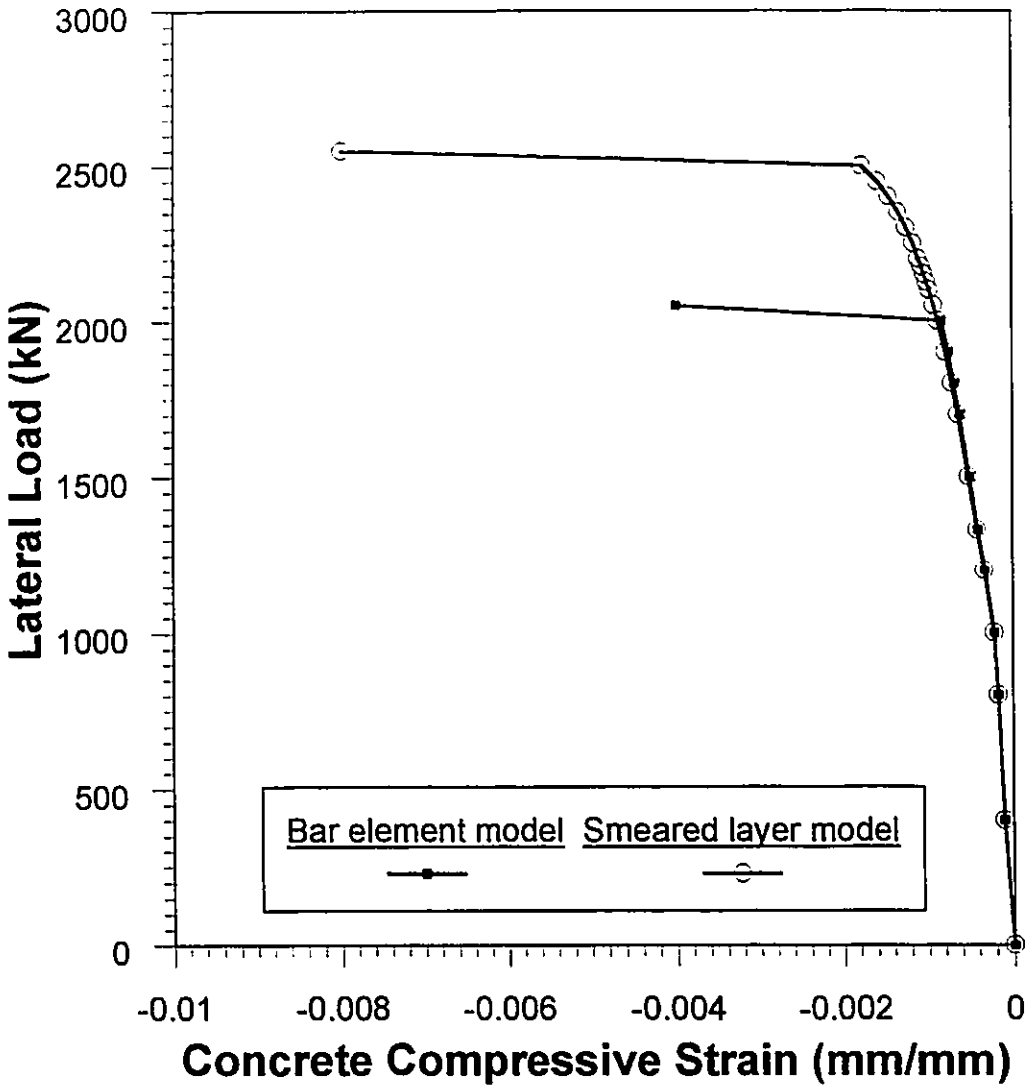

Figure 7.12: Load-concrete strain curves for bar element and smeared idealizations ($E_s^* = 4800$ MPa)

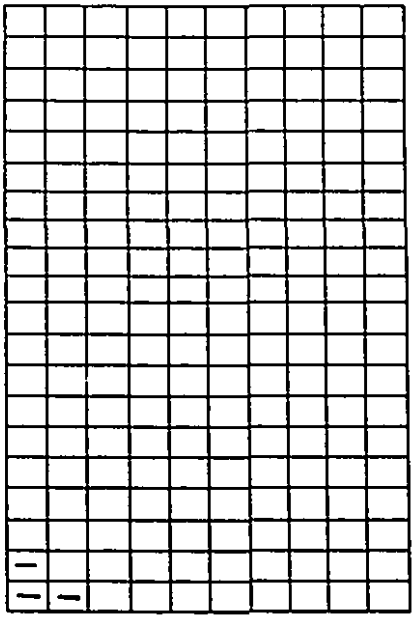

(a) Load Level of 1000 kN

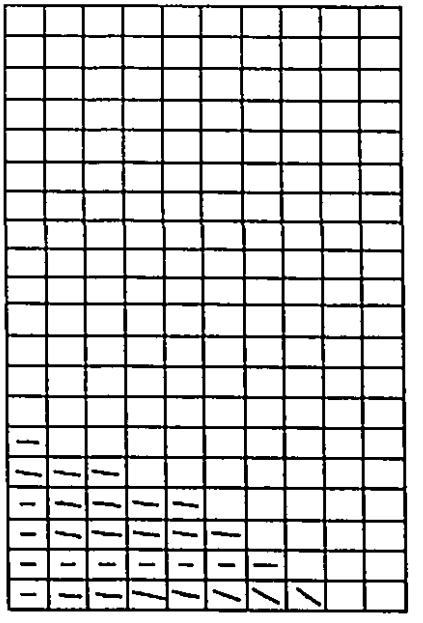

(b) Load Level of 1800 kN

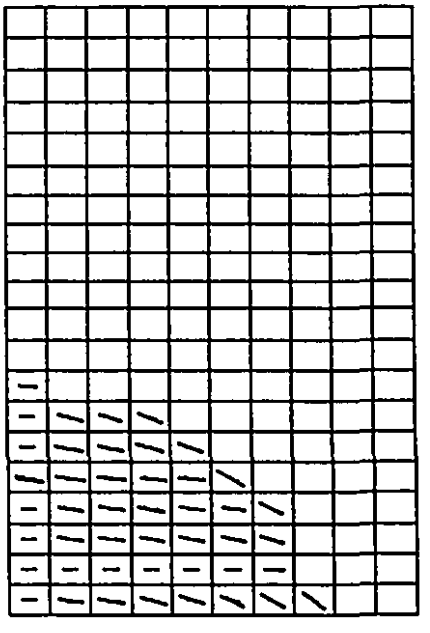

(c) Load Level of 2000 kN

Figure 7.13: Crack patterns for the rectangular wall using bar element model

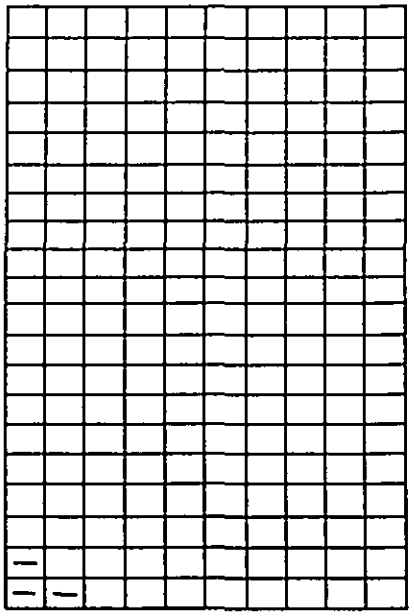

(a) Load Level of 1000 kN

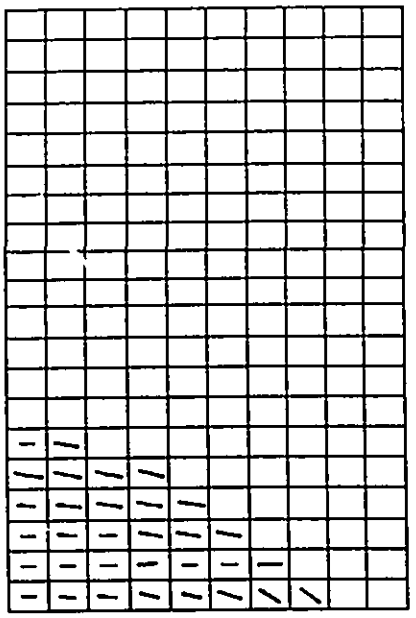

(b) Load Level of 1800 kN

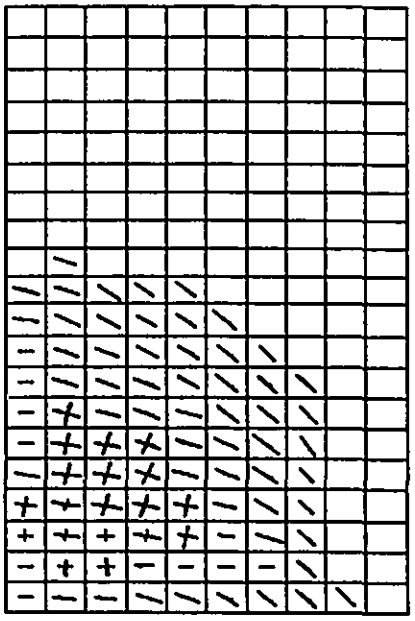

(c) Load Level of 2000 kN

Figure 7.14: Crack patterns for the rectangular wall using smeared steel model

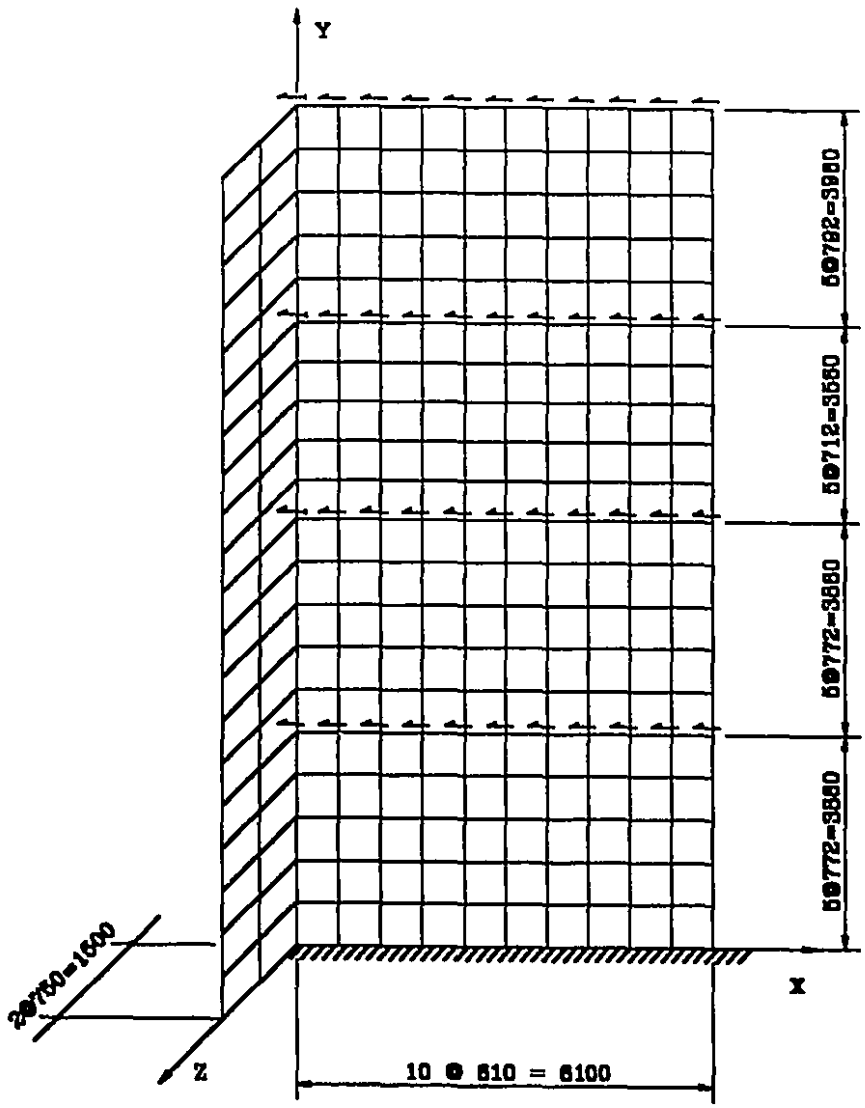

(a)

(b)

Figure 7.15: Idealization of the L-shaped wall:
(a) Finite element idealization, (b) Smeared steel idealization

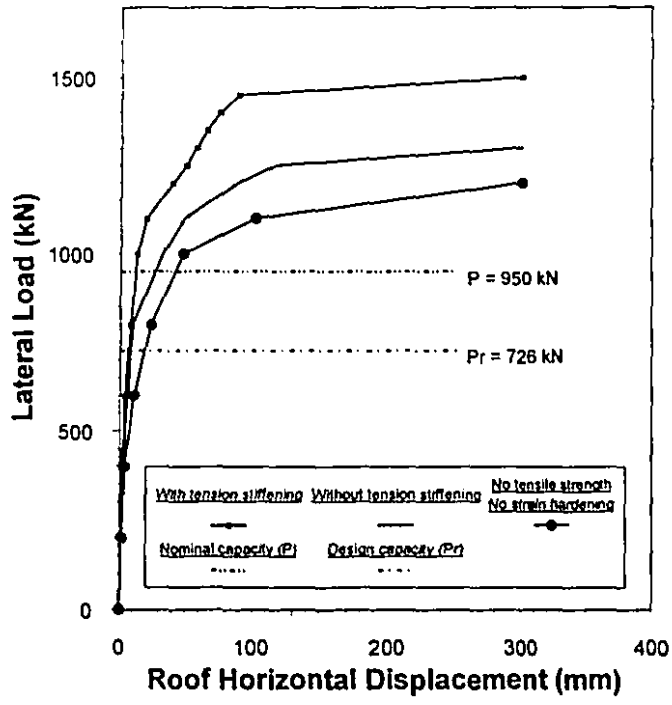

Figure 7.16: Load-deflection curves of the L-shaped wall with and without tension-stiffening ($E_s^* = 4800$ MPa)

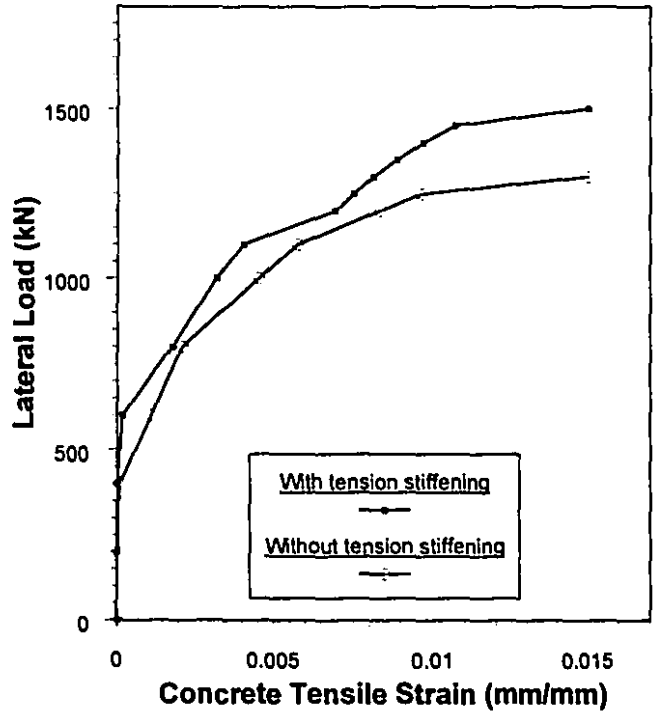

Figure 7.17: Load-concrete strain curves of the L-shaped wall with and without tension-stiffening ($E_s^* = 4800$ MPa)

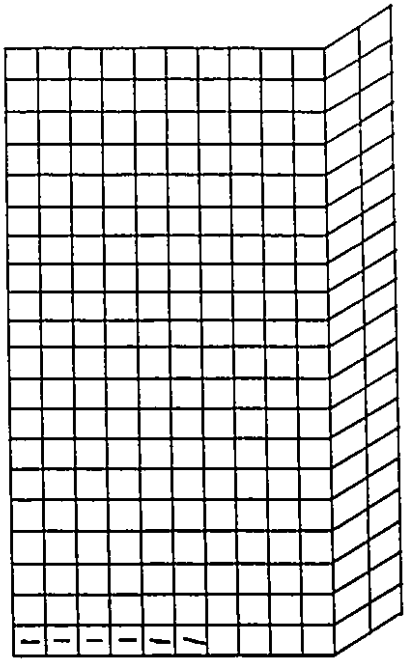

(a) Load Level of 800 kN

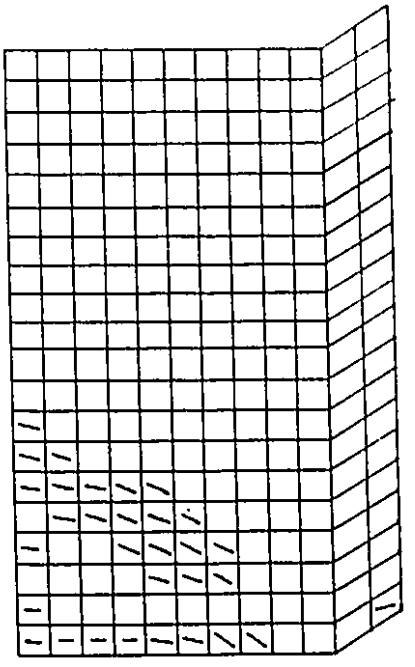

(b) Load Level of 1100 kN

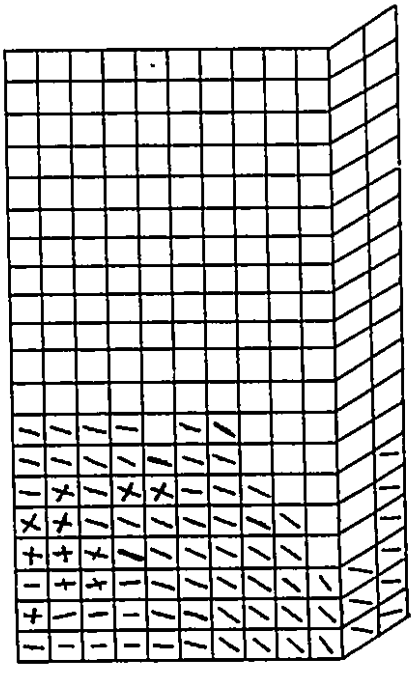

(c) Load Level of 1450 kN

Figure 7.18: Crack patterns for the L-shaped wall using bar element model

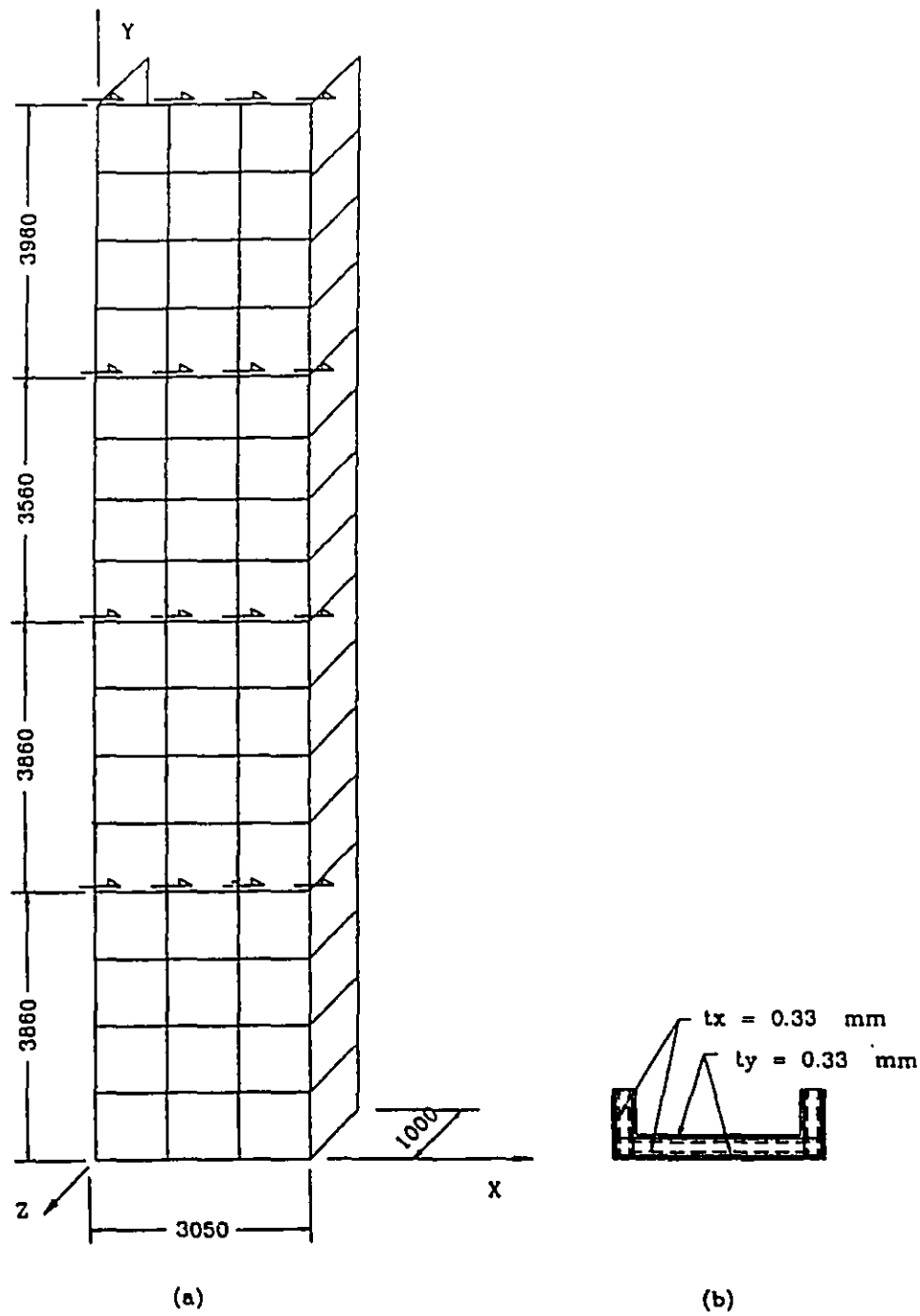

Figure 7.19: Idealization of the C-shaped wall:
(a) Finite element idealization, (b) Smeared steel idealization

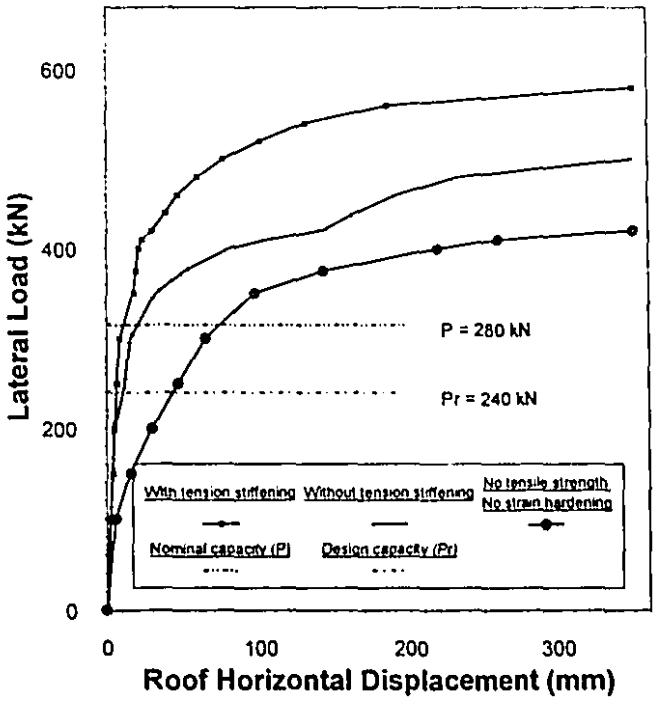

Figure 7.20: Load-deflection curves of the C-shaped wall with and without tension-stiffening ($E_t^* = 4800$ MPa)

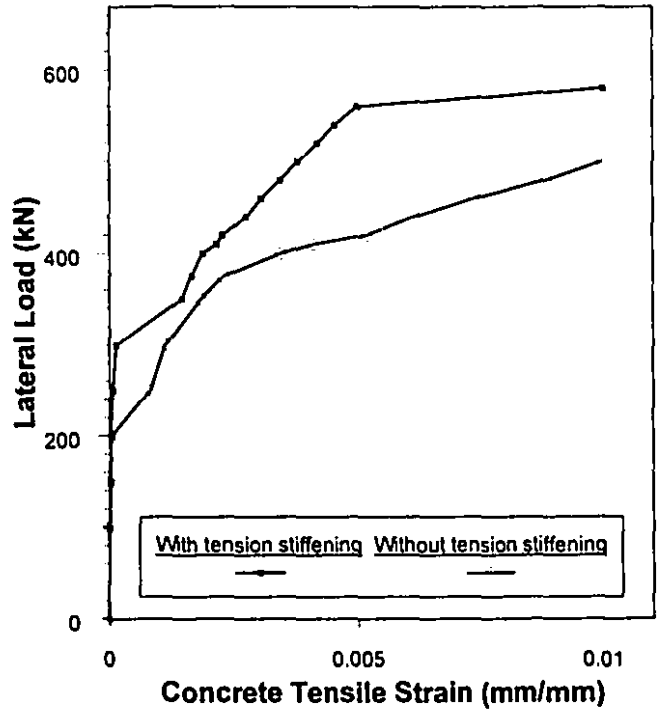

Figure 7.21: Load-concrete strain curves for the C-shaped wall with and without tension-stiffening ($E_t^* = 4800$ MPa)

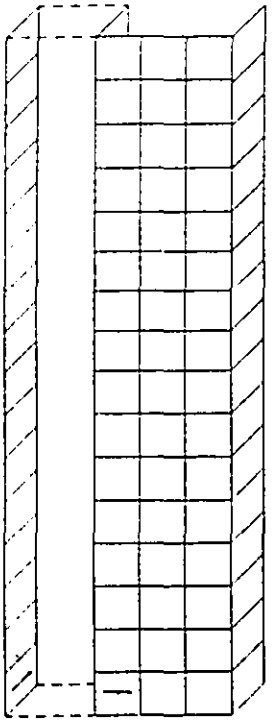

(a) Load Level of 300 kN

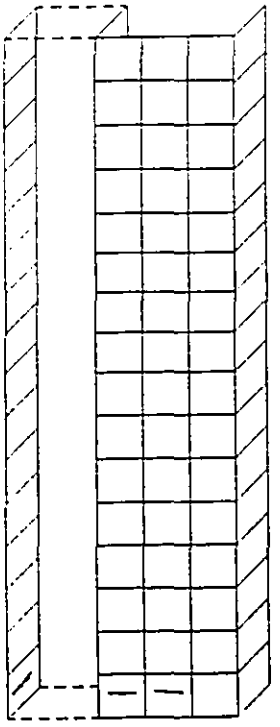

(b) Load Level of 410 kN

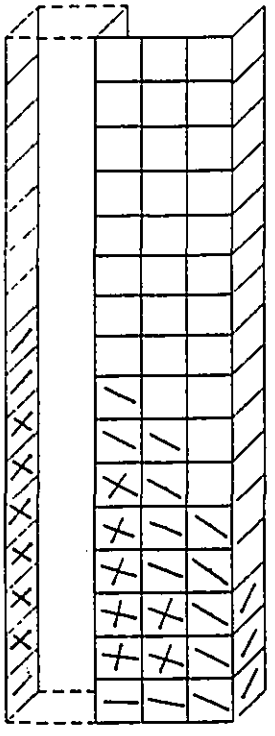

(c) Load Level of 560 kN

Figure 7.22: Crack patterns for the C-shaped wall

CHAPTER 8

CONCLUSIONS

This chapter summarizes the findings of the analytical studies undertaken on different structural elements using the HODA program developed in the course of this study. This includes the validity of the proposed material model for normal and high strength concrete under both monotonically increasing and reversed cyclic loadings, the mesh dependency phenomenon, analytical responses of the normal concrete shear panels and the high strength concrete beams under monotonically increasing loads, the numerical response of the normal concrete shear panel W-4 (deep beam) under reversed cyclic loading, and finally the computed responses of three structural walls of a 4-storey building (a rectangular wall, an L-shaped wall and a C-shaped wall) subjected to monotonically increasing distributed lateral loads. Some new topics relating to the current study are also recommended to be investigated further.

8.1 MATERIAL MODEL

1) The main characteristics of a proper model for concrete materials, can be summarized as follows:

   i) The high nonlinearity of the stress-strain behaviour of the concrete in the pre-peak regime, i. e. growing and propagation of microcracks resulting in a decrease in the material stiffness.

   ii) The softening behaviour of the concrete in the post-peak regime resulting from the localization of macrocracks in narrow bands.

   iii) The stiffness degradation caused by the extension of microcracks during subsequent unloadings and reloadings.

   iv) The irrecoverable volume dilatation at high level of compressive load

resulting in an increase in the Poisson's ratio.

All of the above features for concrete are included in the material model developed during the course of this study.

2) The proposed analytical model for normal and high strength concrete under both monotonically increasing and reversed cyclic loadings compares well with the uniaxial compression test results and represents basic features of the concrete behaviour in compression. For the cyclic loading model, it was observed that with an increase in the number of cycles, the stiffness of the concrete decreases, and the plastic strain increases as supported by experimental findings.

8.2 MESH DEPENDENCY

1) If a fine mesh is used to idealize a reinforced concrete element for nonlinear finite element analysis, the ultimate load is under-estimated when the element size dependency is ignored. Also, from energy considerations, a decrease in the mesh size increases the rate of crack propagation in the structure, and consequently its energy dissipation capacity decreases. This leads to a lower value of the ultimate load than the experimental one. In this case, it is also observed that the structure exhibits a less ductile response. However, if a coarser mesh is used instead, the ultimate load is over-estimated. In this case, the structure behaves in a more ductile manner. From a physical point of view, with an increase in the mesh size, the rate of crack progression will decrease and the capacity of the structure to dissipate energy will increase. This possibly answers the question "Why does the ultimate load increase with an increase in the element size?".

2) The results of the different analyses for over-reinforced beams show that the element size does not have a significant effect on the value of the computed ultimate load, because at higher load levels, the response of the concrete elements in compression governs the overall behaviour, and the response of concrete and steel in tension does not have as significant an effect, as in the under-reinforced concrete beams.

3) The value of the ultimate concrete tensile strain, ε_{tu}, has a considerable influence on the computed values of the ultimate load. It was shown by Shayanfar et al. (1993) that the effect of concrete tensile strength, f'_t, is not as significant. An emperical formula is proposed which gives an appropriate value of ε_{tu} as a function of the element size, h. Along with the crack band model proposed by Bazant and Oh (1983), this formulation is implemented in the nonlinear finite element program HODA to analyze different type of structures. The responses computed using these models showed very good agreement with the experimental results for the ultimate load, load-deflection and load-concrete strain responses, and the concrete cracking patterns. The proposed formula can be used effectively and economically for analysis of structural concrete elements using relatively large finite elements with reasonable accuracy and much smaller computational effort.

8.3 EXPERIMENTAL SPECIMENS

1) Analysis of the five panels tested at the University of Toronto indicates the effect of the steel reinforcement details in different directions and the type of external applied load on the general behaviour of the structure and its mode of failure. If small amounts of reinforcement are provided in the specimen, more demand is placed on the steel and it undergoes large strains and dominates the final response of the structure.

2) If the same amounts of reinforcement are placed in the two orthogonal directions, the rotation of principal strain axis after cracking is negligible and the results of fixed and rotating crack model are the same. On the other hand, if these two sets of reinforcements are considerably different from each other, the results of these two models are quite different. The former exhibits a stiffer response and a higher ultimate load than the latter. Generally, the rotating crack model is more realistic than the fixed crack model in predicting the load-strain relations and the ultimate load of the structure.

3) The use of the Vecchio-Collins failure criterion in the post-cracking regime for all of these panels provides the best response, and and therefore, it is important that it be incorporated in any finite element program to predict the post-cracking response.

4) The computer program HODA predicts the failure mode of all these five panels very close to the experimental findings and establishes the reliability of the program.

5) Close agreement between the analytical and the experimental response in terms of the load-deflection, the failure load and the crack patterns have been obtained for the squat shear wall, SW9. Although several parameters which were not reported in the experiments have been assumed, the failure load predicted by the HODA program is only 5% lower than the experimental results.

6) For high strength concrete beams, the model, with no mesh dependency, in which the ultimate tensile strain of concrete, ε_{tu}, is set to a constant value, exhibits very stiff responses, however, it predicts the ultimate load capacity of the specimen very accurately with a very small discrepancy. The model incorporating the proposed model to eliminate the mesh dependency phenomenon gives a relatively softer response, which is closer to the experimental results but it under-estimates the ultimate load carrying capacity of the structure a little.

7) Incorporation of a sudden drop of the stress after the tensile strength of concrete has been exceeded, has a strong effect on the load-deflection response of the high strength beams at early stage of loading after initial cracking of concrete. The computed load-deflection curves are closer to the experimental results when a smaller value of γ is used. But it was discovered that, decreasing the value of softening branch parameter, γ, is acceptable only up to a value of $\gamma = 0.4$, and a further decrease in the value of γ leads to a softer response than the experimental results at an early stage of loading and under-estimates the ultimate load of the beam significantly, which is not acceptable.

8) By decreasing the value of softening parameter, γ, the ductility ratio, μ_Δ, decreases and for values of γ less than 0.4, it does not match with the experimental findings.

9) There is a maximum dissipation of energy with $\gamma = 1.0$, while it is a minimum with $\gamma = 0.0$, which explains why with $\gamma = 1.0$, the number of cracks at the initial cracking load is a minimum, while with $\gamma = 0.0$, this number is a maximum. For values of $\gamma = 0.6$ and 0.4, the number of cracks is between the two extremes ($\gamma = 1.0$ and $\gamma = 0.0$).

10) The results presented for the shear panel W-4 verify the reliability of the computer program in handling the nonlinear finite element analysis under reversed cyclic loading. The load-deflection response, and computed crack patterns of the panel using the proposed cyclic load model follows closely the experimental results.

8.4 THE STRUCTURAL SHEAR WALLS

1) The current design method recommended by the CSA Standard CAN3-A23.3-M84 for estimating the failure load appears to be rather conservative when compared with the HODA program results. This is basically due to ignoring of the tension-stiffening, the tensile strength of the concrete and the strain-hardening of the reinforcing steel.

2) Tension-stiffening has a significant influence on the load-deflection response and the ultimate load of the structural walls. If tension-stiffening is eliminated from the model, the walls become more flexible and the ultimate load is smaller.

3) Using the smeared steel idealization to model the concentrated reinforcement in the wall, results in a higher failure load than using the bar element idealization. It would be more appropriate to use the bar element idealization for modelling the concentrated reinforcing steel in the structural wall.

8.5 RECOMMENDATIONS FOR FURTHER STUDIES

The following areas relating to the current study are needed to be further investigated:

1) The proposed formula for mesh dependency is mainly concerned with some structural elements such as, beams and shear panels. The same investigation is recommended in conjunction with other structural elements like slabs, structural cores, etc., to examine the validity of the proposed formula or developing new formulas if needed.

2) Although the proposed model for mesh dependency gave reasonable results for high strength beams used in this study, however, more analytical work is needed for structural elements built using high strength concretes.

3) Some more parametric studies can be undertaken on the structural walls to generate the basic data to be used for development of an appropriate practice-oriented design procedure for structural wall systems.

4) The hysteretic response of the structural wall under cyclic loading can also be studied using the HODA program.

STATEMENT OF ORIGINALITY

The analytical study undertaken in this research program is aimed at developing a simple material model for both normal and high-strength concrete structures under different static loadings. The model is implemented into a nonlinear finite element code to be used for the analysis of different concrete structural elements. Fifteen specimens are analyzed using the computer program HODA developed in this study and extensive parametric studies are undertaken on each specimen to examine the performance of the different modelling options available in the program for computing the responses of these structures. The original contributions in this thesis are:

1) A hypoelasticity model is developed based on the concept of equivalent uniaxial strain utilizing the rotation of the material axis during subsequent iteration/ load step.
2) The Popovics' stress-strain curve is modified for application into the above hypoelastic material model.
3) Based on the concept of focal point model, a fully automated algorithm is developed to produce automatically the loading and unloading branches of the concrete stress-strain curve subjected to reversed cyclic loading and corresponding to any point located on the envelope stress-strain curve using only the coordinates of that point.
4) The effect of damage resulting from extensive compressive microcracking is considered on the tensile strength of the concrete.
5) The effect of mesh size on the various behaviourial aspects of RC structures including load-deflection response, failure load, load-strain relationship, and cracks pattern is investigated.
6) A new simple model is proposed to remedy the mesh dependency drawback from nonlinear FE analysis of RC structures.
7) Extensive analytical studies are carried out on three structural shear wall from a medium-rise building, and the computed results are compared with the predicted response using the CSA standard A23.3-M84.

REFERENCES

Aboussalah, M. (1989), "Application of Constitutive Models for Concrete Structures", Ph. D. Dissertation, Department of Civil Engineering, Purdue University, USA.

Abrishami, H.H. (1994), "Studies on Bond and Cracking of Structural Concrete", Ph. D. Dissertation, Department of Civil Engineering and Applied Mechanics, McGill University, Montreal, Canada.

ACI Committee 363 (1992), "State of the Art Report on High Strength Concrete", ACI 363R-92.

ACI Committee 318 (1989), "Building Code Requirements for Reinforced Concrete", ACI 318-89, American Concrete Institute, Detroit, Michigan.

ADINA R&D Inc. (1990), "Automatic Dynamic Incremental Nonlinear Analysis", ADINA Users Manual, ARD 90-4.

Agrawal, A.B., Jaeger, L.G., and Mufti, A.A. (1976), "Crack Propagation and Plasticity of Reinforced Concrete Shear-Wall Under Monotonic and Cyclic Loading", International Conference on Finite Element Method, University of Adelaide, Adelaide, Australia.

Ahmad, S.H., and Shah, S.P. (1982), "Complete Triaxial Stress-Strain Curves for Concrete", Journal of Structural Division, ASCE, 108(4), 728-742.

Aktan, H.M. and Hanson, R.D. (1980), "Nonlinear Cyclic Analysis of R C Plane Stress members", ACI Publication SP-63, 135-152.

Al-Manaseer, A.A., and Phillips, D.V. (1987) "Numerical Study of Some Post-Cracking Material Parameters Affecting Nonlinear Solutions in RC Deep Beams", Canadian Journal of Civil Engineering, 14(5), 655-666.

American Concrete Institute (1991), " Fracture mechanics of concrete: concepts, models and determination of material properties", ACI 446.1R, Reported by ACI Committee 446 on Fracture Mechanics of Concrete.

Aoyama, H., and Neguchi, H. (1979), "Mechanical Properties of Concrete Under Load Cycles Idealizing Seismic Actions," State of the Art Report, AICAP-CEB Symposium on Structural Concrete Under Seismic Actions, Rome, Italy.

Argyris, J.H., Faust, G., Szimmat, J., Warnke, E.P. and William, K.J. (1973), "Recent Developments in the FE Analysis of Prestressed Concrete Reactor Vessels", Second International Conference on Structural Mechanics in Reactor Technology, Berlin, West Germany.

ASCE/ ACI Committee 447 (1991), "Finite Element Analysis of Reinforced Concrete Structures", Edited by J. Isenberg, the American Society of Civil Engineers, New York, USA.

ASCE Task Committee (1982), "Finite Element Analysis of Reinforced Concrete", State-Of-The-Art Report, ASCE, New York, USA.

Aziz, O. (1988), "A Mechanism Free Plane Quadrilateral Element with Rotational Degree of Freedom and the Associated Facet Shell Element", M. Eng. Thesis, Dept. of Civil Engineering., Carleton Univercity, Ottawa, Canada.

Bahlis, J. (1986), "An Experimental-Analytical Investigation of Hypoelastic Models for Plain and Reinforced Concrete", Ph. D. Dissertation, Department of Civil Engineering and Applied Mechanics, McGill University, Montreal, Canada.

Bahlis, J.B., and Mirza, M.S. (1987), "Nonlinear Analysis of Planar Reinforced Concrete Structures ", Canadian Journal of Civil Engineering, 14(6), 771-779.

Balakrishnan, S., and Murray, D.W. (1986), " Finite Element Prediction of R.C. Behaviour", Struct. Engrg. Report No. 138, University of Alberta, Edmonton, Canada.

Balakrishnan, S., Elwi, A. E. and Murray, W. (1988), "Effect of Modelling of NLFE Analysis of Concrete Structures". J. Struct. Engrg., 114(7), 1467-1487.

Balakrishnan, S., and Murrray, D.W. (1988), "Concrete Constitutive Model for NLFE Analysis of Structures," ASCE Journal of Structural of Structural Engineering, 114(7), 1449-1467.

Barzegar, F., and Schnobrich, C.W. (1986), "Nonlinear FE Analysis of R C Under Short Term Monotonic Loading", Structural Research Series No. 530, University of Illinois, Urbana, Illinois.

Barzegar, F., and Ramaswamy, A. (1990), "A Secant Post-Cracking Model for Reinforced Concrete with Particular Emphasis on Tension Stiffening", Proc., Second International Conference on Computer Aided Analysis and Design of Concrete Structures, Pinedridge Press, Vol. II, 1001-1016.

Bashur, F.K., and Darwin, D. (1978), "Nonlinear Biaxial Law for Concrete", Journal of the Structural Division, ASCE, 104(ST1), Proc., 157-170.

Bathe, K.J., Walczak, J., Welch, A., and Mistry, N. (1989), "Nonlinear Analysis of Concrete Structures", Computers & Structures, 32(3/4), 563-590.

Bathe, K.J., and Ramaswamy, S. (1979), "On Three-Dimensional Nonlinear Analysis of Concrete Structures", Nuclear Engineering Design, Vol. 52, 385-409.

Bazant, Z.P. (1983), "Comment on Orthotropic Models for Concrete and Geomaterials", Journal of Engineering Mechanics Division, ASCE, 109(3), 849-865.

Bazant, Z.P., and Cedolin, L. (1980), "Fracture Mechanics of Reinforced Concrete", Journal of Engineering Mechanics Division, ASCE, Vol. 106, 1287-1306.

Bazant, Z.P. and Bhat, P.D. (1976), "Endochronic Theory of Inelasticity and Failure of Concrete." Journal of Engineering Mechanics Division, ASCE, 102(EM4), 701-722.

Bazant, Z.P., and Lin, F.B. (1988), "Nonlocal Smeared Cracking Model for Concrete Fracture", Journal of Structural Engineering, ASCE, 114 (11), 2493-2510.

Bazant, Z.P., and Kim, S.S. (1979), "Plastic Fracturing Theory for Concrete", Journal of Engineering Mechanics Division, ASCE, 105(3), 407-428.

Bazant, Z.P. (1992)," Fracture mechanics of concrete structures", First International Conference on Fracture Mechanics of Concrete Structures, Colorado, USA, 1-5 June 1992.

Bazant, Z.P. (1983), "Comment on Orthotropic Models for Concrete and Geomaterials", Journal of Engineering Mechanics Division, ASCE, 109(3), 849-865.

Bazant, Z.P. (1986), "Mechanics of Distributed Cracking", Appl. Mech. Rev., ASME, 39(5), 675-705.

Bazant, Z.P., and Oh, B.H. (1983), "Crack Band Theory for Fracture of Concrete", Materials and Structures, Research and Testing (RILEM, Paris), 16(93), 155-177.

Bazant, Z.P., and Shieh, C.L. (1978), "Endochronic Model for Nonlinear Triaxial Behaviour of Concrete," Nuclear Engineering Design, 47, 305-315.

Bazant, Z.P., and Shieh, C.L. (1980), "Hysteretic Fracturing Endochronic Theory for Concrete", Journal of Engineering Mechanics Division, ASCE, 106(EM6), 929-950.

Bazant, Z.P. (1976), "Instability, Ductility and Size Effect in Strain-Softening Concrete", Journal of Engineering Mechanics Division, ASCE, 102(EM2), 331-344.

Bazant, Z.P., and Cedolin, L. (1979), "Blunt Crack Band Propagation in FE Analysis", Journal6 Engineering Mechanics Division, ASCE, 105(EM2), 297-315.

Bazant, Z.P., and Tsubaki, T. (1980), "Total Strain Theory and Path Dependence of Concrete", Journal of Engineering Mechanics Division, ASCE, 106(6), 1151-1173.

Bazant, Z.P., and Ozbolt, J. (1990), "Nonlocal Microplane Model for Fracture, Damage, and Size Effect in Structures", Journal of Engineering Mechanics, ASCE, 116(11).

Bazant, Z.P., and Cedolin, L.(1983), "Finite Element Modelling of Crack Band Propagation", Journal of Engineering Mechanics Division, ASCE, 109(ST2), 69-92.

Bello, H. (1992), "Nonlinear Finite Element Analysis of Planar RC Structures", M. Eng. Project G92-17, Department of Civil Engineering and Applied Mechanics, McGill University, Canada.

Buyukozturk, O. (1977), "Nonlinear Analysis of Reinforced Concrete Structures", Computers & Structures, vol.7, 149-156.

Buyukozturk, O., and Tseng, T.M. (1984), "Concrete in Biaxial Cyclic Compression." Journal of Structural Engineering, ASCE, 110(3), 461-476.

Canadian Standards Association (1984) "Design of Concrete Structure for Buildings," CAN3-A23.3-M84., Rexdale, Ontario, Canada.

Cardenas, A.E., Russell, H.G., and Corley, W.G. (1980), "Strength of Low-Rise Structural Walls," Reinforced Concrete Structures Subjected to Wind and Earthquake Forces, SP-63, ACI, 221-241.

Carrasquillo, R.L., Nilson, A.H., and Slate, F.O. (1981), "Properties of High Strength Concrete Subject to Short-Term Loads", ACI Journal, 78(3), 171-178.

Carreina, D. J., and Chu, K.H. (1985), "Stress-Strain Relationship for Plain Concrete Under Compression", ACI Journal, 82(6), 797-804.

Cedolin, L., Crutzen, Y.R.J., and Dei Poli, S. (1977), "Triaxial Stress-Strain Relationship for Concrete, Journal of Engineering Mechanics Division, ASCE, 103(EM3), 423-439.

Cervenka, V., and Gerstle, K. H. (972), "Inelastic Analysis of R C Panels", Proceedings of International Association for Bridge and Structural Engineering, Vol.32-II.

Cervenka, V., and Gerstle, K. H. (1971), "Inelastic Analysis of Reinforced Concrete Panels", Proceedings of International Association for Bridge and Structural Engineering, Vol.31-II.

Cervenka, V. (1985), "Constitutive Model for Cracked Reinforced Concrete", Journal of the American Concrete Institute, 82(6), 877-882.

Cervenka, V. (1970), "Inelastic finite Element Analysis of Reinforced Concrete Panels Under In-Plane Loads", Ph. D. Dissertation, Department of Civil Engineering, University of Colorado.

Chen, E. S., and Buyukozturk, O. (1985), "Constitutive Model for Concrete in Cyclic Compression," Journal of Structural Engineering, ASCE, 111(6), 797-814.

Chen, W.F., and Han, D.J. (1988), "Plasticity for Structural Engineers", Springer-Verlag, New York, 606 pp.

Chen, A.T.C, and Chen, W.F. (1975),"Constitutive Relations for Concrete",Journal of Engineering Mechanics, ASCE, 101(4), 465-481.

Chen, W.F. (1975), "Limit Analysis and Soil Plasticity", Elsevier Science Publishing Co., Amsterdam, The Netherlands.

Chen, W. F. (1982), "Plasticity in Reinforced Concrete" McGraw-Hill Book Co., Inc., New York.

Chen, W.F. (1992), "Concrete Plasticity: Macro and Micro Approaches", Structural Engineering Report No. CE-STR-92-25, School of Civil Engineering, Purdue University, west Lafayette, IN, 63 PP.

Chen, W.F., and Cohen, M.D. (1992), "Micromechanical Considerations in Concrete Constitutive Modelling", Proceeding of 10th ASCE Structures Congress, San Antonio, TX, J. Morgan, Ed., May 13-15, 270-273.

Chinniah, J. (1985), "Finite Element Formulation for Thin Plates and Shell Structures," Ph.D Thesis, Department of Mechanical and Aeronautical Engineering, Carleton Universtiy, Ottawa, Canada.

Choi, C.K., and Kwak, H.G. (1990), "The Effect of FE Mesh Size in Nonlinear Analysis of RC Structures", Computer & Structures, 369(5), 807-815.

Collins, N.P., Mitchell, D., MacGregor, J. G. (1993). "Structural Design Considerations for High-strength Concrete", Concrete International, the Magazine of ACI, 27-34.

Collins, M.P., Vecchio, F.J. and Mehlron, G. (1985), "An International Competition to Predict the response of Reinforced Concrete Panels", Canadian Journal of Civil Engineering, 12(3), 626-644.

Collins, M.P., and Porasz, A. (1989), "Shear Design for High Strength Concrete", CEB Bulletin d'Information, No. 193, 77-83.

Collins, M.P., Mitchell, D. (1991), "Prestressed Concrete Structures", Prentice-Hall Inc., England Cliffs, New Jersey, 766 pp.

Cope, R.J., et al. (1980), "Modelling of Reinforced Concrete Behaviour for Finite Element Analysis of Bridge Slabs," Numerical Methods for Nonlinear Problems, C. Taylor et al., Eds., Vol. 1, Pineridge Press, Swansea, U. K., 457-470.

Crisfield, M.A., and Wills, J. (1987), "Numerical Comparisons Using Different Concrete Models", Proc., IABSE Colloq. on Computational Mechanics of Concrete Structures- Advances and Applications, Delft University Press, Delft, The Netherlands, 177-188.

Crisfield, M.A., and Wills, J. (1989), "Analysis of RC Panels Using Different Concrete Models," Journal of Engineering Mechanics Division, ASCE, 115(3), 578-597.

Darwin, D. and Pecknold, D. (1974), "Inelastic Model for Cyclic Biaxial Loading of Reinforced Concrete", SRS No. 409, University of Illinois at Urban- Champaign, Illinois, USA.

Darwin, D. (1985)." Concrete Crack Propagation - Study of Model Parameters", Proc. F.E. Analysis of R. C. Structures, Eds. Meyer, C., and Okamura, H., ASCE, New York, PP. 184-203.

Darwin, D. and Pecknold, D. (1977), "Analysis of Cyclic Loading of Plain Reinforced Concrete Structures", Journal of Computers and Structures, 7, 137-147.

Darwin, D. and Pecknold, D. (1977), "Nonlinear Biaxial Stress-Strain Law for Concrete", Journal of the Engineering Mechanics Division, Proceedings ASCE, 103(EM 2), 229-241.

Darwin, D. and Pecknold, D. (1975), "Analysis of Shear Panels Under Cyclic Loading," Journal of the Engineering Mechanics Division, Proceedings ASCE, 102(ST 2), 355-369.

Desai, C. S. and Abel, J. F. (1972), "Introduction to the Finite Element Method, a Numerical Method for Engineering Analysis," Van Nostrand Reinhold Company, New York.

Dougill, J.W. (1975), "Some Remarks on Path Independence in the Small in Plasticity", Quarterly of Applied Mathematics, Vol.32, 423-437.

Elwi, A.A., and Murray, D.W. (1979), "A 3D Hypoelastic Concrete Constitutive Relationship", Journal of the Engineering Mechanics Division, ASCE, 105(EM4), 623-641.

Fafitis, A., and Shah, S.P. (1984), "Rheological Model for Cyclic Loading of Concrete." Journal of Structural Engineering, ASCE, 110(9), 2085-2102.

Fafitis, A., Shah, S.P., and Arnold, R. (1983), "Cyclic Loading of Spirally Reinforced Concrete," Journal of Structural Engineering, ASCE, 109(7), 1695-1710.

Fafitis, A., and Shah, S.P. (1984), "Rhelogical Model for Cyclic Loading of Concrete." Journal of Structural Engineering, ASCE, 110(9), 2085-2102.

Fardis, M. N., Alibe, B., and Tassoulas, J. L. (1983), "Monotonic and Cyclic Constitutive Law for Concrete." Journal of Engineering Mechanics , ASCE, 109(2), 516-536.

Feenstra, P.H., de Borst, R. (1993), "Aspects of Robust Computational Modeling for Plain and Reinforced Concrete," Heron Publication, vol. 38, No. 4.

Frantziskonis, G., and Desai, C.S. (1987), "Elasto-Plastic Model with Strain Softening Geomaterials", Acta Mechanics, Vol. 68, a51-170.

Gaston, J.R., and Siess, C.P. and Newmark, N.M. (1952), "An Investigation of the Load-deformation Characteristics of Reinforced Concrete Beams up to the Point of Failure". Structureal Research Series, No. 40, University of Illinois, Urbana.

Ghoneim, G.A.M. and Ghali, A. (1982), "Nonlinear Analysis of Concrete Structures." Canadian J. Civ. Engrg., 9(3), 489-501.

Ghoneim, G.A.M. (1978), "Nonlinear Analysis of Concrete Structures" Ph.D Thesis, Department of Civil Engineering, University of Calgary, Calgary, Canada.

Gilbert, R.I., and Warner, R.F. (1978), "Tension Stiffening in RC Slabs", Journal of structural Engineering, ASCE, Vol. 104, 1885-1900.

Gopalaratnam, V.S., Shah, S.P. (1985), "Softening Response of Plain Concrete in Direct Tension.", ACI J., Proc., 82(3), 310-323.

Gupta, A. K., and Akbar, H. (1984), "Cracking in Reinforced Concrete Analysis," Journal of the Structural Division, ASCE, 110(8), 1735-1746.

Gylltoft, K. (1983), "Fracture Mechanics Models for Fatigue in Concrete Structures," Ph.D Thesis, Division of Structural Engineering, Lulea University, Sweden.

Han, D.J. and Chen, W.F. (1985), "A Uniform Hardening Plasticity Model for Concrete Materials", mechanics of Materials, Vol. 4, 283-302.

Hand, F. R., Pecknold, D. A. and Schnobrich, W. C. (1973), "Nonlinear Layered Analysis of RC Plates and Shells", Journal of the Structural Division, ASCE, 99(ST7), 1491-1505.

Hanna, Y. G. (1983), "Finite Element Modelling of Reinforced Concrete Structures", Ph. D. Dissertation, Department of Civil Engineering and Applied Mechanics, McGill University, Montreal, Canada.

Hanna, Y.G., and Mirza, M.S. (1983). "Post-cracking behaviour of planar concrete structures," Canadian Structural Concrete Conference, Ottawa, Ont., 107-127.

Hu, H.-T., and Schnobrich, W.C. (1990), "Nonlinear analysis of cracked reinforced concrete", Structural Journal of the American Concrete Institute, 87(2), 199-207.

Kabir, A.F. (1976), "Non-Linear Analysis of Reinforced Concrete Panels, Slabs and Shells for Time Dependent Effects," Ph.D thesis, UC-SESM Report No.76-6,Division of Structural Engineering and Structural Mechanics, University of California, Berkeley, Ca.

Kachanov, L.M. (1986), "Introduction to Continuum Damage Mechanics", Martinus, Nijhoff, Netherlands.

Karsan, I.D. and Jirsa, J.O. (1969), "Behaviour of Concrete under Compressive Loading", Journal of the Structural Division, ASCE, 95(12), 2543-2563.

Kheyroddin, A., Shayanfar, M.A., Mirza, M.S. (1994), "Influence of Element Size in Nonlinear Analysis of Concrete Beams", CSCE Annual Conference, June 1-4, 1994, Winnipeg, Manitoba, Canada.

Kolleger, J., and Mehlhorn, G. (1987), "Material Model for Cracked Reinforced Concrete," Proc., IABSE Colloq. on Computational Mechanics of Concrete Structures- Advances and Applications, Delft University Press, Delft, The Netherlands, 63-74.

Kotsovos, M.D., and Newman, J.B. (1978), "Generalized Stress-Strain Relations for Concrete", Journal of the Structural Division, ASCE, 104(EM4), 845-856.

Krajcinovic, D., and Fonseka, G.U. (1981), "The Continuous Damage Theory of Brittle Materials", Journal of Applied Mechanics, ASME, Vol.48, 809-824.

Kupfer, H.B., Gerstle, K. H. (1973), "Behaviour of Concrete under Biaxial Stresses," Journal of the Structural Division, ASCE, 99(EM 4), 852-866.

Kupfer, H.B., Gerstle, K. H., and Rüsch, H. (1969), "Behaviour of Concrete Under Biaxial Stresses," Journal of ACI, 66(8), 656-666.

Lefas, I.D.; Kotsovos, M.D. and Ambraseys, N.N. (1990), "Behaviour of Reinforced Concrete Structural Walls : Strength, Deformation Characteristics, And Failure Mechanism," ACI Structural Journal, 87(S3), 23-31.

Leslie, K.E., Rajagopalan, K.S., and Everard, N.J. (1976), "Flexural Behaviour of High-Strength Concrete Beams", ACI Journal, 517-521.

Lim, S.A. (1994), "Design and Nonlinear Analysis of Low-Rise Structural Walls", M. Eng. Project, Department of Civil Engineering and Applied Mechanics, McGill University, Canada.

Lin, S.C., and Scordelis, A.C. (1975), "Nonlinear Analysis of RC Shells of General Forms," Proceedings, ASCE, 101(ST 3), 523-538.

Lin, S. C. (1973). "Nonlinear Analysis of RC Slabs and Shells", Ph. D. Thesis, Division of Structural Engineering Mechanics, University of California,Berkeley, UC-SESM, Report No.73-7.

Liu, T.C., Nilson, A.H., and Slate, F.O. (1972), "Stress-Strain Response and Fracture of Concrete in Uniaxial and Biaxial Compression", Journal of ACI, 69(5), 291-295.

Lubliner, J., Oliver, J., Oller, S., and Onate, E. (1989), "A Plastic-Damage Model for Concrete", International Journal of Solids and Structures, 25(5), 299-326.

Manatakos, K. (1989), "Analysis of Low- and Medium-Rise Buildings", M.Eng Thesis, Department of Civil Engineering & Applied Mechanics, McGill University, Canada.

Mazars, J. (1986), " A Discription of Micro- and Macro-Scale Damage of Concrete Structures", Engineering Fracture Mechanics, 25(5/6), 523-537.

Mazars, J. (1981), "Mechanical Damage and Fracture of Concrete Structures," Advances in Fracture Research, ICFS, Cannes, Vol.4, 1499-1506.

McNeal, H., and Harder, K.H. (1988), "Refined Four-Noded Membrane Element with Rotational Degree of Freedom," Computers & Structures, 28(1), 75-84.

Meyer, C. and Okamura, H., Eds. (1985), "Finite Element Analysis of R C Structures." ASCE, NewYork.

Mikkola, M. J. and Schnobrich, W. C. (1970), "Material Behaviour Characteristics for R C Shells Stressed Beyond the Elastic Range", SRS-367, University of Illinois.

Milford, R. V., and Schnobrich, W. C. (1984), "Nonlinear Behaviour of Reinforced Concrete Cooling Towers," Report ISSN: 0069-4274, University of Illinois, Urbana, Il1.

Mills, R.H., and Ons, K.V. (1972), "Elastic Modulus of Close-packed Randomly Oriented Maxwell Elements", Journal Materiaux et Constructions, 5(27), 127-133.

Mochizuki, S. and Kawabe, S. (1980), "Experiment of Shear Wall Restricted by Frame Under Repeated Pure Shear (Part 3: FE Analysis)", Proceedings, Annual Convention, AIJ, 1619-1620.

Mufti, A.A., Mirza, M.S., McCutchen, J.O. and Spokowski, R.W. (1971), "A Finite Element Study of R C Structures." Structural Concrete Series No.71-8, McGill University, Montreal, Canada.

Murray, D.W., et al. (1979), "Concrete Plasticity Theory for Biaxial Stress Analysis", Journal of the Structural Division, ASCE, 105(6), 989-1006.

Muto, K., Tsugawa, T., and Masuda, K. (1972), "Nonlinear Analysis of R C Members by FEM (Part 4: Under Repeated Forces)", Proceeding, Annual Convention, AIJ, 685-686.

Nagaraja,V. S. (1987), "Constitutive Modelling for the Nonlinear FE Analysis of Plain and Reinforced Concrete." Ph.D. Thesis, Department of Civil Engineering, Indian Institute of Science, Banglore, India.

National Research Council of Canada (1990), "National Building Code of Canada, 1990" Ottawa, Ontario, Canada.

Nelissen, L. J. M. (1972), "Biaxial Testing of Normal Concrete," Heron Netherlands 18(1).

Ngo, D., and Scordelis, A.C. (1967), "Finite Element Analysis of Reinforced Concrete Beams," Journal of the American Concrete Institute, 64(3), 152-163.

Nilson, A. H. (1968), " Nonlinear Analysis of R C by the FEM", ACI Journal, 65(9).

Nofal, M.E. (1988), "Inelastic Load Distribution of Composite Concrete-Steel Slab-on-Girder Bridges - an Analytical and Experimental Study," M.Eng. Thesis, Department of Civil Engineering, Carleton University, Ottawa, Ont.

Noguchi, H. (1985), "Analytical Models for Cyclic Loading of R C Members", Proceedings of the Conference on Finite Element Analysis of Reinforced Concrete Structures, Edited by C. Meyer and H. Okamura, ASCE.

Nomura, S., Sato, K. and Ono, H. (1978), "Analysis of Hysteresis of R C Members Under Cyclic Loading by FEM." Proceeding, Annual Convention, AIJ, 1469-1470.

Ohtani, Y., and Chen, W.F. (1987), "Hypo-Elastic Perfectly Plastic model for Concrete Materials", Journal of the Structural Division, ASCE, 113(12), 1840-1860.

Oliver, J., Cervenka, M., Oller, S., Lubliner, J. (1990), "Isotropic Damage Models and Smeared Crack Analysis of Concrete", Computer Aided Analysis and Design of Concrete Structures, Pineridge Press, Swansea, Vol. 2, 945-958.

Ortiz, M., and Popov, E.P. (1982), "Plain Concrete as a Composite Material", Mechanics of Materials, 1(2), 139-150.

Ottoson, N.S., (1979), "Constitutive Model for Short-Time Loading of Concrete", Engineering Mechanics.

Palaniswamy, R., and Shah, S.P. (1974), "Fracture and Stress-Strain Relationship of Concrete Under Triaxial Compression", Journal of the Structural Division, ASCE, 100(ST5), 901-916.

Paulay, T., and Priestley, M.J.N. (1992), "Seismic Design of Reinforced Concrete and Masonry Buildings," John Wiley and Sons Inc., USA.

Peterson, P. E. (1981), "Crack Growth and Development of Fracture Zones in Plain Concrete and Similar Materials," Report No. TVBM-1006, Lund Institute of Technology, 174 pp.

Pollak, M.A., and Vecchio, F.J. (1993), "Nonlinear Analysis of Reinforced Concrete Shells", Publication No. 93-03, Department of Civil Engineering, University of Toronto.

Popovics, S. (1973), "A Numerical Approach to the Complete stress-strain Curve of Concrete", Cement and Concrete Research, 3(5). 583-599.

Rashid, Y. R. (1968), "Ultimate Strength Analysis of Prestressed Concrete Pressure Vessels", Nuclear Engineering and Design, 7(4), 334-344.

Razaqpur, A.G. and Nofal, M.E. (1988), "Transverse Load Distribution at Ultimate States in Single Span Slab on Girder Bridges." Final Report, Proj: 23182, Ministry of Transportation of Ontario (MTO), Downsview, Ontario, Canada.

Razaqpur, A.G., and Nofal, M. (1990), "Analytical Modelling of Nonlinear Behaviour of Composite Bridges", ASCE Journal of the Structural Division, 116(ST6), pp. 1715-1733.

Razaqpur, A.G.; Nofal, M. and Mirza, M.S. (1989), "Nonlinear Analysis of Prestressed Concrete Box Girder Bridges under Flexure", Canadian Journal of Civil Engineering, 16(6), pp.845-853.

Razaqpur, A.G. and Nofal, M.E. (1987), "Performance a New Quadrilateral Finite Element With Rotational Degree of Freedom." Proceedings, 5th World Congress on FE Methods. Salzburg, 121-130.

Rots, J.G., Nauta, P., Kusters, G.M.A. and Blaauwendraad, J., (1985), "Smeared Crack Approach and Fracture Localization in Concrete", HERON, 30(1).

Rots, J. G. (1988), "Computational Modelling of Concrete Fracture," Ph. D. Dissertation, Civil Engineering Department, Delft University of Technology, Delft, The Netherlands.

Rule, W.K., and Rowlands, R.E. (1992), "Predicting Behaviour of Cyclically Loaded RC Structures", Journal of Structural Engineering, ASCE, 118(2), 603-616.

Saada, A.S. (1993), "Elasticity, Theory and Applications", Reisman-Herbert Publication.

Saenz, L. P. (1965), "Equation for the Stress-Strain Curve of Concrete in Uniaxial and Biaxial Compression of Concrete", Journal of ACI, 61(9), 1229-1235.

Scanlon, A. (1971), "Time Dependent Deflections of Reinforced Concrete Slabs", Ph. D. Dissertation, University of Alberta, Edmonton, Canada.

Schnobrich, W. C. (1972), Discussion of "Nonlinear Stress Analysis of Reinforced Concrete" by Vallipan and Doolan, Journal of the Structural Division, ASCE, 98(ST10), 2327-2328.

Selby, R.G., and Vecchio, F.J. (1993), "Three-Dimensional Constitutive Relations for Reinforced Concrete", Publication No. 93-02, Department of Civil Engineering, University of Toronto.

Shayanfar M.A., Kheyroddin, A. and Mirza, M.S. (1993), "Fir te Element Size Effects in Nonlinear Analysis of R C Structures," Structural Engineering Report No. 93-3, Department of Civil Engineering and Applied Mechanics. McGill University, Montreal.

Shayanfar, M.A., "Matrix Structural Analysis", Lecture Notes, Department of Civil Engineering and Applied Mechanics, McGill University, Montreal, 1994.

Shayanfar, M.A., Kheyroddin, A., Mirza, M.S. "Element Size Effects in Nonlinear Analysis of Reinforced Concrete Members", A Paper Accepted for Publication in Computers & Structures, London, U. K.

Shayanfar, M.A. and Mirza, M.S. "Stress-Strain Curves for Concrete Under Cyclic Load", Structural Engineering Report No. 94-4, Department of Civil Engineering and Applied Mechanics, McGill University, Montreal, 1994.

Shideler, J.J. (1957), "Light Weight Agregate Concrete for Structural Use", ACI Journal, Proceedings, 54(4), 299-328.

Shipman, J. M., and Gerstle, K.H. (1979), "Bond Deterioration in Concrete Panels Under Load Cycles", ACI Journal, 1469-1470.

Simo, J. C. and Ju, J.W. (1987), "Strain- and Stress-Based Continuum Damage Models- I. Formulation", International Journal of Solids and Structures, 23(7), 821-840.

Imoto, K., and Takeda, T. (1973), "Nonlinear Analysis of R C Members by FEM: Part1,", Proceeding, Annual Convention, AIJ, 505-506.

Sinha, B.P., Gerstle, K.H. and Tulin, L.G. (1964), "Stress-Strain Relations for Concrete under Cyclic Loading", Journal of ACI, Proc., 61(2), 195-211.

Sisodiya, R.G., Cheung, Y.K., and Ghali, A. (1972), "New Finite Elements with Application to Box Girder Bridges", Journal of the Institution of Civil Engineers, Paper No. 7479.

Smith, G.M., and Young, L.E. (1955), "Ultimate Theory in Flexure by Exponential Function," Journal of ACI, 52(3), 349-359.

Sorensen, S. I. (1979), "Plasticity and Endochronic Inelasticity in FE Analysis of R C", Final Report, Vol. Band 29,IABSE Colloquium, Copenhagen, 59-66.

Stevens, N.J., Uzumeri, S.M., Collins, M.P. and Will, G.T. (1991), "Constitutive Model for R C Finite Element Analysis.", ACI Structural J., 88(1), 49-59.

Stevens, N.J., Uzumeri, S.M. and Collins, M.P. (1991), "RC Subjected to Reversed Cyclic Shear-Experiments and Constitutive Model", ACI Structural J., 88(2),135-146.

Suidan, M., and Schnobrich, W.C. (1973), "Finite Element Analysis of Reinforced Concrete", Journal of the Structural Division, ASCE, 99(ST10), 2109-2121.

Suriyachat, P. (1992), "Modelling of Mine Opening Using Nonlinear Finite Element Method", Ph.D. Dissertation, Department of Min. and Met. Eng., McGill University, Montreal, Canada.

Tasuji, M.E., Nilson, A.H., Slate, F.O. (1979), "Biaxial Stress-Strain Relationships for Concrete", Magazine of Concrete Research, 31(109), 217-224.

Thorenfeldt, E., Tamaszemicz, A., Jenson, J.J. (1987), "Mechanical Properties of High Sterngth Concrete and Application in Design", Proceedings of the Symposiumon Utilization of High Strength Concrete, Tahir, Trandheim, 149-159.

Tsai, W.T. (1988), "Uniaxial Compressional Stress-Strain Relation of Concrete", Journal of the Structural Division, ASCE, 114(9), 2133-2136.

Valanis, K.C. (1971), "A Theory of Viscoplasticity Without a Yield Surface, Part I, General Theory", Archives of Mechanics, 23(4), 517-534.

Vecchio, F.J., and Collins, M.P. (1986), "The Modified Compression-Field Theory for Reinforced Concrete Elements Subjected to Shear", Journal of the American Concrete Institute, 83(2), 219-231.

Vecchio, F.J. (1989), "Nonlinear Finite Element Analysis of Reinforced Concrete Membranes", Structural Journal, ACI, 26-35.

Vecchio, F. (1981), "The Response of RC to Inplane Shear Normal Stresses", Ph.D. Thesis, Department of Civil Engineering, University of toronto, Toronto, Canada.

Vecchio, F.J., and Collins, M.P. (1982), "The Response of RC to Inplane Shear Normal Stresses", Publication No. 82-03, Department of Civil Engineering, University of Toronto.

Vonk, R.A. (1990), "Softeneing of Concrete Loaded in Compression", Ph. D. Dissertation, Eindhoven University of Technology, The Netherlands.

Willam, K.J., and Warnke, E.P. (1975), "Constitutive Model for the Triaxial Behaviour of Concrete", International Association for Structural Engineering Proceedings, Vol. 19.

Yamaguchi, E., and Chen, W.F. (1991), "Microcrack Propagation Study of Concrete Under Compression", Journal of Engineering Mechanics, ASCE, 117(3), 653-673.

Yankelevsky, D.Z., and Reinhardt, H.W. (1989), "Uniaxial Behaviour of Concrete in Cyclic Tension", Journal of Structural Engineering, ASCE, 115(1), 166-182.

Yankelevsky, D.Z., and Reinhardt, H.W. (1987), "Model for Cyclic Compression Behaviour of Concrete", Journal of Structural Engineering, ASCE, 113(2), 228-240.

Yankelevsky, D.Z., and Reinhardt, H.W. (1987), "Response of Plain Concrete to Cyclic Tension", ACI Materials Journal, 84(5), 365-373.

Zienkiewicz, O.C., Valliappan, S., and King, I.P. (1969), "Elasto-Plastic Solutions of Engineering Problems-Initial Stress- Finite Element Approach," International Journal for Numerical Methods in Engineering, Vol.1.

Zienkiewicz, O.C. (1983), "The Finite Element Method", 3rd Edition, McGraw-Hill Book Company, Berkshire, United Kingdom, 234-240.

APPENDIX A

INPUT DATA FOR THE HODA PROGRAM

MARCH 1994

```
CSSSSSSSSSSSSSSSSSSSSSSSSSSSSSSSSSSSSSSSSSSSSSSSSSSSSSSSSSSSSSSSSSSSSSSSSSSS

C       MAIN PROGRAM

CSSSSSSSSSSSSSSSSSSSSSSSSSSSSSSSSSSSSSSSSSSSSSSSSSSSSSSSSSSSSSSSSSSSSSSSSSSS
C  READ INPUT CARD # 1  --  TITLE HEADING IDENTIFICATION CARD
   read(55,10) 8[A10]
C
       hed  =  heading title identification of 80 characters  (max)
CRRRRRRRRRRRRRRRRRRRRRRRRRRRRRRRRRRRRRRRRRRRRRRRRRRRRRRRRRRRRRRRRRRRRRRRRRRR
C   READ INPUT CARD # 2  --  CONTROL CARD TYPE OF ANALYSIS
   read(55,*) 11[I5]
C
       numnp   = number of nodes

       neltyp  = number of element types (3 max)

                 --  quadrilateral facet shell element
                 --  boundary element
                 --  one-dimensional bar element




       nquad   = quadrilateral shell element type

                 --  0  = QLC3  +  RBE
                        --  plane stress + bending
                        --  linear n  and cubic  e
                        --  beam behaviour problems
```

-- 1 = RQUAD4 + IDKQ4
-- membrane + thick/thin bending
-- cubic field both n and e
-- general behaviour

ntime = number of time intervals for time-dependent

-- 30 time intervals (max)
-- 1 for instantaneous monotonically increasing load

icreep = creep analysis indicator

-- 0 = not required
-- 1 = is required

ishrink = shrinkage analysis indicator

-- 0 = not required
-- 1 = is required

itemp = temperature analysis indicator

-- 0 = not required
-- 1 = is required

norm = convergence and divergence criteria indicator

-- 0 = force norm -- maximum allowable forces
-- F_x, F_y, F_z, M_x, M_y, M_z

-- 1 = displacement norm -- maximum allowable displacements
-- δ_x, δ_y, δ_z, θ_x, θ_y, θ_z

knorm = type of norm values input

-- 0 = percentages of forces/displacement
-- 1 = actual magnitude of norm values of forces/displacements

kult = ultimate analysis indicator

-- 0 = linear/nonlinear elastic analysis
at one load interval
-- use 1 load step and 1 iteration

-- 1 = nonlinear inelastic analysis

```
      kinteg  = order of numerical integration
                -- gauss integration grid element points

                -- 1  =  1 integration point  (min)
                -- 2  =  2 by 2 integration points
                -- 3  =  3 by 3 integration points  (preferred)
                -- 4  =  4 by 4 integration points  (max special cases)


CRRRRRRRRRRRRRRRRRRRRRRRRRRRRRRRRRRRRRRRRRRRRRRRRRRRRRRRRRRRRRRRRRRRRC
 READ INPUT CARD # 3  --  SELECTION OF NEW OPTIONS IMPLEMENTED
   read(55,*) 7[I5], 2F5.2
C
      mdep= mesh dependency analysis factor
                --1      no mesh dependency analysis
                --2      mesh dependency analysis based on the crack band theory
                --3      mesh dependency analysis based on the proposed model

      munit= unit system option
                --1      Imperial units (in, Psi)
                --2      SI  units (mm, N)

      mcurve= curve selection option
                --1      Saenz and Smith's equations
                --2      Popovics' equation

      iconst= constitutive matrix selection option
                --1 Darwin's constitutive matrix
                --2 Proposed Constitutive matrix utilizing also the transformation of equivalent
                                  uniaxial strains during subsequent iteration

      icolins= tension-compression failure option
                --1      Kupfer and Gerstle
                --2      Vecchio and Collins

      icrack= cracking model option
                --1      Fixed crack model
                --2      Rotating crack model

     icycle=loading type index
                --1      monotonically increasing load
                --N      cyclic loading with n cycles (N<30)

      iunload= tensile loading-unloading option
                --1      Horizontal unloading
                --2      Secant unloading
```

esoft= softening stiffness factor
--0.0 Original version
--A very small value To avoid numerical difficulties

gstif= tensile softening branch option
--1.0 Original version (no dropping at all)
--0.0 Sudden drop to zero after cracking with no tension-stiffening capability
--1.0-0.0 Dropping after cracking with tension-stiffening capability

```
CRRRRRRRRRRRRRRRRRRRRRRRRRRRRRRRRRRRRRRRRRRRRRRRRRRRRRRRRRRRRRRRRRRRRRC
 READ INPUT CARD # 4  --  SELECTION OF REQUIRED OUTPUT
   read(55,*) 6[I5]
C
       kout  = output for every iteration or each load step

             --  0  = results for each load step and last iteration
             --  1  = results for every load iteration

       kdis  = output displacements in element local coord system

             --  0  = not required
             --  1  =  is required

       kcur  = output curvatures

             --  0  = not required
             --  1  =  is required

       kstn  = output strains

             --  0  = not required
             --  1  =  is required

       kiter = output unbalanced forces

             --  0  = not required
                    -- printed for each load step only

             --  1  = is required
                    -- printed for every iteration

       ksoln = solution required
             --  0  = solution
             --  1  = data check
```

```
CRRRRRRRRRRRRRRRRRRRRRRRRRRRRRRRRRRRRRRRRRRRRRRRRRRRRRRRRRRRRRRR
C   READ INPUT CARD # 5  --  OUTPUT STRESSES AT REQUIRED INTEGRATION
    POINTS OF QUADRILATERAL FACET SHELL ELEMENT
C
   read(55,*) 16[I2]

      kotg = element stresses at gauss integration points required:


       enter a total of 16 values of  0's  or  1's
            one value for each gauss integration point

              --  0  = not required
              --  1  =  is required

CRRRRRRRRRRRRRRRRRRRRRRRRRRRRRRRRRRRRRRRRRRRRRRRRRRRRRRRRRRRRRRRC
 READ INPUT CARD # 6  --  CONVERGENCE TOLERANCES -- LIMIT CRITERIA
C
C   For convergence of load increments to proceed to next load step
C   Select displacement type -- realistic values
C
   read(55,*) 6[F10.0]

      toler = six tolerable convergence components
              (DELTA 2 - DELTA 1) = Difference for convergence

      one   =  x- force/displacement  = 0.001 mm

      two   =  y- force/displacement  = 0.001 mm

      three =  z- force/displacement  = 0.001 mm

      four  =  x- moment/rotation  = 0.005 rad

      five  =  y- moment/rotation  = 0.005 rad

      six   =  z- moment/rotation  = 0.005 rad
CRRRRRRRRRRRRRRRRRRRRRRRRRRRRRRRRRRRRRRRRRRRRRRRRRRRRRRRRRRRRRRRC
C   READ INPUT CARD # 7  --  DIVERGENCE TOLERANCES -- LIMIT CRITERIA
C
C   For divergence of load steps to indicate failure of structure
C   Select displacement type -- realistic values
   read(55,*) 6[F10.0]

      vmax = six tolerable divergence components
             maximum permissible values
```

```
      one   =  x- force/displacement  = 10 times elastic results
                                          (mm)
      two   =  y- force/displacement

      three =  z- force/displacement

      four  =  x- moment/rotation  = 15 times elastic results
                                       (rad)
      five  =  y- moment/rotation

      six   =  z- moment/rotation

CRRRRRRRRRRRRRRRRRRRRRRRRRRRRRRRRRRRRRRRRRRRRRRRRRRRRRRRRRRRRRRRRRRRRRRRRRC
C   READ INPUT CARD # 7-A  --  LOAD STEPS AND TYPE 2 NODES LOADED
C
   read(55,*) 2[I5]

      nlstps = number of load steps for analysis  (30 max)

      njl2   = number of type 2 nodes loaded

           -- Type 2 nodes = A different set of nodes loaded in
                             load steps  j-steps

             used for live loads, truck loads, etc
             different set of loads from Type 1 nodes loaded

CRRRRRRRRRRRRRRRRRRRRRRRRRRRRRRRRRRRRRRRRRRRRRRRRRRRRRRRRRRRRRRRRRRRRRRRRRC
 nlstep=nlstps
CRRRRRRRRRRRRRRRRRRRRRRRRRRRRRRRRRRRRRRRRRRRRRRRRRRRRRRRRRRRRRRRRRRRRRRRRRC
C   READ INPUT CARD # 7-B  --  OUTPUT RESULTS AT REQUIRED LOAD STEPS
C
   read(55,*) 40[I2]

      (lstpop(i), i=1,nlstps)

      = output results at load steps required:

        -- enter a number of  0's  or  1's  for every load step
           for a total equal to NLSTPS

        --  0  not required
        --  1   is required

  CAUTION :  Does not work correctly!!
             Always enter  NLSTPS of  1's
```

```
CRRRRRRRRRRRRRRRRRRRRRRRRRRRRRRRRRRRRRRRRRRRRRRRRRRRRRRRRRRRRRRRRRRRRRC
 READ INPUT CARD # 8  --  REFERENCE TEMPERATURE  For ZERO STRESSES
C
   if(itemp .eq. 1)      omit if ITEMP = 0
   read(55,*) 8[F10.0]

       contemp = concrete reference temperature for zero stresses

CSSSSSSSSSSSSSSSSSSSSSSSSSSSSSSSSSSSSSSSSSSSSSSSSSSSSSSSSSSSSSSSSSSSSSSS
C  SUBROUTINE  INPUTJ
CSSSSSSSSSSSSSSSSSSSSSSSSSSSSSSSSSSSSSSSSSSSSSSSSSSSSSSSSSSSSSSSSSSSSSSS
C  READ INPUT CARD # 9  --  NODAL POINT DATA
   read(55,*) 7[I5]  3[F10.0]  [I5]

       n        = node number

       (id(i,n), i=1,6) = boundary conditions for degrees of freedom:

       delta x  = 0  or  1

       delta y  = 0  or  1

       delta z  = 0  or  1

       theta x  = 0  or  1

       theta y  = 0  or  1

       theta z  = 0  or  1

              --  0  = unrestrained DOF
              --  1  =  restrained  DOF

       x(n)     = x-coordinate  --  global axes

       y(n)     = y-coordinate  --  global axes

       z(n)     = z-coordinate  --  global axes

       kn       = generation
```

```
CSSSSSSSSSSSSSSSSSSSSSSSSSSSSSSSSSSSSSSSSSSSSSSSSSSSSSSSSSSSSSSSSSSSSSS
C  SUBROUTINE  ELEMK
CSSSSSSSSSSSSSSSSSSSSSSSSSSSSSSSSSSSSSSSSSSSSSSSSSSSSSSSSSSSSSSSSSSSSSS
C  READ INPUT CARD  --  ELEMENT TYPE IDENTIFICATION
C
C         # 10    --  SHELL ELEMENT      --  STIF1
C
C        (# 19    --  BOUNDARY ELEMENT   --  STIF2)
C        (# 22    --  BAR ELEMENT        --  STIF3)
C
C       Input cards required for element type(s) needed only
C
CRRRRRRRRRRRRRRRRRRRRRRRRRRRRRRRRRRRRRRRRRRRRRRRRRRRRRRRRRRRRRRRRRRRRRC
 READ INPUT CARD # 10  --  Quadrilateral Facet Shell Element
C
   read(55,*) [I5]

       ntype(i) = element type identification

              =  1  =  shell element

CSSSSSSSSSSSSSSSSSSSSSSSSSSSSSSSSSSSSSSSSSSSSSSSSSSSSSSSSSSSSSSSSSSSSSS
C  SUBROUTINE  STIF1
CSSSSSSSSSSSSSSSSSSSSSSSSSSSSSSSSSSSSSSSSSSSSSSSSSSSSSSSSSSSSSSSSSSSSSS
C  READ INPUT CARD # 11 --  SHELL ELEMENT MATERIAL AND LAYER DATA
C
   read(55,*) 8[I5]

       numsh  = number of shell elements

       numcn  = number of concrete material types  (4 max)

       numst  = number of reinf steel material types  (6 max)

       numps  = number of prestressing steel material types  (3 max)

       numsps = number of steel plate material types  (4 max)

       ntcl   = number of concrete layers systems  (10 max)

       ntsl   = number of smeared reinforcing steel layer systems  (24 max)

       ntspl  = number of steel plate layer systems  (10 max)
```

```
CSSSSSSSSSSSSSSSSSSSSSSSSSSSSSSSSSSSSSSSSSSSSSSSSSSSSSSSSSSSSSSSSSSSSSSS
C  SUBROUTINE INDATA
CSSSSSSSSSSSSSSSSSSSSSSSSSSSSSSSSSSSSSSSSSSSSSSSSSSSSSSSSSSSSSSSSSSSSSSSS
C  READ INPUT CARD # 12 (a)  --  CONCRETE MATERIAL PROPERTIES
C                             -- NUMCN (4 max)
C
C                             Omit if  NUMCN = 0
C
   read(55,*) 4[I5]  4[F10.0]

       i       = concrete material type number  (4 max)

       jmt(i)  =  1  input elastic concrete properties
               =  2  evaluate properties using ACI formulae

       jcr(i)  =  0  creep analysis not required
               =  1  input creep properties
               =  2  evaluate using ACI formulae

       jsh(i)  =  0  shrinkage analysis not required
               =  1  input shrinkage properties
               =  2  evaluate using ACI formulae

       fc28(i)  = concrete strength at 28 days (stress)

       cnu(i)   = Poisson's ratio

       rho(i)   = unit weight density
                  (if  jmt(i) = 2 -- must be input in  ib/in3)

       ctemp(i) = coefficient of thermal expansion

CRRRRRRRRRRRRRRRRRRRRRRRRRRRRRRRRRRRRRRRRRRRRRRRRRRRRRRRRRRRRRRRRRRRRRRC
 READ INPUT CARD # 12 (b)  --  CONCRETE STRESS-STRAIN CURVE
    PARAMETERS
C
   if(jmt(i).eq.1)
C
   read(55,*) 7[F10.0]

       ec(i)  = initial tangent modulus

       fcc(i) = compressive strength (stress)

       ftc(i) = tensile strength (stress)

       csc(i) = cracked shear constant/retention factor (max 1.0)
              -- recommended value of  0.1 to 0.5
```

```
      usc(i) = ultimate compressive strain

      ust(i) = ultimate tensile strain

      ecu(i) = maximum compressive strain

      gf(i)        = fracture energy for concrete type number i
                 --recommended value of 0.5 lb/in (0.1 N/mm)

      amagr(i) =  maximum aggregate size for concrete system type number i
                 --recommended value of 1.0 in (25.4 mm)

CRRRRRRRRRRRRRRRRRRRRRRRRRRRRRRRRRRRRRRRRRRRRRRRRRRRRRRRRRRRRRRRRRRRRRC
 READ INPUT CARDS # 12 (c) (i), (ii), (iii), (iv), (v)  --  CREEP DATA
C
C                        Omit creep input data if  JCR(I) = 2  or = 0
C
    if(jcr(i).eq.0) go to 300
    if(jcr(i).eq.2) go to 200
C---------------------------------------
    read(55,*) nage(i), nser(i)
C---------------------------------------
    na=nage(i)
    nb=nser(i)
C---------------------------------------
    read(55,*) (sage(i,j), j=1, na)
C---------------------------------------
    jj=na*nb
C---------------------------------------
    read(55,*) (aci(i,j), j=1, jj)
C---------------------------------------
    read(55,*) (w1(i,j),  j=1,   nb)
C---------------------------------------
    read(55,*) (w2(i,j),  j=1,4)

CRRRRRRRRRRRRRRRRRRRRRRRRRRRRRRRRRRRRRRRRRRRRRRRRRRRRRRRRRRRRRRRRRRRRRC
 READ INPUT CARDS # 12 (d), (e)  --  SHRINKAGE DATA
C
C                        Omit shrinkage input data if  JSH(I) = 2  or = 0
C
    if(jsh(i).eq. 0) go to 80
    if(jsh(i).eq.2) go to 80
C---------------------------------------
    read(55,*) (tepss(i,n), n=1, ntime)
C---------------------------------------
    continue
C---------------------------------------
    read(55,*) slump(i), size(i), rh(i)
```

```
CRRRRRRRRRRRRRRRRRRRRRRRRRRRRRRRRRRRRRRRRRRRRRRRRRRRRRRRRRRRRRRRRRRRRRC
 READ INPUT CARD # 13  --  REINFORCING STEEL MATERIAL PROPERTIES
C                          -- NUMST (6 max)
C
C                         Omit if  NUMST = 0
C
   read(55,*) [I5]  5[F10.0]

       n         = reinforcing steel material type number  (6 max)

       es(n)     = elastic modulus

       fys(n)    = yield strength (stress)

       estar(n)  = strain hardening modulus

       eus(n)    = ultimate strain

       estemp(n) = coefficient of thermal expansion

CRRRRRRRRRRRRRRRRRRRRRRRRRRRRRRRRRRRRRRRRRRRRRRRRRRRRRRRRRRRRRRRRRRRRRC
 READ INPUT CARD # 14  --  PRESTRESSING STEEL MATERIAL PROPERTIES
C                          -- NUMPS (3 max)
C
C                         Omit if  NUMPS = 0
C
   read(55,*) [I5]  4[F10.0]

       j         = prestressing steel material type number  (3 max)

       esp(j)    = elastic modulus

       fpy(j)    = yield strength (stress)

       estrp(j)  = strain hardening modulus

       eup(j)    = ultimate strain

CRRRRRRRRRRRRRRRRRRRRRRRRRRRRRRRRRRRRRRRRRRRRRRRRRRRRRRRRRRRRRRRRRRRRRC
 READ INPUT CARD # 14-A  --  STEEL PLATE MATERIAL PROPERTIES
C                            -- NUMSPS (4 max)
C
C                           Omit if  NUMSPS = 0
C
   read(55,*) [I5]  7[F10.0]

       j         = steel plate material type number  (4 max)
```

```
        csps(j)    = elastic modulus

        fysp(j)    = yield strength (stress)

        estrsp(j)  = strain hardening modulus

        eusp(j)    = ultimate strain

        spnu(j)    = Poisson's ratio

        cstemsp(j) = coefficient of thermal expansion

        unitwt(j)  = unit weight density

CRRRRRRRRRRRRRRRRRRRRRRRRRRRRRRRRRRRRRRRRRRRRRRRRRRRRRRRRRRRRRRRRRRRRC
 READ INPUT CARDS # 15 (a), (b) --  CONCRETE LAYER SYSTEMS
C                                   -- NTCL (10 max)
C
C                                  Omit if  NTCL = 0
C
   if (ntcl .eq. 0) go to 111
C
   do 110 i=1,ntcl
C-----------------------------------------

   read(55,*) 2[I5]

        l       = concrete layer system number  (10 max)

        nclay(l) = number of concrete layers in system  (20 max)

                -- minimum layer thickness = minimum aggregate size

C-----------------------------------------
   nc = nclay(l)
   nc1 = nc+1
C-----------------------------------------

   read(55,*) 8[F10.0]

        (zc(j,l), j=1, nc1)

        = local z-coordinate of concrete layer surfaces
          measured from reference plane surface
           -- negative to positive external surfaces of layer
```

```
CRRRRRRRRRRRRRRRRRRRRRRRRRRRRRRRRRRRRRRRRRRRRRRRRRRRRRRRRRRRRRRRRRRRRRC
 READ INPUT CARDS # 15-A (a), (b)  --  STEEL PLATE LAYER SYSTEMS
C                                      -- NTSPL (10 max)
C
C                                     Omit if  NTSPL = 0
C
   if (ntspl .eq. 0 ) go to 141
C
   do 140 i= 1,ntspl
   cefr(l)=0.0
   cohsn(l)=0.0
C---------------------------------------
   read(55,*) 3[I5]

        l         = steel plate layer system number  (10 max)

        nsplay(l) = number of steel plate layers in system  (20 max)

        ncrit(l)  = Yield criterion code  -- theory of plasticity

                  = 1  --  Von-Mises

                  = 2  --  Tresca

                  = 3  --  Mohr-Coulomb

                  = 4  --  Drucker-Prager
C
C---------------------------------------
C   If  NCRIT = 3 or 4 then input:
C
   if(ncrit(l) .eq. 3 .or. ncrit(l) .eq. 4)
C
   read(55,*) 2[F10.0]

        cefr(l)  = angle of friction in degress

        cohsn(l) = cohesion value

C---------------------------------------
   nsp=nsplay(l)
   nsp1=nsp+1
C---------------------------------------

   read(55,*) 8[F10.0]

        (zsp(j,l), j=1, nsp1)
```

```
        = local z-coordinate of steel plate layer surfaces
          measured from reference plane surface
           -- negative to positive external surfaces of layer

CRRRRRRRRRRRRRRRRRRRRRRRRRRRRRRRRRRRRRRRRRRRRRRRRRRRRRRRRRRRRRRRRRRRRRC
 READ INPUT CARDS # 16 (a), (b) --  SMEARED REINFORCING STEEL LAYER
     SYSTEMS
C                                    -- NTSL (24 max)
C
C                                   Omit if  NTSL = 0
C
   if (ntsl .le. 0) return
C
   do 130 i=1,ntsl
C---------------------------------------

   read(55,*) 3[15]

       l       = smeared reinforcing steel layer system number (24 max)

       nslay(l) = number of smeared steel layers in system  (7 max)


       iang(l)  = steel direction code

                  --  0  angle alpha from local x-axis
                  --  1  angle alpha from global x-axis

C---------------------------------------
   ns1 = nslay(l)
C---------------------------------------
   read(55,*) 2[15]  3[F10.0]

     ( j       = smeared reinforcing steel layer number  (7 max)

       mtn(j,l)  = material type number

       zs(j,l)   = local z-coord of mid-surface of layer
                   measured from reference plane surface
                    -- negative to positive mid-surfaces of layer

       ps(j,l)   = smeared layer thickness

       alph(j,l) = orientation angle alpha of steel

                  --   0 degrees  =  along IJ (horizontal direction)
                  --  90 degrees  =  along JK (vertical direction)
  n=1, ns1 )
```

```
CSSSSSSSSSSSSSSSSSSSSSSSSSSSSSSSSSSSSSSSSSSSSSSSSSSSSSSSSSSSSSSSSSSSS
C   SUBROUTINE  STIF1
CRRRRRRRRRRRRRRRRRRRRRRRRRRRRRRRRRRRRRRRRRRRRRRRRRRRRRRRRRRRRRRRRRRRRC
 READ INPUT CARD # 17  --  GRAVITY LOAD MULTIPLIERS -- GLOBAL
    DIRECTIONS
C
   read(55,*) 3[F10.0]

        (gm(i),i=1,3)

         =  gravity load multipiers in global X Y Z directions
           to calculate dead load components
            -- forces and moments  for self weight

        x-multipier =  0.00

        y-multipier =  0.00

        z-multipier =  -1.25

         -- can factor DL here, to multiply the concrete density value
CRRRRRRRRRRRRRRRRRRRRRRRRRRRRRRRRRRRRRRRRRRRRRRRRRRRRRRRRRRRRRRRRRRRRC
 READ INPUT CARD # 18 (a)  --  QUADRILATERAL FACET SHELL ELEMENT DATA
C
   read(55,*) 11[I5]  4[F6.0]  2[I2]

        mm        = shell element number

        (node(i), i=1,4) = nodes  I  J  K  L  -- counterclockwise direction:

        node I = i

        node J = j

        node K = k

        node L = l

        mc        = concrete material type number

        msp       = steel plate material type number

        ncl       = concrete layer system number

        nsl       = smeared reinforcing steel layer system number

        nspl      = steel plate layer system number
```

kn = generation

pn = normal distributed pressure on element (MPa)
-- used for live loads (factored here)

(pt(i), i=1,3) = intensity of components of additional uniformly distributed surface loads in the direction of the global x y z directions
-- used for wind loads:

pt(x) = x-direction component of pressure (MPa)

pt(y) = y-direction component of pressure (MPa)

pt(z) = z-direction component of pressure (MPa)

kopt = element option type
-- inplane and bending element
= 0 shell element

nebar = number of bar elements within shell element (max 4)
-- input in next section below

```
CRRRRRRRRRRRRRRRRRRRRRRRRRRRRRRRRRRRRRRRRRRRRRRRRRRRRRRRRRRRRRRRRRRRRRC
 READ INPUT CARD # 18 (b) -- BAR ELEMENTS DATA
C                          (located within a shell element)
C                           -- NEBAR (4 max)
C                          Omit if NEBAR = 0
C
   read(55,*) 2[I5]  7[F10.0]
```

ktb(j) = bar element type number

-- 1 prestressing steel bar
-- 2 reinforcing steel bar

ktyn(j) = material type number

x1n(j) = natural coordinate E1 of end 1 of bar

y1n(j) = natural coordinate N1 of end 1 of bar

x2n(j) = natural coordinate E2 of end 2 of bar

y2n(j) = natural coordinate N2 of end 2 of bar

bara(j) = bar cross-sectional area

```
        sigmo(j) = initial stress

        eoo(j)   = initial strain

CRRRRRRRRRRRRRRRRRRRRRRRRRRRRRRRRRRRRRRRRRRRRRRRRRRRRRRRRRRRRRRRRRRRRRRRRRRRRRRC
 READ INPUT CARD # 18 (c) --  TEMPERATURE VARIATION -- SHELL
     ELEMENT
C                              Omit if  ITEMP = 0

   read(55,*) 8[F10.0]

        (temp(i), i=1, nc)

         = temperature in each layer at each integration point
CSSSSSSSSSSSSSSSSSSSSSSSSSSSSSSSSSSSSSSSSSSSSSSSSSSSSSSSSSSSSSSSSSSSSSSSSSSSSSSS
C  SUBROUTINE  ELEMK
CSSSSSSSSSSSSSSSSSSSSSSSSSSSSSSSSSSSSSSSSSSSSSSSSSSSSSSSSSSSSSSSSSSSSSSSSSSSSSSS
C  READ INPUT CARD  --  ELEMENT TYPE IDENTIFICATION
C
C          # 19     --  BOUNDARY ELEMENT   --  STIF2
C
C         (# 10     --  SHELL ELEMENT      --  STIF1)
C         (# 22     --  BAR ELEMENT        --  STIF3)
C
C        Input cards required for element type(s) needed only
C
CRRRRRRRRRRRRRRRRRRRRRRRRRRRRRRRRRRRRRRRRRRRRRRRRRRRRRRRRRRRRRRRRRRRRRRRRRRRRRRC
 READ INPUT CARD # 19  --  Boundary Element
C
   read(55,*) [I5]

        ntype(i) = element type identification

              =  2  =  boundary element

CSSSSSSSSSSSSSSSSSSSSSSSSSSSSSSSSSSSSSSSSSSSSSSSSSSSSSSSSSSSSSSSSSSSSSSSSSSSSSSS
C  SUBROUTINE  STIF2
CSSSSSSSSSSSSSSSSSSSSSSSSSSSSSSSSSSSSSSSSSSSSSSSSSSSSSSSSSSSSSSSSSSSSSSSSSSSSSSS
C  READ INPUT CARD # 20  --  NUMBER OF BOUNDARY ELEMENTS
C
   read(55,*) [I5]

        numbd = number of boundary elements
```

```
CRRRRRRRRRRRRRRRRRRRRRRRRRRRRRRRRRRRRRRRRRRRRRRRRRRRRRRRRRRRRRRRRRRRRRC
 READ INPUT CARD # 21  --  BOUNDARY ELEMENT DATA
C
   read(55,*) 8[I5]  2[F10.0]  [E10.0]

       np    = node P -- location of boundary element

       ni    = orientation node I  of boundary element

       nj    = orientation node J  of boundary element

       nk    = orientation node K  of boundary element

       nl    = orientation node L  of boundary element

       kd    = displacement code

               --  0  node P  free to translate
               --  1  node P  translation or spring specified

       kr    = rotation code

               --  0  node P  free to twist
               --  1  node P  twist or spring specified

       kn    = generation

       sd    = specified displacement at node P

       sr    = specified twist at node P


       trace = specified stiffness of boundary element
               -- default value 10E06

CRRRRRRRRRRRRRRRRRRRRRRRRRRRRRRRRRRRRRRRRRRRRRRRRRRRRRRRRRRRRRRRRRRRRRC
 SUBROUTINE  ELEMK
CSSSSSSSSSSSSSSSSSSSSSSSSSSSSSSSSSSSSSSSSSSSSSSSSSSSSSSSSSSSSSSSSSSSSSS
C  READ INPUT CARD  --  ELEMENT TYPE IDENTIFICATION
C
C          # 22     --  BAR ELEMENT    --  STIF3
C
C         (# 10     --  SHELL ELEMENT      --  STIF1)
C         (# 19     --  BOUNDARY ELEMENT   --  STIF2)
C
C       Input cards required for element type(s) needed only
C
CRRRRRRRRRRRRRRRRRRRRRRRRRRRRRRRRRRRRRRRRRRRRRRRRRRRRRRRRRRRRRRRRRRRRRC
```

```
 READ INPUT CARD # 22  --  One-Dimensional Bar Element
C
   read(55,*) [I5]

        ntype(i) = element type identification

                 =  3  =  one-dimensional bar element

CSSSSSSSSSSSSSSSSSSSSSSSSSSSSSSSSSSSSSSSSSSSSSSSSSSSSSSSSSSSSSSSSSSSSSSSSSSS
C   SUBROUTINE  STIF3
CSSSSSSSSSSSSSSSSSSSSSSSSSSSSSSSSSSSSSSSSSSSSSSSSSSSSSSSSSSSSSSSSSSSSSSSSSSS
C   READ INPUT CARD # 23  --  ONE-DIMENSIONAL BAR ELEMENTS
C
   read(55,*) 2[I5]

        nbar  = number of one-dimensional bar elements

        nbtyp = number of bar element types  (3 max)

                -- uniaxial concrete member
                -- reinforcing steel member
                -- prestressing steel member

CRRRRRRRRRRRRRRRRRRRRRRRRRRRRRRRRRRRRRRRRRRRRRRRRRRRRRRRRRRRRRRRRRRRRRRRRRRC
 READ INPUT CARD # 24  --  BAR ELEMENT DATA
C
   read(55,*) 6[I5]  3[F10.0]

        mm    = bar number

        nodi  = node I  of bar element

        nodj  = node J  of bar element

        nbt   = bar type number

                -- 1  prestressing steel member
                -- 2  reinforcing steel member

        mtyn  = bar material type number

        kn    = generation

        barea = bar cross-sectional area

        sigo  = initial stress

        eo    = initial strain
```

```
CSSSSSSSSSSSSSSSSSSSSSSSSSSSSSSSSSSSSSSSSSSSSSSSSSSSSSSSSSSSSSSSSSSSSSS
C   SUBROUTINE  LOAD  -- NONLINEAR ANALYSIS -- LOAD APPLICATIONS
CSSSSSSSSSSSSSSSSSSSSSSSSSSSSSSSSSSSSSSSSSSSSSSSSSSSSSSSSSSSSSSSSSSSSSS
C   READ INPUT CARD # 25 (a)  --  LOAD STEPS AND ITERATION INCREMENTS
C
    read(55,*) 3[I5]  4[F10.0]  3[I5]

        nlstep = number of load steps to failure  = NLSTPS  (30 max)

        niter  = number of iterations allowed per load step  (15 max)

        nlj    = number of Type 1 nodes loaded -- Concentrated loads

        pdl    = uniformly distributed dead load factor
                 -- gravity load multipliers

        pdsl   = uniformly distributed live load factor
                 -- multiplier for  PN

        pspl   = prescribed displacement of springs
                 -- using boundary elements

        pbrl   = fraction of bar load for initial strain/stress
                 -- one-dimensional bar elements

        nstim  = number of increments for time-dependent analysis

        nitert = number of iterations for time-dependent analysis

        itmpsh = temperature/shrinkage indicator

                 --  0  temperature variation input
                 --  1  shinkage strains input

CRRRRRRRRRRRRRRRRRRRRRRRRRRRRRRRRRRRRRRRRRRRRRRRRRRRRRRRRRRRRRRRRRRRRRC
 READ INPUT CARD # 25 (b)
C
c   TYPE 2 NODES -- Input Forces and Fractions
c   ======================================
C   Additional Concentrated Loads
C
    if(njl2 .eq. 0) go to 1800

    do 25 i=1,njl2   -- type 2 nodes
C-----------------------------------------
    read(55,*) [I5]  6[F10.0]

        n  = type 2  node number loaded
```

```
      (rb2(j), j=1,6) = external applied loads:

        -- these nodal load values are normalized fractions of the
           ultimate total failure load of the structure

      Fx = x-direction force

      Fy = y-direction force

      Fz = z-direction force

      Fx = x-direction force

      Mx = x-direction moment

      My = y-direction moment

      Mz = z-direction moment
C-----------------------------------------
   read(55,*) 30[F10.5]

      (fact1(i), i=1,nlstps) = 30 max values  for type 2 nodes

      -- these values are actual total loads applied at every
         load step in the analysis for a total of NLSTPS values

CRRRRRRRRRRRRRRRRRRRRRRRRRRRRRRRRRRRRRRRRRRRRRRRRRRRRRRRRRRRRRRRRRRRRRC
 READ INPUT CARD # 25 (b)
C
c  TYPE 1 NODES -- Input Forces and Fractions
c  ==========================================
C  External Concentrated Loads
C==========================================
   1800 if(nlj.eq.0) go to 900

   do 21 i=1,nlj   -- type 1 nodes
C-----------------------------------------
   read(55,*) [I5]  6[F10.0]

      n  = type 1  node number loaded

      (rb(j), j=1,6) = external applied loads:

        -- these nodal load values are normalized fractions of the
           ultimate total failure load of the structure

      Fx = x-direction force
```

Fy = y-direction force

Fz = z-direction force

Fx = x-direction force

Mx = x-direction moment

My = y-direction moment

Mz = z-direction moment

```
C----------------------------------------
   read(55,*) 30[F10.5]

      (fact2(i), i=1,nlstps) = 30 max values  for type 1 nodes

      -- these values are actual total loads applied at every
         load step in the analysis for a total of NLSTPS values

CSSSSSSSSSSSSSSSSSSSSSSSSSSSSSSSSSSSSSSSSSSSSSSSSSSSSSSSSSSSSSSSSSSSSSSS
C   SUBROUTINE  TLOD1
CSSSSSSSSSSSSSSSSSSSSSSSSSSSSSSSSSSSSSSSSSSSSSSSSSSSSSSSSSSSSSSSSSSSSSSS
C   READ INPUT CARD # 25 (c)  --  LOAD TEMPERATURE DATA
C
C                              Omit if  ITEMP = 0
C
   read(55,*) 8[F10.0]

      (delt(l), l=1,nc)
```

***

****

****

END OF INPUT DATA

****

****

***